Development of Full Band Monte Carlo Methods for the Simulation of High Energy Electron Transport in Ultra-Wide Band Gap Semiconductors

Patrick John Williams

Thesis submitted for the degree of
Doctor of Philosophy

School of Mathematics, Statistics & Physics
Newcastle University
Newcastle upon Tyne
United Kingdom

1st May 2025

"Finally: it was stated at the outset, that this system would not be here, and at once, perfected. You cannot but plainly see that I have kept my word. But I now leave my [Condensed Matter] System standing thus unfinished, even as the great Cathedral of Cologne was left, with the crane still standing upon the top of the uncompleted tower. For small erections may be finished by their first architects; grand ones, true ones, ever leave the copestone to posterity. God keep me from ever completing anything. This whole book is but a draft - nay, but the draft of a draft. Oh, Time, Strength, Cash, and Patience!"

—Herman Melville, *Moby Dick*

Acknowledgements

This thesis marks the culmination of work that began in 2019 during lockdown. During this time I moved country twice, the second time to a city I'd never been to, and I've met so many wonderful people who have had a huge impact on my life while writing this thesis. As such, writing an appropriate acknowledgement is a Sissiphean task and I will do my best to thank everyone who helped me during this time.

First and foremost I must thank my supervisors Angela and Patrick Briddon. I am incredibly fortunate to have been offered this opportunity to begin with, and I have been doubly lucky to have had Angela as my supervisor. Despite your busy schedule and numerous commitments you have always found time to help with my work and to offer guidance when I got stuck. I will always be grateful for the support you offered when I had to take a break due to poor health and for reminding me to ease back into it when I returned. I must also thank Patrick Briddon for his help with all things DFT, in particular for helping me better understand AIMPRO.

Equally important were the friends I met during this time. Once the lockdowns had ended, and I was able to go to the office; I met Madhava and Patrick O'Neill. You stopped me going mad by offering frequent tea breaks as well as multiple distractions such as heardle and blasting the musical version of The War of The Worlds. Without you this thesis would have been completed a year ago. I must also thank the friends who I knew beforehand. Thank you Raffi and Arran for reminding me that sometimes I need to think about things other than my PhD and for staying in York so that I could see you fairly often during the past 4 years. Thank you also to Seb for sharing pictures of your cat.

None of this would have been possible without the support of my family. A huge thank you must go to my parents Shaun and Denise for always being there for me and encouraging me. Even though we live in different countries it feels like you are never far away and I truly appreciate everything you have done for me. Thank you to my brothers Dan, Tom and Joey for occasionally calling me for a chat, even if I didn't always appreciate it at the time.

Finally, the most thanks go to my life partner and fiancée Emily. I met you on the very first day of my PhD, but it feels like I have known you my entire life. Thank you for being my constant companion no matter my mood. Thank you for making me cups of tea, making me get out the house to go for mental health walks and answering my stupid questions about biology. Now that we're both done I can't wait to see where we go next.

Abstract

Silicon is approaching the physical limits of its capabilities in power electronics and so interest turns instead to ultra-wide bandgap semiconductors. This thesis is primarily concerned with understanding charge transport in two ultra-wide bandgap materials, diamond and cubic boron nitride (cBN). The wider band gaps of these materials mean that devices with smaller form factors and higher operating efficiencies can be fabricated, while their high thermal conductivities and radiation hardness makes them ideal for harsh environment applications.

Due to the nascent stage of research into ultra-wide bandgap semiconductors, theoretical methods are employed to make up for the dearth of experimental results. To this end, density functional theory was used to calculate the ideal crystal structure from which the band structure was calculated and stored on a non-uniform tetrahedral grid that refines itself to minimise error. This was then used to calculate the numerical density of states (DOS) which compared well with what was given in the literature on diamond and cBN. Density functional perturbation theory was also utilised in the calculation of scattering parameters that are generally calculated empirically.

A pre-existing Monte Carlo code was modified to enable the simulation of indirect band gap semiconductors with scattering rates determined by the numerically calculated DOS and scattering parameters.

These methods were initially applied to silicon to benchmark the process, and the simulation results showed excellent agreement with analytic simulation and experimental results. These methods were then applied to diamond and cBN. The results for diamond compared well with analytic simulation and experimental results given by the literature. Similarly, the results for cBN compared well with analytic simulations from literature. The use of these methods then allows for the simulation of semiconductors at higher energies and for new and emerging materials where experimental results are sparse and empirical methods cannot be employed.

Declaration of Authorship

I declare that the work presented in this thesis is my own, original work, and it has not been previously submitted for examinations for any other award. Where I have used the results, concepts, or work of others, they have been acknowledged at the point of use.

Some of the work that has formed part of this thesis has been the source of the following conference presentations:

Conference Presentations

- P. Williams, A. Dyson, P. Briddon, "An *ab initio* Study of Electron Transport in Ulltra-Wide Band Gap Semiconductors", UK Nitrides Consortium Winter Meeting, January 2024
- P. Williams, A. Dyson, P. Briddon, "An *ab initio* Study of Electron Transport in Ulltra-Wide Band Gap Semiconductors", UK Semiconductors Conference, July 2023
- P. Williams, A. Dyson, P. Briddon, "An *ab initio* Study of Electron Transport in Ulltra-Wide Band Gap Semiconductors", Condensed Matter and Quantum Materials, June 2023

Patrick J. Williams
May 1st, 2025

Contents

Acknowledgements ii

Abstract iii

Declaration of Authorship iv

Lists of Abbreviations and Symbols x

1 Introduction 1

1.1 Theoretical Framework . . . 2

1.1.1 Boltzmann Transport Equation . . . 2

1.1.2 Band Structure . . . 4

1.1.3 Scattering . . . 11

1.2 Ultra-Wide Band Gap Semiconductors . . . 13

1.2.1 Material Properties of Diamond and cubic Boron Nitride . . . 14

1.3 Outline of Thesis . . . 18

2 Monte Carlo Methods for Simulation 19

2.1 Band Structure Approximations in Monte Carlo Simulation . . . 20

2.2 General Monte Carlo Algorithm . . . 20

2.2.1 Initial Electron State . . . 21

2.2.2 Calculation of Free Flight Time . . . 22

2.2.3 Electron Free Flight . . . 23

2.2.4 Electron Scattering . . . 24

2.3 Scattering Rates . . . 27

2.3.1 Non-Polar Phonon Scattering . . . 27

2.3.2 Polar Scattering 29
2.3.3 Charged Impurity Scattering 32
2.3.4 Equivalent Valley Scattering 33
2.3.5 Other Scattering Mechanisms 34
2.4 Bulk Ensemble Monte Carlo Simulation 35
2.5 Summary 36

3 Solving the Many-Body Electron Problem 37
3.1 The Many-Body Electron Problem 37
3.2 Born-Oppenheimer Approximation 38
3.3 Mean Field Methods 40
3.4 Density Functional Theory 42
3.4.1 Hohenberg and Kohn 43
3.4.2 Kohn-Sham Equations 44
3.4.3 The Exchange and Correlation Functional 45
3.4.4 Self-Consistent Field Cycles 46
3.4.5 Basis Functions 46
3.4.6 Pseudopotentials 48
3.4.7 Density Functional Perturbation Theory 48
3.5 Summary 51

4 *Ab Initio* Scattering Rates 52
4.1 Density of States Calculation 53
4.1.1 Definitions 54
4.1.2 Initial Grid 55
4.1.3 Refining the Grid 56
4.1.4 Density of States Interpolation 58
4.1.5 Valley Allocation 59
4.2 Deformation Potential Calculation 60
4.3 Choice of DFT Program 64
4.4 Summary 64

5 Selection of DFT Inputs **65**
5.1 AIMPRO 66
5.1.1 Test Results 67
5.2 Quantum Espresso 69
5.2.1 Test Results 69
5.3 Summary 71

6 Bulk Silicon Results **73**
6.1 Properties of Silicon 74
6.2 Density of States Calculation 74
6.2.1 Band Structure and Effective Mass 74
6.2.2 Comparison to AIMPRO DOS 76
6.2.3 Non-Parabolicity Constant Calculation 77
6.3 Scattering Parameters 78
6.3.1 Phonon Dispersion 78
6.3.2 Acoustic Deformation Potential 78
6.3.3 Optical Deformation Potential 80
6.4 MC Simulation 84
6.4.1 Parameters 84
6.4.2 Scattering Rates 84
6.4.3 Simulation Results 86
6.5 Summary 88

7 Diamond Results **90**
7.1 Density of States Calculation 91
7.1.1 Band Structure and Effective Mass 91
7.1.2 Comparison to AIMPRO DOS 92
7.1.3 Non-Parabolicity Constant Calculation 93
7.2 Scattering Parameters 94
7.2.1 Phonon Dispersion 94
7.2.2 Acoustic Deformation Potential 96

7.2.3 Optical Deformation Potential 99

7.3 MC Simulation 103

7.3.1 Parameters 103

7.3.2 Scattering Rates 103

7.3.3 Simulation Results 107

7.4 Summary 110

8 Cubic Boron Nitride Results 112

8.1 Density of States Calculation 113

8.1.1 Band Structure and Effective Mass 113

8.1.2 Comparison to AIMPRO DOS 114

8.1.3 Non-Parabolicity Constant Calculation 115

8.2 Scattering Parameters 117

8.2.1 Phonon Dispersion 117

8.2.2 Acoustic Deformation Potential 117

8.2.3 Optical Deformation Potential 121

8.3 MC Simulation 124

8.3.1 Parameters 124

8.3.2 Scattering Rates 124

8.3.3 Simulation Results 128

8.4 Summary 131

9 Conclusions and Further Work 134

9.1 Density of States Calculation 134

9.2 Deformation Potentials Calculations 135

9.3 MC Simulations 137

9.4 Sensitivity Analysis 138

9.5 Further Work 138

A Calculation of the Coefficients of Cubic Splines 141

B Formulation of Density Of States Equation 143

C Derivation of Density Functional Perturbation Theory 149

D DFT Input Parameters 152

D.1 Si 152

D.2 Diamond 153

D.3 Boron 154

D.4 Nitrogen 154

E Results for Variable Intervalley Separation in cBN 155

Bibliography 158

List of Figures

1.1 Three parts of the BTE in position-momentum space. 3
1.2 Kronig-Penney 1D approximations of a crystal 5
1.3 Band structure of the Kronig-Penney Model 6
1.4 DFT Band Structure of Si 7
1.5 DFT Conduction Bands of Si with Analytic Approximations 10
1.6 DFT Diamond Band Structure 16
1.7 DFT cBN Band Structure 17

2.1 f and g scattering processes between six equivalent valleys 34

3.1 Growth of number of basis sets compared to number of particles. 41

4.1 The $k_z = 0$ plane of the discretisation of the irreducible wedge of Si. 57

5.1 AIMPRO Si Inputs Test. 67
5.2 AIMPRO diamond Inputs Test. 68
5.3 AIMPRO cBN Inputs Tests. 69
5.4 Quantum Espresso Si Inputs Tests. 70
5.5 Quantum Espresso diamond Inputs Tests. 71
5.6 Quantum Espresso cBN Inputs Tests. 72

6.1 DFT Band Structure of Si. 75
6.2 Comparison of Si Numerical DOS. 76
6.3 Conduction Band Minimum Valley DOS in Si. 77
6.4 Polar Dependence of the Acoustic Deformation Potential in Si. 79
6.5 Si Electron-Phonon BZ overlay for f-type scattering 81

6.6 Si Electron-Phonon BZ overlay for g-type scattering 81
6.7 Scattering Rates for Si. 86
6.8 Velocity-Field Results for bulk Si. 87
6.9 Energy-Field Results for bulk Si. 87

7.1 DFT Band Structure of diamond 91
7.2 Comparison of diamond Numerical DOS 92
7.3 Conduction Band Minimum Valley DOS in diamond. 93
7.4 Second Conduction Band Valley DOS in diamond. 94
7.5 Diamond Phonon Dispersion 95
7.6 Polar Dependence of the Acoustic Deformation Potential in diamond. 96
7.7 Diamond Electron-Phonon BZ overlay for f-type scattering 100
7.8 Diamond Electron-Phonon BZ overlay for g-type scattering 100
7.9 Diamond Electron-Phonon BZ overlay for intervalley scattering 102
7.10 Low Energy Scattering Rates for Conduction Band Minimum Valley in diamond.105
7.11 High Energy Scattering Rates for Conduction Band Minimum Valley in diamond.105
7.12 Scattering Rates Second Conduction Band Valley in diamond. 106
7.13 Velocity-Field Results for diamond. 107
7.14 Energy-Field Results for diamond. 109

8.1 DFT Band Structure of cBN. 113
8.2 Comparison of cBN Numerical DOS. 114
8.3 Conduction Band Minimum Valley DOS in cBN. 116
8.4 Second Conduction Band Valley DOS in cBN. 116
8.5 cBN Phonon Dispersion. 118
8.6 Polar Dependence of the Acoustic Deformation Potential in cBN. 119
8.7 cBN Electron-Phonon BZ overlay for g-type scattering 121
8.8 cBN Electron-Phonon BZ overlay for g-type scattering 122
8.9 123
8.10 Low Energy Scattering Rates for Conduction Band Minimum Valley in cBN. . 126
8.11 High Energy Scattering Rates for Conduction Band Minimum Valley in cBN. . 126
8.12 Scattering Rates Second Conduction Band Valley in cBN. 128

8.13 Velocity-Field Results for cBN. 129
8.14 Energy-Field Results for cBN. 130
8.15 Occupancy-Field Results for cBN. 131

B.1 Intersections of a Plane with a Tetrahedron. 144

E.1 Velocity-Field Results for cBN. 156
E.2 Energy-Field Results for cBN. 156
E.3 Occupancy-Field Results for cBN. 157

List of Tables

6.1 Comparison of Acoustic Deformation Potential in Si. 80

6.2 Comparison of Optical Deformation Potential in Si. 83

6.3 Parameters for MC simulation of Si. 85

7.1 Comparison of Acoustic Deformation Potential in diamond. 97

7.2 Comparison of Optical Deformation Potential in diamond. 101

7.3 Parameters for MC simulation of diamond. 104

8.1 Parameters for MC simulation of cBN. 125

D.1 Description of AIMPRO inputs Si 152

D.2 Description of AIMPRO inputs diamond 153

D.3 Description of AIMPRO inputs boron 154

D.4 Description of AIMPRO inputs nitrogen 154

Lists of Abbreviations and Symbols

These lists describe abbreviations and symbols used throughout this document.

List Of Abbreviations

ADP Acoustic Deformation Potential

BTE Boltzmann Transport Equation

BZ Brillouin Zone

CBM Conduction Band Minimum

cBN cubic Boron Nitride

DFPT Density Functional Perturbation Theory

DFT Density Functional Theory

DOS Density of States

EPM Empirical Pseudopotential Methods

FBMC Full Band Monte Carlo

FCC Face Centred Cubic

GGA Generalised Gradient Approximation

HEG Homogeneous electron gas

HGH Hartwigsen-Goedeker-Hutter

IW Irreducible Wedge

LDA Local Density Approximation

MC Monte Carlo

NPOP Non-polar Optical Phonon

ONCV Optimised norm-conserving Vanderbilt

Si Silicon

TISE Time Independent Schrödinger Equation

UWBG Ultra-Wide Band Gap

WBG Wide-Band Gap

List Of Symbols

$1/q_D$ Debye length

$\hbar$ Reduced Planck's Constant, $\hbar = \frac{h}{2\pi}$

$\mathbf{F}$ External Force

$\mathbf{k}$ Electron Wave Vector

$\mathbf{p}$ Momentum Vector

$\mathbf{q}$ Phonon Wave Vector

$\mathbf{r}$ Position Vector

$\mathbf{v}$ Velocity

Ω Crystal Volume

$\psi(\mathbf{r})$ Electronic Wavefunction

$|H_{\mathbf{k}',\mathbf{k}}|$ Scattering Mechanism Matrix Element

E Energy

$f(\mathbf{r}, \mathbf{p}, t)$ Distribution Function

k, k' Magnitude of Electron Wave Vector before and after scattering event

m^* Effective Electron Mass

m_e Free Electron Mass

$P(\phi', \theta')d\phi' d\theta'$ Probability density function for post scattering azimuthal, ϕ', and polar, θ', angles

q Magnitude of Phonon Momentum Vector

Chapter 1

Introduction

The simulation of carrier transport is an important tool in both the academic setting and the world at large. In the mid 20th century, semiconductors revolutionized the way the world works by allowing for the transition from vacuum tubes to the smaller, cheaper and more efficient transistor. As companies have fulfilled the prediction of Moore [1], the number of transistors on an integrated circuit has roughly doubled every 18 months while also becoming drastically cheaper. This has resulted in the mass production of electronics that are now indispensable to life in the modern world.

Despite their widespread use, there is still a lot of active research being done on semiconductors. One such area of interest is in wide-band gap (WBG) and ultra-wide band gap (UWBG) semiconductors. WBG semiconductors, as the name suggests, have large band gaps usually defined as lying in the range of 2.4-3.5 eV giving these materials characteristics that make them desirable over existing devices made from conventional semiconducting materials such as silicon (Si) . WBG electronic devices can be made with a smaller profile than Si devices while still sustaining the same applied voltage which results in lower conduction and switching losses allowing for higher switching speeds. WBG semiconductors also boast higher operating temperatures and can handle greater voltages than conventional devices making them ideal for high temperature and power applications [2–4]. All of these properties make them ideal for power electronics and use in the electrical power sector as WBG semiconductors promise smaller more efficient devices than the Si devices that dominate the market. Similarly, UWBG semiconductors have band gaps beyond 3.5 eV, much greater than those of the conventional semiconductors. This group of materials has all the benefits of the WBG group discussed

above plus the possibility of extending the working wavelengths of photonics into the deep UV as well as increased thermal stability and radiation hardness, this would make these materials suitable for applications in harsh environments such as space borne technology or detectors inside nuclear reactors [5–8]. However, due to the nascent stage of UWBG semiconductor research there are still many challenges to overcome before these materials can be utilised. The work presented here looks at two UWBG semiconductors that have gained much interest in recent years, diamond and cubic Boron Nitride (cBN) , and investigates how *ab initio* methods may be used to extend Monte Carlo (MC) simulations such that electron transport inside these materials can be modelled accurately at higher fields. This chapter opens with a discussion of the major theoretical framework underpinning electron transport and semiconductor physics before going on to give a description of the properties of diamond and cBN in section 1.2, finally closing with an outline of the thesis.

1.1 Theoretical Framework

1.1.1 Boltzmann Transport Equation

To model the transport of charge carriers, the probability that a given charge carrier is within the volume $d\mathbf{r}$ in real space and within a region $d\mathbf{p}$ in momentum space during time t must be known. This is given by the distribution function $f(\mathbf{r}, \mathbf{p}, t)$ which is found by solving the Boltzmann Transport Equation (BTE), an equation describing the statistical behaviour of a system in a non-equilibrium state. The BTE can be found by first considering a small change to the distribution function, $\delta f(\mathbf{r}, \mathbf{p}, t)$, within the region $\delta\mathbf{r}\delta\mathbf{p}$ during the time interval δt, as shown in figure 1.1. Within this interval, $\mathbf{v}\delta f(\mathbf{r}, \mathbf{p}, t)\delta\mathbf{p}\delta t$ particles will enter $\delta\mathbf{r}\delta\mathbf{p}$ and $\mathbf{v}\delta f(\mathbf{r} + \delta\mathbf{r}, \mathbf{p}, t)\delta\mathbf{p}\delta t$ will exit along the space axes and $\mathbf{F}\delta f(\mathbf{r}, \mathbf{p}, t)\delta\mathbf{r}\delta t$ particles will enter $\delta\mathbf{r}\delta\mathbf{p}$ and $\mathbf{F}\delta f(\mathbf{r}, \mathbf{p}+\delta\mathbf{p}, t)\delta\mathbf{r}\delta t$ will exit along the momentum axes. Here $\mathbf{v} = \frac{d\mathbf{r}}{dt}$ is the velocity of the particles and $\mathbf{F} = \frac{d\mathbf{p}}{dt}$ is the external force applied. This can be expressed mathematically as,

$$\frac{\delta f(\mathbf{r}, \mathbf{p}, t)}{\delta t}\delta\mathbf{r}\delta\mathbf{p} = \mathbf{v}(f(\mathbf{r}, \mathbf{p}, t) - f(\mathbf{r} + \delta\mathbf{r}, \mathbf{p}, t))\delta\mathbf{p} + \mathbf{F}(f(\mathbf{r}, \mathbf{p}, t) - f(\mathbf{r}, \mathbf{p} + \delta\mathbf{p}, t))\delta\mathbf{r} \quad (1.1)$$

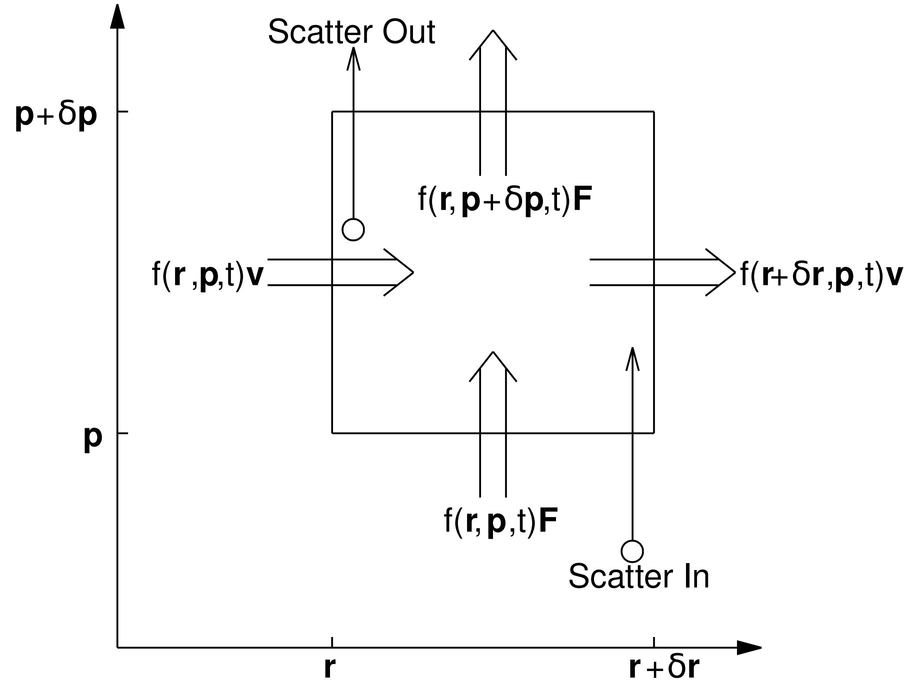

Figure 1.1: Figure shows the three parts of the BTE in position-momentum space.

Dividing equation 1.1 by $\delta\mathbf{r}\delta\mathbf{p}$ and finding the limit as $\delta\mathbf{r}, \delta\mathbf{p}, \delta t \rightarrow 0$ then gives,

$$\frac{df(\mathbf{r},\mathbf{p},t)}{dt} = -\mathbf{v}\cdot\nabla_{\mathbf{r}}f(\mathbf{r},\mathbf{p},t) - \mathbf{F}\cdot\nabla_{\mathbf{p}}f(\mathbf{r},\mathbf{p},t) \tag{1.2}$$

However, equation 1.2 assumes a collisionless system. Charge carriers experience scattering events, see section 1.1.3, which are assumed to instantaneously change the particles' momentum but not their position, shown in figure 1.1 by scatter in and scatter out. Adding a term that takes into account the effect of collisions gives the full BTE.

$$\frac{df(\mathbf{r},\mathbf{p},t)}{dt} = -\mathbf{v}\cdot\nabla_{\mathbf{r}}f(\mathbf{r},\mathbf{p},t) - \mathbf{F}\cdot\nabla_{\mathbf{p}}f(\mathbf{r},\mathbf{p},t) + \left.\frac{\partial f(\mathbf{r},\mathbf{p},t)}{\partial t}\right|_{coll} \tag{1.3}$$

Unfortunately, as this is a partial differential equation with 6 dimensions, it is impossible to find distribution functions that solve it analytically in all but a few simple cases. Steady state solutions have been found, but these generally rely on having prior knowledge of the system or making assumptions to simplify the problem being solved [9]. Chapter 2 describes in detail how a Monte Carlo simulation method which may be used to solve the BTE numerically [9].

1.1.2 Band Structure

To solve the BTE, the way the charge carriers move through the material of interest must be modelled. As the charge carriers of interest here are electrons, this amounts to solving the Time independent Schrödinger equation (TISE) .

$$-\frac{\hbar^2}{2m_e}\nabla^2\psi(\mathbf{r}) + V(\mathbf{r})\psi(\mathbf{r}) = E\psi(\mathbf{r}) \tag{1.4}$$

Solving the TISE for a single electron far away from any potential results in a simple relation between the energy, E, and the wave vector, $\mathbf{k}$, of the electron,

$$E(\mathbf{k}) = \frac{\hbar^2 k^2}{2m_e} \tag{1.5}$$

where $\hbar$ is the reduced Planck's constant, m_e is the electron mass and k is the magnitude of the electron wave vector. As $\hbar\mathbf{k}$ gives the momentum of a particle, equation 1.5 is equivalent to the kinetic energy of the electron in classical physics.

Electron in Periodic Potential

Consider, instead, that the electron is placed within a crystal lattice with a periodic potential, $V(\mathbf{r})$ such that,

$$V(\mathbf{r}) = V(\mathbf{r} + a\mathbf{T}) \tag{1.6}$$

where $\mathbf{T}$ is a translation vector of the lattice and a is an integer. The wavefunction of such an electron can be found using Bloch's theorem [10] which states that the wavefunction of a particle in a periodic potential is the product of a plane wave and a periodic function,

$$\psi(\mathbf{r}) = u(\mathbf{r})e^{i\mathbf{k}\cdot\mathbf{r}} \tag{1.7}$$

where $u(\mathbf{r})$ is a function which has the same periodicity as the potential,

$$u(\mathbf{r}) = u(\mathbf{r} + a\mathbf{T}) \tag{1.8}$$

This simplifies the problem and means that the solution can be obtained by considering only the unit cell, as this solution will apply to all other cells.

Kronig-Penney Model

Kronig and Penney [11] simplified the problem further by considering a 1D array of square potentials representing the potential barriers an electron experiences between atoms in a crystal, shown in figure 1.2. Solving equation 1.4 in 1D with a potential of V_0 and width b at the limit where $b \to 0$ and $V_0 \to \infty$ such that $V_0 b = constant$, yields the solution,

$$\frac{P}{\alpha a} sin(\alpha a) + cos(\alpha a) = cos(ka) \tag{1.9}$$

where $\alpha = \sqrt{2m_e E}/\hbar$, $P = \frac{\beta^2 ba}{2}$ and $\beta = \sqrt{2m_e(V_0 - E)}/\hbar$. Clearly this equation can only hold true while the left-hand side lies between -1 and +1 and as α is proportional to energy, there are regions of energy for which there is no solution to the electron wavefunction.

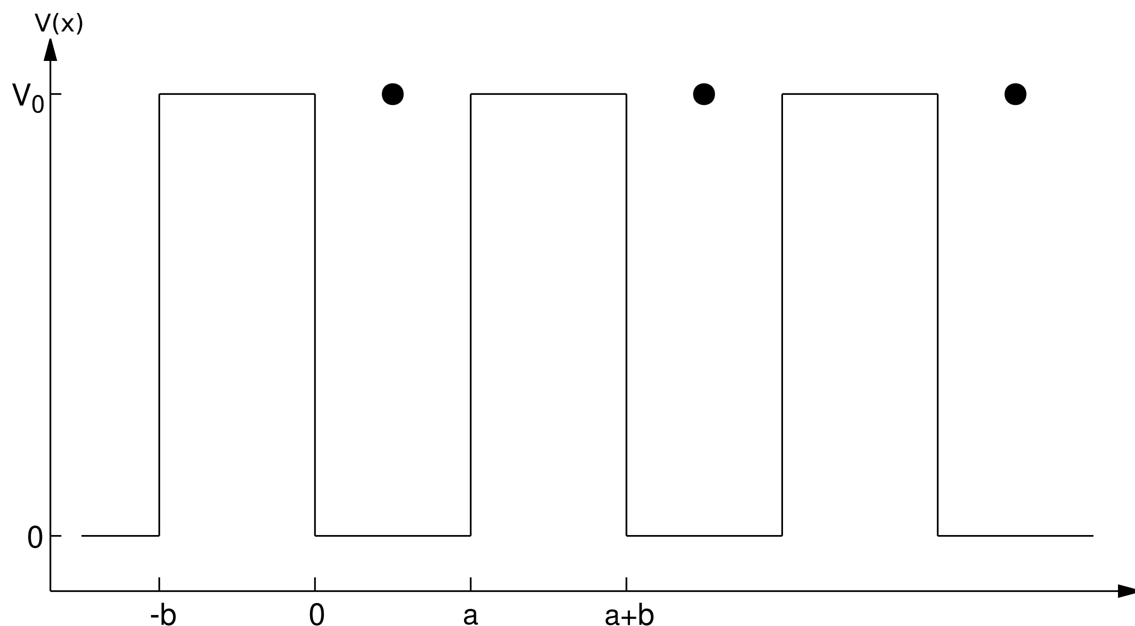

Figure 1.2: Kronig-Penney 1D approximations of a crystal

Figure 1.3 shows the allowed energies as a function of ka according to the Kronig-Penney model where $P = \frac{3\pi}{2}$. As can be seen, there are bands of forbidden energy between the allowed energy states. Figure 1.3 also illustrates Bloch's Theorem as it shows the periodic nature of the solution to the wave equation. As the solution is periodic, all the information

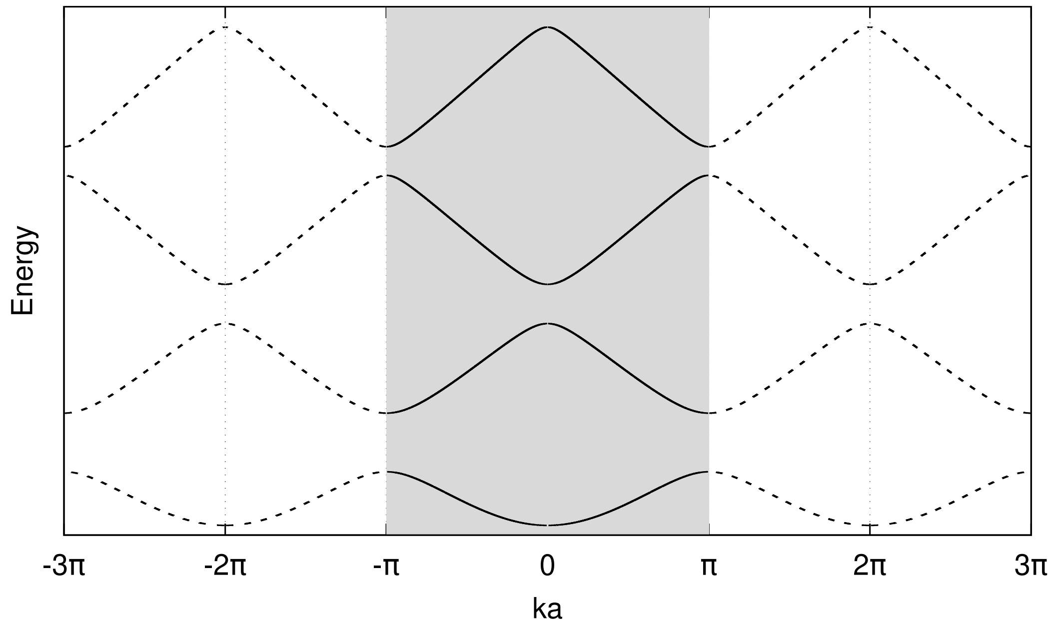

Figure 1.3: Band structure of the Kronig-Penney Model

about the electronic wavefunction is contained within the domain between $ka = -\pi$ and $ka = \pi$, known as the first Brillouin Zone (BZ), and as such only this region needs to be considered. In this model the solution is symmetric around the BZ centre, however this is not always the case in more physically realistic systems, but symmetry operations may still allow for an irreducible region that holds the minimum information necessary for the entire system. Appendix A of reference [12] shows how the minimum volume of the Irreducible Wedge (IW) is found for the BZ of all the Bravais Lattices.

The Kronig-Penney model also shows that there are infinitely many bands, however, electrons will generally populate the lowest energy bands possible with excitation only possible due to external fields or thermal energy. At 0K, the highest energy band populated with electrons is termed the valence band and the lowest energy band without electrons is termed the conduction band.

Real Band Structure

The Kronig-Penney model is a good demonstration of how the band structure arises from the periodic nature of the crystal lattice, but real band structures are much more complex due to their 3D nature and the interactions of the electrons with nuclei of different charges and sizes, and all the other electrons. Figure 1.4 shows the band structure for silicon as calculated using

the Density Functional Theory (DFT) program AIMPRO [13] (see chapter 3 for more detail) with the valence bands in black and the conduction bands in red. As can be seen, there are many valleys, peaks, saddle points, crossings and anti-crossing within the band structure.

As such, finding an analytic solution to the full band structure is impossible and finding solutions numerically is computationally expensive. Due to this expense, many MC simulations use models with analytical forms to approximate the band structure over given ranges of energy close to the conduction band valley minima.

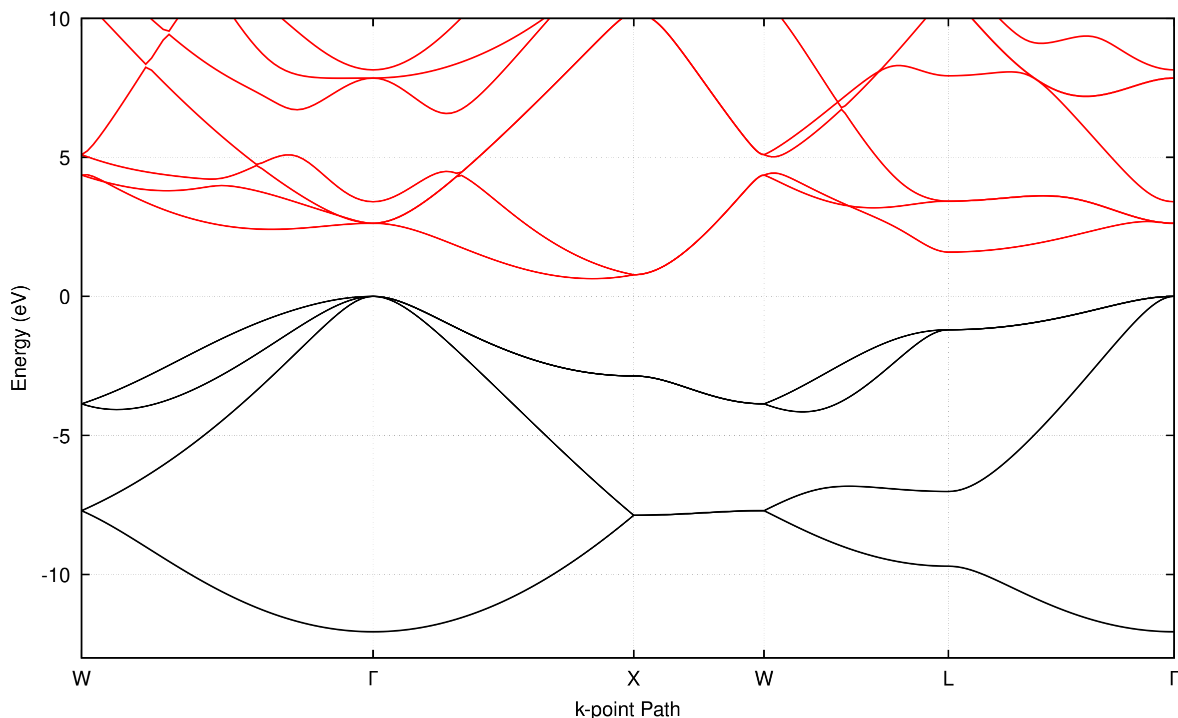

Figure 1.4: Band structure of Si calculated using DFT with valence bands shown in black and conduction bands in red. Energy scale relative to the valence band maximum.

Analytic Approximations

Electrons will generally populate the states closest to the valley minima. Therefore, considering the valley as a Taylor series expansion, near the valley minima the higher order terms become vanishingly small and the dispersion can be considered parabolic. This is the simplest case where the electron's energy is considered to be like that of the free electron of equation 1.5 shifted by the energy of the minimum [9],

$$E(\mathbf{k}) = \frac{\hbar^2 k^2}{2m^*} + E_0 \tag{1.10}$$

where E_0 is the energy at a valley minimum and m^* is the effective mass of the electron,

$$(m^*)^{-1} = \frac{1}{\hbar^2}\frac{d^2E(\mathbf{k})}{dk^2} \tag{1.11}$$

and describes the motion of an electron as if it were a classical particle with mass m^*.

This approximation is often not enough as the effective mass for parabolic bands is constant, whereas the curvature of the band structure does change as the energy increases. In order to take this into account, the Schrödinger equation can be solved using the Bloch theorem and $\mathbf{k}\cdot\mathbf{p}$ perturbation theory to get the so called $\mathbf{k}\cdot\mathbf{p}$ approximation [14],

$$\frac{\hbar^2k^2}{2m^*} + E_0 = \gamma(E(\mathbf{k})) \tag{1.12}$$

where $\gamma(E(\mathbf{k}))$ is generally of the form

$$\gamma(E(\mathbf{k})) = E(\mathbf{k})(1+\alpha E(\mathbf{k}))^2 \tag{1.13}$$

α is a first order non-parabolicity constant, which is generally found using [15]

$$\alpha = \frac{1}{E_g}\left(1-\frac{m^*}{m_e}\right)^2 \tag{1.14}$$

and E_g is the difference between the valence band maximum and the conduction valley minimum.

An important quantity used in the determination of scattering rates that is derived from the band structure is the Density of States (DOS) , which is defined as the number of electron states per unit volume per unit energy. To find the DOS in 3D for analytic bands of the form given in equation 1.12, first plot the allowed wavevectors on a grid. Each allowed state will take up a volume of $\frac{(2\pi)^3}{\Omega}$ and so the number of allowed states per unit volume in reciprocal space is $\frac{1}{(2\pi)^3}$. The number of allowed states for a wavevector of magnitude k is then found as those that are contained by the volume of a spherical shell of radius k and thickness dk multiplied by the number of allowed states per unit volume,

$$g(k) = \frac{1}{(2\pi)}4\pi k^2 dk \tag{1.15}$$

By substitution of the relationship between the wavevector and the energy,

$$k = \left(\frac{2m^*}{\hbar^2}\right)^{\frac{1}{2}} (\gamma(E_{\mathbf{k}}) - E_0)^{\frac{1}{2}} \tag{1.16}$$

$$dk = \frac{1}{2}\left(\frac{2m^*}{\hbar^2}\right)^{\frac{1}{2}} (\gamma(E_{\mathbf{k}}) - E_0)^{-\frac{1}{2}} \frac{d\gamma(E_{\mathbf{k}})}{dE_{\mathbf{k}}} \tag{1.17}$$

the DOS per unit energy is given by,

$$g(E_{\mathbf{k}}) = \frac{1}{4\pi^2}\left(\frac{2m^*}{\hbar^2}\right)^{\frac{3}{2}} (\gamma(E_{\mathbf{k}}) - E_0)^{-\frac{1}{2}} \frac{d\gamma(E_{\mathbf{k}})}{dE_{\mathbf{k}}} \tag{1.18}$$

This is the DOS for spherical bands, however, not all bands are spherical and so the energy-wavevector relationship may be of the form

$$\gamma(E(\mathbf{k})) - E_0 = \frac{\hbar^2 k_a^2}{2m_a^*} + \frac{\hbar^2 k_b^2}{2m_b^*} + \frac{\hbar^2 k_c^2}{2m_c^*} \tag{1.19}$$

where a, b and c are three perpendicular directions. This can be rewritten as and equation of an ellipsoid,

$$\begin{aligned} 1 &= \frac{k_a^2}{\frac{2m_a^*}{\hbar^2}(\gamma(E(\mathbf{k})) - E_0)} + \frac{k_b^2}{\frac{2m_b^*}{\hbar^2}(\gamma(E(\mathbf{k})) - E_0)} + \frac{k_c^2}{\frac{2m_c^*}{\hbar^2}(\gamma(E(\mathbf{k})) - E_0)} \\ &= \frac{k_a^2}{\alpha^2} + \frac{k_b^2}{\beta^2} + \frac{k_c^2}{\epsilon^2} \end{aligned} \tag{1.20}$$

This ellipsoidal band can be transformed into a spherical one by defining an effective wavevector,

$$k_{eff} = (\alpha\beta\epsilon)^{1/3} = \left(\frac{2m_{DOS}^*}{\hbar^2}\right)^{\frac{1}{2}} (\gamma(E_{\mathbf{k}}) - E_0)^{\frac{1}{2}} \tag{1.21}$$

where $m_{DOS}^* = (m_a^* m_b^* m_c^*)^{1/3}$ is the DOS effective mass.

Figure 1.5 shows the band structure of the conduction bands of Si using DFT (see chapter 3) in red and the analytic approximations of the X, L and Γ valleys in black dashed line, generated using data from table 3.1 of reference [16]. These approximations work for low energy electrons around the band minima but as the energy increases so does the error [17, 18]. One major issue with these methods is that there are no energy maxima and so these methods lack the negative mass transport present at higher energies in semiconductors [19].

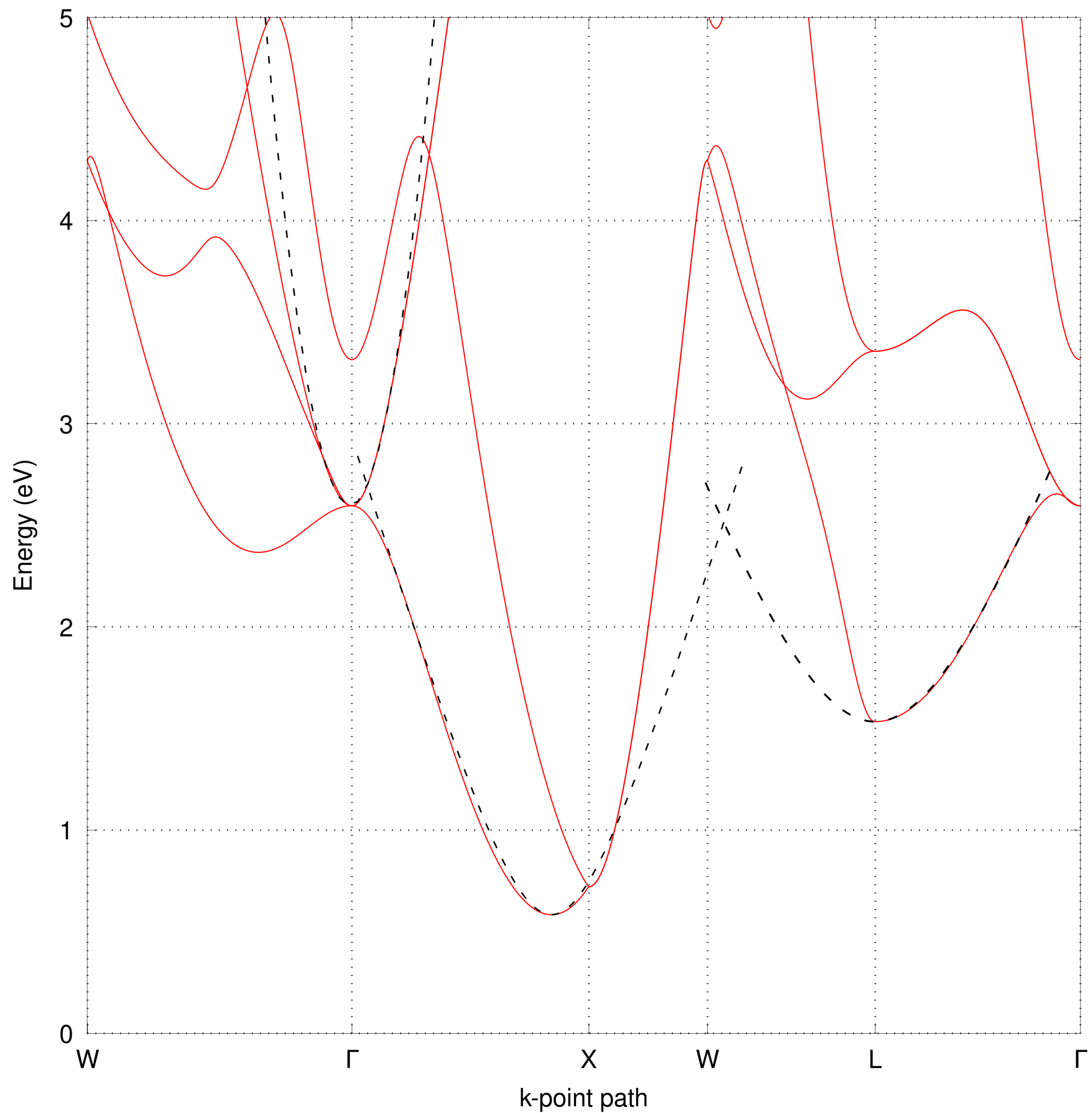

Figure 1.5: Conduction band of Si calculated using DFT in red and the analytic approximations of the valleys in black dashed lines.

Nevertheless, these analytic and 'full band cuisine' methods [20] are implemented due to their simplicity and because it is frequently stated that Full Band Monte Carlo (FBMC) simulations are too computationally expensive [19, 21–23], quoting the methods of M.V. Fischetti and S.E. Laux [24] and the method detailed in Full Band and Beyond by K. Hess [25]. However, one of the reasons these methods are so expensive is due to their exhaustive search for a final electron state after scattering. Despite this computational complexity, there are many examples of these methods still being applied in the literature [17, 26–32]. This will have been due to the fact that analytic methods fail to capture the features of the band structure at higher energies.

In this thesis, a full band structure is employed for the calculation of quantities used in electron transport to more accurately model the distribution function at higher energies.. Chapter 4 details how the full band structure is calculated using DFT and discretised into a non-uniform tetrahedral grid.

1.1.3 Scattering

As shown in equations 1.6 to 1.8, solving the TISE for a periodic potential gives wavefunctions with the same periodicity. As the charge carriers are then in an eigenstate of this idealised potential they would move undisturbed through the crystal, which describes the first two terms on the right-hand side of the BTE, equation 1.3. However, these aren't particularly useful on their own as it would mean the carriers would accelerate linearly, dependent on the strength of the external field applied, to unrealistic velocities. In reality the crystal potential isn't perfectly periodic, but is perturbed by various mechanisms. If a charge carrier encounters one of these changes to the potential while drifting it is scattered, altering its momentum and possibly its energy. As shown by the BTE, the inclusion of scattering is important for the correct distribution function to be found.

There are many scattering mechanisms that affect the motion of electrons, but in this work only the most common mechanisms are presented, scattering induced by impurities and by lattice vibrations. In the following sections these are described and the method by which scattering rates are treated quantum mechanically is introduced.

Impurity Scattering

Impurity scattering occurs due to impurities in the crystal that are introduced either deliberately or accidentally during crystal growth. These imperfections disrupt the usually periodic nature of the crystal thus, altering the potential around the impurities. When electrons encounter these abnormal fields their motion is disrupted and they are scattered.

These disruptions are generally localised, therefore this scattering method is dominant at low fields as the electrons are moving slower and so spend more time in the region of the impurity [15, 33].

Lattice Vibrations

At temperatures above 0K, thermal energy causes oscillations in the lattice, deforming slightly the otherwise periodic potential. As the mass of an electron is much smaller than that of the nuclei in a crystal, electrons can react instantaneously to the changes in the crystal potential which disrupts their motion and causes them to scatter. To simplify the treatment, the energy of these vibrations can be quantised into quasi-particles called phonons with a wave-vector, $\mathbf{q}$[1]; and frequency $\omega_{\mathbf{q}}$. The phonons can then be treated as if they have momentum $\hbar\mathbf{q}$ and energy $\hbar\omega_{\mathbf{q}}$, which then allows for the application of the principles of conservation of energy and momentum when dealing with their interaction with electrons. If an electron with wave-vector $\mathbf{k}$ and energy $E_{\mathbf{k}}$ absorbs/emits a phonon with wave-vector $\mathbf{q}$ and energy $\hbar\omega_{\mathbf{q}}$, through conservation of momentum and energy the electron would have wave-vector $\mathbf{k} \pm \mathbf{q}$ and an energy of $E_{\mathbf{k}} \pm \hbar\omega_{\mathbf{q}}$ after the event, where $+$ indicates absorption and $-$ emission.

In solids, there are two major phonon modes that can occur, low frequency acoustic modes which occur when neighbouring nuclei oscillate in phase with each other; and high frequency optical modes which occur when neighbouring atoms oscillate out of phase with each other. These two modes can then be subdivided into longitudinal and transverse modes, with multiple of each existing in the crystal [10]. Acoustic and optical phonons can deform the periodic crystal structure resulting in acoustic and non-polar optical phonon scattering when the electrons interact with the potential altered by the phonons [15, 33, 9]. In polar materials, optical and acoustic phonons can also induce polarisation waves in the crystal, causing macroscopic time-dependent electric fields that the electrons can scatter from [15, 33, 9]. These scattering methods are known as polar optical phonon and piezoelectric phonon scattering. Polar optical scattering is generally the dominant scattering mechanism in polar materials whereas piezoelectric scattering is only dominant at low temperatures.

Fermi's Golden Rule

The scattering mechanisms discussed can be considered as weak perturbations to the crystal potential and as such can be treated using Fermi's Golden Rule, this states that the probability per unit time that an electron in initial state $\mathbf{k}$ will transition to final state $\mathbf{k}'$ via any mechanism

[1] $\mathbf{q}$ is used for the wave-vector of phonons and $\mathbf{k}$ for charge carriers to avoid confusion, following convention.

is given by [15, 9],

$$S(\mathbf{k}, \mathbf{k}') = \frac{2\pi}{\hbar} |H_{\mathbf{k}',\mathbf{k}}|^2 \delta(E_{\mathbf{k}'} - E_{\mathbf{k}}) \tag{1.22}$$

where $|H_{\mathbf{k}',\mathbf{k}}|$ is the scattering mechanism matrix element that links the initial and final states and $E_{\mathbf{k}}$ & $E_{\mathbf{k}'}$ are the electron energies of the initial and final states, respectively. To obtain the three-dimensional scattering rate, equation 1.22 can be integrated over all potential final states in a crystal with volume Ω. For a scattering mechanism where the electron energy is changed by E_{trans}, the scattering rate is given by,

$$W(\mathbf{k}) = \frac{\Omega}{(2\pi)^3} \frac{2\pi}{\hbar} \int |H_{\mathbf{k}',\mathbf{k}}|^2 \delta(E_{\mathbf{k}'} - E_{\mathbf{k}} \mp E_{trans}) d^3\mathbf{k}' \tag{1.23}$$

where $\mp$ arises from the absorption (-) and emission (+) of energy as part of the scattering event e.g. through absorption/emission of a phonon.

1.2 Ultra-Wide Band Gap Semiconductors

As stated previously, one area of interest in condensed matter research is into wide and ultra-wide band gap semiconductors. The width of the forbidden energy range in WBG semiconductors corresponds to wavelengths of light from green to the near ultraviolet and research into the direct band gap materials GaN and InGaN in the 1990s lead to the fabrication of efficient blue LEDs, for which Isamu Akasaki, Hiroshi Amano and Shuji Nakamura were awarded the Nobel Prize in physics in 2014 [34, 5]. This achievement lead to an explosion in research which means WBG semiconductors are indispensable to modern optoelectronics with applications in full colour displays, white light illumination, blue-violet LASER diodes and UV light sources. Other than optoelectronics, materials like GaN and SiC have been studied for their electronic properties as, with the advent of electric vehicles and the phasing out of fossils fuels, more strain will be placed on the electrical power sector where most power devices are Si based. It has been predicted that at least 70% of electricity generated passes through power electronics and as this number will only increase in the coming years [2, 3, 35], it is necessary to reduce losses and increase device performance to reduce the consumption of power by these devices. A wider band gap results in a plethora of characteristics that make these materials ideal replacements for Si based devices that make up the vast majority of devices used in

power electronics. 4H-SiC and GaN have band gaps around 3.2 [36] eV and 3.4 eV [37, 36], respectively, roughly 3 times that of Si. Consequently, the breakdown voltage of these two materials is an order of magnitude greater than that of Si, meaning that devices can be made 1/10 the size while still sustaining the same applied voltage resulting in lower switching and conduction losses, in turn allowing for higher switching speeds meaning smaller more efficient devices [2–4].

As UWBG semiconductors have even greater band gaps, they have the potential to be utilised in ways that WBG materials cannot. However, due to the nascent stage of semiconductor research into these materials, they are not as well understood as WBG and conventional semiconductors. In particular, two UWBG materials, diamond and cBN, have been the subject of recent interest and form much of the work of this thesis. Therefore, the following sections discuss properties of these two materials that make them desirable as semiconductors.

1.2.1 Material Properties of Diamond and cubic Boron Nitride

Structural Properties and Growth

Being isoelectronic with one another, the two carbon basis and boron nitride pair basis form similar allotropes, the best known of which are the stable sp2 bonded hexagonal phase (graphene and hexagonal boron nitride) and the metastable sp3 bonded cubic phase (diamond and cBN). While the 2D phases and their interaction are of extreme interest [38], the focus here is on the 3D cubic phases of the two materials. Both form Face Centred Cubic (FCC) structures with lattice constants of 3.567 Å[39, 40] and 3.615 Å[36, 41] for diamond and cBN, respectively. The short bond lengths of these two materials results in strong covalent bonds between neighbouring atoms giving them Vickers hardnesses of 100 GPa (diamond) [39] and 70 GPa (cBN) [39, 41] making them the hardest and second-hardest materials available and for this reason they are commonly used as abrasives and cutting edges [42–45]. The synthesis of diamond and cBN powders under high temperature and high pressure for industrial applications has been possible since the 1960s [46–48], and larger crystals of both materials can also be grown via various gas-phase deposition methods, however, this technology is more mature for diamond where wafers larger than 90 mm and of high structural quality have been

produced through pure chemical vapour deposition [49, 50, 7], whereas the growth of cBN requires the growing surface to be bombarded by energetic ions [43, 7].

Thermal Properties

Diamond and cBN also top the list in terms of heat transfer, possessing thermal conductivities of 2200 $Wm^{-1}K^{-1}$ [7, 5] and 740 $Wm^{-1}K^{-1}$ [36], respectively. This puts their thermal conductivity way above GaN (130 $Wm^{-1}K^{-1}$) [36], SiC (360-490 $Wm^{-1}K^{-1}$) [36] and Si (140-156 $Wm^{-1}K^{-1}$) [51, 52]; making them ideal as heat sinks. Due to its incredibly high thermal conductivity, diamond substrates are already used as heat sinks in various commercial technologies such as semiconductor lasers and microwave devices. This high thermal conductivity also makes diamond and cBN ideal for applications in power electronics where the operation is currently limited by heat removal.

Radiation Hardness

One area in which UWBG semiconductors excel over conventional and WBG semiconductors is in their ability to operate in high radiation environments. Commercial SiC and GaN devices are being adopted into many applications, however susceptibility to damage by ion bombardment impedes their use in space and other harsh environment applications. Both NASA and the ESA have been researching the use of WBG semiconductors for communication and control devices, and this research has shown that both GaN and SiC will fail at less than 50% of their rated voltage [5, 2] due to radiation from cosmic rays, with SiC fairing much worse. There are GaN devices that are space qualified however the operation of these devices is limited to 300V[2, 53–66].

The radiation hardness of UWBG materials, in combination with their thermal properties, makes them ideal for use in harsh environment applications. This radiation hardness comes from the large band gaps, as impacting radiation would require a larger energy to produce an electron-hole pair. The heterostructures formed between two UWBG materials could also form larger energy gap discontinuities, a region in which a two-dimensional electron gas can form. This could be used in a high electron mobility transistor [5] similar to GaN devices currently rated for high radiation applications [67] as the electron channel has reduced sensitive to

radiation induced damage.

Electrical Properties

As UWBG semiconductors, both diamond and cBN have band gaps much greater than that of Si at around 5.5eV [68, 69] and 6.4eV [36, 41], respectively. Figures 1.6 and 1.7 show the

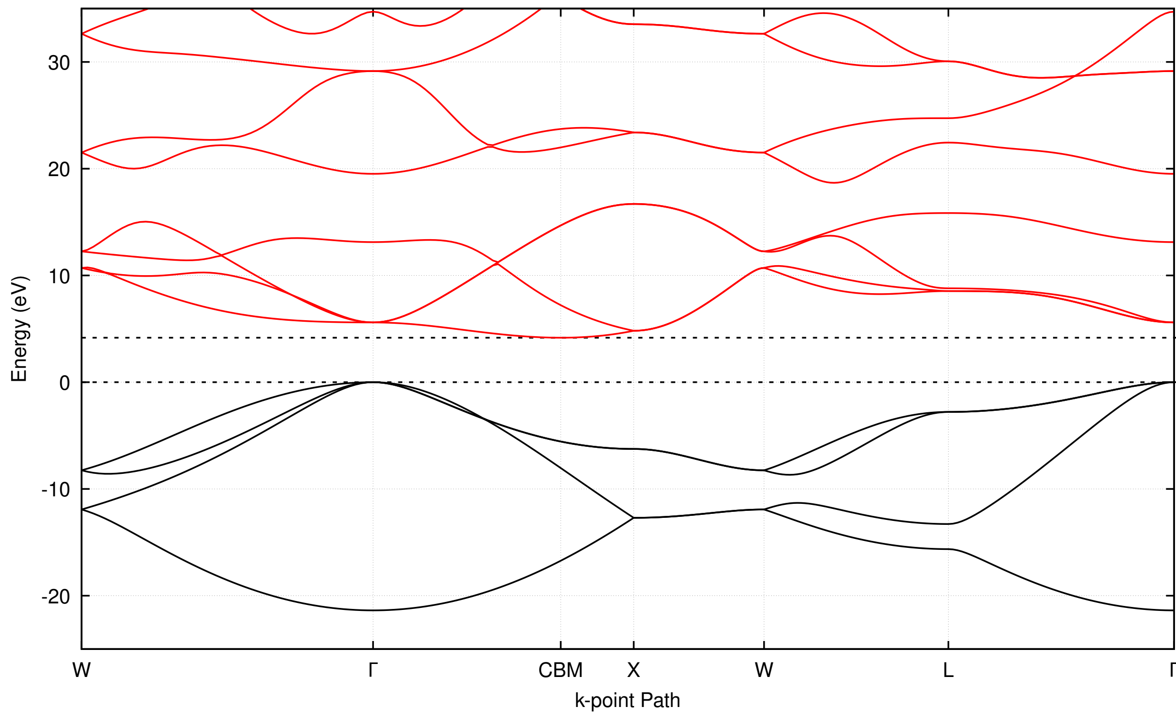

Figure 1.6: The band structure of diamond with the valence bands in black and the conduction bands in red calculated using DFT program AIMPRO. Energy scale relative to the valence band maximum. Conduction band minimum labelled as CBM

band structures of diamond and cBN calculated numerically using the DFT program AIMPRO [13]. As can be seen, these two materials both have indirect band gaps with conduction band minima along the Δ directions at roughly 72% towards the X point for diamond, labelled CBM , and on the X point for cBN. The symmetry of the Δ direction means that both these materials have 6 equivalent conduction band minima. The large band gaps lead to arguably the highest breakdown fields for any semiconductors with a value greater than 10 MV/cm [70, 71] for diamond and greater than 15 MV/cm for cBN [5] leading to a Baliga figure of merit [72], defined to minimise the conduction losses in power FETs, much greater than that of SiC and GaN. Diamond has also been shown to have high low-field electron mobilities with a value greater than 2000 cm^2/Vs for natural diamond [73] and Isberg *et al.* giving a value of 4500 cm^2/Vs in a high purity single crystal of diamond grown using CVD [74]. On

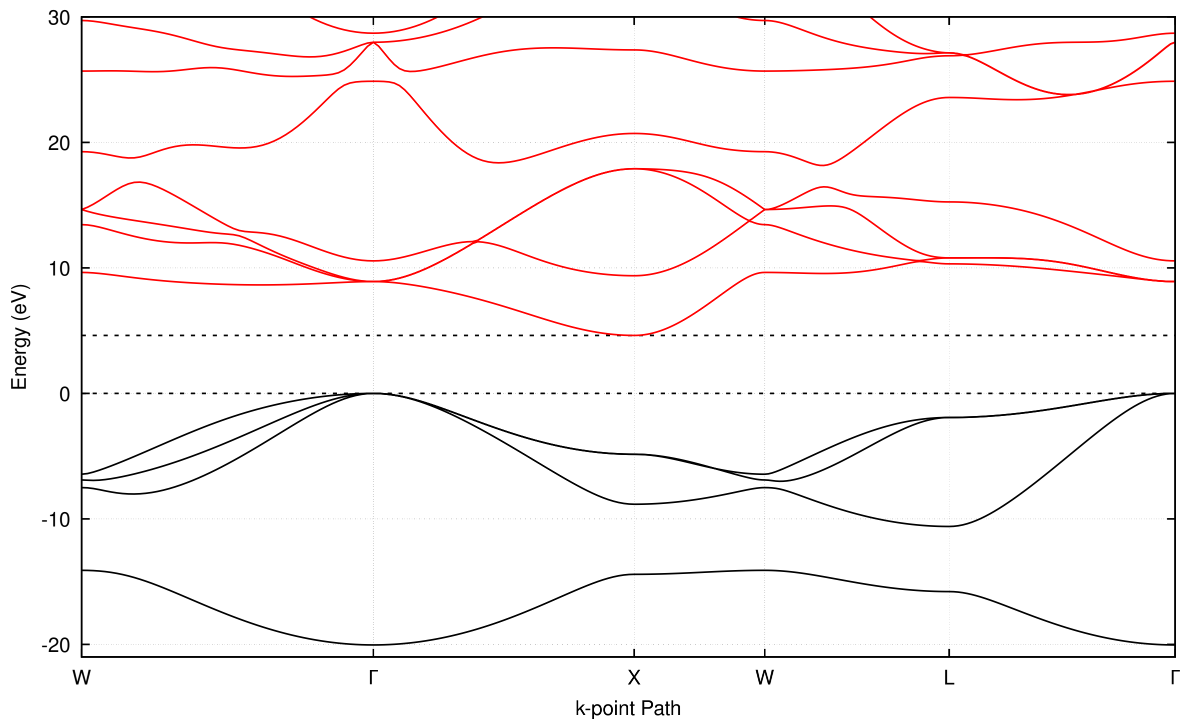

Figure 1.7: The band structure of cBN with the valence bands in black and the conduction bands in red calculated using DFT program AIMPRO. Energy scale relative to the valence band maximum.

the other hand, cBN has been measured to have a low-field mobility between 200 cm^2/Vs [75] and 825 cm^2/Vs [73] but theoretical simulations of electron transport in cBN measure mobilities somewhat higher at somewhere between 600 cm^2/Vs [75] and 1610 cm^2/Vs [73]. This disparity between the experimental and theoretical mobilities is generally put down to the high concentration of defects in the samples used in the experimental measurements [75].

For these materials to be used effectively, it is necessary for there to be dopants that introduce states in the band gap from which the electrons can be excited into the conduction band (n-type doping) or to which electrons can be excited into from the valence band (p-type doping). P-type doping with a substitutional boron atom in diamond has been observed in nature [40], and so by introducing boron containing molecules to the gas mixture in CVD, lab grown p-type diamonds can be produced, leading to an acceptor level at 0.37 eV above the valence band maximum. However, nature has not been forthcoming with what dopant is best for n-type doping of diamond. N-type doping is possible with a substitutional phosphorus however, this leads to a fairly deep donor level at 0.6 eV below the conduction band which are too low for efficient operation at ambient temperatures [76–79]. On the other hand, cBN can be doped with a variety of both n-type and p-type impurities [80–91]. Despite this advantage over diamond, there has been difficulty in studying these materials due to the issues with

synthesis, as mentioned previously, and the formation of unintentional defects in the samples grown.

1.3 Outline of Thesis

Chapter 2 details Monte Carlo methods used to solve the BTE and derives the equations for scattering rates. Chapter 3 introduces DFT and what approximations are needed for it to be a useful computational method. Chapter 4 then describes the methods applied to Si, diamond and cBN. The first part shows how the band structure produced by DFT is stored on a non-uniform tetrahedral grid and how this can then be used to calculate the DOS. The second part of chapter 4 then describes how DFT can be employed to calculate scattering parameters.

Chapter 5 details how the particular pseudopotentials were chosen for the DFT programs involved. Chapters 6, 7 and 8 then present the results of applying the methods of chapter 4 to Si, diamond and cBN, respectively; to calculate scattering parameters and DOS that are used in MC simulation. This thesis is brought to a close in chapter 9 by drawing conclusions from this work and discussing potential future extensions.

Chapter 2

Monte Carlo Methods for Simulation

As mentioned previously in section 1.1.1, the BTE can only be solved analytically in a few simple cases [9], however, approximations can be applied to the system and numerical methods employed to find solutions. Many of these methods, such as the relaxation time approximation, are only applicable at low fields with elastic or isotropic scattering. Other methods, such as the numerical drift diffusion methods, use a set of simplified equations but are not suitable for sub-micron or non-equilibrium simulation that this project wished to study. To calculate the transport properties of electrons, the most accurate results would be produced via numerical solution of the Schrödinger equation, however, the computational cost for even a few particles would be prohibitively expensive. Striking a balance of accuracy without prohibitive computational cost and applicability to calculating charge carrier transport in devices is solving the BTE via MC simulation. Despite being a semi-classical method, the solution found to the BTE are sufficiently accurate, however, quantum corrections can be added if necessary.

This chapter will describe the MC method used, and the changes made to incorporate full band methods into the scattering step. The MC methods presented here are based on the book by Tomizawa [15] and were implemented by Naylor [19] in FORTRAN 95 code. This chapter first discusses the band structure models that have been used in the implementation before going on to introduce the algorithms for MC simulation. Finally, the necessary scattering methods employed are introduced and derived.

2.1 Band Structure Approximations in Monte Carlo Simulation

For a given conduction electron with momentum $\mathbf{k}$, the conduction band defines its energy, $E(\mathbf{k})$; velocity, $\frac{dE(\mathbf{k})}{d\mathbf{k}}$; and the DOS, which effects the scattering rate of the electrons. The accuracy of the band structure used is then one of the most important aspect of the simulation. The most accurate simulation would then be achieved by calculating the band structure numerically to generate a full band model. However, MC simulations generally use the analytic approximations of section 1.1.2 for the band structure. The aim of this work was to improve the MC simulation results by including more information from the numerical band structure. Chapter 3 details how DFT is used to calculate the electronic structure and chapter 4 shows how this is stored and used to calculate the DOS. The MC simulation has then been modified to use the numerical DOS to calculate the scattering rates of various mechanisms.

In MC simulations that use analytic approximations to the band structure, the local minima and their surrounding structure are considered to be independent valleys rather than as a continuous distribution. Each valley is then defined using an analytic $E - \mathbf{k}$ relationship such as those given in section 1.1.2 which can be used to calculate the necessary quantities for MC simulation. This reduces the complexity and, therefore, the time taken for the simulation to run. These analytic approximations are accurate at low energies, however, at higher energies they deviate from the true band structure; have no maxima; and, as they are treated as seperate, electrons can only move between valleys through scattering events. These approximations can then lead to slight overestimation of the average energies, however if the correct parameters and energy ranges are chosen for MC simulations with analytic band structure approximations, then there is good agreement with experimental data.

2.2 General Monte Carlo Algorithm

The MC method aims to simulate the motion of charge carriers through position and momentum space. Much like the BTE, equation 1.3, it can be split into a drift and a scattering section. The duration of free flight and a scattering mechanism are chosen stochastically and so the simulation relies on the generation of random numbers. After pre-generating the

scattering rates for the necessary mechanism for later use and setting the initial conditions, the following algorithm is employed for MC simulation of bulk materials.

1. Free flight time, τ, for an electron is found.
2. Electron drifts for time τ and the position and momentum are updated.
3. Scatter electron according to a randomly chosen scattering mechanism.

These three steps are repeated until some predetermined time limit is reached.

2.2.1 Initial Electron State

Before the simulation can start, the electron energies and momenta are initialised according to the Fermi-Dirac function so as to have a realistic distribution.

$$f(E_{\mathbf{k}}) = \frac{1}{1 + exp\left(\frac{E_{\mathbf{k}} - E_F}{k_B T}\right)} \tag{2.1}$$

Here, k_B is the Boltzmann constant, T is the lattice temperature, E_F is the Fermi energy, and $0 \leq f(E_{\mathbf{k}}) \leq 1$. This can be simplified by assuming that $exp\left(\frac{E_{\mathbf{k}} - E_F}{k_B T}\right) >> 1$ and $E_F = 0$, as it corresponds to the conduction band minimum, giving,

$$f(E_{\mathbf{k}}) = \frac{1}{exp\left(\frac{E_{\mathbf{k}}}{k_B T}\right)} \tag{2.2}$$

which can be rearranged in terms of energy to give,

$$E_{\mathbf{k}} = -\frac{3k_B T}{2} ln(f(E_{\mathbf{k}})) \tag{2.3}$$

As $0 \leq f(E_{\mathbf{k}}) \leq 1$, the initial energy of a given electron can be found by generating a random number from a uniform distribution. The band structure approximation can then be used to calculate the magnitude of the initial wave vector from the energy and the direction generated using two more random numbers giving all directions equal probability.

The selection of a wavevector based on the energy is only simple while using analytic band structures and is much more complex when using full band structures. However, this

complexity can be reduced by precalculating some essential values and storing them in well-structured lookup tables [18, 21–23, 92–100].

2.2.2 Calculation of Free Flight Time

The free flight time of an electron with energy, $E_{\mathbf{k}}$, depends on the total scattering rate at $E_{\mathbf{k}}$. To save on computation time, these scattering rates are pre-generated over a predetermined range of energies with given energy intervals for each valley, and then stored in lookup tables. This decrease in computational complexity comes at the cost of a decrease in accuracy as the scattering rates for an electron are found using the interval they are in, however, this can be reduced by choosing appropriately sized intervals. The probability per unit time that an electron travels for time τ before scattering is given by [9, 15],

$$P(\tau)d\tau = W_T(E_{\mathbf{k}})exp\left(-\int_0^{\tau} W_T(E_{\mathbf{k}})dt\right)d\tau \tag{2.4}$$

where $W_T(E_{\mathbf{k}})$ is the sum of all N scattering rates at $E_{\mathbf{k}}$, given by

$$W_T(E_{\mathbf{k}}) = \sum_{j=1}^{N} W_j(E_{\mathbf{k}}) \tag{2.5}$$

The free flight time can then be found by solving equation 2.4 for τ, however, the integral in equation 2.4 cannot be solved analytically due to the form of $W_T(E_{\mathbf{k}})$. To overcome this issue, an extra scattering term is added, called the self scattering term, such that the total scattering rate is constant for all energies.

$$\Gamma = \sum_{j=0}^{N} W_j(E_{\mathbf{k}}) \tag{2.6}$$

The self scattering term, $W_0(E_{\mathbf{k}})$, is defined such that it makes no change to the momentum, $\mathbf{k}$, of the electron.

Equation 2.4 can then be rewritten as

$$P(\tau)d\tau = \Gamma exp\left(-\int_0^{\tau} \Gamma dt\right)d\tau \tag{2.7}$$

The duration of the free flight must be determined by equation 2.7 and is then found by generating a uniformly distributed random number between 0 & 1. For this, the probability of selecting a random number between r & $r + dr$ must be equal to the probability of the free flight time being between τ & $\tau + d\tau$, therefore,

$$P(r)dr = P(\tau)d\tau \tag{2.8}$$

For a uniform distribution of numbers between 0 & 1, $P(r) = 1$, therefore equation 2.7 becomes,

$$dr = \Gamma exp\left(-\int_0^\tau \Gamma dt\right) d\tau \tag{2.9}$$

which can be solved to find the free flight time before a collision τ_c based on a random number from a uniform distribution,

$$\tau_c = -\frac{ln(r_1)}{\Gamma} \tag{2.10}$$

The self scattering rate must be chosen such that $W_0(E_\mathbf{k}) \geq 0$ for all values of $E_\mathbf{k}$ and so $\Gamma \geq W_T(E_\mathbf{k})$ For all energies. However, it is desirable to set Γ to be as small as possible to minimise the number of self scattering events. Currently, Γ is set equal to $MAX(W_T(E_\mathbf{k}))$.

2.2.3 Electron Free Flight

At the start of the drift phase, the free flight time is generated using equation 2.10 and the electron then drifts for that amount of time. As a uniform electric field is assumed, the change in momentum of the electron is found using,

$$\Delta\mathbf{k} = -\frac{e\mathbf{F}}{\hbar}\tau \tag{2.11}$$

where $\Delta\mathbf{k}$ is the update to the wave vector over time τ, e is the electron charge and $\mathbf{F}$ is the external applied field. The rate of change of $\mathbf{k}$ is assumed to be constant throughout the drift step, so when the position is updated it is assumed that the velocity of the electron throughout the drift step is also constant, corresponding to the mean of the wave vector.

$$\Delta\mathbf{x} = \frac{\hbar}{m*}\left(\mathbf{k}_{initial} + \frac{\Delta\mathbf{k}}{2}\right) \tag{2.12}$$

2.2.4 Electron Scattering

After drifting, an electron will be scattered and so a scattering method must be selected at random and the electron state post scattering determined. A scattering mechanism is selected through the use of the cumulative scattering probabilities, $\Lambda_n(E_{\mathbf{k}})$ defined as,

$$\Lambda_n(E_{\mathbf{k}}) = \frac{\sum_{j=1}^{n} W_j(E_{\mathbf{k}})}{\Gamma}, \text{ for } n = 1, 2, ..., N \tag{2.13}$$

which are the successive summations of the scattering rates normalised by Γ from equation 2.6. A uniformly distributed random number, r_2, is generated and compared to Λ_n, the nth scattering mechanism is chosen if the condition

$$\Lambda_{n-1}(E_{\mathbf{k}}) < r_2 \leq \Lambda_n(E_{\mathbf{k}}) \tag{2.14}$$

is met. If $r_2 > \Lambda_N(E_{\mathbf{k}})$ then the self scattering method is chosen and no change is made to the energy or momentum of the electron.

Once the scattering mechanism is selected, the electron state post scattering must be determined. The change in energy is straight forward and depends on the scattering mechanism chosen and the magnitude of the post scattering wave vector, $|k'|$, can then easily be found. Determining the direction of the wave vector, however, is more involved. To find the new direction, the post scattering polar, θ', and azimuthal, ϕ', angles post scattering must be found. If the scattering mechanism is isotropic then the scattering angles can be found by considering that the probability density, $P(\phi', \theta')d\phi' d\theta'$, is proportional to a uniform distribution of points on a sphere of radius k', which represents all the allowed post scattering states, as such the probability density function is $P(\phi', \theta')d\phi' d\theta' = sin(\theta')d\phi' d\theta'$ as any value of ϕ' is allowed. Therefore, ϕ' and θ' can be determined through the use of two uniformly distributed random numbers, r_3 and r_4,

$$\phi' = 2\pi r_3 \tag{2.15}$$

$$cos(\theta') = 1 - 2r_4 \tag{2.16}$$

For the anisotropic processes, impurity, polar optical and piezoelectric scattering; the determination of ϕ' stays the same as the transition rates are independent of the azimuthal angle but the determination of θ' is more complicated.

The probability of scattering between 0 and θ' can be found by solving $\frac{W_j(E_{\mathbf{k}})_{\theta:0-\theta'}}{W_j(E_{\mathbf{k}})_{\theta:0-\pi}}$ in terms of $cos(\theta')$. Where the subscript θ denotes the limit of the polar integration. For ionised impurity scattering, the polar scattering angle is given by [15],

$$cos(\theta') = 1 - \frac{2r_4}{1 + (1 - r_4)\left(\frac{2k}{q_D}\right)^2} \tag{2.17}$$

This is based off the Brooks-Herring approach [33, 9] to ionised impurity scattering which treats it as a screened potential where $1/q_D$ is known as the Debye length, which describes the characteristic screening length.

$$\frac{1}{q_D} = \sqrt{\frac{\epsilon_s k_B T}{e^2 n_0}} \tag{2.18}$$

Here ϵ_s is the static dielectric constant of the material and n_0 is the concentration of charged impurities.

The scattering angle for polar optical phonon scattering is given by [15],

$$cos(\theta') = \frac{1 + f - (1 + 2f)^{r_4}}{f} \tag{2.19}$$

$$f = \frac{2\sqrt{E_{\mathbf{k}} E_{\mathbf{k}'}}}{(\sqrt{E_{\mathbf{k}}} - \sqrt{E_{\mathbf{k}'}})^2} \tag{2.20}$$

Finally, the scattering angle for piezoelectric scattering can be found as [101],

$$cos(\theta') = 1 + \frac{q_0^2}{2k^2}\left(1 - exp\left(1 + \chi r_4 + W_0\left(-e^{-1-\chi r_4}\right)\right)\right) \tag{2.21}$$

the derivation of which is shown in appendix A of reference [101]. Here, $\chi = ln\left(1 + \frac{4k^2}{q_0^2}\right) - \frac{4k^2}{q_0^2 + 4k^2}$, W_0 is the principal branch of the Lambert function and $q_0 = \sqrt{2m^* \frac{\omega_L}{\hbar}}$ is the electronic screening.

In the anisotropic case, these angles don't represent the direction of the wave vector in the lab reference frame (k_x^L, k_y^L, k_z^L) but instead the change in direction of the final state $\mathbf{k}'$ from

the initial state $\mathbf{k}$ and so the angles can be thought of as a direction in a rotated reference frame (k_x^R, k_y^R, k_z^R) in which the k_z-axis is parallel to the initial wave vector. This rotated frame is obtained by rotating (k_x^L, k_y^L, k_z^L) by an angle α about the k_x-axis and then angle β about the k_z-axis. The final state wave vector in the rotated frame is given by,

$$\mathbf{k}'^R = \begin{pmatrix} k' sin(\theta')cos(\phi'), \\ k' sin(\theta')sin(\phi'), \\ k' cos(\theta') \end{pmatrix} \tag{2.22}$$

where k' is the magnitude of the electron state post scattering.

In order to properly apply the effect of the external field in the next drift step, $\mathbf{k}'^R$ must be transformed back into the lab reference frame by multiplication with matrix

$$\begin{pmatrix} cos(\beta) & cos(\alpha)sin(\beta) & sin(\alpha)sin(\beta) \\ -sin(\beta) & cos(\alpha)cos(\beta) & sin(\alpha)cos(\beta) \\ 0 & -sin(\alpha) & cos(\alpha) \end{pmatrix} \tag{2.23}$$

The angles α and β do not need to be calculated as the trigonometric functions can be written in terms of the original wave vector $\mathbf{k}$ in the lab reference frame.

$$\begin{aligned} sin(\alpha) &= \tfrac{\sqrt{k_x^2+k_y^2}}{k}, \quad cos(\alpha) = \tfrac{k_z}{k} \\ sin(\beta) &= \tfrac{k_x}{\sqrt{k_x^2+k_y^2}}, \quad cos(\beta) = \tfrac{k_y}{\sqrt{k_x^2+k_y^2}} \end{aligned} \tag{2.24}$$

The final wave vector in the lab reference frame is then given by,

$$\mathbf{k}' = \begin{pmatrix} k'_x \\ k'_y \\ k'_z \end{pmatrix} = \begin{pmatrix} \frac{k_y}{\sqrt{k_x^2+k_y^2}} & \frac{k_x k_z}{k\sqrt{k_x^2+k_y^2}} & \frac{k_x}{k} \\ -\frac{k_x}{\sqrt{k_x^2+k_y^2}} & \frac{k_y k_z}{k\sqrt{k_x^2+k_y^2}} & \frac{k_y}{k} \\ 0 & -\frac{\sqrt{k_x^2+k_y^2}}{k} & \frac{k_z}{k} \end{pmatrix} \begin{pmatrix} k' sin(\theta')cos(\phi'), \\ k' sin(\theta')sin(\phi'), \\ k' cos(\theta') \end{pmatrix} \tag{2.25}$$

This process of transforming vectors between reference frames is not necessary for isotropic scattering methods as the angles θ' and ϕ' are uniformly distributed about the sphere.

2.3 Scattering Rates

Accurately solving the BTE via MC simulation then requires the implementation of appropriate scattering methods. The starting point for the derivation of all the scattering rates is Fermi's Golden Rule, as seen in section 1.1.3, as it is an expression of the probability of an electron transitioning from an initial state, $\mathbf{k}$, to a final state, $\mathbf{k}'$, due to a given scattering mechanism perturbing the periodic potential, given by equation 1.22 and rewritten here,

$$S(\mathbf{k},\mathbf{k}') = \frac{2\pi}{\hbar}|H_{\mathbf{k}',\mathbf{k}}|^2\delta(E_{\mathbf{k}'} - E_{\mathbf{k}}) \quad \text{(1.22 repeated)}$$

where $S(\mathbf{k},\mathbf{k}')$ is the transition rate, $|H_{\mathbf{k}',\mathbf{k}}|$ is the scattering mechanism matrix element linking the initial and final states and $E_{\mathbf{k}}$ & $E_{\mathbf{k}'}$ are the electron energies of the initial and final state, respectively. The delta function then ensures the conservation of energy. Integrating equation 1.22 over all potential final states in a crystal with volume Ω gives the scattering rate for the three-dimensional system, as given in equation 1.23 and also rewritten here,

$$W(\mathbf{k}) = \frac{\Omega}{(2\pi)^3}\frac{2\pi}{\hbar}\int |H_{\mathbf{k}',\mathbf{k}}|^2\delta(E_{\mathbf{k}'} - E_{\mathbf{k}} \mp E_{trans})d\mathbf{k}' \quad \text{(1.23 repeated)}$$

with the $\mp$ signifying the absorption $(-)$ or emission $(+)$ of energy. This equation can be used to find the scattering rates of different mechanisms by defining the matrix element and computing the integral. The following sections show the derivations of the non-polar and polar optical and acoustic phonon and charged impurity scattering mechanisms.

2.3.1 Non-Polar Phonon Scattering

Non-polar optical phonon (NPOP) and acoustic phonon (also known as acoustic deformation potential (ADP)) scattering are caused by the interaction of electrons with the optical and acoustic phonon modes. ADP scattering causes intra-valley scattering and so is an important scattering mechanism at low energies, whereas NPOP interactions are only considered to cause intervalley scattering between both equivalent and satellite valleys. As both these scattering mechanisms are due to interactions with phonons, they both have scattering matrix elements

of the form,

$$|H_{\mathbf{k}',\mathbf{k}}|^2 = \kappa_q \left(n_q + \frac{1}{2} \mp \frac{1}{2} \right) \delta(\mathbf{k}' - \mathbf{k} \mp \mathbf{q}) \tag{2.26}$$

where κ_q is an energy independent constant dependent on the phonon mode chosen, and the delta function takes into account conservation of momentum during the interaction. By substitution into equation 1.23, the scattering rate is given by,

$$W(\mathbf{k}) = \frac{\Omega}{(2\pi)^3} \frac{2\pi}{\hbar} \kappa_q (n_q + \frac{1}{2} \mp \frac{1}{2}) \int \delta(E_{\mathbf{k}'} - E_{\mathbf{k}} \mp \hbar\omega_q) \delta(\mathbf{k}' - \mathbf{k} \mp q) d\mathbf{k}' \tag{2.27}$$

where $\hbar\omega_q$ is the change in energy of the electron after interacting with a phonon with frequency ω_q. A simplification that can be made here is to ignore the angular dependence of the integrand, and so, the integral in equation 2.27 can be converted into one over energy using the relation,

$$\frac{1}{2\pi^3} \int \delta(E_{\mathbf{k}'} - E_{\mathbf{k}} \mp E_{trans}) d\mathbf{k}' = \int \delta(E_{\mathbf{k}'} - E_{\mathbf{k}} \mp E_{trans}) g(E_{\mathbf{k}'}) dE_{\mathbf{k}'} \tag{2.28}$$

where $g(E_{\mathbf{k}'})$ is the density of states per unit volume at energy $E_{\mathbf{k}'}$. This can be done in the case of acoustic phonon scattering as the phonon energy is much less than $k_B T$ at room temperature, therefore the interaction is considered elastic and $\hbar\omega_q \rightarrow 0$. This is not the case in optical phonon scattering, however, the optical phonon frequency can be treated as constant with respect to $\mathbf{q}$. Therefore, ω_q and n_q can be replaced by constants ω_0, and n_0. For non-polar optical phonon scattering the energy dependent prefactor, κ_q is given by,

$$\kappa_q = \frac{D_o^2 \hbar}{2\rho\omega_0\Omega} \tag{2.29}$$

and for acoustic phonon scattering, κ_q is given by

$$\kappa_q = \frac{\pi \Xi_{ADP}^2 q^2}{\hbar\rho\omega_0\Omega} \tag{2.30}$$

where D_o and Ξ_{ADP} are the optical and acoustic phonon deformation potentials [102, 103], respectively; and ρ is the mass density. The integral of equation 2.27 can then be converted

as in equation 2.28 giving the non-polar optical phonon scattering rate as,

$$W_{NPOP}(\mathbf{k}) = \frac{\pi D_o^2}{\rho\omega_0}(n_0 + \frac{1}{2} \mp \frac{1}{2})g(E_\mathbf{k} \mp \hbar\omega_0) \tag{2.31}$$

and the acoustic phonon scattering rate as,

$$W_{ADP}(\mathbf{k}) = \frac{\pi \Xi_{ADP}^2 q^2}{\hbar\rho\omega_q}(n_q + \frac{1}{2} \mp \frac{1}{2})g(E_\mathbf{k}) \tag{2.32}$$

The acoustic phonon scattering rate can be further simplified by once again considering the fact that at room temperature, the phonon energies are much less than thermal energies. Phonons are bosons, therefore the number of phonons with wavevector **q** at a given temperature is given by the Bose-Einstein distribution,

$$\langle n_\mathbf{q} \rangle = \frac{1}{exp\left(\frac{\omega_q}{k_B T}\right) - 1} \tag{2.33}$$

As $\hbar\omega_q << k_B T$, the number of phonons can be approximated as,

$$\langle n_\mathbf{q} \rangle = \frac{k_B T}{\hbar\omega_q} \tag{2.34}$$

where $n_\mathbf{q} >> 1$ and so $n_\mathbf{q} \approx n_\mathbf{q} + 1$. As acoustic phonon scattering is considered an elastic process, the scattering rate is doubled to take into account emission and absorption of phonons. The acoustic phonon scattering rate is then given by,

$$W_{ADP}(\mathbf{k}) = \frac{2\pi \Xi_{ADP}^2 k_B T}{\hbar\rho v_s^2} g(E_\mathbf{k}) \tag{2.35}$$

where $v_s = \frac{\omega_q}{q}$ is the longitudinal sound velocity of the material.

2.3.2 Polar Scattering

In addition to the short range deformation potential scattering, lattice vibration in polar materials result in long range polarisation waves that the electrons interact with. Like the non-polar case, these scattering mechanisms can be split into inelastic polar optical phonon scattering (POP) and elastic polar acoustic phonon scattering, known as piezoelectric scattering. How-

ever, unlike the non-polar case, polar scattering is far more complicated and so in this work the expressions used for the scattering rates are those using analytic band structure as shown in references [15, 33]. The scattering matrix elements for POP and piezoelectric scattering are given by,

$$|H_{\mathbf{k}',\mathbf{k}}|^2_{POP} = \frac{e^2\hbar\omega_0}{2\epsilon_p\Omega}\frac{q^2}{q^2+q_0^2}\left(n(\omega_0)+\frac{1}{2}\mp\frac{1}{2}\right)\delta(\mathbf{k}'-\mathbf{k}\mp\mathbf{q}) \tag{2.36}$$

$$|H_{\mathbf{k}',\mathbf{k}}|^2_{PZ} = \frac{e^2K_{av}^2k_BT}{2\epsilon_s\hbar\Omega}\frac{q^2}{q^2+q_0^2}\delta(\mathbf{k}'-\mathbf{k}\mp\mathbf{q}) \tag{2.37}$$

where q is the magnitude of the phonon momentum and once again, the equations have been simplified in an analogous way to the non-polar cases, i.e. the phonon energy is constant with respect to $\mathbf{q}$ and so $\omega_q \rightarrow \omega_0$ and $n_q \rightarrow n_0$ for optical phonons; and $\hbar\omega_q << k_BT$ for acoustic phonons. In equations 2.36 and 2.37 q_0 is the electron screening; $\frac{1}{\epsilon_p} = \frac{1}{\epsilon_\infty} - \frac{1}{\epsilon_s}$, where ϵ_∞ and ϵ_s are the high frequency and static dielectric coefficients, respectively; and K_{av}^2 is an average electromechanical coupling coefficient which for zinc blende structures is given by,

$$K_{av}^2 = \frac{e_{14}^2}{\epsilon_s}\left(\frac{12}{35c_L}+\frac{16}{35c_T}\right) \tag{2.38}$$

Here, c_L and c_T are the longitudinal and transverse spherical elastic constants, respectively; and e_{14} is a piezoelectric constant defined by the piezoelectric tensor. The scattering rate can be found by substituting the scattering matrix elements into equation 1.22. In both cases, finding the scattering rate requires solving an integral of the form,

$$I_q = \int \frac{q^2}{q^2+q_0^2}\delta(\mathbf{k}'-\mathbf{k}\mp\mathbf{q})\delta(E_{\mathbf{k}'}-E_{\mathbf{k}}\mp\hbar\omega_0)d\mathbf{k}' \tag{2.39}$$

However, it is more convenient to write this integral in terms of the phonon momentum, $\mathbf{q}$; and expand into spherical coordinates.

$$I_q = \int_0^{2\pi} d\phi \int_0^{q_{zb}} \int_{-1}^{1} \frac{q^4}{(q^2+q_0^2)^2}\delta(\mathbf{k}'-\mathbf{k}\mp\mathbf{q})\delta(E_{\mathbf{k}'}-E_{\mathbf{k}}\mp\hbar\omega_0)dqd(cos(\theta)) \tag{2.40}$$

where q_{zb} is the zone boundary of the phonon BZ. The integration over the azimuthal angle, ϕ, just contributes a factor of 2π. The other two integrals can be done by considering the

conservation of momentum and energy as enforced by the delta functions. As stated previously, POP and piezoelectric scattering are dealt with using analytic bands and, as such, the energy can be expanded in terms of the momentum using equation 1.10. From conservation of energy,

$$\frac{\hbar^2\mathbf{k}'^2}{2m^*} = \frac{\hbar^2\mathbf{k}^2}{2m^*} \pm \hbar\omega_0 \tag{2.41}$$

and from conservation of momentum,

$$\mathbf{k}'^2 = k^2 + q^2 \pm 2|\mathbf{k}||\mathbf{q}|cos(\theta) \tag{2.42}$$

where θ is the angle between $\mathbf{k}$ and $\mathbf{q}$. This can then be substituted into equation 2.41, giving,

$$\frac{\hbar^2\mathbf{k}^2}{2m^*} + \frac{\hbar^2\mathbf{q}^2}{2m^*} \pm \frac{\hbar^2|\mathbf{k}||\mathbf{q}|cos(\theta)}{m^*} = \frac{\hbar^2\mathbf{k}^2}{2m^*} \pm \hbar\omega_0 \tag{2.43}$$

The first terms on both sides of equation 2.43 cancel and this can then be substituted into 2.40,

$$I_q = 2\pi \int_0^{q_{zb}} \int_{-1}^{1} \frac{q^4}{(q^2+q_0^2)^2} \delta\left(\frac{\hbar^2\mathbf{q}^2}{2m^*} \pm \frac{\hbar^2|\mathbf{k}||\mathbf{q}|cos(\theta)}{m^*} \mp \hbar\omega_0\right) dq d(cos(\theta)) \tag{2.44}$$

The integral over $cos(\theta)$ can then easily be computed, however, it imposes limits on the maximum and minimum values of q,

$$I_q = \frac{2\pi m^*}{\hbar^2 k} \int_{q_{min}}^{q_{max}} \frac{q^3}{(q^2+q_0^2)^2} dq = \frac{2\pi m^*}{\hbar^2 k} \frac{1}{2} \left[ln\left(q^2+q_0^2\right) + \frac{q_0^2}{q^2+q_0^2} \right]_{q_{min}}^{q_{max}} \tag{2.45}$$

Combining equations 1.22, 2.36 and 2.45 gives the POP scattering rate as,

$$W_{POP}(\mathbf{k}) = \frac{e^2\omega_0 k}{8\pi\epsilon_p E_{\mathbf{k}}} \left(n(\omega_0) + \frac{1}{2} \mp \frac{1}{2}\right) \frac{1}{2} \left[ln\left(q^2+q_0^2\right) + \frac{q_0^2}{q^2+q_0^2} \right]_{q_{min}}^{q_{max}} \tag{2.46}$$

Screening is only important in highly doped semiconductors and so the POP scattering rate can be simplified by setting $q_0 = 0$.

$$W_{POP}(\mathbf{k}) = \frac{e^2\omega_0 k}{8\pi\epsilon_p E_{\mathbf{k}}} \left(n(\omega_0) + \frac{1}{2} \mp \frac{1}{2}\right) ln\left(\frac{q_{max}}{q_{min}}\right) \tag{2.47}$$

where q_{max} and q_{min} are given by [15, 33],

$$q_{min} = k \left| \left(1 - \left(1 \pm \frac{\hbar\omega_0}{E_{\mathbf{k}}} \right)^{\frac{1}{2}} \right) \right|$$
$$q_{max} = k \left(1 + \left(1 \pm \frac{\hbar\omega_0}{E_{\mathbf{k}}} \right)^{\frac{1}{2}} \right) \tag{2.48}$$

Similarly, combining equations 1.22, 2.37 and 2.45 gives the piezoelectric scattering rate as,

$$W_{PZ}(\mathbf{k}) = \frac{e^2 K_{av}^2 k_B T}{8\pi\hbar^2 \epsilon_s v} \left[ln\left(q^2 + q_0^2\right) + \frac{q_0^2}{q^2 + q_0^2} \right]_{q_{min}}^{q_{max}} \tag{2.49}$$

For acoustic scattering, the maximum and minimum values for the phonon momentum are given by,

$$q_{min} = 0$$
$$q_{max} = 2k \tag{2.50}$$

Therefore, the piezoelectric scattering rate is given by,

$$W_{PZ}(\mathbf{k}) = \frac{e^2 K_{av}^2 k_B T}{8\pi\hbar^2 \epsilon_p v} \left(ln\left(1 + \frac{8E_{\mathbf{k}m^*}}{\hbar^2 q_0^2}\right) - \frac{1}{1 + \frac{\hbar^2 q_0^2}{8E_{\mathbf{k}m^*}}} \right) \tag{2.51}$$

Unlike the non-polar phonon scattering, polar phonon scattering is anisotropic and so the post scattering angle must be calculated according to equations 2.19 to 2.21.

2.3.3 Charged Impurity Scattering

During the growth of a crystal, impurities disrupt the periodic structure of the lattice. This cannot be avoided as these impurities may be added deliberately to alter the transport of the material. Using the Brooks-Herring approach [33, 9], the scattering matrix element for a single impurity is given by,

$$|H_{\mathbf{k}',\mathbf{k}}|^2 = \left(\frac{Ze^2}{\Omega\epsilon_s}\right)^2 \frac{1}{(|(\mathbf{k}' - \mathbf{k})|^2 + q_D^2)^2} \tag{2.52}$$

where Ze is the charge on an impurity atom, $1/q_D$ is the Debye length and ϵ_s is the dielectric constant. As $|\mathbf{k}'| = |\mathbf{k}|$,

$$\mathbf{k}' - \mathbf{k} = 2k^2(1 - cos(\theta)) \tag{2.53}$$

where θ is the angle between the initial and final wave vectors. By substituting equations 2.52 and 2.53 into equation 1.23 and multiplying by the number of impurities in the volume, $N_I\Omega$, the total scattering rate for charged impurity scattering is given by,

$$W(\mathbf{k}) = \frac{2\pi}{\hbar}\frac{N_I Z^2 e^4}{(2\pi)^3\epsilon_s}\int_0^{2\pi} d\phi \int_{-1}^{1} d(cos(\theta)) \int_0^{\infty} dk' \frac{k'^2\delta(E_{k'} - E_k)}{(2k^2(1 - cos(\theta)) + q_D^2)^2} \tag{2.54}$$

The integrand has no dependence on ϕ and so the integral over ϕ adds a factor of 2π. The integral over dk' can be transformed to an integral over $dE_{\mathbf{k}}$ with the substitution,

$$\frac{4\pi k'^2}{(2\pi)^3}dk' = g(E_{\mathbf{k}'})dE_{\mathbf{k}'} \tag{2.55}$$

Substituting these results into 2.54 gives

$$W(\mathbf{k}) = \frac{\pi N_I Z^2 e^4}{\hbar\epsilon_s} g(E_{\mathbf{k}'}) \int_{-1}^{1} d(cos(\theta)) \frac{1}{(2k^2(1 - cos(\theta)) + q_D^2)^2} \tag{2.56}$$

Finally, integrating equation 2.56 gives the scattering rate for charged impurity scattering.

$$W_{IMP}(\mathbf{k}) = \frac{\pi N_I Z^2 e^4}{\hbar\epsilon_s} \frac{1}{q_D^2(4k^2 + q_D^2)} g(E_{\mathbf{k}'}) \tag{2.57}$$

2.3.4 Equivalent Valley Scattering

As stated in section 2.3.1, NPOP interactions cause scattering between valleys. The materials of interest all have conduction band minima along the Δ direction which results in 6 equivalent conduction band minima due to the symmetries of the reciprocal space lattice. Scattering from one of these to another can be broken down into two different cases. Figure 2.1 shows the two types of equivalent valley scattering from the initial (red) to the final (blue) ellipsoidal valley. The scattering between parallel initial and final valleys is termed g-type scattering and the scattering between perpendicular initial and final valleys is termed f-type scattering. This is an important distinction to make as the deformation potentials and energies for these two

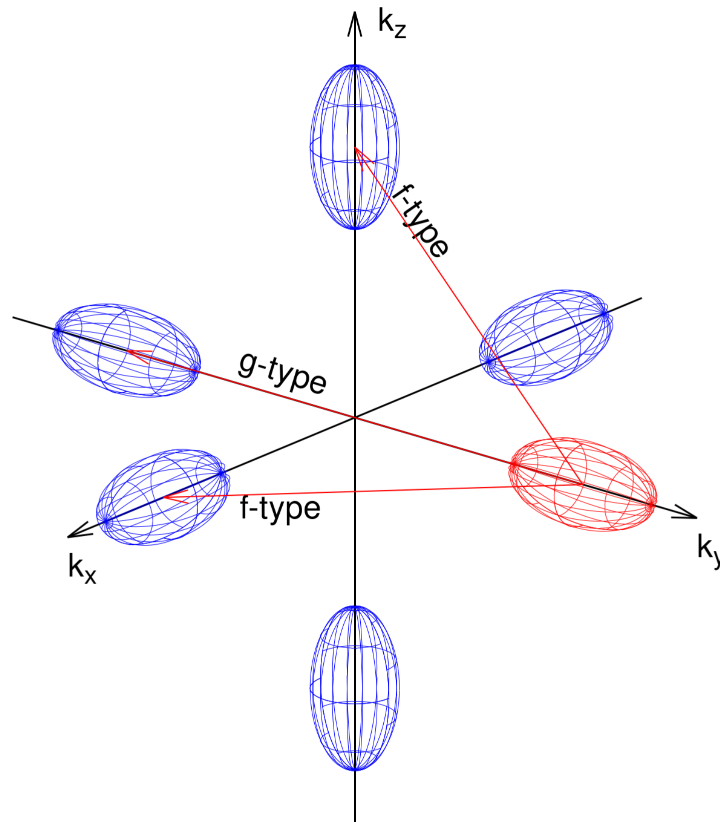

Figure 2.1: f and g scattering processes between six equivalent valleys

scattering types may be different and so the two are treated as separate scattering methods.

While it is not considered in this work, this method can be extended to consider each of the equivalent valleys separately as if there is a field accelerating the electrons in the k_x direction, then an electron scattering from the k_x valley to the k_z valley would experience a change in its effective mass, resulting in a change in the velocity. This leads to the emerging field of valleytronics and has been shown to have an impact on the motion of charge carriers at low temperatures [104].

2.3.5 Other Scattering Mechanisms

The scattering methods described above are for the most common scattering mechanisms found in semiconductor transport, however this is by no means an exhaustive list of scattering mechanisms that could be experienced by an electron. One scattering mechanism not included here that may be of importance at very high energies is impact ionisation [33]. This scattering event occurs when a high energy electron in the conduction band interacts with a valance

band electron to promote it to the conduction band. If this promoted electron has high energy then it can in turn experience impact ionisation scattering resulting in an avalanche effect, rapidly increasing the electron density. Despite its importance, this scattering mechanism is not included as most of the simulated electrons do not reach the energies required for this scattering to occur, and the implementation was beyond the scope of this work.

If the MC methods were extended beyond treating bulk systems and started to treat heterostructures between diamond and cBN then scattering mechanisms such as threaded dislocation scattering would need to be considered at the junction between the two materials due to the difference in the lattice constant. Similar to charged impurity scattering, this would predominantly impact slow moving electrons, increasing scattering at lower fields.

2.4 Bulk Ensemble Monte Carlo Simulation

The general MC algorithm given in section 2.2 can be run on a single electron or many electrons at the same time. The latter case, known as the Ensemble Monte Carlo (EMC) method, is the more expensive of the two, however it can be used to calculate transient transport properties and generate distribution functions of attributes of the electrons. The EMC simulates a system with many electrons undergoing drift and scattering simultaneously, measuring the distribution of electrons at given time intervals to follow how the system evolves. All the electrons are considered to be independent particles with motion governed by identical scattering rates. This means that the scattering rates only have to be calculated once at the start of the simulation. The code then loops through each of the electrons and applies the base MC algorithm from section 2.2 for time dt. The drift time τ may be less than dt and therefore a given electron may experience more than one scattering event before time dt elapses. If the electron's drift step takes it past the end of the time period then its motion is "paused" and continues during the next time step. Once all electrons have completed the time step, quantities of interest, such as the velocities and energies, are measured and in this way distributions and time evolution of these quantities can be found.

Ensemble averaged data can then be extracted from the simulation at any time step by calculating the required quantities and averaging over all n electrons. The average energies

and velocities at time t can then be found as,

$$\langle E(\mathbf{k})\rangle_t = \frac{1}{n}\sum_{i=1}^{n} E(\mathbf{k})_i \tag{2.58}$$

$$\langle v\rangle_t = \frac{1}{n}\sum_{i=1}^{n} \frac{1}{\hbar}\frac{\partial E(\mathbf{k})_i}{\partial k} \tag{2.59}$$

2.5 Summary

In this chapter, the implementation of MC methods for solving the BTE for charge carriers in bulk materials has been discussed. The MC algorithm introduced provides ensemble output data from which steady-state transport properties can be collected. The various scattering angles and scattering rates included in the simulation were also derived from Fermi's golden rule. The introduction of equivalent valley scattering means that the MC methods can also be extended to indirect band gap semiconductors.

Chapter 3

Solving the Many-Body Electron Problem

The aim of this work is to model the transport of electrons at higher energies and therefore, as seen in section 1.1.2, models beyond the analytic approximations are required to represent the band structure. However, due to the effect electrons have on each other, the difficulty of solving the Schrödinger equation increases exponentially with the number of electrons [105].

This chapter starts with a description of the many-body electron problem before detailing methods for solving it including the formulation of DFT. Following this, there is a description of how approximations can be applied to DFT so that it can be used to make predictions about many-electron systems in a tractable time.

3.1 The Many-Body Electron Problem

Within the quantum framework, a system of interacting electrons and nuclei can be described by solving the time-independent many-body Schrödinger equation.

$$\hat{H}_{mb}\Psi(\{\mathbf{r}_i\},\{\mathbf{R}_I\}) = E\Psi(\{\mathbf{r}_i\},\{\mathbf{R}_I\}) \tag{3.1}$$

Here $\Psi(\{\mathbf{r}_i\},\{\mathbf{R}_I\})$ is the many-body wavefunction of a set of n electron coordinates $\{\mathbf{r}_i : i = 1, 2, 3...n\}$ and a set of K nuclear coordinates $\{\mathbf{R}_I : I = 1, 2, 3...K\}$; E is the corresponding energy; and $\hat{H}$ is the many-body Hamiltonian operator, for which $\Psi(\{\mathbf{r}_i\},\{\mathbf{R}_I\})$ and E are the

eigenfunctions and eigenenergies respectively. This many-body Hamiltonian can be expanded in atomic units, $m_e = q_e = \hbar = 4\pi\epsilon_0 = 1$, as;

$$\begin{aligned}\hat{H}_{mb} &= \hat{T}_e + \hat{T}_N + \hat{V}_{Ne} + \hat{V}_{NN} + \hat{V}_{ee} \\ &= -\frac{1}{2}\sum_{i=1}^{n}\nabla_i^2 - \frac{1}{2}\sum_{I=1}^{K}\frac{1}{M_I}\nabla_I^2 \\ &\quad -\sum_{J=1}^{K}\sum_{j=1}^{n}\frac{Z_J}{|\mathbf{R}_J - \mathbf{r}_j|} + \sum_{P=1}^{K}\sum_{L>P}^{K}\frac{Z_P Z_L}{|\mathbf{R}_P - \mathbf{R}_L|} + \sum_{p=1}^{n}\sum_{l>p}^{n}\frac{1}{|\mathbf{r}_p - \mathbf{r}_l|}\end{aligned} \tag{3.2}$$

Here, $\hat{T}_e$ and $\hat{T}_N$ are the electron and nucleus momentum operators, respectively; $\hat{V}_{N-e}$, $\hat{V}_{N-N}$ and $\hat{V}_{e-e}$ are the nucleus-electron, nucleus-nucleus and electron-electron Coulomb potentials, respectively; Z_J and M_J are the Jth nucleus charge and mass, respectively; and the upper and lower case summation indices are used for nuclei and electrons, respectively. Solving this equation would then give the exact multi-body wavefunction, however, this is not possible in cases where $n + N > 3$, and so some approximations must be applied so that this can be solved numerically in a reasonable amount of time.

3.2 Born-Oppenheimer Approximation

The first approximation made here is the adiabatic approximation. In the context of quantum mechanics, an adiabatic process is defined as one where a given perturbation is acting slowly enough on a system such that if the system is in an eigenstate of the initial Hamiltonian, it will be in the corresponding eigenstate of the final Hamiltonian [106, 107]. One such adiabatic approximation, the Born-Oppenheimer approximation [108], can then be applied to the many-body electron problem by fixing the positions of the nuclei and separating the electronic and nuclear wavefunctions.

$$\Psi_{total}(\{\mathbf{r}_i\}, \{\mathbf{R}_I\}) = \Psi_e^{\mathbf{R}}(\{\mathbf{r}_i\})\Psi_N(\{\mathbf{R}_I\}) \tag{3.3}$$

Here, $\Psi_N(\{\mathbf{R}_I\})$ is the nuclear wavefunction and $\Psi_e^{\mathbf{R}}(\{\mathbf{r}_i\})$ is the electronic wavefunction that depends parametrically upon the nuclear co-ordinates.

Applying the Hamiltonian of equation 3.2 to this separated wavefunction then gives

$$\hat{H}_{mb}\Psi_e^{\mathbf{R}}(\{\mathbf{r}_i\})\Psi_N(\{\mathbf{R}_I\}) = \hat{T}_e\Psi_e^{\mathbf{R}}(\{\mathbf{r}_i\})\Psi_N(\{\mathbf{R}_I\}) + \hat{T}_N\Psi_e^{\mathbf{R}}(\{\mathbf{r}_i\})\Psi_N(\{\mathbf{R}_I\}) + (\hat{V}_{N-e} + \hat{V}_{N-N} + \hat{V}_{e-e})\Psi_e^{\mathbf{R}}(\{\mathbf{r}_i\})\Psi_N(\{\mathbf{R}_I\}) \tag{3.4}$$

Expanding the nuclear momentum operator and applying the derivatives to the wavefunction gives,

$$\begin{aligned}\hat{T}_N\Psi_e^{\mathbf{R}}(\{\mathbf{r}_i\})\Psi_N(\{\mathbf{R}_I\}) = &-\frac{1}{2}\sum_{I=1}^{K}\frac{m_e}{M_I}\Psi_e^{\mathbf{R}}(\{\mathbf{r}_i\})\nabla_I^2\Psi_N(\{\mathbf{R}_I\}) \\ &-\frac{1}{2}\sum_{I=1}^{K}\frac{m_e}{M_I}\Psi_N(\{\mathbf{R}_I\})\nabla_I^2\Psi_e^{\mathbf{R}}(\{\mathbf{r}_i\}) \\ &-\sum_{I=1}^{K}\frac{m_e}{M_I}(\nabla_I\Psi_e^{\mathbf{R}}(\{\mathbf{r}_i\}))(\nabla_I\Psi_N(\{\mathbf{R}_I\}))\end{aligned} \tag{3.5}$$

The Born-Oppenheimer approximation then amounts to saying that the terms which include $\nabla_I\Psi_N(\{\mathbf{R}_I\})$ are negligible as $\nabla_I\Psi_N(\{\mathbf{R}_I\})$ is of the same order of magnitude as $\nabla_i\Psi_N(\{\mathbf{R}_I\})$ whereas $m_e << M_I$, therefore the kinetic energy of the nuclei doesn't impact the electronic states, and so the total energy is given by,

$$E = E_N + E_e \tag{3.6}$$

where,

$$E_e\Psi_e^{\mathbf{R}}(\{\mathbf{r}_i\}) = \left(\hat{T}_e + \hat{V}_{N-e} + \hat{V}_{e-e}\right)\Psi_e^{\mathbf{R}}(\{\mathbf{r}_i\}) \tag{3.7}$$

is the contribution to the total energy of the electron states and,

$$E_N\Psi_N(\{\mathbf{R}_I\}) = \left(\hat{T}_N + \hat{V}_{N-N}\right)\Psi_N(\{\mathbf{R}_I\}) \tag{3.8}$$

is the contribution to the total energy of the nuclear states. The electrons can therefore be thought to respond instantaneously to any change in the state of the nuclei and equilibrate to the new ground state. The Born-Oppenheimer approximation means that the electron ground state wavefunction can be solved for first before solving the nuclear wavefunction. Generally, the nuclei are treated classically and as such finding $\Psi_N(\{\mathbf{R}_I\})$ is unnecessary [105, 109].

Furthermore, the kinetic energy of the nuclei can be ignored by varying the positions of the nuclei to find the equilibrium position such that the ground state energy of the system is minimised. The Hamiltonian of equation 3.2 can then be paired back to be a Hamiltonian of electrons in an external potential generated by stationary nuclei,

$$\hat{H}_{BO} = \hat{T}_e + \hat{V}_{ext} + \hat{V}_{e-e} \tag{3.9}$$

Although the Born-Oppenheimer approximation is applicable in the presented work, it should be noted that equation 3.5 indicates that it will break down in cases where $\nabla_I \Psi_e^{\mathbf{R}}(\{\mathbf{r}_i\})$ changes rapidly and the electrons and nuclei become coupled, such as the Jahn-Teller effect [110] where the ground state degeneracy is broken in a molecule due to a geometric distortions that lower the overall energy.

3.3 Mean Field Methods

Even though the decoupling of the nuclear and electronic wavefunctions has reduced the difficulty of the problem, the electronic wavefunction that is left is still a complex function of $3n$ coupled degrees of freedom[1] due to the electron-electron interaction. As the number of electrons is increased, this interaction quickly results in the problem becoming too large to store, let alone calculate a solution to. To illustrate this, imagine the wavefunction of an independent electron. This can be expanded as a linear combination of a complete basis set, $\{\phi_i(\mathbf{r})\}$, as,

$$\psi_e(\mathbf{r}) = \sum_{i=1}^{\text{inf}} c_i \phi_i(\mathbf{r}) \tag{3.10}$$

For computational purposes, this must be reduced to a finite basis set of b_1 functions, chosen such that they approach the infinite case. The number of basis functions then required for a system of n electrons is given by $b_n = \binom{b_1}{n}$ [105]. Figure 3.1 shows how the amount of space required to store the coupled wavefunction on a course 10^3 grid with an 8 byte complex number storing the value at each grid point increases with the number of electrons. It shows how even for a single silicon atom, the amount of data required becomes unworkably large. It is then necessary to reduce this complexity by simplifying the interactions of the electrons.

[1]The spin degree of freedom in the wavefunction is taken to be implied throughout this chapter.

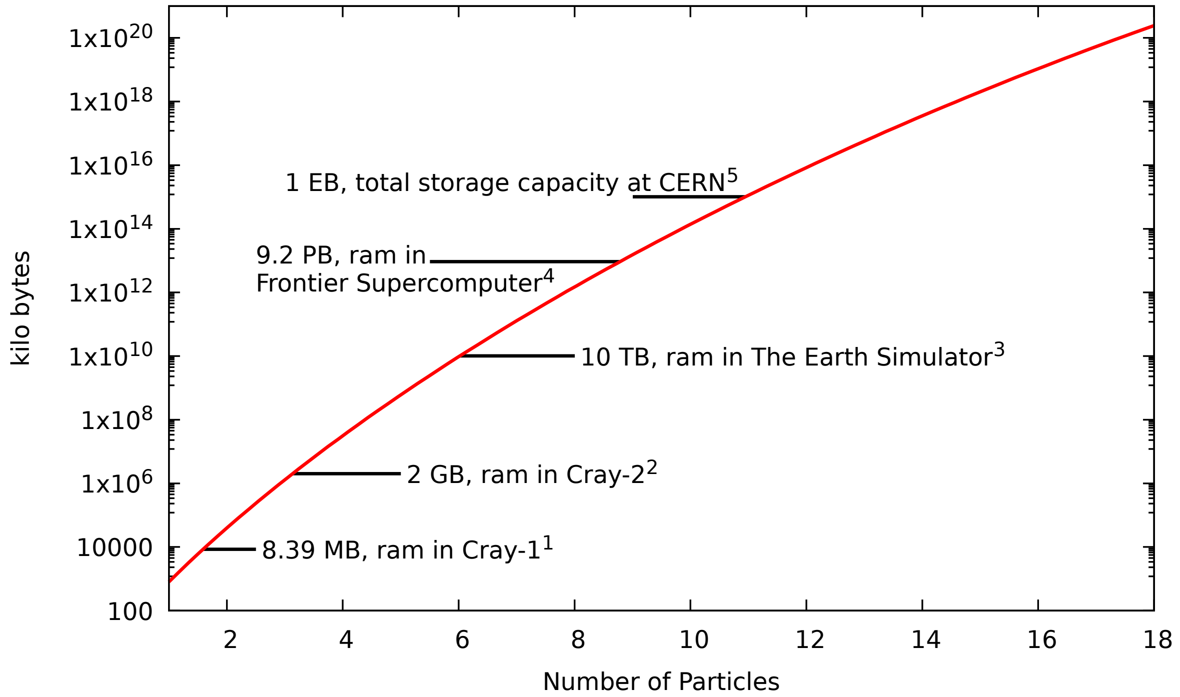

Figure 3.1: How the number of basis sets grows with increasing numbers of particles for a coupled wavefunction on 10^3 grid points with an 8 byte complex number at each grid point. Data points from references [111][1], [112][2], [113][3], [114][4], [115][5]

One such simplification is the use of mean field theories.

In the approach of D.R. Hartree [116], the electron wavefunction is separated into a product of independent electron wavefunctions

$$\Psi_e(\{\mathbf{r}_i\}) = \prod_{i=0}^{n} \psi_i(\mathbf{r}_i) \tag{3.11}$$

The Coulomb interaction is then replaced by an average potential of all the other electrons and wavefunction $\psi_i(\mathbf{r}_i)$ is the eigenfunction of the Hartree Hamiltonian,

$$\hat{H}_H\psi_i(\mathbf{r}_i) = -\frac{1}{2}\nabla_i^2\psi_i(\mathbf{r}_i) + \hat{V}_{ext}\psi_i(\mathbf{r}_i) + \sum_{j\neq i}\int \psi_j(\mathbf{r}_j)^* \frac{1}{|\mathbf{r}_j - \mathbf{r}_i|}\psi_j(\mathbf{r}_j)d\mathbf{r}_j\psi_i(\mathbf{r}_i) \tag{3.12}$$

which would then only require nb_1 basis functions. This non-interacting particle approach forms the foundation of more advanced methods such as DFT, however it does not correctly represent a fermionic wavefunction as it ignores the fact that the wavefunction for fermions should be antisymmetric under the exchange of any two coordinates. This was corrected by the Hartree-Fock method [117–119] where exchange is introduced by including an antisymmetric

wavefunction given by a single Slater determinant

$$\Psi_e(\{\mathbf{r}_i\}) = \frac{1}{(n!)^{\frac{1}{2}}} \begin{vmatrix} \psi_1(\mathbf{r}_1) & \psi_2(\mathbf{r}_1) & \dots & \psi_n(\mathbf{r}_1) \\ \psi_1(\mathbf{r}_2) & \psi_2(\mathbf{r}_2) & \dots & \psi_n(\mathbf{r}_2) \\ \vdots & \vdots & \ddots & \vdots \\ \psi_1(\mathbf{r}_n) & \psi_2(\mathbf{r}_n) & \dots & \psi_n(\mathbf{r}_n) \end{vmatrix} \tag{3.13}$$

where wavefunction $\psi_i(\mathbf{r}_i)$ is the ith eigenfunction of the Hartree Hamiltonian,

$$\hat{H}_H \psi_i(\mathbf{r}_i) = -\frac{1}{2}\nabla_i^2 \psi_i(\mathbf{r}_i) + \hat{V}_{ext}\psi_i(\mathbf{r}_i) + \sum_{j \neq i} \left(\hat{J}\psi_i(\mathbf{r}_i) - \hat{X}\psi_i(\mathbf{r}_i) \right) \tag{3.14}$$

Here, $\hat{J}$ is the Hartree potential, given by the final term of equation 3.12 and $\hat{X}$ is the exchange operator, given by

$$\hat{X}\psi_i(\mathbf{r}_i) = \sum_{j \neq i} \int \psi_j(\mathbf{r}_j)^* \frac{1}{|\mathbf{r}_j - \mathbf{r}_i|} \psi_i(\mathbf{r}_j) d\mathbf{r}_j \psi_j(\mathbf{r}_i) \tag{3.15}$$

The Hartree-Fock method, therefore, demonstrates the accessibility of computational methods to the many-body electron problem. Although the Hartree-Fock method explicitly deals with exchange, it does not treat correlation effects at all [105] which leads to the possibility of large quantitive errors. Therefore, more computationally efficient methods that introduce correlation effects are required to be able to model larger systems.

3.4 Density Functional Theory

Density Functional Theory is an exact reformulation of quantum mechanics that focusses on the electron density, $\rho(\mathbf{r})$ rather than the wavefunction. For a normalised wavefunction of n electrons, this density is given by,

$$\rho(\mathbf{r}) = n \prod_{i=2}^{n} \int d\mathbf{r}_i |\Psi(\mathbf{r}, \mathbf{r}_2, \dots, \mathbf{r}_n)|^2 \tag{3.16}$$

This reformulation reduces the complexity as instead of solving the many-body electron wavefunction of $3n$ coupled degrees of freedom, the electron density is a scalar function with 3

degrees of freedom.

Section 3.4.1 shows the reformulation of quantum mechanics by Hohenberg and Kohn [120] where the operators are functionals of the electron density, however, the form of some functionals is unknown and approximations must be made. Section 3.4.2 shows one such approximation of Kohn and Sham [121] that turns DFT into a usable method for the calculation of ground state properties.

3.4.1 Hohenberg and Kohn

In their 1964 paper [120], Hohenberg and Kohn set out the foundation of DFT through two postulates:

1. The ground state electron density is uniquely determined by the external potential, except for an additive constant.
2. The energy is a unique and universal functional of this electron density and the potential such that it is minimised for the density of the ground state wavefunction.

Proofs of these theorems are detailed in references [105, 109, 120, 122]. The energy functional proposed by the Hohenberg and Kohn postulates is then given as,

$$E[\rho](\mathbf{r}) = F[\rho](\mathbf{r}) + \int \rho(\mathbf{r})\hat{V}_{ext} d\mathbf{r} \tag{3.17}$$

where $\hat{V}_{ext}$ is the external potential and $F[\rho](\mathbf{r})$ is a universal functional of the electron density that is the same for all systems and is given by,

$$F[\rho](\mathbf{r}) = T[\rho](\mathbf{r}) + E_{ee}[\rho](\mathbf{r}) \tag{3.18}$$

where $T[\rho](\mathbf{r})$ and $E_{ee}[\rho](\mathbf{r})$ are the electron kinetic energy and Coulomb interaction functional, respectively. The functional $F[\rho](\mathbf{r})$ required is one such that the minimum energy is given by the electron density of the ground state wavefunction.

$$E_0 = E[\rho_0](\mathbf{r}) \tag{3.19}$$

Although this is an exact formulation of quantum mechanics, the form of this energy functional is unknown. The widespread use of DFT is then down to the application of approximations that transform this into a solvable problem.

3.4.2 Kohn-Sham Equations

Similar to the Hartree method of section 3.3, the Kohn-Sham approach to DFT is to replace the system of interacting electrons who's wavefunctions are the solution to the many-body Hamiltonian of equation 3.2 with an auxiliary system of non-interacting particle wavefunctions, $\{\phi_i(\mathbf{r})\}$, which experience an effective potential, $\hat{V}_{eff}$, such that they reproduce the ground state density of the interacting electrons,

$$\rho_0(\mathbf{r}) = \sum_{i=1}^{n} |\phi_i(\mathbf{r})|^2 \tag{3.20}$$

These non-interacting single particle wavefunctions are then the solution to the single particle Kohn-Sham Hamiltonian,

$$\hat{H}_{KS}\phi_i(\mathbf{r}) = \left(\hat{T} + \hat{V}_{eff}\right)\phi_i(\mathbf{r}) = \epsilon_i\phi_i(\mathbf{r}) \tag{3.21}$$

with the constraint that these non-interacting particle wavefunctions are orthogonal and normalised,

$$\int \phi_i^*(\mathbf{r})\phi_j(\mathbf{r})d\mathbf{r} = \delta_{ij} \tag{3.22}$$

where the electronic contribution to the ground state energy is given by,

$$E_{KS} = \sum_{i=1}^{n} \epsilon_i \tag{3.23}$$

These equations can then be reformulated into an energy functional

$$E_{KS}[\rho](\mathbf{r}) = T_{KS}[\rho](\mathbf{r}) + E_{eff}[\rho](\mathbf{r}) + \int \rho(\mathbf{r})\hat{V}_{ext}d\mathbf{r} \tag{3.24}$$

where T_{KS} is the single particle kinetic energy, and $E_{eff}[\rho](\mathbf{r})$ is made up of contributions from a mean field Hartree interaction, $E_H[\rho](\mathbf{r})$; and a final term known as the Exchange-Correlation

energy, $E_{XC}[\rho](\mathbf{r})$. This final term is defined as,

$$E_{XC}[\rho](\mathbf{r}) = F[\rho](\mathbf{r}) - (T_{KS}[\rho](\mathbf{r}) + E_H[\rho](\mathbf{r})) \tag{3.25}$$

It therefore makes up the difference of the many-body electron interactions that are missing by considering a system of non-interacting particles. These differences are considered in two parts, the exchange interaction, which contributes the change in energy due to the anti-symmetry of the wavefunction; and the correlation interaction, which contributes the change in energy due to the impact of an electron's electrostatic potential on another electron.
The full Kohn-Sham energy functional is then,

$$E_{KS}[\rho](\mathbf{r}) = T_{KS}[\rho](\mathbf{r}) + E_H[\rho](\mathbf{r}) + E_{XC}[\rho](\mathbf{r}) + \int \rho(\mathbf{r})\hat{V}_{ext}d\mathbf{r} \tag{3.26}$$

with the kinetic energy of the independent particle wavefunctions given by,

$$T_{KS}[\rho](\mathbf{r}) = -\frac{1}{2}\int \phi_i(\mathbf{r})^*\nabla^2\phi_i(\mathbf{r})d\mathbf{r} \tag{3.27}$$

and the Hartree energy given by,

$$E_H[\rho](\mathbf{r}) = \frac{1}{2}\int\int \frac{\rho(\mathbf{r})\rho(\mathbf{r}')}{|\mathbf{r}-\mathbf{r}'|}d\mathbf{r}d\mathbf{r}' \tag{3.28}$$

Currently, the form of the exchange-correlation functional is unknown and so approximations must be used.

3.4.3 The Exchange and Correlation Functional

In their paper outlining the theory, Kohn and Sham suggested an approximation that is now known as the Local Density Approximation (LDA) [121]. This assumes that the electron density at a given point would experience a many-body response as if the entire system were a homogeneous electron gas (HEG) with that density. The functional would then be of the form,

$$E_{XC}^{LDA}[\rho](\mathbf{r}) = \int \rho(\mathbf{r})\epsilon_{HEG}[\rho](\mathbf{r})d\mathbf{r} \tag{3.29}$$

where $\epsilon_{HEG}[\rho](\mathbf{r})$ is the energy per particle of the HEG with density $\rho(\mathbf{r})$. An extension of the LDA known as the Generalised Gradient Approximation (GGA) [123–126] also includes information about the gradient of the charge density and is given by,

$$E_{XC}^{GGA}[\rho](\mathbf{r}) = \int \rho(\mathbf{r})\epsilon_{HEG}[\rho, \nabla\rho](\mathbf{r})d\mathbf{r} \tag{3.30}$$

However, as these are both approximations to the exchange-correlation functional, they both introduce errors that impact their predictive abilities. More advanced forms for the exchange-correlation functional exist that include more information about the system to which they are applied, but LDA and GGA still see widespread use.

3.4.4 Self-Consistent Field Cycles

The Kohn-Sham equations of section 3.4.2 form a set of Schrödinger like equations that can be solved to find the independent particle wavefunctions. However, the functionals of equation 3.26 require the charge density which is defined using the independent particle wavefunction in equation 3.20, this is somewhat of a "Catch 22"[127]. To solve this problem, an initial guess of the charge density is supplied. This is then used in equation 3.26 to define the potentials from which a new set of wavefunctions and charge densities can be found. Unless the initial charge density is the ground state, the input and output charge densities will be different. These two charge densities can then be combined to give a new input charge density which is used to generate new potentials from which a new output density can be found. This process is repeated until the energy of the input and output charge densities agree within a defined tolerance threshold, a situation referred to as self-consistency.

3.4.5 Basis Functions

As seen in section 3.3, the single particle wavefunctions can be represented computationally as the linear combination of a finite number of b basis functions.

$$\psi_e(\mathbf{r}) = \sum_{i=1}^{b} c_i\phi_i(\mathbf{r}) \tag{3.31}$$

There are then two common choices for the basis set, plane waves and Cartesian Gaussian orbitals; both of which have advantages and drawbacks.

The use of plane waves is the same as finding the Fourier expansion of the wavefunction. A plane wave basis set is then particularly useful in a periodic crystal as Bloch's theorem states that a particle in a periodic potential has a wavefunction that is the product of plane waves and a periodic function that has the same periodicity as the potential, equation 1.7. Using plane waves, the periodic part of equation 1.7 can be written as,

$$u(\mathbf{r}) = \sum_{\mathbf{G}} c_{\mathbf{G}} e^{i\mathbf{G}\cdot\mathbf{r}} \tag{3.32}$$

Here, $\mathbf{G}$ is a reciprocal lattice vector, $c_{\mathbf{G}}$ is a complex coefficient, and plane waves are constrained by the periodicity of the unit cell, such that $\mathbf{G}\cdot\mathbf{r} = 2\pi m$ where m is a positive integer. For values of $\mathbf{k}$ inside the first Brillouin zone, the Bloch wavefunction can then be rewritten as,

$$\psi(\mathbf{r}) = \sum_{\mathbf{G}} c_{\mathbf{k}+\mathbf{G}} e^{i(\mathbf{k}+\mathbf{G})\cdot\mathbf{r}} \tag{3.33}$$

Due to the periodicity, a plane wave basis set allows for the easy use of the fast Fourier transform which can be used to efficiently transform the system to a space in which a given calculation is more suited. Plane waves are also inherently orthogonal to one another and the accuracy of a plane wave basis will converge monotonically as the number of basis functions is increased. However, this convergence may require many basis functions for a suitable degree of accuracy if the wavefunction oscillates rapidly, for example, when it is close to the atomic core. Also, plane wave methods treat the whole space equally, not just areas of interest; this results in the number of basis functions required for suitable accuracy scaling with the volume being calculated.

Another option for a basis set is then a localised one such as Cartesian Gaussian orbitals. These require fewer basis functions when compared to plane waves and analytic expressions are available for the integrals. Cartesian Gaussian orbitals centred at position $\mathbf{R}_i$ are of the form,

$$\phi_i(\mathbf{r} - \mathbf{R}_i) = (\mathbf{r}_x - \mathbf{R}_{i,x})^{n_x}(\mathbf{r}_y - \mathbf{R}_{i,y})^{n_y}(\mathbf{r}_z - \mathbf{R}_{i,z})^{n_z} e^{-\alpha_i(\mathbf{r}-\mathbf{R}_i)^2} \tag{3.34}$$

Here α_i is a real number and $n_x + n_y + n_z = n_i \geq 0$. For a given value of i, different

values of n_i represent orbital symmetries. For example, $n_i = 0$ represents a single spherically symmetric s-orbital, $n_i = 1$ gives three p-orbitals and $n_i = 2$ gives six d-orbitals, however three of these combine to give an s-orbital of the form $(\mathbf{r} - \mathbf{R}_i)^2 e^{-\alpha_i(\mathbf{r}-\mathbf{R}_i)^2}$. As these are localised functions, they can be centred on areas of interest such as the nuclei or the bonding sites. However, unlike plane waves, Gaussian orbitals aren't necessarily orthogonal. This means that the solution is found using a generalised eigenvalue problem, and so the overlap integral of the Gaussian functions must be calculated, however, as the size of the basis set is increased this overlap becomes singular[128]. Also, although Gaussian orbitals allow for the calculation to be focussed on sites of interest, these must generally be decided before the calculation is begun. Finally, unlike plane wave functions, there are several parameters that control the accuracy of the system and cannot generally be systematically improved.

3.4.6 Pseudopotentials

Further reductions in complexity can be made by considering which of the electrons it is necessary to model explicitly. The core state electrons are tightly bound to the nucleus and so contribute very little to bonding and other quantities of interest. In addition to this, the requirement of orthogonality means that the valence electrons have wavefunctions near the cores that have many nodes, requiring more basis states to model to a desired degree of precision. Therefore, by combining the effect of the core electrons with those of the nuclei, the valence electron wavefunctions can be calculated using a smoother screened effective potential. This pseudopotential must match the exact potential at some radius, r_c, such that the valence electron pseudo-wavefunctions match the exact wavefunctions above r_c. This reduces the complexity as fewer basis states will be required to represent the pseudo-wavefunction and the calculation only needs to consider the valence electrons.

3.4.7 Density Functional Perturbation Theory

As detailed, DFT is a method for calculating ground state properties, however, if the system is perturbed such that it remains close to the ground state then methods similar to regular perturbation theory can be applied, giving rise to density functional perturbation theory (DFPT) [129]. Taking the Hamiltonian of equation 3.21 as a reference, a small perturbation,

λ, can then be applied to this system. The operators, wavefunctions, energy and densities in equations 3.20 to 3.22 can be expanded in terms of this perturbation,

$$X(\lambda) = X + \lambda \frac{\partial X}{\partial \lambda}\bigg|_{\lambda=0} + \frac{\lambda^2}{2}\frac{\partial^2 X}{\partial \lambda^2}\bigg|_{\lambda=0} + \dots \tag{3.35}$$

where $X = \hat{H}, \epsilon_i, \phi_i \dots$ The perturbed system is then,

$$\hat{H}_{KS}(\lambda)\phi_i(\mathbf{r};\lambda) = \epsilon_i(\lambda)\phi_i(\mathbf{r};\lambda) \tag{3.36}$$

Following the derivation shown in appendix C, the first order change in the eigenenergy with respect to λ is given by the Hellmann-Feynman theorem [130–133],

$$\frac{\partial \epsilon_i}{\partial \lambda} = \int \phi_i^*(\mathbf{r})\frac{\partial \hat{H}}{\partial \lambda}\phi_i(\mathbf{r})d\mathbf{r} \tag{3.37}$$

To calculate the first order change in the eigenenergy with respect to some variable, λ, only the change in the Hamiltonian with respect to λ is needed. However, to find $\frac{\partial \hat{H}}{\partial \lambda}$ requires $\frac{\partial \phi_i(\mathbf{r})}{\partial \lambda}$ which is found via the Sternheimer equation [134, 135],

$$\left(\hat{H} - \epsilon_i\right)\frac{\partial \phi_i(\mathbf{r})}{\partial \lambda} = -\left(\frac{\partial \hat{H}}{\partial \lambda} - \frac{\partial \epsilon_i}{\partial \lambda}\right)\phi_i(\mathbf{r}) \tag{3.38}$$

Similar to the unperturbed system, $\frac{\partial \hat{H}}{\partial \lambda}$ is needed to calculate $\frac{\partial \phi_i(\mathbf{r})}{\partial \lambda}$, but $\frac{\partial \phi_i(\mathbf{r})}{\partial \lambda}$ is needed to calculate $\frac{\partial \hat{H}}{\partial \lambda}$. Therefore, a self-consistent method is required to calculate the perturbed wavefunction with the constraint,

$$\int \phi_i^*(\mathbf{r})\frac{\partial \phi_j(\mathbf{r})}{\partial \lambda} + \frac{\partial \phi_i^*(\mathbf{r})}{\partial \lambda}\phi_j(\mathbf{r})d\mathbf{r} = 0 \tag{3.39}$$

However, if an analytic form for the first order change in $\hat{H}$ with respect to λ can be found then $\frac{\partial \epsilon_i}{\partial \lambda}$ can be found easily.

Chapter 4 shows how the band structure is stored on a tetrahedral grid, a necessary quantity for the refinement of this grid is $\frac{\partial E(\mathbf{k})}{\partial \mathbf{k}}$. According to Bloch's theorem, equation 1.7,

in a periodic potential a shift of $\mathbf{T}$ would cause the wavefunction to change as,

$$\phi_i(\mathbf{r}+\mathbf{T}) = \phi_i(\mathbf{r})e^{i\mathbf{k}\cdot\mathbf{T}} \tag{3.40}$$

from which the first order change in the independent particle wavefunctions with respect to $\mathbf{k}$ can be found. This then leads to a computationally inexpensive calculation to be made to find $\frac{\partial E(\mathbf{k})}{\partial \mathbf{k}}$ using the equations C.11, C.10 and 3.37.

By following a similar method, the second order change in eigenenergy with respect to a general perturbation, λ, is given by

$$\frac{\partial^2 \epsilon_i}{\partial \lambda^2} = \int \phi_i^*(\mathbf{r})\frac{\partial^2 \hat{H}}{\partial \lambda^2}\phi_i(\mathbf{r})d\mathbf{r} + \int \left(\phi_i^*(\mathbf{r})\frac{\partial \hat{H}}{\partial \lambda}\frac{\partial \phi_i(\mathbf{r})}{\partial \lambda} + \frac{\partial \phi_i^*(\mathbf{r})}{\partial \lambda}\frac{\partial \hat{H}}{\partial \lambda}\phi_i(\mathbf{r})\right) d\mathbf{r} \tag{3.41}$$

A relevant example needing the second order change in eigenenergy is the calculation of phonon frequencies. Due to the Born-Oppenheimer approximation, section 3.2, the Hamiltonian for the nuclei is given by,

$$\hat{H}_N = \hat{T}_N + \hat{V}_{N-N} + E_{gs} \tag{3.42}$$

where E_{gs} is the sum of the ground state energies of the non-interacting particles moving in the field of fixed nuclei, with a Hamiltonian given by equation 3.21; $\hat{V}_{N-N}$ is the nucleus-nucleus Coulomb energy and $\hat{T}$ is the nuclear kinetic energy. The equilibrium geometry of the system is found when the forces acting on the individual nuclei is zero.

$$\mathbf{F}_I = -\frac{\partial E(\mathbf{R})}{\partial \mathbf{R}_I} = 0 \tag{3.43}$$

The nuclei will oscillate about these equilibrium positions with frequencies ω, which are the set of eigenvalues of the Hessian of the nuclear energy scaled by the nuclear masses [129],

$$det\left|\frac{1}{\sqrt{M_I M_J}}\frac{\partial^2 E(\mathbf{R})}{\partial \mathbf{R}_I \partial \mathbf{R}_J} - \omega^2 \mathbb{I}\right| = 0 \tag{3.44}$$

The second order change in nuclear energy with respect to nuclear positions can then be found

by substituting the Hamiltonian of equation 3.42 into equation 3.41, giving

$$\frac{\partial^2 E}{\partial R_I \partial R_J} = \sum_{i=1}^{n} \frac{\partial^2 \epsilon_i}{\partial R_I \partial R_J} = \int \rho(\mathbf{r}) \frac{\partial^2 V_{N-N}(\mathbf{r}, \mathbf{R})}{\partial R_I \partial R_J} d\mathbf{r} + \int \frac{\rho(\mathbf{r})}{\partial R_J} \frac{\partial^2 V_{N-N}(\mathbf{r}, \mathbf{R})}{\partial R_I} d\mathbf{r} + \frac{\partial^2 E_{gs}(\mathbf{R})}{\partial R_I \partial R_J} \tag{3.45}$$

3.5 Summary

In this chapter, an overview of the many-body electron problem has been discussed, and the computational methods developed to deal with it introduced. In particular, the formulation of DFT has been described as this is the method employed in this thesis due to its ability to calculate material parameters from first principles. In the discussion of DFT, approximations that allow for it to be a usable method have been introduced as well as the extension through perturbation theory that allows for the efficient calculation of the first derivative of the band structure and the method by which the phonon frequencies can be found.

Chapter 4

Ab Initio Scattering Rates

As shown in section 2.2, the MC simulations deal with the drift step and scattering step separately. The accuracy of both of these steps, and therefore the final result, depends on the accuracy of the set of the input parameters and the choice of the band structure approximation.

This work focusses on the improvement of the calculation of the scattering rates by introducing numerically calculated quantities from DFT. The methods employed were chosen such that they could be extended to improve the drift step as well, see section 4.1, however this was beyond the scope of this work. As seen in section 2.3, the scattering rate from a state $\mathbf{k}$ to a state $\mathbf{k}'$ for non-polar optical phonon, acoustic phonon, and charged impurity mediated scattering are all of the form,

$$W(\mathbf{k}) = C(E_{\mathbf{k}})g(E_{\mathbf{k}'}) \tag{4.1}$$

where $C(E_{\mathbf{k}})$ is an energy dependent factor determined by the specific mechanism chosen and $g(E_{\mathbf{k}'})$ is the DOS of the post scattering state with $E_{\mathbf{k}'} = E_{\mathbf{k}} \pm E_{trans}$.

This chapter starts by detailing the steps taken to calculate the DOS numerically. Section 4.1 starts with a review of various methods used to store the band structure calculated using DFT before going on to describe how the chosen method generates and refines a non-uniform tetrahedral grid from which the DOS can be calculated. The following sections then go on to discuss the energy dependent prefactor. For ADP and NPOP scattering, this prefactor depends on the deformation potential, which are generally calculated empirically. Section 4.2 details two methods that can be used to approximate the deformation potential numerically via DFPT methods.

4.1 Density of States Calculation

Although this project focusses only on the scattering step, the methods described in this section were chosen such that it is possible for them to be extended so that the full band structure can be used in both the drift and the scattering steps resulting in a (FBMC) simulation.

As seen in sections 1.1.2 and 1.1.3, it is necessary to have the energy, velocity and DOS to solve the BTE via Monte Carlo simulation and all these quantities rely on the band structure [9, 136]. However, due to the complexity of calculating the band structure numerically, it is necessary to have a reliable method for storing the band structure for later use in such a way that the necessary quantities can be found more efficiently for a given electron wave vector.

More advanced FBMC simulations [18, 21–23, 92–100] shift the burden of these calculations from the processor to the memory by pre-calculating essential values and storing them in well-structured look up tables. These techniques discretise the band structure into cubic or tetrahedral grids, and then store lists of these volumes that intersect a given constant energy surface. As such, when it comes time for costly searches through a volume that contains a given energy and/or momentum, the use of these lookup tables dramatically decreases the required search space. In this work, the band structure was calculated using DFT and discretised onto a non-uniform tetrahedral grid.

Until recently the band structure in FBMC simulators had been calculated via empirical pseudopotential methods (EPM). Although EPM gives good agreement with experimental results, this is because it uses parameters which are determined empirically and as such may be limited in its predictive abilities of new and emerging materials. Here, DFT is employed as it allows for the *ab initio* calculation of the necessary parameters. Another benefit of using DFT is that DFPT allows for the easy calculation of the gradient of the band structure with respect to the electron momentum, $\mathbf{k}$, as seen in section 3.4.7. Along with the energy at a given momentum, $E(\mathbf{k})$, the first derivative of the energy with respect to the momentum vector, $\frac{\partial E(\mathbf{k})}{\partial k_i}$, is also a required quantity in the discretisation of the band structure, as shown in section 4.1.3.

A non-uniform tetrahedral grid was chosen over a cubic grid for several reasons. Firstly, a non-uniform tetrahedral grid can completely fill the IW of the BZ without any grid points being outside the volume. This means that there are no edge case calculations to be considered and

all the tetrahedra contribute fully. Secondly, as the discretisation is non-uniform, the accuracy of interpolation can be improved in areas of higher curvature with the addition of more grid points without more being added in areas of lower curvature. This means that fewer grid points, and therefore fewer tetrahedra, are required overall when compared to a uniform or cubic grid. This non-uniform refinement can be done in a cubic grid, however this will result in some grid points being located on the edges or faces of cubes with smaller neighbours. Generally in these grids there are restrictions on the difference in size of two neighbouring cubes and so the refinement of one edge may ripple out requiring more grid points to be calculated. Finally, a non-uniform tetrahedral grid was chosen as when a plane intersects a tetrahedron, the shape of the intersection can only be a triangle or a quadrilateral. This then simplifies the calculations that depend on the area of intersection, as seen in appendix B

This project mostly followed the method of Jungemann *et al.* [21, 22, 96] to discretise the band structure over a non-uniform tetrahedral grid. As such, many of the definitions detailed here are the same.

4.1.1 Definitions

A non-uniform tetrahedral grid is generated for each energy band, the nth energy band will be split into N_n^{tet} tetrahedra defined by N_n^{nod} k-vector grid points. As mentioned above, unlike the work of C. Jungemann *et al.* [21, 22, 96] which uses a non-local EPM, the energy at a given k-point was found by solving the DFT equations for the given k-point.

Tetrahedron i of energy band n is defined by four grid points; $\mathbf{k}_{t(n,i,0)}$, $\mathbf{k}_{t(n,i,1)}$, $\mathbf{k}_{t(n,i,2)}$ and $\mathbf{k}_{t(n,i,3)}$. These are ordered within tetrahedron i in terms of their energies such that they are in ascending order; $E_{n,t(n,i,0)} \leqslant E_{n,t(n,i,1)} \leqslant E_{n,t(n,i,2)} \leqslant E_{n,t(n,i,3)}$. With the tetrahedra defined, the energy within any tetrahedron can be interpolated linearly using the equation

$$E_n(\mathbf{k}) = E_{n,t(n,i,0)} + \nabla_{\mathbf{k}} E_{n,i} \cdot (\mathbf{k} - \mathbf{k}_{t(n,i,0)}) \tag{4.2}$$

where $\nabla_{\mathbf{k}} E_{n,i}$ is a linear interpolation constant that approximates the gradient of the band structure energy with respect to the wavevector, found for each tetrahedron such that equation 4.2 exactly reproduces the band energies found at the vertices of the tetrahedron.

$$
\begin{aligned}
E_{n,t(n,i,1)} &= E_{n,t(n,i,0)} + \nabla_{\mathbf{k}} E_{n,i} \cdot \left(\mathbf{k}_{n,t(n,i,1)} - \mathbf{k}_{n,t(n,i,0)}\right), \\
E_{n,t(n,i,2)} &= E_{n,t(n,i,0)} + \nabla_{\mathbf{k}} E_{n,i} \cdot \left(\mathbf{k}_{n,t(n,i,2)} - \mathbf{k}_{n,t(n,i,0)}\right), \\
E_{n,t(n,i,3)} &= E_{n,t(n,i,0)} + \nabla_{\mathbf{k}} E_{n,i} \cdot \left(\mathbf{k}_{n,t(n,i,3)} - \mathbf{k}_{n,t(n,i,0)}\right)
\end{aligned}
\tag{4.3}
$$

Defining the shorthand notation $\Delta E_{j,k} = E_{n,t(n,i,j)} - E_{n,t(n,i,k)}$ and $\Delta \mathbf{k}_{j,k} = \mathbf{k}_{n,t(n,i,j)} - \mathbf{k}_{n,t(n,i,k)}$, and subtracting $E_{n,t(n,i,0)}$ from both sides; equations 4.3 can be re-written as a matrix equation.

$$
\begin{pmatrix} \Delta E_{1,0} \\ \Delta E_{2,0} \\ \Delta E_{3,0} \end{pmatrix} = \begin{pmatrix} \Delta \mathbf{k}_{1,0} \\ \Delta \mathbf{k}_{2,0} \\ \Delta \mathbf{k}_{3,0} \end{pmatrix} \begin{pmatrix} (\nabla_{\mathbf{k}} E_{n,i})_{k_x} \\ (\nabla_{\mathbf{k}} E_{n,i})_{k_y} \\ (\nabla_{\mathbf{k}} E_{n,i})_{k_z} \end{pmatrix} \tag{4.4}
$$

As each of the rows in the first term on the right-hand side of equation 4.4 are k-space vectors, this is a square matrix and so the interpolation constant for a tetrahedron can be found by inverting this matrix and left multiplying equation 4.4 by it.

$$
\nabla_{\mathbf{k}} E_{n,i} = \begin{pmatrix} \Delta \mathbf{k}_{1,0} \\ \Delta \mathbf{k}_{2,0} \\ \Delta \mathbf{k}_{3,0} \end{pmatrix}^{-1} \begin{pmatrix} \Delta E_{1,0} \\ \Delta E_{2,0} \\ \Delta E_{3,0} \end{pmatrix} \tag{4.5}
$$

The four faces of the tetrahedra are shared with either one of the adjacent tetrahedra or with the boundary of the IW. As the interpolation constant is defined to exactly reproduce the energies at the vertices of the tetrahedra, the energy is continuous throughout the Brillouin Zone (BZ). However, $\nabla_{\mathbf{k}} E_{n,i}$ is not continuous as it is constant inside the tetrahedra and changes instantaneously as it crosses from one tetrahedron to another, and so is not differentiable. Jungemann *et al.* demonstrate methods for calculating the second derivative of the energy in reference [96], however these were not needed here.

4.1.2 Initial Grid

An initial grid must be supplied before the refinement process can occur. The initial grid points are generally the high symmetry points for the BZ, however, if it is not on a high symmetry

point then an additional grid point is placed at the position of the conduction band minimum, to improve the accuracy around this point. These initial grid points are then grouped to form tetrahedra that are given as the starting point for the refinement process.

4.1.3 Refining the Grid

As the interpolation used is linear, the grid must be refined by adding new vertices and creating smaller tetrahedra to reduce the error to an acceptable level. The grid is refined by creating a list of the edges of all the tetrahedra, ordered in terms of their lengths. Starting from the longest edge, an edge is marked for splitting if it breaks one of two rules. The first is if it is longer than a user defined length threshold. The second is if the interpolation at the centre of an edge differs from the 'true' band structure energy by more than a user defined energy threshold. In references [21, 22, 96] the exact band structure energy is calculated at 5 points, evenly distributed, along an edge for comparison with the linearly interpolated answer. Using DFT, this would require the diagonalisation of a matrix 5 times, once for each of the k-points, of which only one may be used if the error is greater than the threshold. In this work, a second, higher accuracy interpolation method is used instead. When solving the DFT equations, the first derivative of the band structure, $\frac{\partial E}{\partial \mathbf{k}}$, can also be calculated. This provides extra information about the band structure and is used in this project to produce a cubic spline between the k-points on either end of the edge being checked. See appendix A for details on how the splines are calculated.

This spline is then used to interpolate the energy halfway along the edge to check that the linear interpolation constant that has been calculated for a given tetrahedron is within error tolerance. As cubic splines are also an interpolation method, they will also have an associated error, however, as this is a higher accuracy interpolation method, the associated error should be less than that of the linear interpolation. Also, the shorter the edges of the tetrahedra are, the smaller this error will be for both methods. Therefore, the first condition for splitting, the edge being shorter than a user defined length tolerance, should reduce this error to a negligible level before the cubic splines are employed.

As stated previously, if the longest edge breaks either of the two rules then it is marked for splitting. However, as a tetrahedron with a highly irregular shape (e.g. one that is extremely

long and narrow) may introduce numerical errors [137]; a final step is taken before the marked edge is split to ensure that the volume quality is kept above a certain tolerance. When a tetrahedron is created, the volume quality is calculated as,

$$Q_{n,i}^{tet} = 6\sqrt{2}\frac{V_{n,i}^{tet}}{(h_{max,n,i}^{tet})^3} \tag{4.6}$$

where $V_{n,i}^{tet}$ is the volume of the ith tetrahedron in the nth energy band and $h_{max,n,i}^{tet}$ is the length of the longest edge of the tetrahedron. Therefore, the quality of a tetrahedron is given by the ratio of the actual volume to the theoretical maximum volume. When an edge is marked for splitting, all the tetrahedra it belongs to are checked to see whether the volume quality is less than 5%. If any tetrahedra have a volume quality below this threshold, then the longest edge from all these tetrahedra is marked for splitting instead. This process is repeated until there

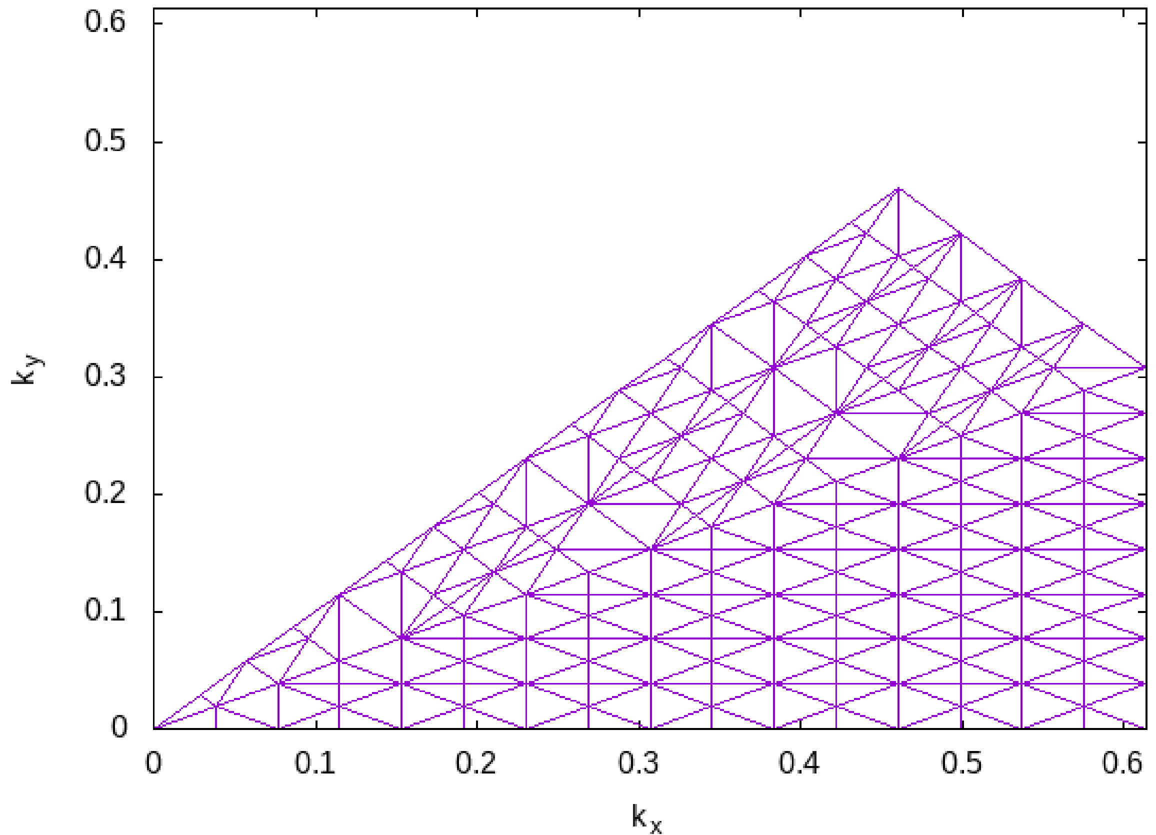

Figure 4.1: The $k_z = 0$ plane of the discretisation of the irreducible wedge of Si.

are no more violations of the conditions for splitting. Figure 4.1 shows the $k_z = 0$ plane of the discretisation of the irreducible wedge of Si after the application of the methods detailed in this section.

4.1.4 Density of States Interpolation

The DOS is a measure of the allowed states a charge carrier can be in at a particular energy and for a given band, n, is given by,

$$g_n(E) = \frac{1}{\Omega}\sum_{i=1}^{N}\delta(E - E_n(\mathbf{k}_i)) \tag{4.7}$$

Where Ω is the crystal volume, N is the number of countable states in the BZ, n is the index for the energy bands and $E_n(\mathbf{k}_i)$ is the energy at $\mathbf{k}_i$. As there are many available states, the distribution may be treated as continuous, converting the sum to an integral over all k-space,

$$g_n(E) = \frac{1}{(2\pi)^3}\int \delta(E - E_n(\mathbf{k}))d^3\mathbf{k} \tag{4.8}$$

Following the work of Gilat *et al.* [138–142], equation 4.8 can be rewritten as a surface integral

$$g_n(E) = \frac{1}{(2\pi)^3}\int_{A_n(E)} \frac{d^2\mathbf{k}}{|\nabla_{\mathbf{k}} E_n(\mathbf{k})|}, \tag{4.9}$$

where $A_n(E)$ is the iso-energy surface with energy E for band n in the BZ. As the grid is discretised into tetrahedra where the gradient of the band structure, $\nabla_{\mathbf{k}} E_n(\mathbf{k})$, is constant; the DOS for each tetrahedron can be found independently as

$$g_{n,i}^{tet}(E) = \frac{1}{(2\pi)^3}\frac{A_{n,i}(E)}{|\nabla_{\mathbf{k}} E_{n,i}(\mathbf{k})|}, \tag{4.10}$$

where i is the tetrahedron index, and $A_{n,i}(E)$ is the area of the intersection of the iso-energy surface and the ith tetrahedron. To ensure that the denominator in equation 4.10 is never equal to zero, a small random perturbation is applied to the vertices of the initial grid and those added during the grid refinement step which means that equation 4.5 does not result in the zero vector. The DOS can then be found for the entire BZ by summing over the contributions from the individual tetrahedra in each band.

$$g(E) = \sum_n \sum_i g_i^{tet}(E) \tag{4.11}$$

Although the denominator of equation 4.10 is already known from equation 4.5, a more efficient way to calculate the contribution to the DOS is via the form given by Müller and Wilkins [143],

$$g_i^{tet}(E) = \begin{cases} \frac{3V_{n,i}^{tet}}{(2\pi)^3}\frac{(E-E_{n,t(n,i,0)})^2}{\Delta E_{1,0}\Delta E_{2,0}\Delta E_{3,0}} & \text{if } E_{n,t(n,i,0)} < E < E_{n,t(n,i,1)} \\ \frac{3V_{n,i}^{tet}}{(2\pi)^3}\left(\frac{(E-E_{n,t(n,i,0)})^2}{\Delta E_{1,0}\Delta E_{2,0}\Delta E_{3,0}} + \frac{(E-E_{n,t(n,i,1)})^2}{\Delta E_{0,1}\Delta E_{2,1}\Delta E_{3,1}}\right) & \text{if } E_{n,t(n,i,1)} < E < E_{n,t(n,i,2)} \\ \frac{3V_{n,i}^{tet}}{(2\pi)^3}\frac{(E-E_{n,t(n,i,3)})^2}{\Delta E_{3,0}\Delta E_{3,1}\Delta E_{3,2}} & \text{if } E_{n,t(n,i,2)} < E < E_{n,t(n,i,3)} \end{cases} \tag{4.12}$$

Here, $V_{n,i}^{tet}$ is the volume of the ith tetrahedron in the nth energy band. A derivation of the first case is shown in appendix B.

As the maximum and minimum energy within a tetrahedron are known, it doesn't make sense to check the intersecting area of the iso-energy surface with a tetrahedron with which it doesn't overlap. Therefore, for a given energy, these methods are only applied to those tetrahedra that contain said energy, so as to not waste processing time.

4.1.5 Valley Allocation

The scattering rates given in section 2.3 are calculated for each valley being considered. Therefore, for the scattering methods that depend on the DOS, the DOS used is not the total DOS but the DOS of the valley. In the analytic approximation, information about the valley is encapsulated in the effective mass. Here, the tetrahedra are partitioned into specific valleys from which the valley DOS is calculated. In the work of Jungemann *et al.* [21, 22, 96], this partition is done using symmetry operations. Here, as in reference [92], a modified steepest descent method is implemented.

For a given tetrahedron, i, in band n, the valley to which it belongs is found by first considering all the adjacent tetrahedra that contain the vertex with the lowest energy, $\mathbf{k}_{t(n,i,0)}$. The adjacent tetrahedra are then searched for a tetrahedron, j, such that $E_{n,t(n,j,0)} < E_{n,t(n,i,0)}$. If more that one of the adjacent tetrahedra fulfils this condition then the next tetrahedron is chosen to minimise the angle between a line drawn between $\mathbf{k}_{t(n,i,0)}$ and $\mathbf{k}_{t(n,j,0)}$ and the

interpolation gradient,

$$\theta = arccos\left(\frac{\left(\mathbf{k}_{t(n,i,0)} - \mathbf{k}_{t(n,j,0)}\right) \cdot \nabla_{\mathbf{k}} E_{n,i}}{|\left(\mathbf{k}_{t(n,i,0)} - \mathbf{k}_{t(n,j,0)}\right)||\nabla_{\mathbf{k}} E_{n,i}|}\right) \tag{4.13}$$

This process is then repeated with tetrahedron j and vertex $\mathbf{k}_{t(n,j,0)}$ until no adjacent tetrahedra contain a vertex with a lower energy, at which point a conventional steepest gradient method using DFT is employed to find the exact minimum. During this process of moving between tetrahedra, special care must be taken for tetrahedra and vertices that lie on the boundary of the IW to ensure that the next tetrahedron in the process is the correct one. If the current vertex being considered is on the boundary of the IW, then symmetry operations are applied so that the correct set of tetrahedra inside the boundary are considered as being adjacent.

Another consideration is for tetrahedra in bands above the lowest conduction band. When a minimum is found, this could be a true valley minimum or instead there may be a band crossing. In these cases, once the steepest descent method is complete, the energy at the minimum in the current band is compared to the energy at the same point in the band below. If the energies are degenerate and the gradient in the current band is not flat, the minimum is instead considered to be a band crossing and the tetrahedra belong to a valley in the band below.

This is not a perfect method as it will miss out on band crossings that do not occur at minima, and it may count cases where the bands approach but don't cross as crossings. This method will produce an error in the allocation of tetrahedra to valleys and therefore the valley DOS, however this error should be negligible, and it is an improvement over the method of assigning tetrahedra to the nearest valley as employed by Jungemann *et al.* [21, 22, 96].

4.2 Deformation Potential Calculation

The deformation potential describes the shift in the band structure from a change in the lattice caused by phonon vibrations. The theory was originally developed by Bardeen and Shockley [102] and generalised by Herring and Vogt [103], their use in scattering stems from the fact that they act as proportionality constants for the perturbed potentials. For acoustic scattering,

the perturbation is proportional to the induced strain,

$$H' = \Xi_d \nabla \cdot \mathbf{u}(\mathbf{r}, t) \tag{4.14}$$

whereas, for optical scattering the perturbation is proportional to the displacement,

$$H' = D_o \mathbf{u}(\mathbf{r}, t) \tag{4.15}$$

These perturbations lead to the scattering matrix of equation 2.26 in section 2.3.1, as shown in references [15, 33]. Generally, the deformation potentials are found empirically by calibration simulations. MC simulations are set to run at a temperature where all NPOP scattering mechanisms are 'frozen' out and so the acoustic scattering is dominant. The simulation is then run while varying the acoustic deformation potential to find the value such that the simulation results are in agreement with experimental results measured at the same temperature. This process is repeated, increasing the temperature to 'defrost' one scattering mechanism at a time until all the deformation potentials are found. As this is an empirical method, it requires a reliable set of experimental data that in reality may be incomplete or totally unavailable. This method is also dependent on what experimental results the simulation results are being matched to; for example, time of flight results or charge carrier mobilities.

This method of calculating the deformation potential also requires a significant amount of time to run the simulation at multiple temperatures and information on which phonon modes are involved and the corresponding energies. This imposes restrictions on what can be studied to materials that are already well characterised and understood; materials with some experimental data, resulting in a huge range in published deformation potentials for a given material; or guessing the parameters for materials where there is little or no experimental data, based on the parameters of other similar materials. Recently, several papers have been published that address this very problem [144–146]. The deformation potentials and other scattering parameters can be calculated via first principles' calculation, which means that the transport properties of new and emerging materials can be studied with greater confidence.

DFPT can be used to directly calculate the deformation potentials from the electron-phonon coupling matrix and extracting the relevant elements [144, 145]. The acoustic phonon

deformation potential for phonon mode ν is calculated as,

$$\Xi_\nu = \frac{d}{d|\mathbf{q}|}\left|\sqrt{\frac{2m_0\omega_{\nu\mathbf{q}}}{\hbar}}g^\nu_{mn}(\mathbf{k},\mathbf{q})\right| \tag{4.16}$$

The non-polar phonon deformation potential for phonon mode ν is calculated as,

$$D_\nu = \sqrt{\frac{2m_0\omega_{\nu\mathbf{q}}}{\hbar}}g^\nu_{mn}(\mathbf{k},\mathbf{q}) \tag{4.17}$$

Here, m_0 is the sum of the masses of all atoms in the unit cell; $\omega_{\nu\mathbf{q}}$ is the phonon frequency for a phonon with mode ν and momentum $\mathbf{q}$; and $g^\nu_{mn}(\mathbf{k},\mathbf{q})$ is the electron phonon coupling matrix, where an electron in band n and state $\mathbf{k}$ is scattered to band m and state $\mathbf{k}+\mathbf{q}$ by a phonon with mode ν and momentum $\mathbf{q}$.

The first derivative in equation 4.16 arises due to the dependence of acoustic scattering on strain, equation 4.14, and as it is calculated as $\mathbf{q} \to 0$. The acoustic deformation potential, however, also has a dependence on the angle between $\mathbf{k}$ and $\mathbf{q}$ [103, 33, 144, 145], given by

$$\Xi_{LA}(\theta) = \Xi_d + \Xi_u cos^2(\theta) \tag{4.18a}$$

$$\Xi_{TA}(\theta) = \Xi_u sin(\theta)cos(\theta) \tag{4.18b}$$

where Ξ_d and Ξ_u are the dilatation and uniaxial deformation potential constants, respectively. These deformation potential constants can then be found by fitting equations 4.18a and 4.18b to longitudinal and transverse acoustic deformation potentials calculated using equation 4.16 for a range of angles between 0 and π. A value for the longitudinal and transverse deformation potentials, independent of the angle between $\mathbf{k}$ and $\mathbf{q}$, can be found by the average of the integral of the square of equations 4.18a and 4.18b between 0 and π. These averages are given by,

$$\Xi^2_{LA} = \Xi^2_d + \Xi_d\Xi_u + \frac{3}{8}\Xi^2_u \tag{4.19a}$$

$$\Xi^2_{TA} = \frac{\Xi^2_u}{8} \tag{4.19b}$$

Generally, only a single value is given for the acoustic deformation potential and so the contribution of the longitudinal and transverse acoustic deformation potentials can then be combined using,

$$\Xi_{ADP}^2 = \Xi_{LA}^2 + \left(\frac{v_l^2}{v_t^2}\right) \Xi_{TA}^2 \tag{4.20}$$

where v_l and v_t are the longitudinal and transverse velocities of sound, respectively.

The optical deformation potential, on the other hand, is found directly from the corresponding elements of the electron-phonon coupling matrix. As stated in sections 2.3.1 and 2.3.4, NPOP scattering is only considered to take part in intervalley scattering. This type of scattering requires phonons with large momenta, far away from the Γ point. At these momenta, all the phonon modes reach similar energies and have little dispersion, therefore, all phonon modes are considered when calculating the intervalley scattering deformation potential.

It is also important to consider how the deformation potentials are combined such as the addition of the two transverse acoustic modes or in finding an average, as well as the effective phonon frequency in the average of the optical phonon deformation potential. By following the method of Fischetti [147] and considering equation 2.35, it can be seen that the addition of n acoustic scattering rates has the impact of summing the square of the n acoustic deformation potentials,

$$\Xi_{tot} = \sqrt{\sum_{i=1}^{n} \Xi_i^2} \tag{4.21}$$

and the average is found as the root means square of the n deformation potentials,

$$\Xi_{avg} = \sqrt{\frac{\sum_{i=1}^{n} \Xi_i^2}{n}} \tag{4.22}$$

Similarly, by considering equation 2.31, the combination of n optical deformation potentials is found as,

$$D_{o,tot} = \sqrt{\sum_{i=1}^{n} D_{o,i}^2} \tag{4.23}$$

with an associated effective energy found using

$$\frac{1}{\hbar\omega^*} = \frac{\sum_i \frac{D_{o,i}^2}{\hbar\omega_i}}{{D_{o,tot}}^2} \tag{4.24}$$

where $\hbar\omega_i$ is the phonon energy associated with deformation potential $D_{o,i}$.

4.3 Choice of DFT Program

For the two processes detailed in the sections above, two different DFT programs were used to best make use of their strengths under different circumstances.

The software suite AIMPRO was used to calculate the band structure when calculating the DOS using the method detailed in section 4.1.4. AIMPRO uses a Gaussian basis set and the methods it employs allows for the treatment of larger cells of atoms and faster solutions of the DFT equations. [13].

However, for the calculations that find the deformation potentials, the open-source software suite Quantum Espresso [148, 149] was used. Quantum Espresso uses a plane wave basis set and has an extension, EPW, that can be used to calculate the electron-phonon coupling matrix [150].

As two different DFT programs with differing basis sets are used, there will be some disagreement in the results. However, as shown in the next chapter, the pseudopotentials used were chosen to minimise the error between the prediction of some physical quantity and the corresponding experimental value.

Finally, it should be noted that the code developed to calculate the DOS does not have to be coupled to AIMPRO and therefore in the future a modification could be made to couple the DOS calculation with Quantum Espresso, thus eliminating this source of error entirely.

4.4 Summary

This chapter detailed the methods developed that used DFT to calculate materials parameters for use in MC simulation. A self refining non-uniform tetrahedral grid method was developed to store the band structure calculated via DFT, this grid can then be used to calculate the DOS numerically via an interpolative method. Methods for calculating the deformation potential for the acoustic and optical phonon modes from DFPT were described, allowing for the calculation of scattering parameters that were previously determined empirically.

Chapter 5

Selection of DFT Inputs

As discussed previously, there are many choices to be made for the inputs of a DFT calculation.

Section 3.4.3 introduced the concept of the exchange-correlation functional as well as some of the approximations made in DFT. Although more complex approximations are available, the exchange-correlation functionals employed here are either LDA or GGA. The use of LDA and GGA approximations will come at the cost of errors in the predictions of DFT, for example, LDA generally underestimates the lattice constant while GGA generally underestimates it. Both of these approximations also underestimate the band gap in semiconductors, sometimes going so far as predicting metallic behaviour in non-metals. These errors may be improved by the use of more in depth functionals, however, these are not the only cause as these errors are a result of the use of approximating the interacting electronic wavefunctions with non-interacting particle wavefunctions. LDA and GGA functionals are applied here due to their simplicity and widespread use, however, due to their effect on the lattice constant and band structure, the DOS and deformation potentials will be impacted. A discussion of the sensitivity of the results to the inputs is given in chapter 9.

Another point to consider is use of pseudopotentials. As discussed in section 3.4.5, these fictitious potentials are implemented to reduce the complexity of the DFT calculation by simplifying the potential and removing core state wavefunctions while reproducing the exact potential and valence state wavefunctions past a given radius. For AIMPRO, these pseudopotentials either take the form proposed by C. Hartwigsen, S. Goedeker and J. Hutter (HGH) [151] or that of M. Krack [152, 153]. For Quantum Espresso, these pseudopotentials either take the form of HGH or are Optimised norm-conserving Vanderbilt (ONCV) pseudopotentials

[154, 155].

In this thesis, for both AIMRPO and Quantum Espresso the DFT inputs were used to predict the lattice constant and bulk modulus of the relaxed system due to their relation to and effect on the phonon modes [156, 157]. The input used was then selected based on its ability to predict the lattice constant and bulk modulus as compared to values calculated experimentally at room temperature. This is not an exhaustive method and by no means an optimised one as there are many pseudopotentials available and there are other methods that could have been employed for comparison, for example by comparison to DFT simulations that do not employ pseudopotentials but model all electrons. However, the DFT inputs presented here were chosen for their simplicity and don't require empirical parameters.

5.1 AIMPRO

The names used in the following sections for AIMPRO summarise the input parameters used. Full details are given in appendix D. The first part of the name obviously indicates the atom the parameters are for, with the preceding and following numbers indicating the total number of electrons and the number of those which are modelled, respectively. The second part refers to the exchange-correlation functional used, either LDA or GGA. The third part refers to how the basis functions are combined to give the guess wavefunction. Each letter in the string refers to the number of Gaussian functions with a given exponent that are included in the wavefunction. As an example, consider the case where a wavefunction is represented by a Gaussian basis set with four exponents and the string *ddpp*. The first and second exponent would contribute all combinations of equation 3.34 for which $n_i \leq 2$, therefore 10 functions each. The last two would contribute all combinations of equation 3.34 for which $n_i \leq 1$, therefore 4 functions each. The guess wavefunction would then be a linear combination of 28 Gaussian functions. The set of exponents used in each Gaussian are not necessarily the same, further detail about the exponents used in each case are given by tables D.1, D.2 and **??**. The final part indicates the pseudopotential method used, either HGH or Krack.

5.1.1 Test Results

Figures 5.1, 5.2 and 5.3 show the predicted values for the lattice constant and bulk modulus for bulk Si, diamond and cBN calculated using AIMPRO. The lattice constant and bulk modulus were calculated by finding the total energy of the system while varying the input lattice constant and fitting the Birch-Murnaghan equation of state.

Si

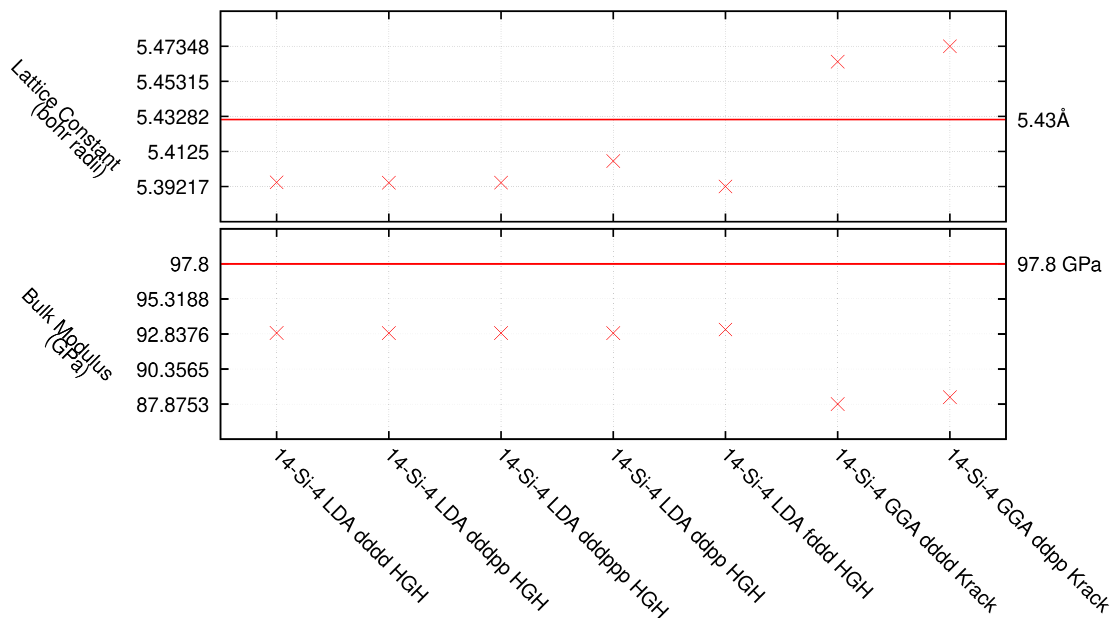

Figure 5.1: Comparison of the ability of a set of DFT inputs for Si to predict the lattice constant [158] and bulk modulus [159] using AIMPRO.

Figure 5.1 shows a comparison of the predicted values for the relaxed lattice constant and bulk modulus of Si calculated via DFT with the experimentally determined values. This figure shows the tendency for LDA calculations to overbind and GGA to underbind, however in all cases, the error in the lattice constant is less than 1%. On the other hand, the error in the prediction of the bulk modulus is much more significant, and as such the DFT inputs selected for the simulation to minimise this error was 14-Si-4 LDA fddd HGH.

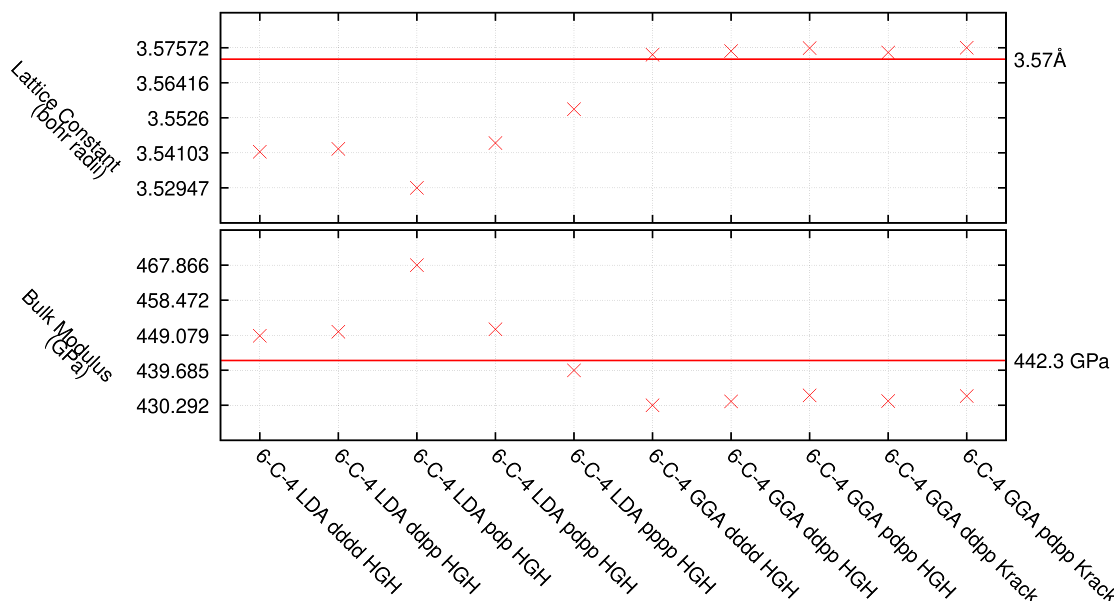

Figure 5.2: Comparison of the ability of a set of DFT inputs for diamond to predict the lattice constant [39, 40] and bulk modulus [160] using AIMPRO.

Diamond

Figure 5.2 shows a comparison of the predicted values for the relaxed lattice constant and bulk modulus of diamond calculated via DFT with the experimentally determined values. This figure once again shows the tendency for LDA calculations to overbind and GGA to underbind. The only case where the error in the lattice constant is greater than 1% is 6-C-4 LDA pdp, but this could be due to the relatively small number of basis functions employed. The figure also shows that the calculations employing GGA exchange-correlation functionals give excellent predictions of the lattice constant. For all the calculations the error in the predicted value of the bulk modulus is less than 3%. The set of DFT inputs selected for the simulation was 6-C-4 GGA pdpp HGH as this minimises the error in the bulk modulus for the systems using GGA functionals.

cBN

Figure 5.3 shows a comparison of the predicted values for the relaxed lattice constant and bulk modulus of cBN calculated via DFT with experimentally determined values. In all cases, the error in the lattice constant when compared with the experimental value is less than 1% with

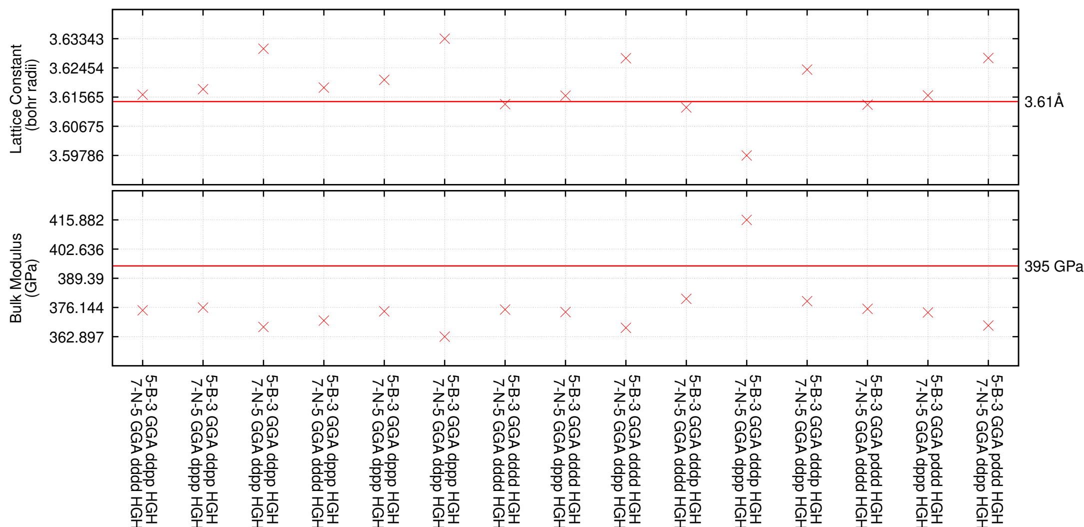

Figure 5.3: Comparison of the ability of a set of DFT inputs for cBN to predict the lattice constant [36, 41] and bulk modulus [36] using AIMPRO.

several having an even smaller error less than 0.1%. As with Si and diamond, the error in the prediction of the bulk modulus is much more significant. In order to minimise this error, the best combination of parameters for cBN was found to be 5-B-3 GGA dddp HGH for boron and 7-N-5 GGA dddd HGH for nitrogen.

5.2 Quantum Espresso

Similar to AIMPRO, the names of the inputs used with Quantum Espresso summarise the input parameters employed. Once again the first part of the name indicates the element the parameters are for. The second part of the name indicates the exchange-correlation functional employed, either GGA or LDA. The final part indicates the pseudopotential method used, either HGH or ONCV, with the numbers indicating a version and FR indicating that the pseudopotential is fully relativistic [161].

5.2.1 Test Results

Figures 5.4, 5.5 and 5.6 show the predicted values for the lattice constant and bulk modulus and cohesive energy for bulk Si, diamond and cBN calculated using Quantum Espresso for a range of pseudopotentials. The lattice constant was calculated by allowing the structure to relax and minimise the calculated stress. The bulk modulus was calculated by finding the

total energy of the system while varying the input lattice constant about the optimised lattice constant and fitting the Birch-Murnaghan equation of state.

Si

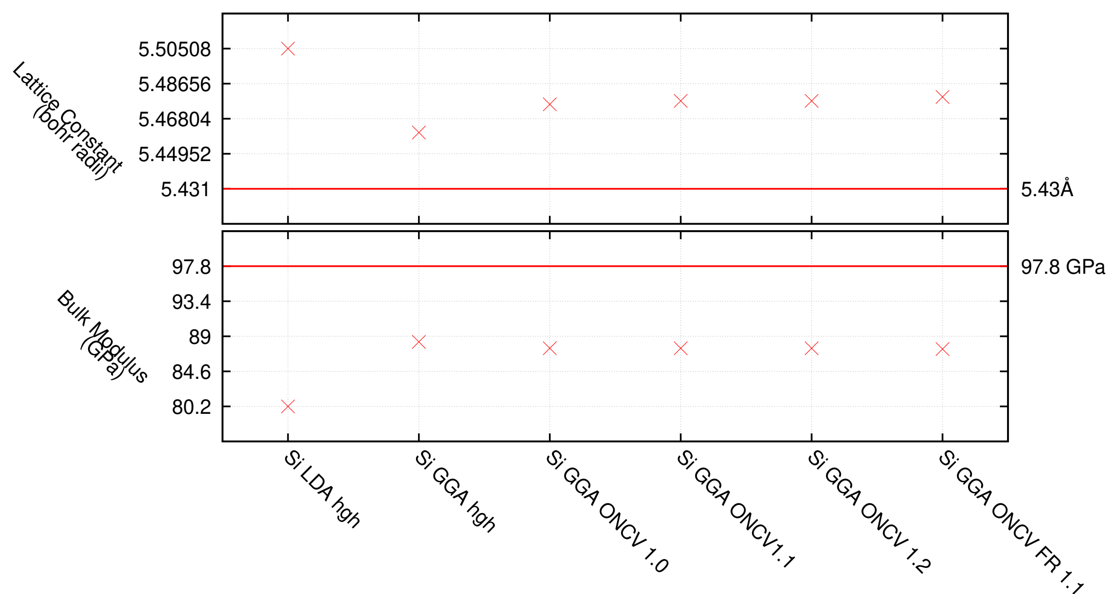

Figure 5.4: Comparison of the ability of a set of DFT inputs for Si to predict the lattice constant [158] and bulk modulus [159] using Quantum Espresso

Figure 5.4 shows the predicted values for the relaxed lattice constant and bulk modulus of Si calculated via DFT for a range of input parameters as compared to the experimentally determined values. Although generally LDA overbinds, in this case all the systems tested predicted the lattice constant to be longer than what has been measured experimentally, however, all the calculations using GGA functionals calculated the lattice constant with an error of less than 1%. The calculated bulk moduli, however, have a much greater error, with the lowest being 10.6%. The DFT inputs selected for further calculation were then Si GGA HGH as this minimises the error in these predictions.

Diamond

Figure 5.5 shows the predicted values for the relaxed lattice constant and bulk modulus of diamond calculated via DFT for a range of input parameters as compared to the experimentally determined values. In all cases, the error in the predicted lattice constant in less than 0.5%

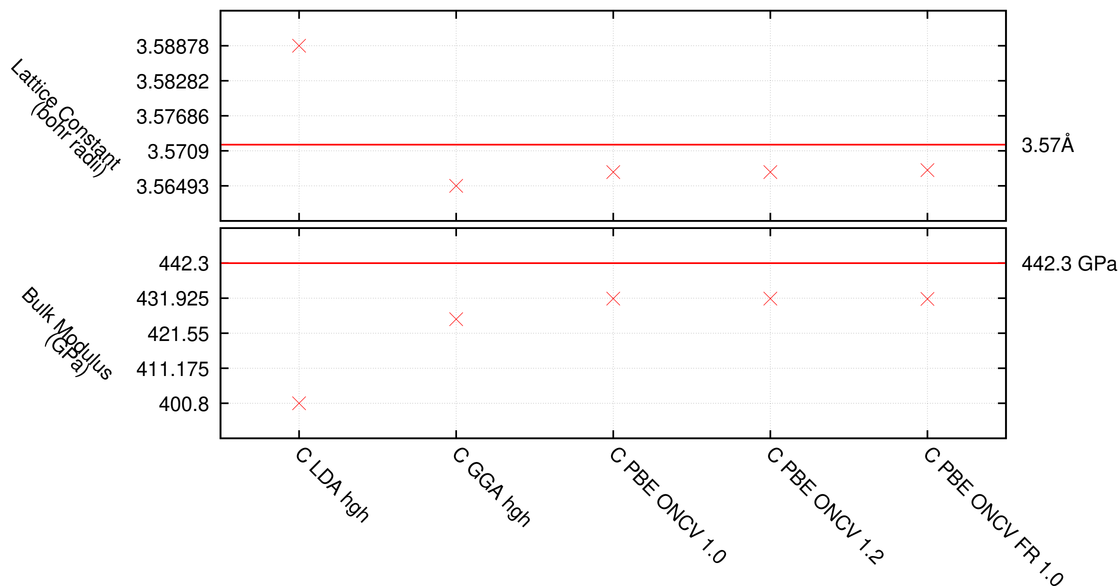

Figure 5.5: Comparison of the ability of a set of inputs for diamond to predict the lattice constant [39, 40] and bulk modulus [160] using Quantum Espresso.

and for all the cases using GGA functionals, the error in the predicted bulk modulus was less than 5%. The set of DFT inputs selected for further calculation were then C GGA ONCV 1.0.

cBN

Figure 5.6 shows the predicted values for the relaxed lattice constant and bulk modulus of cBN calculated via DFT for a range of input parameters as compared to the experimentally determined values. In all cases, the error in the predicted lattice constant in less than 1%. The set of inputs chosen for further calculations were then B GGA HGH for boron and N GGA HGH for nitrogen as this minimises the error in the predicted bulk modulus with an error of 3.9%.

5.3 Summary

This chapter detailed a quick comparison of a range of input parameters for Si, diamond and cBN for AIMPRO and Quantum Espresso. As stated, this is not an exhaustive search through the available inputs and this limited subset were chosen based on their simplicity. Undoubtedly, better predictions could be achieved through the use of more complicated exchange-correlation

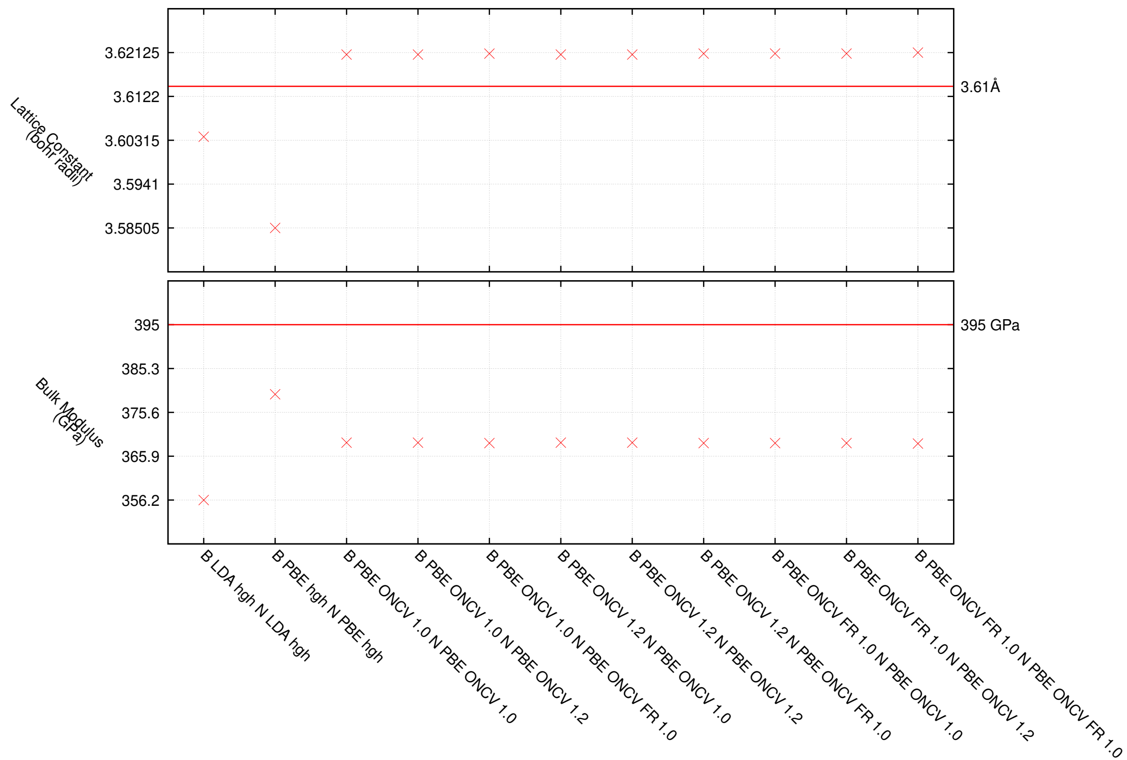

Figure 5.6: Comparison of the ability of a set of Inputs for cBN to predict lattice constant [36, 41], bulk modulus [36] and cohesive energy [162] using Quantum Espresso

potentials, however even with the ideal functionals some disagreement would still be expected due to the underlying approximations of DFT [163–165]. It is possible to include further information such as hybrid functionals to further improve DFT, however these require the setting of empirical parameters [166–168].

Although the methods applied here could be improved, the DFT inputs should allow for the calculation of results that are indicative of the system under study.

Chapter 6

Bulk Silicon Results

The MC simulator written by D. Naylor [19, 101] (as described in chapter 2 and based on the algorithms presented by K. Tomizawa [15]) was modified to be able to model indirect band gap semiconductors using DOS and scattering parameters calculated numerically (via the methods presented in chapter 4) during the scattering step. However, before these methods can be applied to new systems, they must first be applied to a well studied system with well known characteristics such that there is confidence in the ability of these methods to correctly predict the properties of a new material.

To this end, this chapter demonstrates that these methods can be successfully applied to bulk Si and produce results that compare well to what can be found in the literature. Section 6.2 shows how the DOS was calculated via tetrahedral discretisation as detailed in section 4.1 and compared to the DOS calculated directly via AIMPRO. The effective mass and non-parabolicity constant were then calculated and compared to previous work. Following this, section 6.3 presents the acoustic and optical deformation potentials as calculated via Quantum Espresso. As the electron transport of bulk Si is extensively studied, these scattering parameters can be compared to empirically calculated values to ensure that they make sense. Finally, the results from the MC simulation using the numerically calculated scattering parameters and both analytic and numerical DOS are presented in section 6.4. As these simulations were run at low energies, the simulations using numerical and analytic DOS should have good agreement. These results were also compared to simulation results using scattering parameters from literature and experimentally measured results. The chapter concludes with a summary which argues that the use of numerically calculated DOS and scattering parameters in MC

simulation can give better insight into the transport characteristics of materials with fewer experimental results.

6.1 Properties of Silicon

Silicon is an extensively studied material that is inextricably linked to the semiconductor industry which is now indispensable in the modern day. As the two silicon atom basis is isoelectronic with the two carbon basis and boron nitride pair basis, it also forms similar allotropes. The focus here is on the FCC structure that has a lattice constant of 5.431 Å [158] and a Vickers hardness around 12.5 GPa [169]. Unlike diamond and cBN; large, monocrystalline, high purity samples of Si can be grown using the Czochralski method [170] which act as the starting point in the production of the wide array of integrated circuits available.

Si is an intrinsic semiconductor with a bandgap of 1.1 eV [26] which can easily be doped to form n-type or p-type semiconductors. Similar to diamond, there are 6 conduction band minima along the Δ direction at roughly 84% the distance to the X symmetry point. Previous electron transport studies in Si have reported a saturation velocity of around 1.0×10^7 cm/s and a low field mobility of around 1400 cm^2/Vs [171, 172]. However, Si has breakdown field of 0.3 MV/cm, which is much less than that of diamond and cBN. As such, the MC simulation of Si will be done at low fields to ensure the results converge with those found using analytic methods.

6.2 Density of States Calculation

6.2.1 Band Structure and Effective Mass

Section 5.1.1 details how the pseudopotential and wavefunction basis were chosen for bulk silicon with AIMPRO. Figure 6.1 then shows the band structure calculated for Si with this chosen pseudopotential. As can be seen, the conduction band minimum lies roughly 84% along the Δ direction with the secondary and tertiary minima at the L and Γ points. The figure also shows that AIMPRO gives the band gap to be 0.64eV which is just over half of the experimentally measured band gap, however, this is due to the well known band gap problem

in DFT. A better prediction of the band gap may be calculated using more complex exchange-correlation functionals, however the band gap energy is not needed in the simulations presented here. Using equation 1.11, the effective mass was calculated directly from the curvature of the

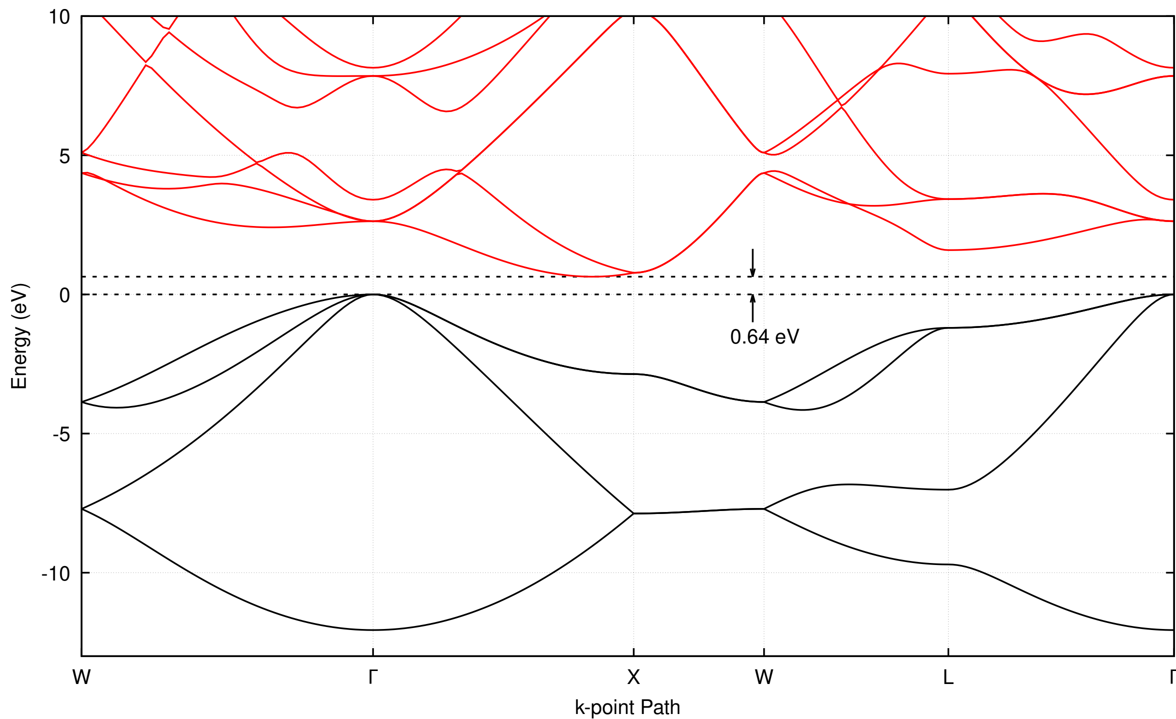

Figure 6.1: The band structure of Si calculated via DFT with a prediction of 0.64eV for the bandgap. Black lines indicate the valence bands and red lines indicate the conduction band.

band structure at the conduction band minimum. The longitudinal effective mass was found as the curvature along the major axis of the valley and the transverse effective mass was found as the curvature along the two minor axes. The longitudinal effective mass was found to be $m_l^* = 0.96m_e$ and the two transverse effective masses were found to be $m_t^* = 0.20m_e$. These are in good agreement with the values of $m_l^* = 0.9163m_e$ and $m_t^* = 0.1905m_e$ seen in the literature [173]. Following equation 1.21, the DOS effective mass for Si used in the calculation of the analytic DOS is found as the geometric mean of the longitudinal and transverse effective masses, giving $m_{DOS}^* = 0.33m_e$.

Despite the band gap being underestimated, the band structure can still be used in the calculation of the DOS as neither holes nor impact ionisation scattering are considered in this work and so the valence bands are not used. However, the band gap problem extends beyond just the band gap and means that the energy difference between the conduction band minimum and the secondary and tertiary valleys may also be underestimated. This is not an issue in silicon where only the lowest valley is used but needs to be treated with care when

considering diamond and cBN.

6.2.2 Comparison to AIMPRO DOS

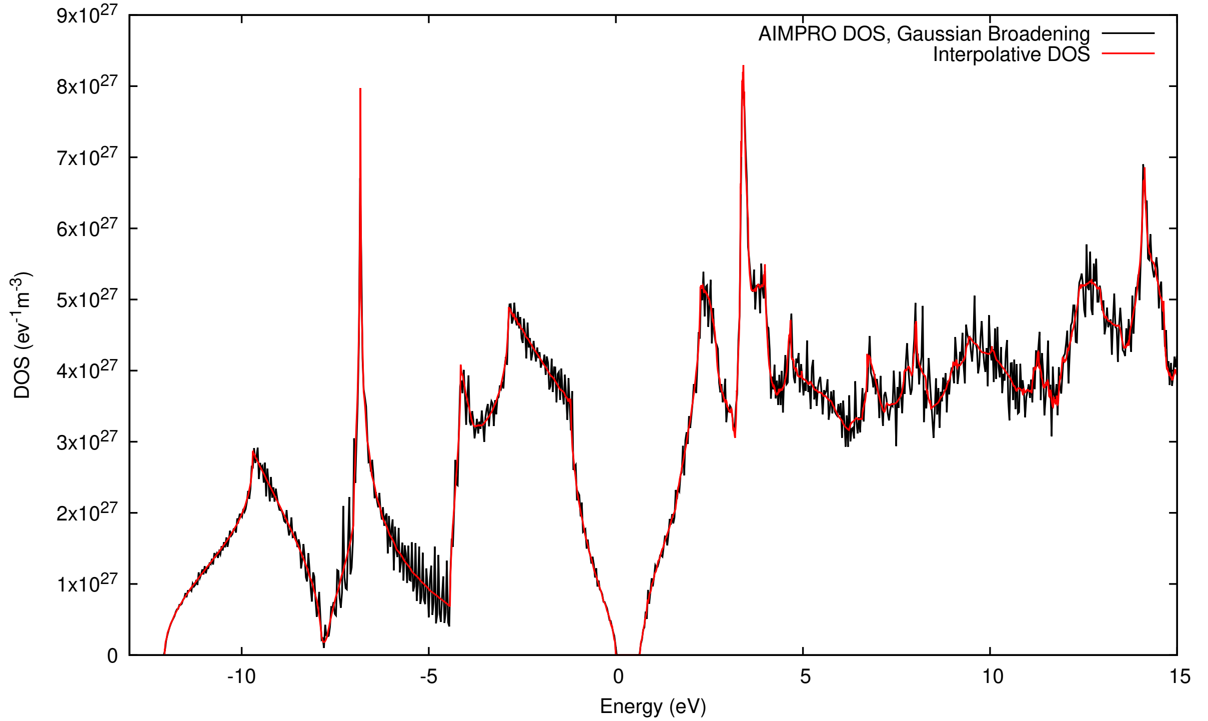

Figure 6.2: Comparison of the DOS calculated numerically via Gaussian broadening in AIMPRO (black) and tetrahedral interpolation (red).

Figure 6.2 shows a comparison of the DOS calculated using AIMPRO in black and using the interpolative DOS detailed in section 4.1. The interpolative DOS was calculated on a grid of 24611 vertices on the lowest 20 bands with an average of 51857 simplices per band. The tetrahedral edge length tolerance was set to be 5% of the length of the reciprocal lattice constant and the energy tolerance was set to be 0.05eV. The difference in energy when sampling for the DOS was 0.002eV.

AIMPRO uses Gaussian broadening to calculate the DOS. This method samples the reciprocal space and replaces the delta function in equation 4.7 with a Gaussian function with width σ to smear the contribution of each k-point [174],

$$\delta(E - E_n(\underline{k})) \rightarrow \frac{1}{\sigma\sqrt{2\pi}} \cdot exp\left(-\frac{1}{2}\left(\frac{E - E_n(\underline{k})}{\sigma}\right)^2\right) \tag{6.1}$$

The accuracy of the DOS then depends on the sampling rate and the Gaussian width. Here, the width of the Gaussian function was set to be $\sigma = 0.01$ eV. In figure 6.2 there is good

agreement between the two DOS which means that the interpolative DOS has been correctly applied to Si. The oscillations in the DOS calculated by AIMPRO are due to the choice of the number of sampling points and width of the Gaussian functions used to smear the delta functions. As such, this DOS could be improved by careful choice of these parameters, however, this would take more time and the calculated DOS is already indicative and suitable for comparison to the DOS calculated via tetrahedral interpolation.

6.2.3 Non-Parabolicity Constant Calculation

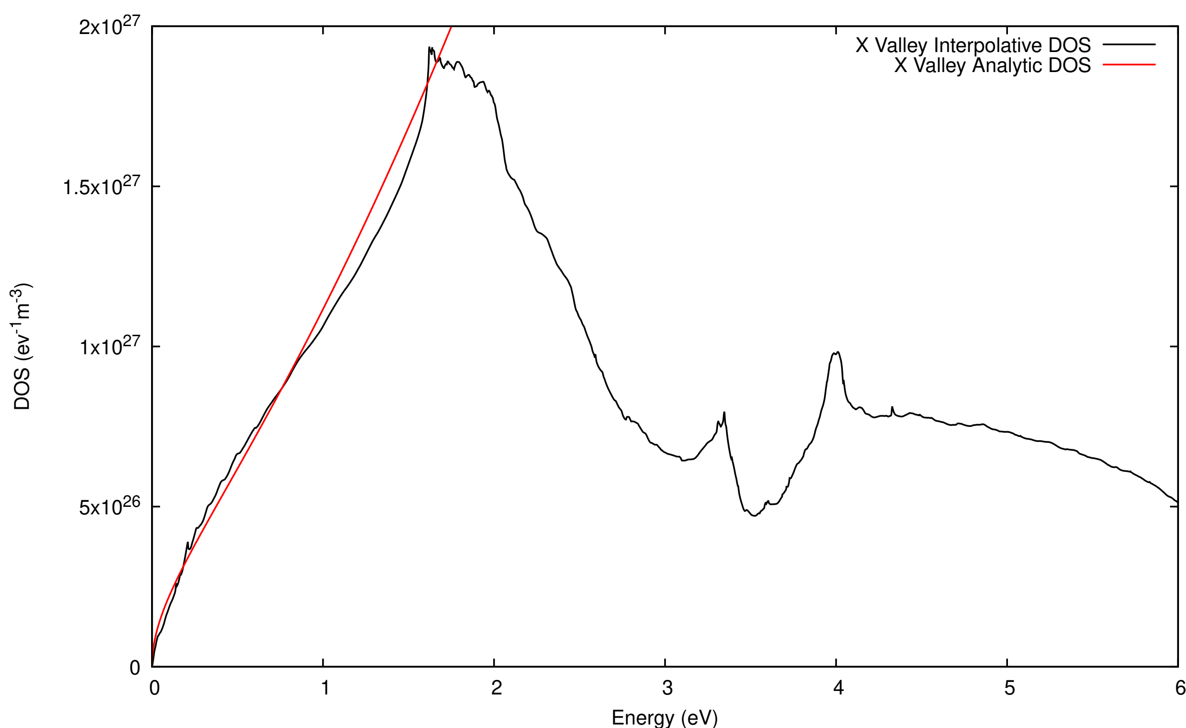

Figure 6.3: The numerically calculated DOS for the first conduction band valley of Si (black) and the analytic DOS (red) with effective mass calculated from the curvature of the band structure and α calculated by fitting to the numerical DOS.

Following the method of section 4.1.5, tetrahedra can be assigned to a valley and the DOS calculated using just that subset of tetrahedra. The DOS of the first conduction band valley is shown by the black line in figure 6.3. As the band structure should be parabolic near the valley minima, equations 1.13 and 1.18 should then be a good approximation of the numerical DOS at lower energies. The red line in figure 6.3 shows the analytic DOS found by using least squares regression to fit equations 1.13 and 1.18 to the numerical DOS; with the non-parabolicity constant, α, used as a fitting parameter. The analytic and numerical DOS show excellent agreement below 1eV and good agreement up to around 1.75eV before the numerical

DOS starts to decrease. The non-parabolicity constant found by fitting the analytic to the numerical DOS was 0.26eV^{-1}, which is smaller than the value of 0.4eV^{-1}, given by equation 1.14 with $E_g = 1.12eV$ [15, 16]; and almost half the value 0.5eV^{-1} seen in the literature [15, 16]. Despite this disagreement, the MC simulation of Si will proceed with $\alpha = 0.26$eV^{-1} as this is the value that is found to best reproduce the DOS at low energies using equations 1.13 and 1.18.

6.3 Scattering Parameters

6.3.1 Phonon Dispersion

Section 5.2.1 details how the pseudopotential and wavefunction basis were chosen for bulk silicon with Quantum Espresso.

6.3.2 Acoustic Deformation Potential

The longitudinal and transverse acoustic deformation potentials were found using equation 4.16 with the polar angle between the phonon wavevector and the longitudinal axis of the k_z conduction band minimum valley found at twenty evenly spaced angles from 0 to π. For each polar angle, the azimuthal angle was varied and the average, calculated using equation 4.22, of the deformation potentials found from eight evenly spaced points from 0 to 2π. Figure 6.4 shows the angular dependence of the acoustic deformation potentials, with the red plots showing the angular dependence of the longitudinal acoustic deformation potential and the black plots showing the sum of the deformation potential of the two transverse acoustic modes, combined using equation 4.21. The points show the average deformation potential for a given polar angle and the bars show the range of values calculated for the deformation potential with a given polar angle and varied azimuthal angle. The lines in figure 6.4 show the fit of equations 4.18a and 4.18b to the calculated deformation potentials.

The solid lines show the case where Ξ_u and Ξ_d were found separately by first fitting equation 4.18b to the average polar angle transverse acoustic deformation potential to find the value of Ξ_u and then fixing this while fitting equation 4.18a to the average polar angle longitudinal acoustic deformation potential to find the value of Ξ_d. The uniaxial and dilata-

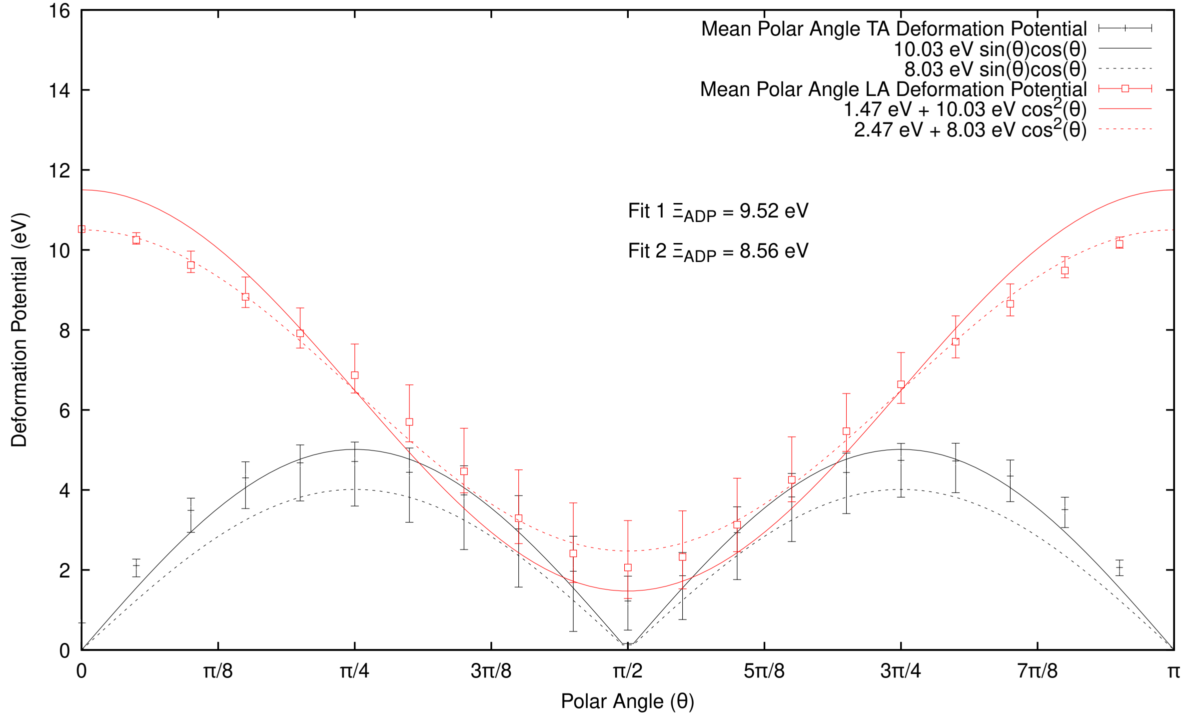

Figure 6.4: Polar dependence of the longitudinal (red) and transverse (black) acoustic deformation potential in the first conduction band valley of Si calculated via Quantum Espresso (points) and equations 4.18a and 4.18b. The bars indicate the range of values found by varying the azimuthal angle for a given polar angle.

tion deformation potentials were found to be $\Xi_u = 10.03$eV and $\Xi_d = 1.47$eV. The dashed lines show the case where Ξ_u and Ξ_d were found together by fitting equation 4.18a to the average polar angle longitudinal acoustic deformation potential. The uniaxial and dilatation deformation potentials were found to be $\Xi_u = 8.03$eV and $\Xi_d = 2.47$eV. The black dashed line is then the plot of equation 4.18b for $\Xi_u = 8.03$eV.

Values for the longitudinal and transverse acoustic deformation potential were found using equations 4.19a and 4.19b, which are the average of the integrals of the square of equations 4.18a and 4.18b. The contributions of the longitudinal acoustic and transverse acoustic modes can then be combined into a single value using equation 4.20 with $v_l = 9.04 \times 10^3$ m/s and $v_t = 5.34 \times 10^3$ m/s [16, 144, 172]. The acoustic deformation potential found by fitting equation 4.18b to the mean polar angle transverse acoustic deformation potential to find Ξ_u and then fitting 4.18a to the mean polar angle longitudinal acoustic deformation potential to find Ξ_d, referred to as fit 1, was $\Xi_{ADP} = 9.52$eV. The acoustic deformation potential found by fitting equation 4.18a to the mean polar angle longitudinal acoustic deformation potential to find both Ξ_d and Ξ_u, referred to as fit 2, was $\Xi_{ADP} = 8.56$eV. Table 6.1 shows a comparison of the deformation potentials and effective masses calculated here for the first conduction

	$\Xi_d(eV)$	$\Xi_u(eV)$	Ξ_{ADP} (eV)	m_l/m_0	m_t/m_0	m_{DOS}/m_0
Canali *et al.* [175]	-	-	9.0	0.9163	0.1905	0.322
Tomizawa [15]	-	-	9.0	0.92	0.19	0.32
Fischetti and Laux [20]	1.1	10.5	9.7	0.9163	0.1905	0.322
Li *et al.* [144]	1.01	8.84	8.2	-	-	-
Yang *et al.* [145]	0.8	9.0	8.2	-	-	-
Fit 1	1.47	10.03	9.52	0.958	0.204	0.341
Fit 2	2.47	8.03	8.56	0.958	0.204	0.341

Table 6.1: Comparison of the acoustic deformation potential for Si quoted in literature and values presented in this work.

band of Si as quoted in the literature and calculated here numerically. The effective masses presented here in the final two rows were calculated using the curvature of the conduction band minimum produced by Quantum Espresso in a method similar to the one presented in section 6.2 with AIMPRO. There is good agreement between these two numerically calculated effective masses and what is seen in the literature however the Quantum Espresso effective masses are slightly larger than what was calculated using AIMPRO and what is seen in the literature. This overestimate would lead to a slightly higher DOS and therefore an increase in the number of acoustic phonon scattering events occurring. Despite this overestimate in the effective mass, the results of both fitting methods are in excellent agreement with what is seen in the literature, however, the deformation potential calculated using fit 2 is the value used in the MC simulation as it is in better agreement with what is seen in the literature. It can also be seen in figure 6.4 that the spread of values about the average for each polar angle is smaller for the longitudinal modes resulting in a more accurate fit, further supporting the choice of acoustic deformation potential.

6.3.3 Optical Deformation Potential

As stated in section 2.3.4, the NPOP scattering mechanism causes the electron to move to either a parallel or perpendicular valley, termed g-type and f-type scattering respectively. The optical deformation potential for f- and g-type scattering can be calculated using equation 4.17. However, the electron-phonon coupling matrix may be calculated for any combination of electron and phonon wavevectors and so, the correct combination must be used to get the correct value for the optical deformation potential. Figures 6.5 and 6.6 show how the optical

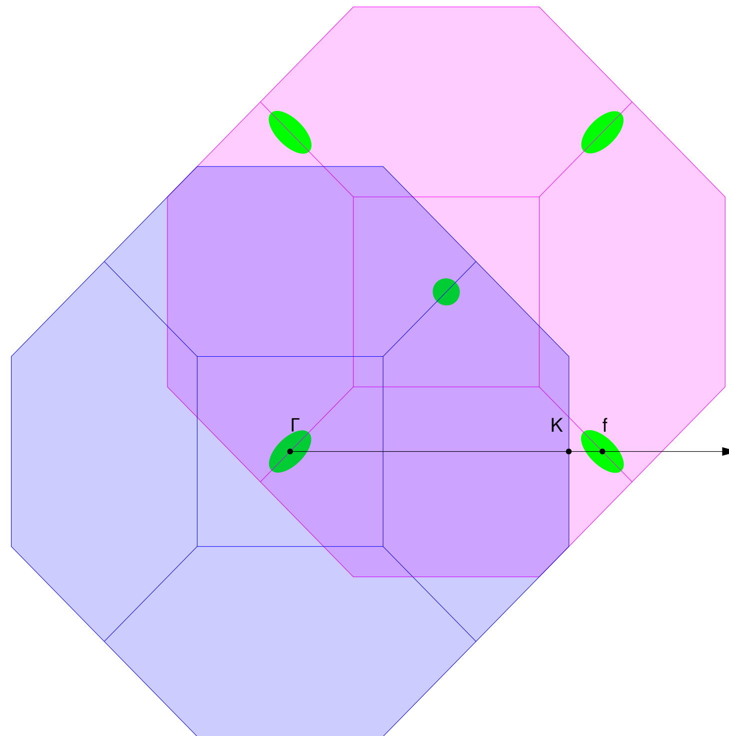

Figure 6.5: 2D projection of the electron (pink) and phonon (blue) BZ of Si with conduction band minima indicated by the green ellipsoids. The arrow indicates the path of an electron scattering through an f-type scattering.

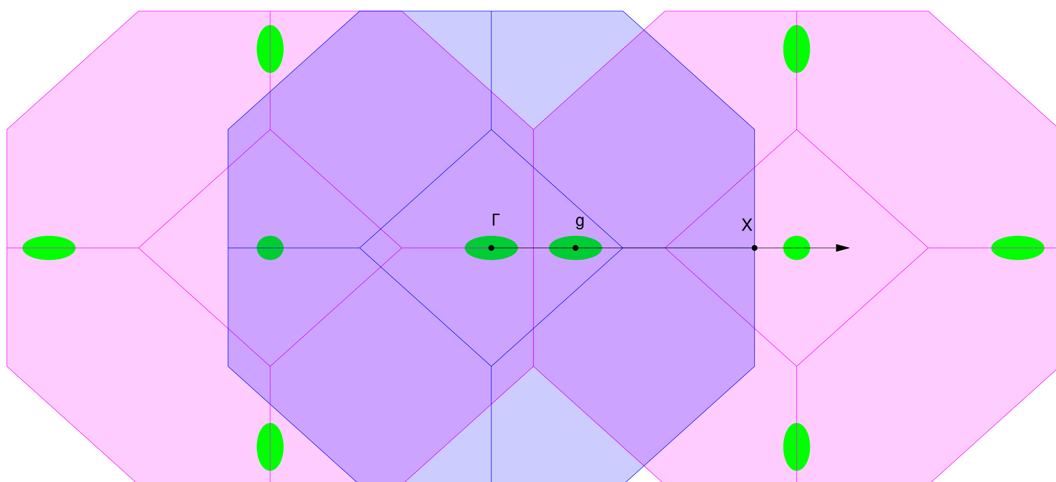

Figure 6.6: 2D projection of the electron (pink) and phonon (blue) BZ of Si with conduction band minima indicated by the green ellipsoids. The arrow indicates the path of an electron scattering through a g-type Umklapp process.

f- and g-type scattering deformation potentials were calculated for the first conduction band of Si. In these figures, the pink region shows the 2D projection of the BZ for the electrons, with the first conduction band valley indicated by the green ellipsoids centred at 84% of the distance along the Δ directions. To find the phonon wavevector that would transfer an electron from the initial conduction band minimum to an equivalent valley, the first BZ for the phonons is overlaid in blue with the Γ point positioned at the initial conduction band minimum. The arrow then indicates a path through these combined BZ along which the electron phonon coupling matrix can be calculated, with the labels K and X indicating the high symmetry point on the surface of the phonon BZ that the path intersects. The deformation potential is then calculated at the point where the path intersects the new conduction band minimum labelled f and g for the f- and g-type scattering respectively. For f-type scattering, this moves the electron into an equivalent perpendicular valley within the first BZ, however, g-type scattering in silicon occurs via an Umklapp process and so the electron scatters to a parallel valley in the second BZ.

By calculating the electron-phonon coupling matrix for an electron with a wavevector at the conduction band minimum interacting with a phonon with a wavevector such that the electron is transferred to a perpendicular valley show that only the LA and TO phonon modes had significant coupling, indicating that these are the only two modes that mediate f-type scattering. The deformation potential for the LA phonon mode was found to be 1.99 eV/Å with an corresponding change in energy of 0.0469 eV and the deformation potential for the TO phonon mode was found to be 3.65 eV/Å with a corresponding change in energy of 0.0566 eV. Similarly, calculating the electron-phonon coupling matrix for an electron with a wavevector at the conduction band minimum interacting with a phonon with a wavevector such that the electron is transferred to a parallel valley show that only the LO phonon modes has significant coupling, indicating that it is the mode that mediates g-type scattering. The deformation potential for the LO phonon mode was found to be 3.79 eV/Å with a corresponding change in energy of 0.0613 eV. These data are summarised in table 6.2 and compared to deformation potentials found in references [15, 175, 144, 145]. The deformation potentials found in references [144] and [145] were calculated using the same methods as detailed in section 4.2. As can be seen, the extracted deformation potentials fall within the range of

	Present Work	Tomizawa [15]	Canali *et al.* [175]	Li *et al.*[144]	Yang *et al.* [145]
$f1$ (eV/Å) LA	1.99	3.4	3.0	1.83	1.36
E_{f1} (eV)	0.0469	0.063	0.043	0.0467	0.0467
$f2$ (eV/Å) TO	3.65	4.0	4.0	3.55	3.52
E_{f2} (eV)	0.0566	0.063	0.056	0.0564	0.0580
$g1$ (eV/Å) LO	3.79	3.0	3.0	3.86	3.32
E_{g1} (eV)	0.0613	0.063	0.060	0.061	0.0623

Table 6.2: Comparison of the optical deformation potentials and corresponding phonon energies for Si quoted in literature and values presented in this work.

values presented in the literature, with better agreement found with data from Li *et al.* and Yang *et al.*, which is to be expected as these use the same method. However, by combining the deformation potentials using equation 4.23 for all sets, the effective deformation potential is between 5.5eV/Å and 6.0eV/Å , suggesting that they will all have a similar effect on the total scattering rate. This indicates that these are viable values for the deformation potential of Si.

The calculated phonon energies agree with what is seen in references [175, 144, 145] which also indicates that these are viable deformation potentials as it means that the correct phonon modes for the electron-phonon interaction have been selected and that the correct scattering mechanisms will become available to the electrons with a given energy. From Tomizawa, the same phonon energy is used for all three scattering mechanisms which means that optical phonon emission will not become available until the electrons reach 0.063eV but the probability of absorbing a phonon that gives the electron 0.063eV of energy is quite large. This could lead to higher velocities at lower fields as the electrons can gain more energy through acceleration from the external field before the NPOP scattering begins.

Intervalley Scattering

Although intervalley scattering to higher energy valleys is not considered in the simulation of Si, here the method of calculating the deformation potential is presented with comparison to the literature as a benchmark. The method used to find the deformation potentials and associated phonon energies is exactly the same as what was presented in previous sections on f-type and g-type scattering, however the phonon path now goes from the conduction band minimum to the L valley symmetry point where the secondary valley is located. At the point

where the phonon path crosses the minimum of the secondary valley, there are four phonon modes with significant terms in the coupling matrix. However, in the MC code there is only one input for the intervalley scattering mechanism and so an effective deformation potential and associated phonon energy are calculated using equations 4.23 and 4.24. The effective intervalley deformation potential was found to be $D^*_{iv} = 2.90\text{eV/Å}$ with an associated effective energy of $\hbar\omega^*_{iv} = 0.043\text{eV}$. These are only slightly larger than the values seen in reference [147] of $D^*_{iv} = 2.34\text{eV/Å}$ and $\hbar\omega^*_{iv} = 0.03716\text{eV}$, but they also state how their method for calculating the deformation potentials underestimates them to counteract the overestimate in the calculation of the DOS. Therefore, these effective deformation potentials should be indicative of the probability for intervalley transitions.

6.4 MC Simulation

In the previous sections, the results for the numerical DOS and deformation potentials were presented for bulk silicon, the following sections present how these are used in the simulation of electron transport in bulk silicon.

6.4.1 Parameters

Table 6.3 details the parameters used in the MC simulation for Si. The mass density, static dielectric constant and sound velocities were taken from literature. The calculation of the effective masses, non-parabolicity constant, deformation potentials and associated phonon energies are detailed in the previous sections of this chapter.

6.4.2 Scattering Rates

Figure 6.7 shows the various scattering rates that were calculated as part of the MC simulation of Si using the parameters presented in table 6.3. In each case, the solid lines show the scattering rate where the analytic DOS were employed, and the dashed lines show the scattering rate where the numerical DOS were employed. The acoustic phonon scattering rate is given by the magenta line; the sum of the g-type and f-type, emission and absorption NPOP scattering rates are given by the blue lines; and the charged impurity scattering is given by the orange

Parameter	Symbol	Value
Mass Density (kg/m^3)	ρ	2329
Static Dielectric Constant (ϵ_0)	ϵ_s	11.7
Longitudinal Sound Velocity (m/s)	v_l	9.04×10^3
Transverse Sound Velocity (m/s)	v_t	5.34×10^3
Longitudinal Effective Mass (m_e)	m_l	0.916
Transverse Effective Mass (m_e)	m_t	0.191
Non-Parabolicity Constant (eV^{-1})	α	0.26
Acoustic Deformation Potential (eV)	Ξ_{ADP}	8.58
Optical Deformation Potentials (eV/Å)	D_O	
$f1$ Process LA		1.99
$f2$ Process TO		3.65
$g1$ Process LO		3.79
Optical Phonon Energies (eV)	$\hbar\omega_0$	
$f1$ Process LA		0.0469
$f2$ Process TO		0.0566
$g1$ Process LO		0.0613
Charged Impurity Concentration (m^{-3})	n_0	10^{19}

Table 6.3: Parameters for MC simulation of Si.

lines. The black lines then show the total scattering rate found as the sum of the acoustic, NPOP and charged impurity scattering rates. As Si is not a polar material, there is no POP or piezoelectric scattering and so, all of the scattering methods employed depend on the DOS. As such, there is good agreement between the scattering rates calculated using the numerical and analytic DOS.

However, at energies lower than roughly 0.2eV, the charged impurity scattering rate calculated using the numerical DOS deviates from that calculated using the analytic DOS. This is because the analytic DOS grows at a faster rate than the numerical DOS and this slight

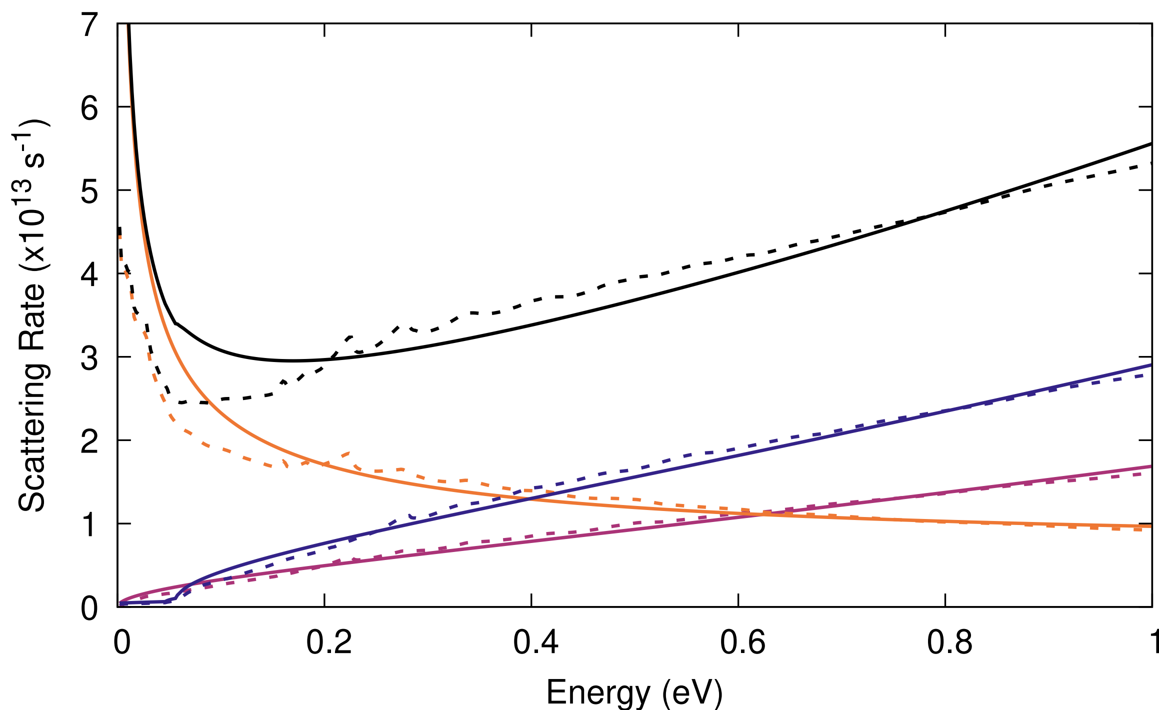

Figure 6.7: Comparison of the scattering rates calculated using analytic (solid) and numerical (dashed) DOS for Si at 300K. With Charged Impurity scattering (orange), NPOP scattering (blue), ADP scattering (magenta), and total scattering rate (black). Energy scale relative to the conduction band minimum.

deviation is exacerbated by the divergence of the scattering rate as it approaches 0eV. This is not expected to have a huge impact on the final results, however it may mean that at very low field strengths the average velocity in simulations using the numerical DOS will be higher than the average velocity at corresponding fields in simulations using the analytic DOS.

Another cause of inflated average velocities in all simulations of Si is the fact that there are scattering rates that dominate at the high and low energies but none in between. This means that at these energies, the self scattering rate will dominate resulting in a large proportion of "scattering" events that do not change the energy or momentum of the electron. For a poorly chosen fixed value of the total scattering rate, the velocity of these "lucky" electrons can easily become inflated to be much larger than expected.

6.4.3 Simulation Results

Figure 6.8 shows the steady-state velocity-field characteristics that have been produced by MC simulation for Si along with experimental data with the electric field parallel with the x-axis. The simulation results were found using parameters from Tomizawa [15] (dark blue) and Canali

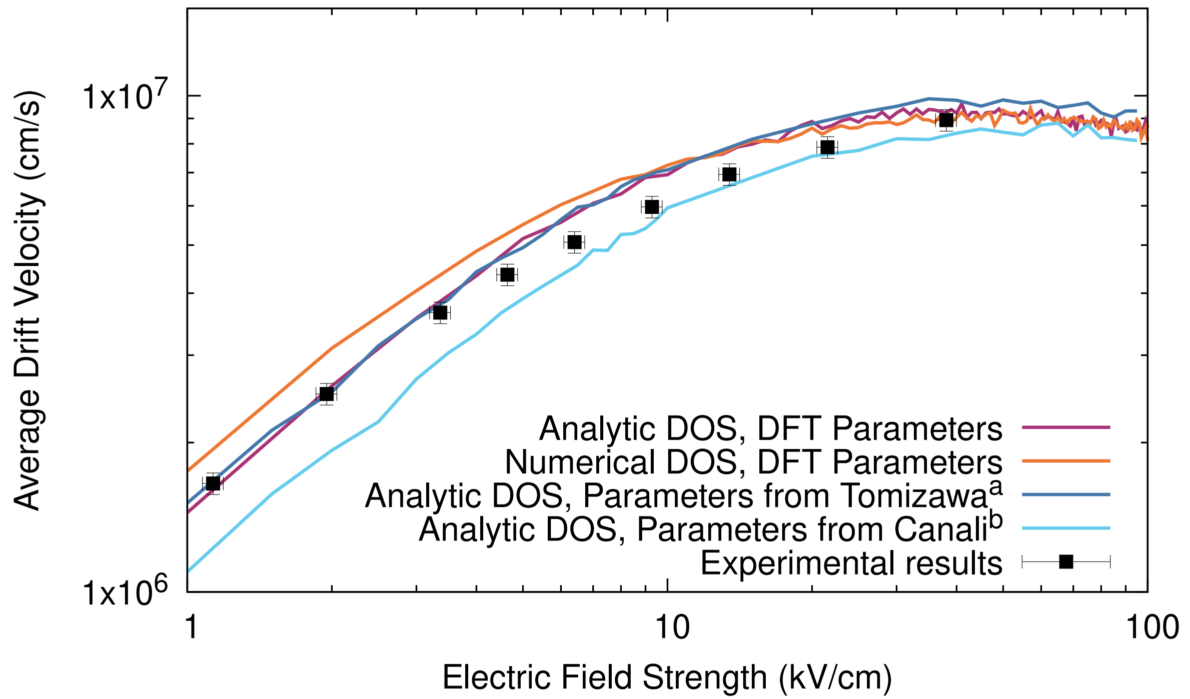

Figure 6.8: Velocity-field data for bulk Si. Lines are MC simulation with parameters from Tomizawa [15] (a) and Canali *et al.* [175] (b), with analytic DOS; and parameters calculated via DFT with analytic (magenta) and numerical (orange) DOS. Points are experimentally determined data from Canali *et al.* [175].

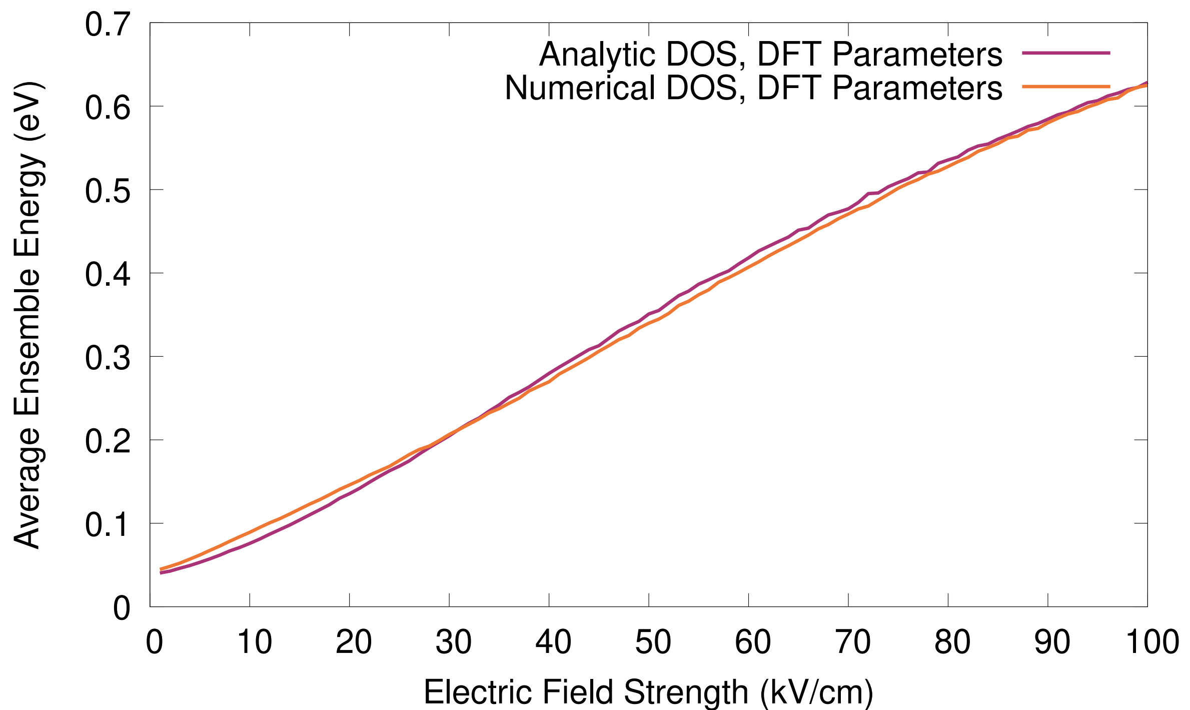

Figure 6.9: Energy-field characteristics for bulk Si found using MC simulation with parameters calculated via DFT with analytic (magenta) and numerical (orange) DOS. Average energy is relative to the conduction band minimum.

et al. [175] (light blue), with analytic DOS; and parameters calculated via DFT with analytic (magenta) and numerical (orange) DOS. As can be seen, there is close agreement between all

four simulations and the experimental results, with all four models converging on a saturation velocity just below the experimentally measured velocity around 1×10^7cm/s.

Comparing just the two sets of data calculated using the parameters from table 6.3, it can be seen that the simulation that used the numerical DOS has a higher average drift velocity below field strengths of 10kV/cm, with a percentage difference of roughly 19.2%. This indicates that the simulation using numerical DOS experienced fewer scattering events at lower fields. However, at higher fields, there is excellent agreement between the two methods, and they converge on the same velocity at 100kV/cm.

Looking at the energy-field characteristic in figure 6.9, at low field strengths below 30kV/cm, the average ensemble energy is below 0.2eV where the discrepancy in the numerical and analytic DOS is exacerbated by the charged impurity scattering rate. This then explains the features of the velocity-field results as in lower field strengths, there are fewer scattering events when using the numerical DOS and as such the average velocity is higher.

6.5 Summary

In this chapter, the methods described in chapter 4 have been tested using bulk silicon as a benchmark material due to the abundance of data to which tests can be compared. Section 6.2 presented the results for the numerical calculation of the DOS and found they matched what was calculated in AIMPRO. This was then followed by the calculation of the effective mass from the curvature of the band structure which was in good agreement with experimental results. The numerical DOS was then used to calculate the non-parabolicity constant for use in the MC simulation.

In section 6.3, the values of the acoustic and optical phonon deformation potentials as calculated using Quantum Espresso were shown to agree well with what is seen in the literature.

These two parts were then brought together in 6.4, where they were used in MC simulation and found to have excellent agreement with the results of simulations that employed parameters from literature and experimentally measured results. As such, these methods can now be applied to diamond and cBN to better understand these materials that have fewer experimental results with confidence in the results that are produced.

Finally, these simulation results rely on many input parameters and so the sensitivity to

these parameters must be considered. Changing the functionals used in the DFT calculations would result in a change in the optimised lattice constants and band structure. These would have a knock on effect on the other parameters extracted as a change to the curvature of the bands would affect the effective masses and a change in the lattice constant would impact the deformation potentials. These in turn would result in changes to the scattering rates. Poncé *et al.* [176] found that the intrinsic mobilities calculated for electrons at 300K in Si using LDA and PBE functionals differ by 16%. They also showed that this difference was primarily a result of the change in the optimised lattice constant, as the use of the same lattice constant resulted in intrinsic mobilities calculated using LDA and PBE functionals that differ by 0.4%. In terms of the MC simulation, the scattering rates are proportional to the square root of the DOS effective mass but are proportional to the square of the deformation potential. Therefore, the deformation potentials are going to have more of an impact on the MC simulation results. At lower fields where acoustic scattering dominates, a change in the acoustic deformation potential will have more of an impact. At higher fields, however, changes to the optical deformation potentials will have more of an impact as this is the dominant scattering mechanism.

Chapter 7

Diamond Results

As seen in the previous chapter, the methods detailed in chapter 2 were successfully combined with a MC simulator when applied to bulk Si. As carbon and silicon are both group IV elements, bulk Si and diamond have similar crystal and band structures, therefore, the methods can be applied to diamond with a high degree of confidence in their efficacy. This chapter then shows the application of these same methods to diamond. Section 7.1 shows how the DOS was calculated via tetrahedral discretisation as detailed in section 4.1 and compared to the DOS calculated directly via AIMPRO. The effective mass and non-parabolicity constant were then calculated and compared to previous work. Following this, section 7.2 presents the acoustic and optical phonon deformation potentials as calculated via Quantum Espresso. There have been several studies into the transport of electrons in diamond [104, 177–184] to which results were compared, however, these give a huge range of values for the deformation potentials depending on what aspect of electron transport the authors were interested in. Finally, the results from the MC simulation using the numerically calculated scattering parameters and both analytic and numerical DOS are presented in section 7.3. These are compared to simulations using the range of parameters seen in the literature and available experimental results at lower field strengths before seeing how the numerical and analytic bands differ in the high field regime.

7.1 Density of States Calculation

7.1.1 Band Structure and Effective Mass

Section 5.1.1 details how the pseudopotential and wavefunction basis were chosen for diamond with AIMPRO. Figure 7.1 then shows the band structure calculated for diamond with this chosen pseudopotential. As can be seen, the conduction band minimum lies roughly 72% along the Δ direction with the secondary and tertiary minima at the Γ point. The figure also shows that AIMPRO gives the band gap to be 4.17eV which is 23.8% smaller than the experimentally measured value of 5.47eV [68, 69]. Once again, this is expected due to the band gap problem and better predictions may be possible using more advanced exchange-correlation functionals. Using equation 1.11, the effective mass can be calculated directly

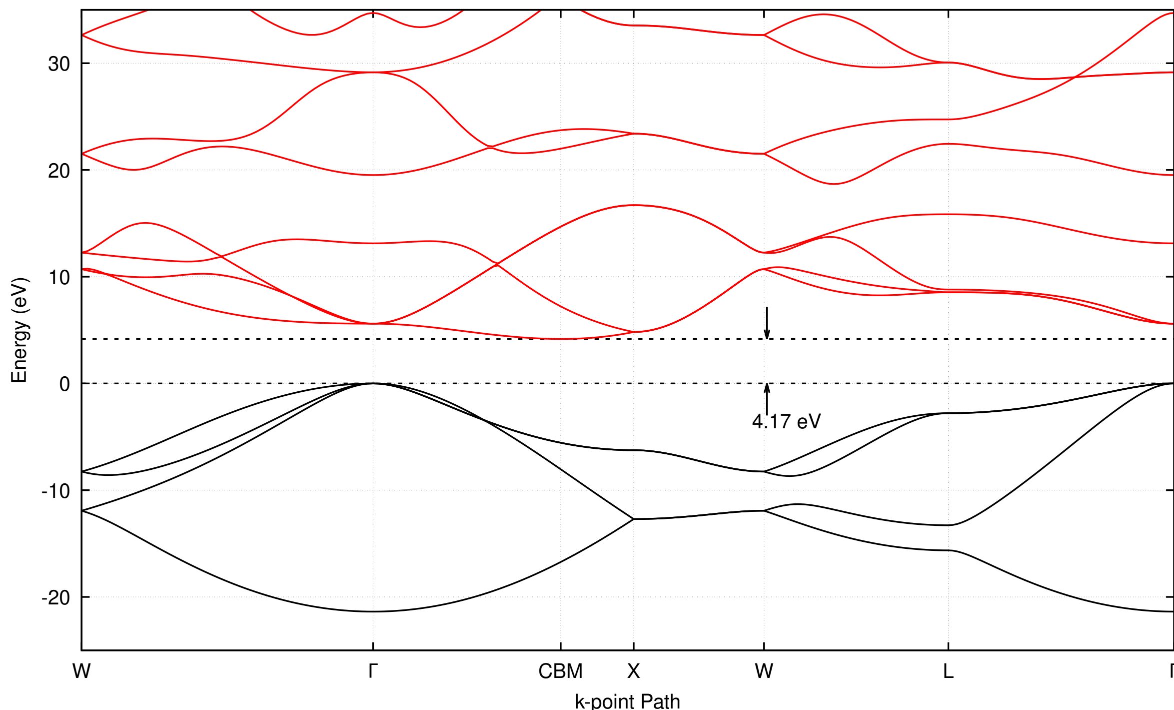

Figure 7.1: The band structure of diamond calculated via DFT with a prediction of 4.17eV for the bandgap. Black lines indicate the valence bands and red lines indicate the conduction band.

from the curvature of the band structure at the conduction band minimum. The longitudinal effective mass was found to be $m_l^* = 1.64m_e$ and the transverse effective mass was found to be $m_t^* = 0.29m_e$. These are in good agreement with the range of values of $m_l^* = 1.15m_e - 1.81m_e$ and $m_t^* = 0.22m_e - 0.36m_e$ seen in the literature [104, 177–184]. The effective mass used in the calculation of the analytic DOS is then found as the geometric mean of the longitudinal and transverse effective masses which gives $m^* = 0.51m_e$.

7.1.2 Comparison to AIMPRO DOS

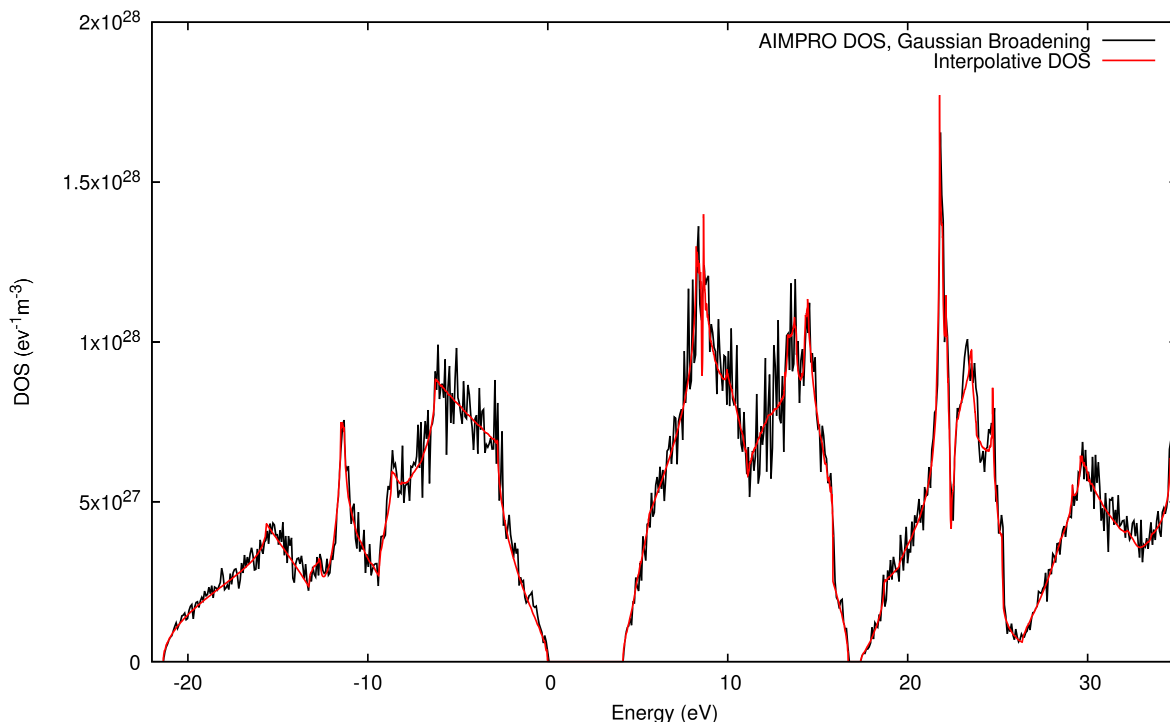

Figure 7.2: Comparison of the DOS calculated numerically via Gaussian broadening in AIMPRO (black) and tetrahedral interpolation (red).

Figure 7.2 shows a comparison of the DOS calculated using AIMPRO in black and using the interpolative DOS detailed in section 4.1. The interpolative DOS was calculated on a grid of 33427 vertices on the lowest 20 bands with an average of 53322 simplices per band. The tetrahedral edge length tolerance was set to be 5% of the length of the reciprocal lattice constant and the energy tolerance was set to be 0.05eV. The difference in energy when sampling for the DOS was 0.002eV.

In figure 7.2 there is good agreement between the two DOS which means that the interpolative DOS has been correctly applied to diamond. The oscillations in the DOS calculated by AIMPRO are due to the choice of the number of sampling points and width of the Gaussian functions used to smear the delta functions. As such, this DOS could be improved by careful choice of these parameters, however, this would take more time and the calculated DOS is already indicative and therefore suitable for comparison to the DOS calculated via tetrahedral interpolation.

7.1.3 Non-Parabolicity Constant Calculation

As with Si, the modified gradient descent method, section 4.1.5, was applied to the tetrahedral grid generated for the band structure of diamond to assign tetrahedra to a valley. Figures 7.3 and 7.4 show a comparison of the DOS calculated numerically from the tetrahedral grid (black) and analytically from equations 1.13 and 1.18 (red) for the lowest and second-lowest valleys, respectively. Using the gradient descent method, these valleys were found to have local

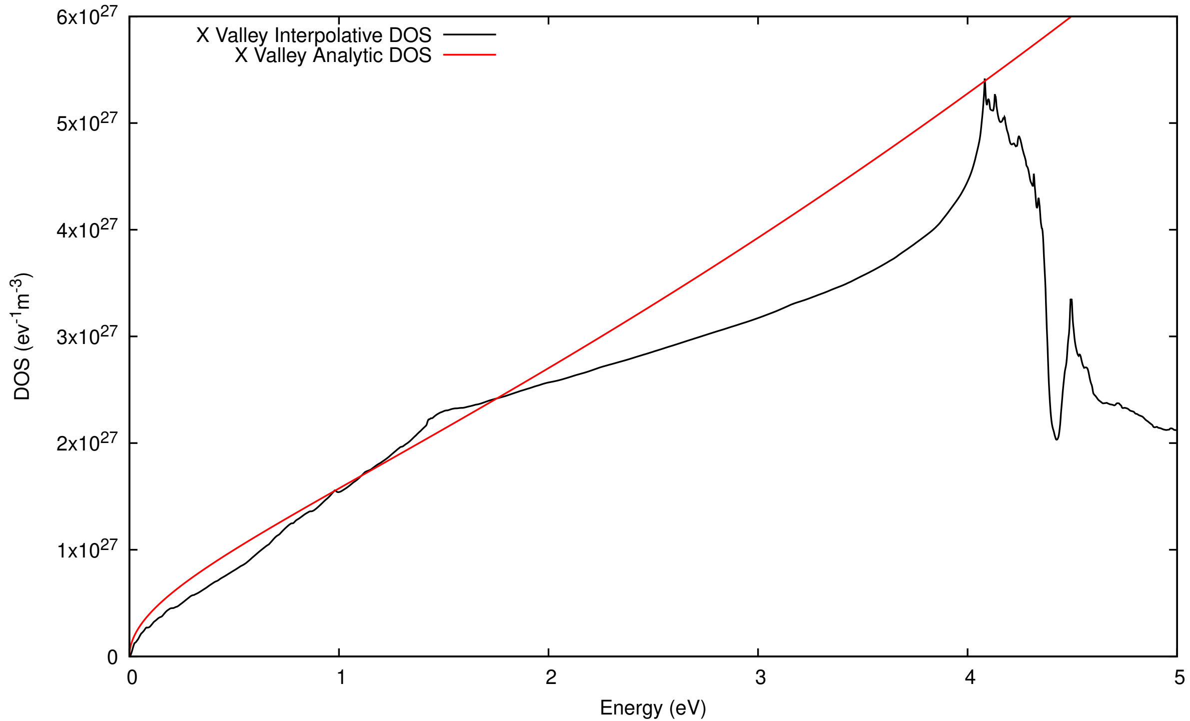

Figure 7.3: The numerically calculated DOS for the first conduction band valley of diamond (black) and the analytic DOS (red) with effective mass calculated from the curvature of the band structure and α calculated by fitting to the numerical DOS.

minima at 72% along the Δ direction and at the Γ point, respectively, with a separation of 1.43eV. This is once again a slight underestimate of the experimentally measured value of 1.8eV [69, 185, 186]. In both cases, the analytic DOS was found by calculating the curvature of the bands at the valley minimum to find the effective mass and then fitting equations 1.13 and 1.18 to find the non-parabolicity constant. As stated previously, the effective mass of DOS for the lowest valley is $m^* = 0.51m_e$, and it was found to have a non-parabolicity constant of 0.097eV^{-1}. The effective mass of DOS for the second-lowest band was then found to be $m^* = 0.25m_e$, with a non-parabolicity constant of 0.12eV^{-1}. Due to the width of the band gap, equation 1.14 would give a non-parabolicity constant much smaller than that of the fitted value at 0.044eV^{-1} for the lowest valley and 0.033eV^{-1} for the second lowest.

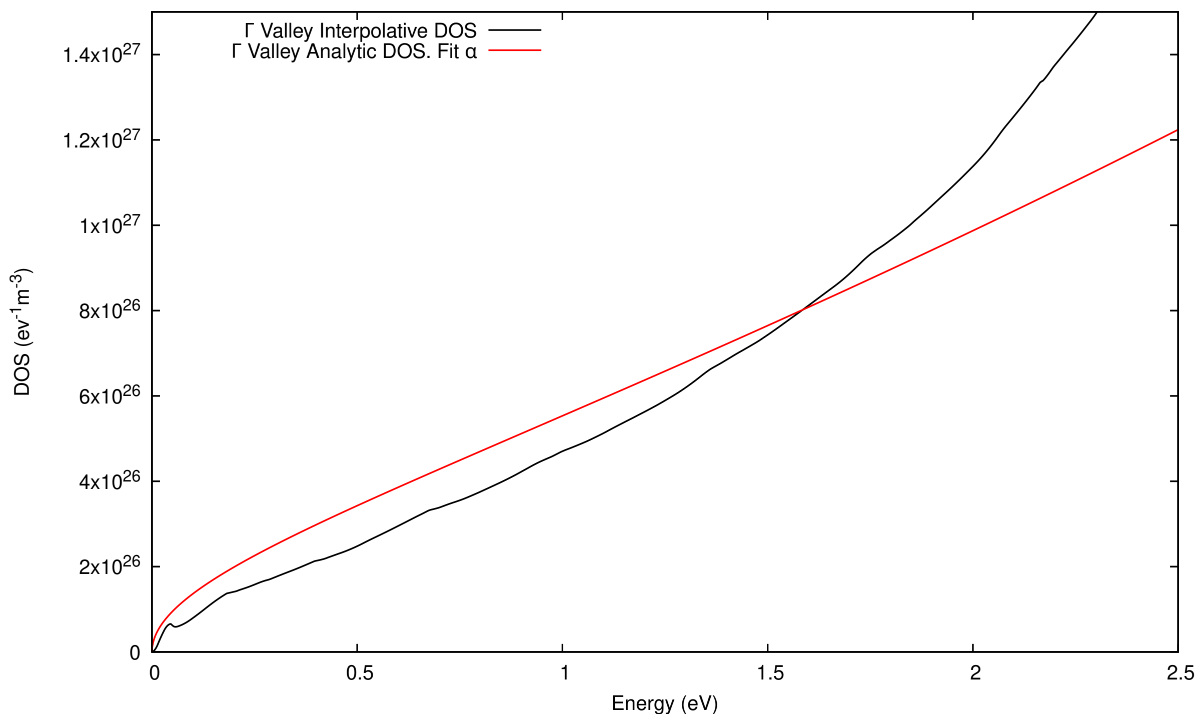

Figure 7.4: The numerically calculated DOS for the second conduction band valley of diamond (black) and the analytic DOS (red) with effective mass and α calculated by fitting to the numerical DOS.

As with Si, at lower energies, below roughly 1.5eV, there is generally good agreement between the analytic and numerical DOS and above 1.5eV the DOS diverge. However, figure 7.4 shows some anomalous oscillations in the numerical DOS near 0eV. These are thought to be due to the shape of the tetrahedra used in the discretisation process. As seen in figure 4.1, towards the Γ point there are fewer tetrahedra, and they are long and skinny which could indicate that they are of a lower quality. These features combined mean that interpolation in these areas may not be as accurate, producing oscillations in the DOS. This would lead to a slight reduction in the scattering rates at lower energies in the upper valley when using the numerical DOS.

7.2 Scattering Parameters

7.2.1 Phonon Dispersion

Section 5.2.1 details how the pseudopotential was chosen for the carbon atoms in diamond with Quantum Espresso. Figure 7.5 then shows the phonon dispersion curves calculated for diamond with this chosen pseudopotential compared to experimental results calculated via

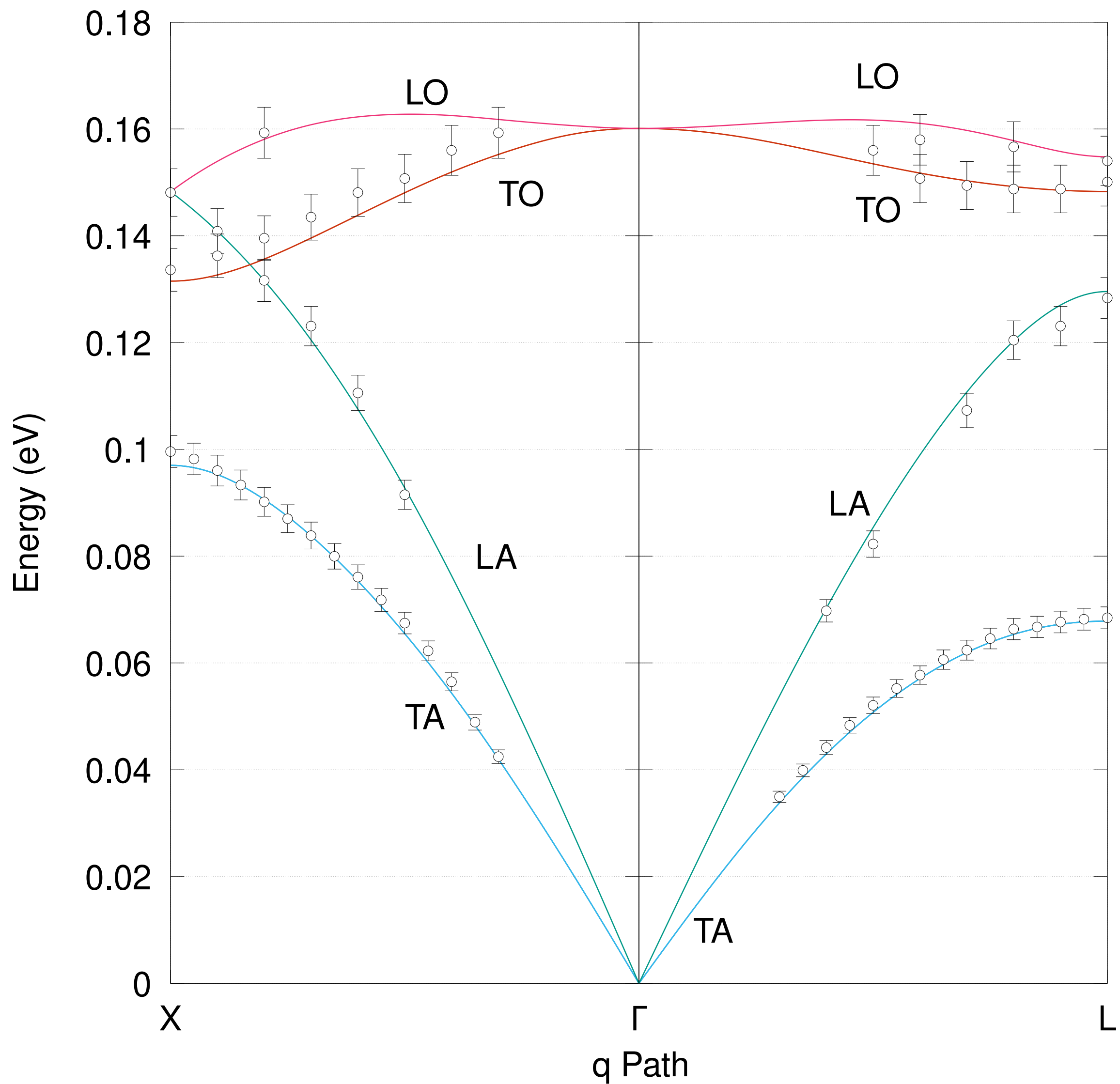

Figure 7.5: The phonon dispersion along lines of symmetry in diamond. Lines calculated via DFT and points calculated experimentally using inelastic neutron scattering, circles from reference [187] and squares from reference [188].

inelastic neutron scattering, circles from reference [187] and squares from reference [188]; along $\Gamma - X$, $X - W - X'$, $X' - K - \Gamma$ and $\Gamma - L$, where X' refers to a point outside the first BZ that would transform on to the X symmetry point. As can be seen, there is good agreement between the phonon dispersion calculated via DFT and the experimentally measured phonon energies across all four regions, Some dispersion curves do deviate from their corresponding experimental measurements, however these are generally still within the error tolerance.

7.2.2 Acoustic Deformation Potential

As with Si, the longitudinal and transverse acoustic deformation potentials were found using equation 4.16 with the polar angle between the phonon vector and the longitudinal axis of the k_z conduction band minimum valley found at twenty evenly spaced angles from 0 to π. For each polar angle, the azimuthal angle was varied and the average of the deformation potential found from eight evenly spaced points from 0 to 2π. Figure 7.6 shows the angular

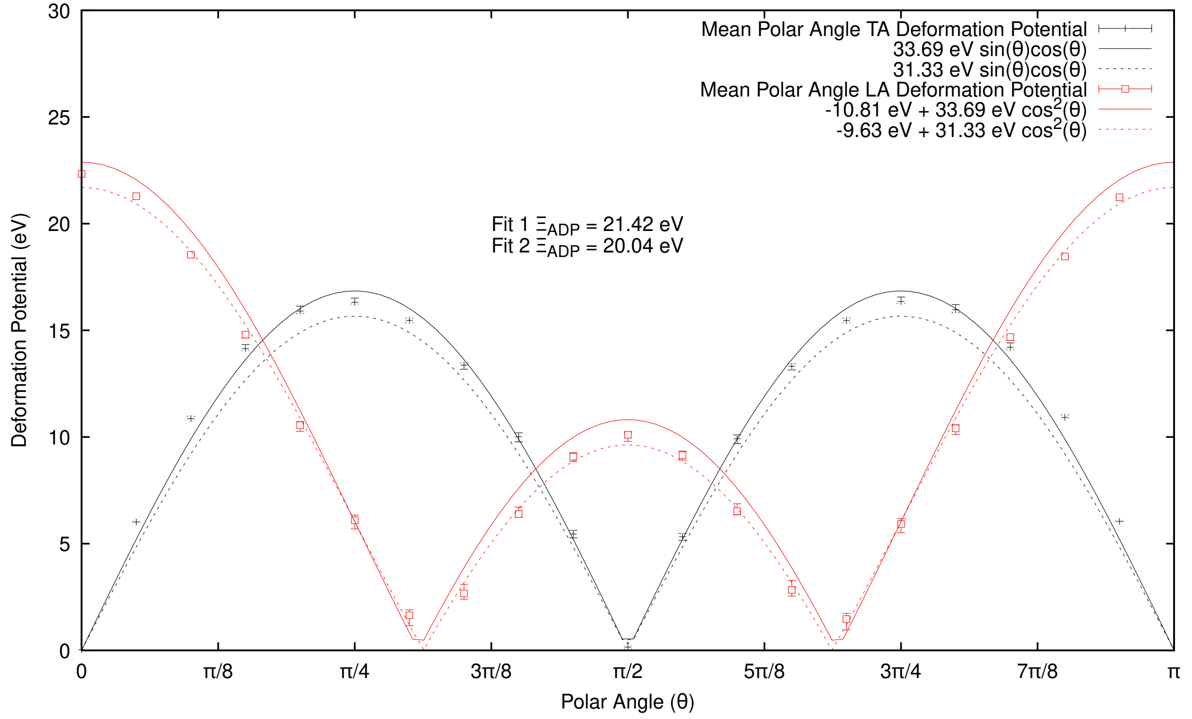

Figure 7.6: Polar dependence of the longitudinal (red) and transverse (black) acoustic deformation potential in the first conduction band valley of diamond calculated via Quantum Espresso (points) and equations 4.18a and 4.18b. The bars indicate the range of values found by varying the azimuthal angle for a given polar angle.

dependence of the acoustic deformation potentials for the longitudinal, red, and the sum of the two transverse, black, acoustic phonon modes. The points show the average deformation potential for a given polar angle and the bars show the range of values calculated while varying the azimuthal angle for a given polar angle. The lines in figure 7.6 show the fit of equations 4.18a and 4.18b to the calculated deformation potentials. Unlike Si, there is very little variation in the acoustic deformation potential calculated at different azimuthal angles, resulting in very narrow bars.

The lines in figure 7.6 show the fit of equations 4.18a and 4.18b to the calculated deformation potentials. The solid lines show the case where Ξ_u and Ξ_d were found separately by

first fitting equation 4.18b to the average polar angle transverse acoustic deformation potential to find the value of Ξ_u and then fixing this while fitting equation 4.18a to the average polar angle longitudinal acoustic deformation potential to find the value of Ξ_d. The uniaxial and dilatation deformation potentials were found to be $\Xi_u = 33.69$eV and $\Xi_d = -10.81$eV. The dashed lines show the case where Ξ_u and Ξ_d were found together by fitting equation 4.18a to the average polar angle longitudinal acoustic deformation potential. The uniaxial and dilatation deformation potentials were found to be $\Xi_u = 31.33$eV and $\Xi_d = -9.63$eV. The black dashed line is then the plot of equation 4.18b for $\Xi_u = 31.33$eV.

Values for the longitudinal and transverse acoustic deformation potential can then be found using equations 4.19a and 4.19b, which are the average of the integrals of the square of equations 4.18a and 4.18b. The contributions of the longitudinal acoustic and transverse acoustic modes can then be combined into a single value using equation 4.20 with $v_l = 18.038 \times 10^3$ m/s and $v_t = 12.834 \times 10^3$ m/s [189]. The acoustic deformation potential found by fitting equation 4.18b to the mean polar angle transverse acoustic deformation potential to find Ξ_u and then fitting 4.18a to the mean polar angle longitudinal acoustic deformation potential to find Ξ_d, referred to as fit 1, was $\Xi_{ADP} = 21.42$eV. The acoustic deformation potential found by fitting equation 4.18a to the mean polar angle longitudinal acoustic deformation potential to find both Ξ_d and Ξ_u, referred to as fit 2, was $\Xi_{ADP} = 20.04$eV.

	Ξ_d (eV)	Ξ_u (eV)	Ξ_{ADP} (eV)	m_l/m_0	m_t/m_0	m_{DOS}/m_0
Nava et al. [177]	-	-	8.7	1.4	0.36	0.57[1]
Tsukioka [178, 179]	-	-	8.8,8.0	-	-	0.65[2]
Pernot et al. [180]	-	-	17.7	1.81	0.306	0.55[3]
Isberg et al. [184]	-	-	15	1.15	0.22	0.38[4]
Hammersberg et al. [104]	-	-	12.0	1.56	0.28	0.50[5]
Majdi et al. [181]	-	-	11.5	1.56	0.28	0.50[5]
Djurberg et al. [182]	-5.7	18.5	11.8	1.56	0.28	0.50[5]
Fit 1	-10.81	33.69	21.42	1.64	0.29	0.52
Fit 2	-9.63	31.33	20.04	1.64	0.29	0.52

Table 7.1: Comparison of the acoustic deformation potential for diamond quoted in literature and values presented in this work.

[1] Empirically calculated by fitting simulation to experimental results.
[2] Calculated by fitting to DFT DOS
[3] Taken from reference [190].
[4] Taken from reference [191].
[5] Taken from reference [192].

Table 7.1 shows a comparison of the acoustic deformation potentials and effective masses for the first conduction band of diamond as quoted in the literature and calculated here numerically. The effective masses presented here in the final two rows were calculated using the curvature of the conduction band minimum produced by Quantum Espresso in a method similar to the one presented in section 7.1 and they show excellent agreement with the values calculated using AIMPRO. In the case of Djurberg *et al.* [182] where only the uniaxial and dilatation deformation potentials included, the combined acoustic deformation potential was calculated using equations 4.19a, 4.19b and 4.20. As can be seen, there are a large range of values given for the acoustic deformation potential, with the lower end giving similar values to Si, table 6.1; and the upper end giving values more than double that. The results of both fitting methods give a combined acoustic deformation potential greater than what is seen in the literature with fit 2 being slightly closer. It is also interesting to note that the dilatation and uniaxial deformation potentials from both fits are almost double what is given by Djurberg *et al.* [182]. This large range of values is also seen in the effective masses presented depending on the method of calculation, which are shown as a footnote to the table.

This discrepancy may then be due to the choice of parameters employed in the calculation. As seen in equation 2.35, the acoustic phonon scattering rate depends on the acoustic deformation potential and the DOS which in turn depends on the effective mass. This means that these can act as free parameters when fitting the model to the experimental results and so the value chosen for the effective mass has an impact on the empirically determined deformation potential, chosen to obtain the best possible agreement with experimental results. Although the acoustic deformation potential is larger than values previously reported, the effective mass is in good agreement with the values used by references [104, 181, 182], which was found experimentally via cyclotron resonance [192].

As the deformation potential of fit 2 is closer to what is seen in the literature, this is the value used in the MC simulation. Once again, it can also be seen in figure 7.6 that the spread of the values about the average is smaller for the longitudinal mode which results in fit 2 being more accurate.

7.2.3 Optical Deformation Potential

Due to the band structure, diamond also exhibits g-type and f-type NPOP scattering, similar to Si. The optical deformation potential can then be calculated for the equivalent valley scattering using equation 4.17. However, as with Si, the correct combination for the electron and phonon wavevectors must be used to calculate the correct value for the optical deformation potential.

Figures 7.7 and 7.8 show how the optical f- and g-type scattering deformation potentials were calculated for the first conduction band of diamond. In these figures, the pink region shows the 2D projection of the BZ for the electrons, with the first conduction band valley indicated by the green ellipsoids centred at 72% of the distance along the Δ directions. To find the phonon wavevector that would transfer an electron from the initial conduction band minimum to an equivalent valley, the first BZ for the phonons is overlaid in blue with the Γ point positioned at the initial conduction band minimum. The arrow then indicates a path through these combined BZ along which the electron phonon coupling matrix can be calculated, with the labels K and X indicating the high symmetry point on the surface of the phonon BZ that the path intersects. The deformation potential is then calculated at the point where the path intersects the new conduction band minimum labelled f and g for the f- and g-type scattering respectively. For f-type scattering, this moves the electron into an equivalent perpendicular valley within the first BZ, however, g-type scattering in diamond occurs via an Umklapp process and so the electron scatters to a parallel valley in the second BZ.

By calculating the electron-phonon coupling matrix for an electron with a wavevector at the conduction band minimum interacting with a phonon with a wavevector such that the electron is transferred to a perpendicular valley shows that only the LA and TO phonon modes had significant coupling, indicating that these are the only two modes that mediate f-type scattering. The deformation potential for the LA phonon mode was found to be 2.31 eV/Å with an corresponding change in energy of 0.122 eV and the deformation potential for the TO phonon mode was found to be 16.6 eV/Å with a corresponding change in energy of 0.152 eV. Similarly, calculating the electron-phonon coupling matrix for an electron with a wavevector at the conduction band minimum interacting with a phonon with a wavevector such that the electron is transferred to a parallel valley show that only the LO phonon modes has significant

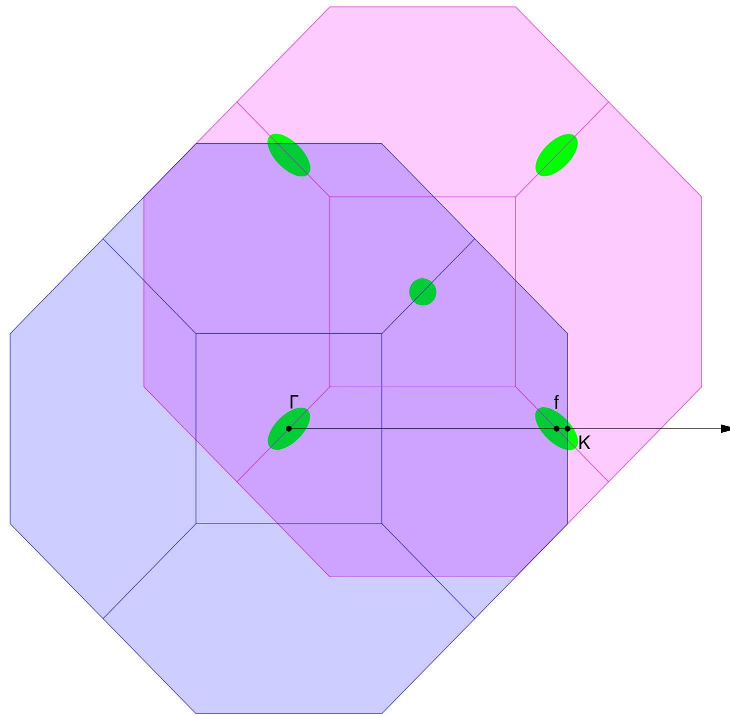

Figure 7.7: 2D projection of the electron (pink) and phonon (blue) BZ of diamond with conduction band minima indicated by the green ellipsoids. The arrow indicates the path of an electron scattering through an f-type scattering.

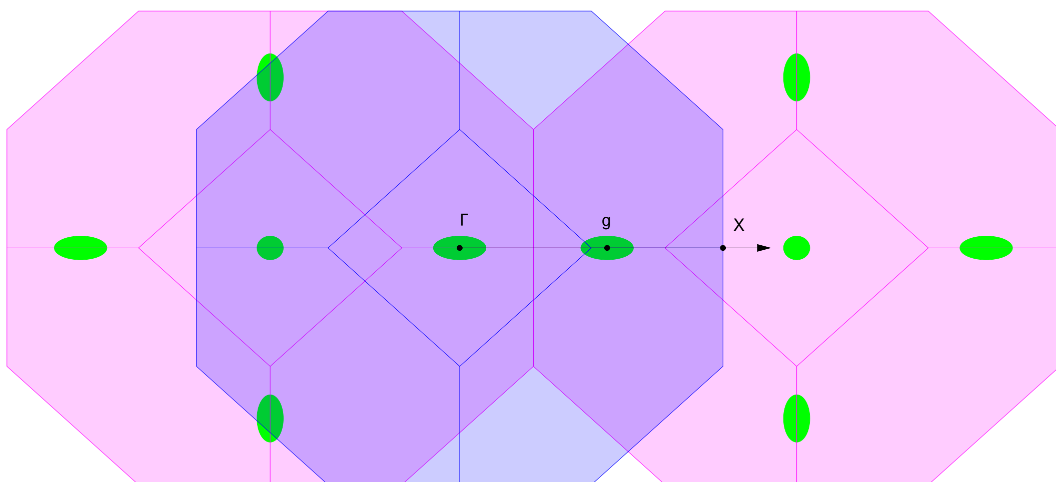

Figure 7.8: 2D projection of the electron (pink) and phonon (blue) BZ of diamond with conduction band minima indicated by the green ellipsoids. The arrow indicates the path of an electron scattering through a g-type Umklapp process.

coupling, indicating that it is the mode that mediates g-type scattering. The deformation potential for the LO phonon mode was found to be 7.78 eV/Å with a corresponding change in energy of 0.163 eV. Table 7.2 shows a comparison of the optical deformation potentials and

	Present Work	Hammersberg *et al.* [104]	Nava *et al.* [177]	Tsukioka [178, 179]	Pernot *et al.* [180]	Isberg *et al.* [184]
$f1$ (eV/Å) LA	2.31	-	8.0	9.0, 22.0	-	15.0
E_{f1} (eV)	0.122	-	0.134	0.133	-	0.120
$f2$ (eV/Å) TO	16.6	4.0	8.0	9.0, 22.0	42.0*	15.0
E_{f2} (eV)	0.152	0.130	0.148	0.147	0.140	0.130
$g1$ (eV/Å) LO	7.78	-	8.0	9.0, 22.0	42.0*	15.0
E_{g1} (eV)	0.163	-	0.164	0.165	0.165	0.165

Table 7.2: Comparison of the optical deformation potentials and corresponding phonon energies for diamond quoted in literature and values presented in this work. *These values may be a typographic error in reference [180].

corresponding energies extracted from figures 7.7 and 7.8, to deformation potentials found in references [104, 177–180, 184]. As mentioned previously, the deformation potentials for equivalent valley scattering cited in the literature cover a large range of values that depend on what exactly is being studied. Also, due to the complexity of fitting the optical deformation potentials, the values given in the literature are all set to be the same value and only vary in the corresponding phonon energies. By combining the deformation potentials using equation 4.23, the deformation potentials calculated here for diamond have an effective deformation potential of $D^*_{eq} = 18.7$eV/Å which is just greater than the effective deformation potential given by the set deformation potentials from Nava *et al.* [177], $D^*_{eq} = 13.9$eV/Å ; and the first set from Tsukioka [178], $D^*_{eq} = 15.6$eV/Å ; but much less than the effective deformation potentials of the other sets. This would lead to lower NPOP scattering rates at lower energies in a MC simulation using the parameters calculated here, however this maybe counteracted by the larger acoustic deformation potential calculated in section 7.2.2

The phonon energies agree with what is seen in references [104, 177–180, 184] and correspond to the same phonon modes that took part in the equivalent valley scattering in Si, this all suggests that the correct phonon modes for the electron-phonon interaction have been selected and that the correct scattering mechanisms will become available to the electrons with a given energy.

Intervalley Scattering

Figure 7.9 shows how the optical intervalley scattering deformation potentials were calculated for scattering between the first and second conduction band valleys. The pink region shows the 2D projection of the BZ for the electrons. The conduction band minimum valleys are indicated by the green ellipsoids centred at 72% of the distance along the Δ directions and the secondary valley is indicated by the magenta circle at the Γ point in the centre of the BZ. The phonon vector, **q**, is then indicated by the blue region, which shows the 2D projection of the first BZ for the phonons with the Γ point centred on the conduction band minimum. The arrow then indicates the path along which the electron phonon coupling matrix was calculated. Where this line intersects the Γ valley, IV, is then where the value for the deformation potential was taken. X indicates where the X symmetry on the surface of the phonon BZ. Only the longitudinal optical phonon mode is absent from this scattering process and so an effective deformation potential and energy was found using equations 4.23 and 4.24 from section , the effective deformation potential was found to be $D^*_{iv} = 17.1\text{eV/Å}$, with a corresponding effective phonon energy found to be $\hbar\omega^*_{iv} = 0.133\text{eV}$.

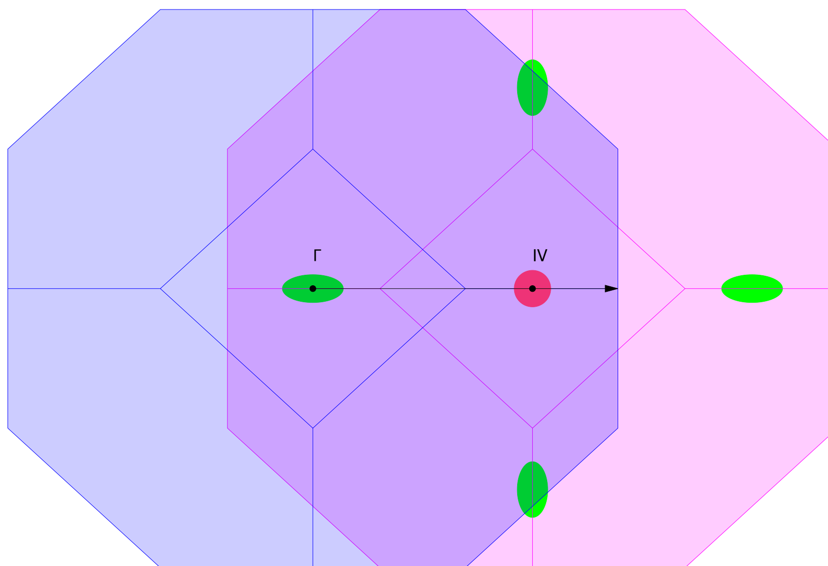

Figure 7.9: 2D projection of the electron (pink) and phonon (blue) BZ of diamond with conduction band minima indicated by the green ellipsoids and the secondary valley indicated by the magenta circle. The arrow indicates the path of an electron scattering from the conduction band minimum valley to the secondary valley.

7.3 MC Simulation

In the previous sections, the results for the numerical DOS and deformation potentials were presented for diamond, the following sections present how these are used in the simulation of electron transport in diamond.

7.3.1 Parameters

Table 7.3 details the parameters used in the MC simulation for diamond. The mass density, static dielectric constant, sound velocities and intervalley separation were taken from literature [104, 177–184]. The calculation of the effective masses, non-parabolicity constants, deformation potentials and associated phonon energies are detailed in the previous sections of this chapter.

7.3.2 Scattering Rates

Figures 7.10, 7.11 and 7.12 show the various scattering rates that were used in the MC simulation of diamond using the parameters presented in table 7.3, with figures 7.10 and 7.11 showing the scattering rates for the low and high energy regime for the lowest conduction band valley, and figure 7.12 showing the scattering rates for the Γ-valley. In all three figures, the solid lines show the scattering rate where the analytic DOS were employed, and the dashed lines show the scattering rate where the numerical DOS were employed. The acoustic phonon scattering rate is given by the magenta line; the sum of the g-type and f-type, emission and absorption NPOP scattering rates are given by the blue lines; the intervalley scattering between the X-valley and the Γ-valley is given by the cyan line; and the charged impurity scattering is given by the orange lines. The black lines then show the total scattering rate found as the sum of the acoustic, NPOP, intervalley and charged impurity scattering rates. As with Si, diamond is non-polar and so POP and piezoelectric scattering are not present. Also, NPOP scattering is not present in the Γ as intravalley scattering via non-polar optical phonons is forbidden due to symmetry. Once again, broadly speaking there is good agreement between the scattering rates using numerical DOS and those using analytic DOS in the X-valley scattering rates. However, in the lower energy regime below 1eV, the numerical DOS is lower than the analytic

Parameter	Symbol	Value
Mass Density (kg/m^3)	ρ	3510
Static Dielectric Constant (ϵ_0)	ϵ_s	5.7
Longitudinal Sound Velocity (m/s)	v_l	18.038×10^3
Transverse Sound Velocity (m/s)	v_t	12.834×10^3
X-Valley Longitudinal Effective Mass (m_e)	m_{Xl}	1.64
X-Valley Transverse Effective Mass (m_e)	m_{Xt}	0.288
X-Valley Non-Parabolicity Constant (eV^{-1})	α_X	0.099
Γ-Valley Effective Mass (m_e)	m_Γ	0.247
Γ-Valley Non-Parabolicity Constant (eV^{-1})	α_Γ	0.12
Acoustic Deformation Potential (eV)	Ξ_{ADP}	20.043
Optical Deformation Potentials (eV/Å)	D_O	
$f1$ Process LA		2.32
$f2$ Process TO		16.6
$g1$ Process LO		7.78
Optical Phonon Energies (eV)	$\hbar\omega_O$	
$f1$ Process LA		0.122
$f2$ Process TO		0.152
$g1$ Process LO		0.163
Intervalley Deformation Potential (eV/Å)	D^*_{iv}	17.1
Intervalley Phonon Energy (eV)	$\hbar\omega^*_{iv}$	0.133
X-Γ Valley Separation (eV)	$E_{X\Gamma}$	1.84
Charged Impurity Concentration (m^{-3})	n_0	10^{20}

Table 7.3: Parameters for MC simulation of diamond.

DOS. Once again, this will result in the MC simulation using numerical DOS having reduced scattering at lower energies and so the average electron velocity will be higher at lower fields.

Similar to Si, the NPOP scattering quickly becomes the dominant scattering mechanism in

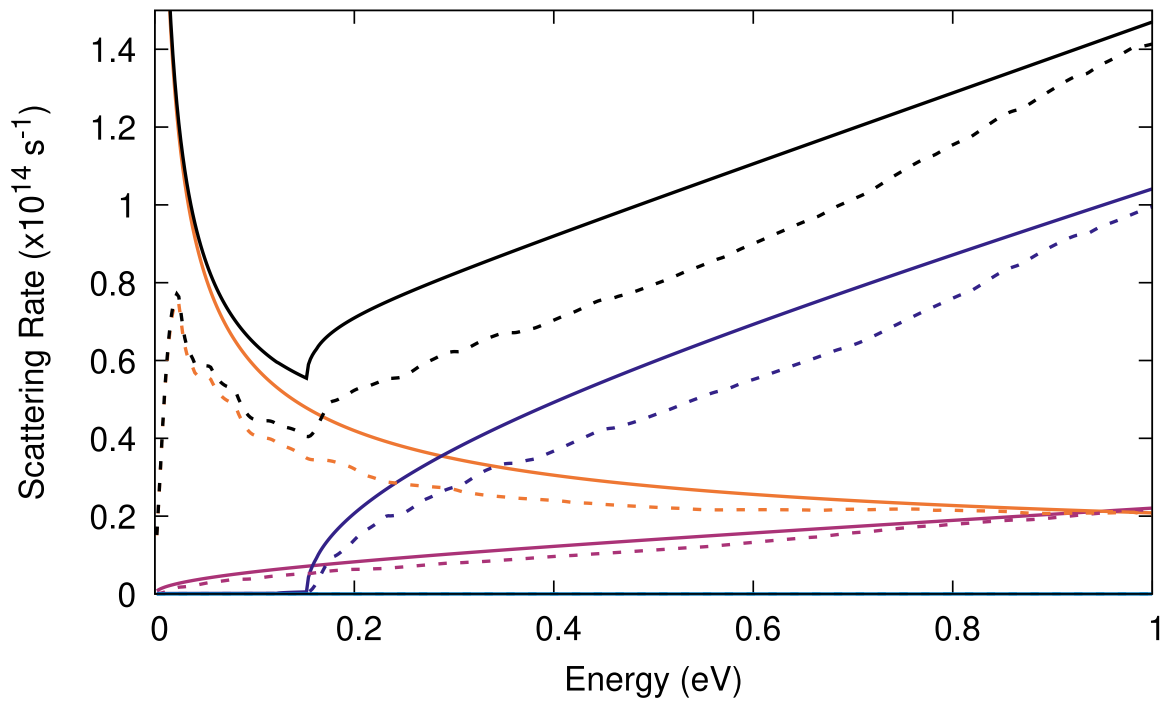

Figure 7.10: Comparison of the X-valley scattering rates calculated using analytic (solid) and numerical (dashed) DOS for diamond at 300K at electron energies below 1eV. With Charged Impurity scattering (orange), NPOP scattering (blue), ADP scattering (magenta), and total scattering rate (black). Energy scale relative to the conduction band minimum.

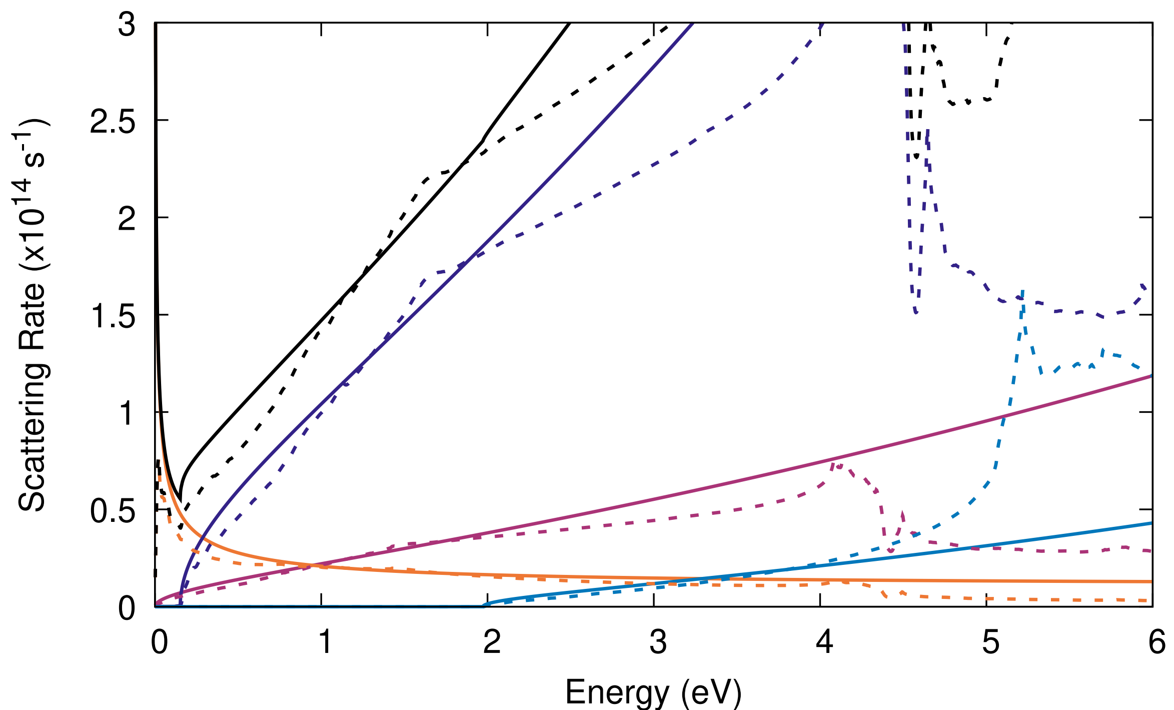

Figure 7.11: Comparison of the X-valley scattering rates calculated using analytic (solid) and numerical (dashed) DOS for diamond at 300K at electron energies below 6eV. With Charged Impurity scattering (orange), NPOP scattering (blue), $X \rightarrow \Gamma$ Intervalley Scattering (cyan), ADP scattering (magenta), and total scattering rate (black). Energy scale relative to the conduction band minimum.

the X-valley, however as this causes the total scattering rate to grow just as fast, this can lead to problems in the simulation. If the scattering rates are calculated up to 6eV, but the average electron energy remains below 1eV then the vast majority of scattering events experienced by an electron would be self scattering which has no effect on the energy or momentum and so the velocities would be artificially increased. This would also mean that the simulation would take a lot longer as the time step is the inverse of the maximum of the total scattering rate. To counteract this issue, the simulation was split over multiple runs so that a suitable maximum energy for the scattering rates could be used. The maximum energy was selected so as to minimise the maximum of the total scattering rate but without setting a barrier for the energy of the electrons over the given range of electric fields. Due to the inclusion of a secondary

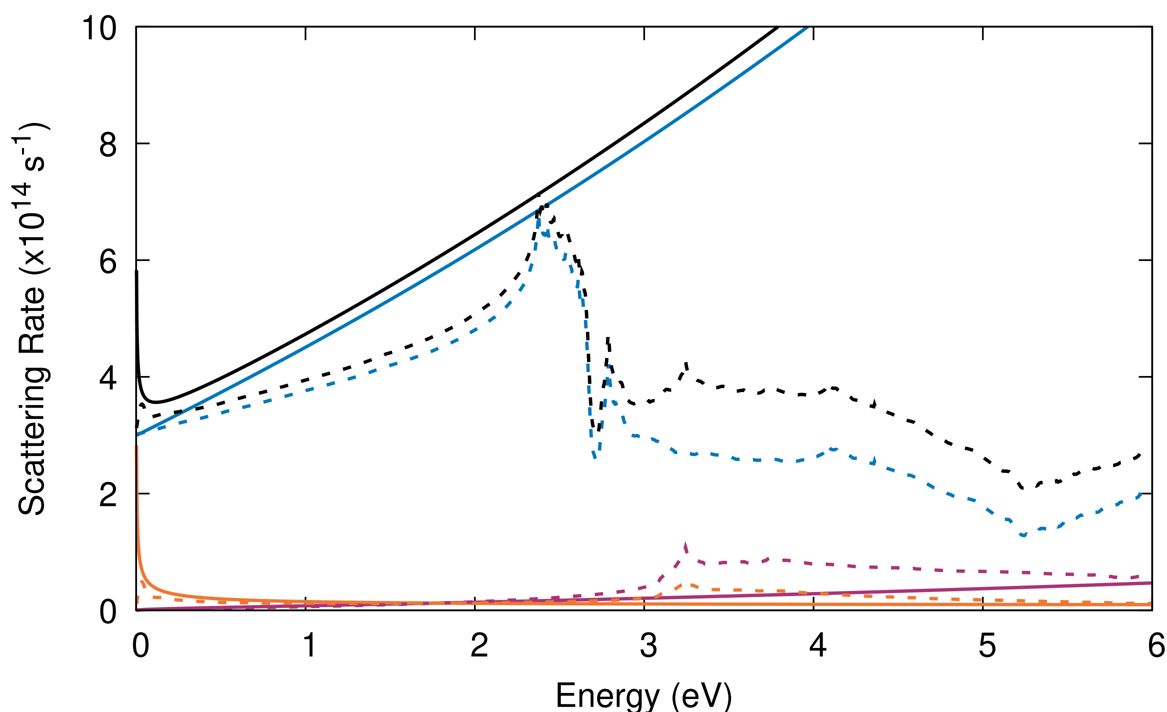

Figure 7.12: Comparison of the Γ-valley scattering rates calculated using analytic (solid) and numerical (dashed) DOS for diamond at 300K. With Charged Impurity scattering (orange), $\Gamma \rightarrow X$ Intervalley Scattering (cyan), ADP scattering (magenta), and total scattering rate (black). Energy scale relative to the secondary valley minimum.

valley figure 7.11 shows intervalley scattering turning on beyond 1.84eV, which is the energy difference between the two valleys. However, this scattering mechanism is much lower than the other scattering mechanisms and only becomes significant when using the numerical DOS beyond 5eV. On the other hand as the conduction band minimum valley DOS is larger than the secondary Γ-valley DOS, figure 7.12 shows the intervalley scattering back to the conduction band minimum valley to be the dominant scattering mechanism. This means that although

there are available states for the electrons to scatter into in the Γ-valley, the probability that they will scatter to this valley are low and, once they do scatter to the upper valley, the next scattering event they experience will likely scatter them back to the lower valley. This effect should be seen in simulations using both analytic and numerical DOS until the electrons reach higher energies. As mentioned, figure 7.11 shows that beyond 5eV, the intervalley scattering becomes a significant portion of the total scattering rate. At this point an electron scattering into the Γ-valley would have an energy above 3eV where the intervalley scattering starts to decrease due to the decrease in the DOS. Therefore, at higher fields the numerical DOS predict a greater population of electrons in the upper valley than the analytic DOS.

7.3.3 Simulation Results

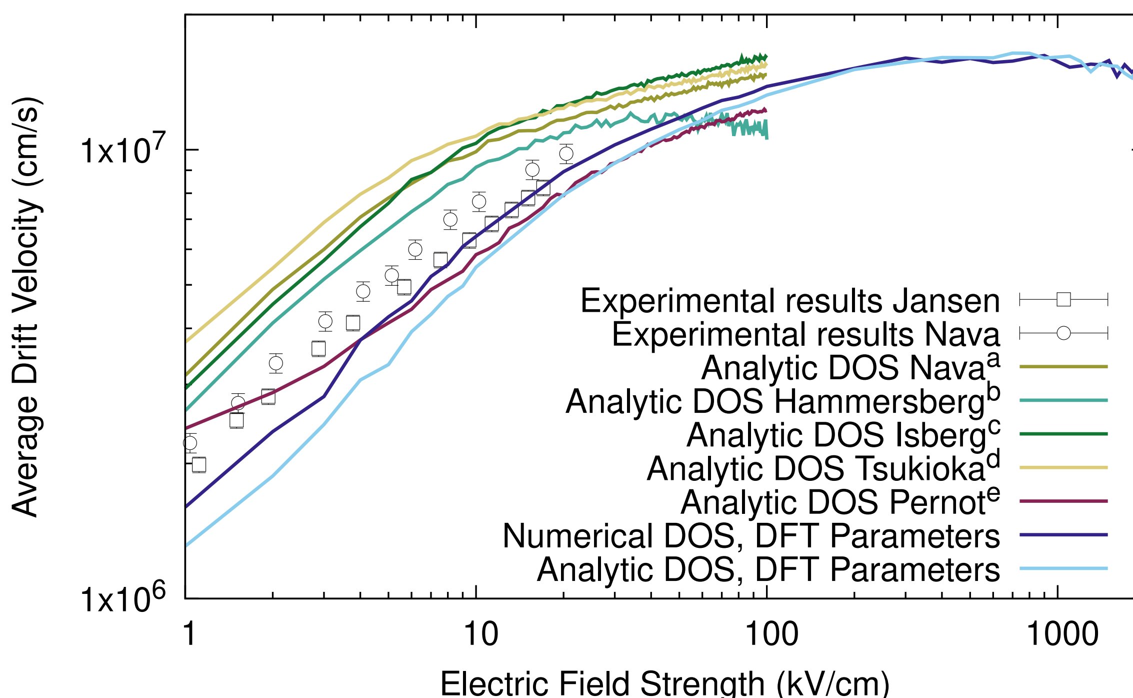

Figure 7.13: Velocity-field data for diamond. Lines are MC simulation with parameters from Nava *et al.* [177] (a), Hammersberg *et al.* [104] (b), Isberg *et al.* [184] (c), Tsukioka [178, 179] (d) and Pernot *et al.* [180] (e), with analytic DOS; and parameters calculated via DFT with analytic (light-blue) and numerical (dark-blue) DOS. Points are experimentally determined data from Jansen [193] (squares) and Nava *et al.* [177].

Figure 7.13 shows the steady-state velocity-field characteristics that have been produced by MC simulation for diamond along with experimental data with the electric field parallel with the x-axis. The simulation results were found using parameters from literature as detailed in tables 7.1 and 7.2; and as determined using the methods presented in section 4.2 with analytic

(light-blue) and numerical (dark-blue) DOS. As with Si, there is close agreement between the simulation results using the parameters presented here and the experimental results, in particular between the simulation using the numerical DOS and the experimental results from Jansen [193] in the range of 6kV/cm to 20kV/cm. When compared to the simulation results, the MC simulation using the parameters presented here have a lower average velocity over the lower range of field strengths. This makes sense as the DFT methods utilised here predicted a much higher acoustic deformation potential that would lead to more scattering at lower energies. At low fields, the simulations underestimate the average velocity as compared to the experimental measured results. As acoustic deformation potential scattering dominates at lower energies, it could be that the deformation potential calculated using DFT was overestimated. This is supported by the velocity-field characteristic when using the parameters of Pernot *et al.* [180] as this simulation has much higher optical deformation potentials but a lower acoustic deformation potential and as the field strength decreases, the simulation results cross the experimental results.

At higher fields, most of the simulation results appear to be approaching a saturation velocity around 1.5×10^7cm/s, in agreement with what is seen in the literature [177]. The simulation using the parameters from Hammersberg *et al.* [104] reaches a saturation velocity just above 1×10^7 at much lower field strengths. This is a result of the choice of scattering parameters as there is reduced NPOP scattering due to there being only one f-type scattering mechanism. However, the work of Hammersberg *et al.* [104] was conducted at low temperatures where the electrons are unlikely to achieve energies where they can undergo g-type scattering and so the associated deformation potential is difficult to determine.

Figure 7.14 shows the energy-field characteristic for the MC simulations of diamond using the scattering parameters calculated here with analytic (light-blue) and numerical (dark-blue) DOS. Over the entire range of field strengths, the simulation using the numerical DOS has a higher energy. The patterns in the average energy up to field strengths of around 1000kV/cm can be explained easily by considering the scattering rates shown in figures 7.10 and 7.11. As the average velocity stays below 1eV, the simulation using the numerical DOS has a higher energy as there is lower total scattering rate meaning that electrons can be accelerated by the field to higher momenta and thus higher energies more easily. As the field approaches

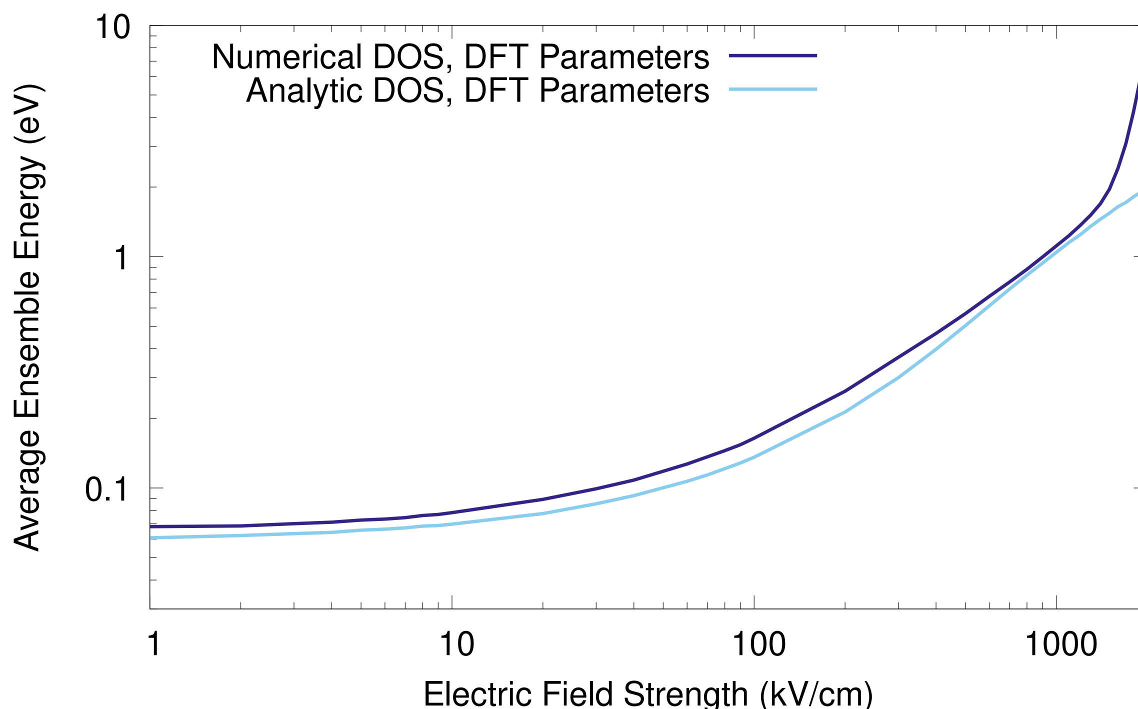

Figure 7.14: Energy-field characteristics for diamond found using MC simulation with parameters calculated via DFT with analytic (light-blue) and numerical (dark-blue) DOS. Average energy is relative to the conduction band minimum.

1000kV/cm, the average energies get closer together, and it can be seen in figures 7.10 and 7.11 that as the energies approach 1eV, the scattering rates using the numerical and analytic DOS get closer together. So as the average velocity approaches 1eV, the electrons in the simulations using analytic and numerical DOS have a similar total scattering rate.

However, beyond 1000kV/cm, the average ensemble energy using the numerical DOS increases exponentially, hitting 8eV. This is thought to be due to a limitation in the model employed, as although the scattering rates are using the numerical DOS the drift step is still evolving according to a parabolic band structure. Figure 7.3 shows the comparison of the numerical and analytic DOS of diamond for the first valley, and it shows that beyond 2eV the analytic DOS continues to grow whereas the numerical DOS peaks at around 4eV and rapidly decreases. Electrons at these higher energies will continue to be accelerated during the analytic drift step, however they will experience fewer scattering events due to the decrease in the DOS used in the scattering rate.

Finally, at higher energies it is possible for some of the electrons to scatter into the secondary Γ-valley. However, as mention previously, 7.11 shows that the $X - \Gamma$ scattering rate makes up a small proportion of the first valley's total scattering rate whereas 7.12 shows that

the $\Gamma - X$ scattering rate dominates the second valley's total scattering rate. This means that although there are available states for the electrons to scatter to, the probability of scattering to the Γ-valley is low, and any electrons that do scatter into the Γ-valley have a high probability of immediately scattering back into the X-valley. As such, even at fields of 2000kV/cm, the proportion of electrons in the Γ-valley is only just above 1% when using the analytic DOS. This may then explain the lack of intervalley scattering in diamond seen in the literature, the energy difference in the conduction band minimum and the Γ-valley as well as the low DOS means that intervalley scattering has a negligible effect on electron transport in diamond. When using the numerical DOS, there is a significant population of the upper valley at higher fields, approaching 20% at 2000kV/cm, however this is most likely due to the runaway energies discussed above and does not accurately reflect the real system.

7.4 Summary

In this chapter, the methods described in chapter 4 have been applied to diamond. Section 7.1 presented the results for the numerical calculation of the DOS for diamond as calculated by tetrahedral interpolation using the band structure from AIMPRO. This interpolated DOS was found to agree with the DOS found by AIMPRO via Gaussian broadening, found with a broadening width of $\sigma = 0.01$ eV. The conduction band minimum and secondary conduction band valley were found, and their positions agreed with what was seen in the literature. From these, the effective mass was calculated from the curvature of the bands and used with the DOS to calculate the non-parabolicity constant.

In section 7.2, the values of the acoustic and optical deformation potentials were calculated and compared to what is seen in the literature. The acoustic deformation potential was found to be greater than what has been reported previously. The optical deformation potential was found to be within the large range of previously reported values.

These were then brought together in 7.3, where they were used in the MC simulation of the electrons in diamond. At high field strengths, the parameters in concert with both analytic and numerical DOS converged on a saturation velocity of 1.5×10^7cm/s, in agreement with the literature. Between 6kV/cm to 20kV/cm, there was excellent agreement between the MC simulation using the numerical DOS and the experimental results, however below this range

both the MC simulations using the parameters presented here underestimated the average velocity. It is thought that this could be due to an overestimate in the acoustic deformation potential calculated via DFT which may improve with more advanced functionals. Finally, it was found that at the higher field strengths, there was an exponential increase in the average ensemble energy in the simulation using numerical DOS in the scattering mechanisms. This is thought to be due to the disagreement in the analytic band used in the drift step and the numerical DOS used in the scattering step. During the drift step there is nothing stopping the electrons from being accelerated to higher energies whereas the scattering rates are reduced due to a reduction in the numerical DOS that means these extremely high energy electrons are experiencing fewer scattering events.

These methods have been shown to work well in simulating the transport of electrons in diamond, however there is a limit to their ability due to the reliance of the drift step on the analytic band structure. This is discussed further in chapter 9.

Finally, as with Si, it is important to consider the sensitivity of the simulation results on the input parameters. As shown in table 7.1 and discussed in section 7.2.2, the acoustic deformation potential calculated here numerically is almost double what is presented in references [104, 181, 182]. As the acoustic scattering rate depends on the square of the deformation potential, this doubling results in an acoustic scattering rate leads to a quadrupling of the acoustic phonon scattering rate. If the simulations were to use a value closer to those presented in references [104, 181, 182], this would lead to a lower total scattering rate, reducing the chances of scattering. This reduced scattering rate would have the most effect at lower energies where the impact of acoustic scattering is more pronounced and so may lead to higher average drift velocities at the lower field strengths. However, this will only have an effect on the simulation results at lower field strengths, as the non-polar optical phonon scattering dominates at energies.

Chapter 8

Cubic Boron Nitride Results

As seen in the previous two chapters, the *ab initio* methods detailed in chapter 2 can be used to make predictions about scattering parameters that can be then used in MC simulation. Similar to Si and diamond, cBN also has FCC crystal structure with conduction band minima along the Δ direction. However, unlike Si and diamond, cBN is polar and so POP and piezoelectric scattering must also be considered. As mentioned previously, these scattering mechanisms are found analytically following the methods detailed in section 2.3.2. Section 7.1 shows how the DOS was calculated via tetrahedral discretisation as detailed in section 4.1 and compared to the DOS calculated directly via AIMPRO. The effective mass and non-parabolicity constant were then calculated and compared to previous work. Following this, section 8.2 presents the acoustic and optical deformation potentials as calculated via Quantum Espresso. There have been relatively few studies into the transport of electrons in cBN, [73, 75, 146, 194–196]. References [75, 194–196] do present the scattering parameters employed to which the calculated parameters will be compared however it is noted in the paper by Siddiqua *et al.* [75] "that as some of the parameters are unknown at present, reasonable estimates are employed when necessary" as the "particular material parameter has yet to be experimentally determined". These estimates include the acoustic deformation potential, the intervalley deformation potentials and the associated intervalley phonon energies. Finally, the results from the MC simulation using the numerically calculated scattering parameters and both analytic and numerical DOS are presented in section 8.3. These are compared to simulations using the range of parameters seen in the literature at lower field strengths before seeing how the numerical and analytic bands differ in the high field regime.

8.1 Density of States Calculation

8.1.1 Band Structure and Effective Mass

Section 5.1.1 details how the pseudopotentials and wavefunction basis were chosen for boron and nitrogen with AIMPRO. Figure 8.1 then shows the band structure calculated for cBN with these chosen pseudopotentials. As can be seen, the conduction band minimum lies exactly on the X symmetry point, the secondary minimum is at the Γ symmetry point and a tertiary minimum lies at the X symmetry point. This is in contrast to references [75, 194–196] where the third minimum is placed at the L symmetry point. The disagreement in the ordering of the valleys may also be a consequence of the bandgap problem as DFT may have incorrectly predicted the higher energies at the X symmetry point. However, the third valley has very little impact on the transport of electrons in cBN and so is neglected.

The figure also shows that AIMPRO gives the band gap to be 4.62eV which is 27.8% smaller than the experimentally measured value of 6.4eV. This is again due to the band gap problem and better predictions may be achieved using more complex exchange-correlation functionals. Using equation 1.11, the effective mass can be calculated directly from the curvature of the

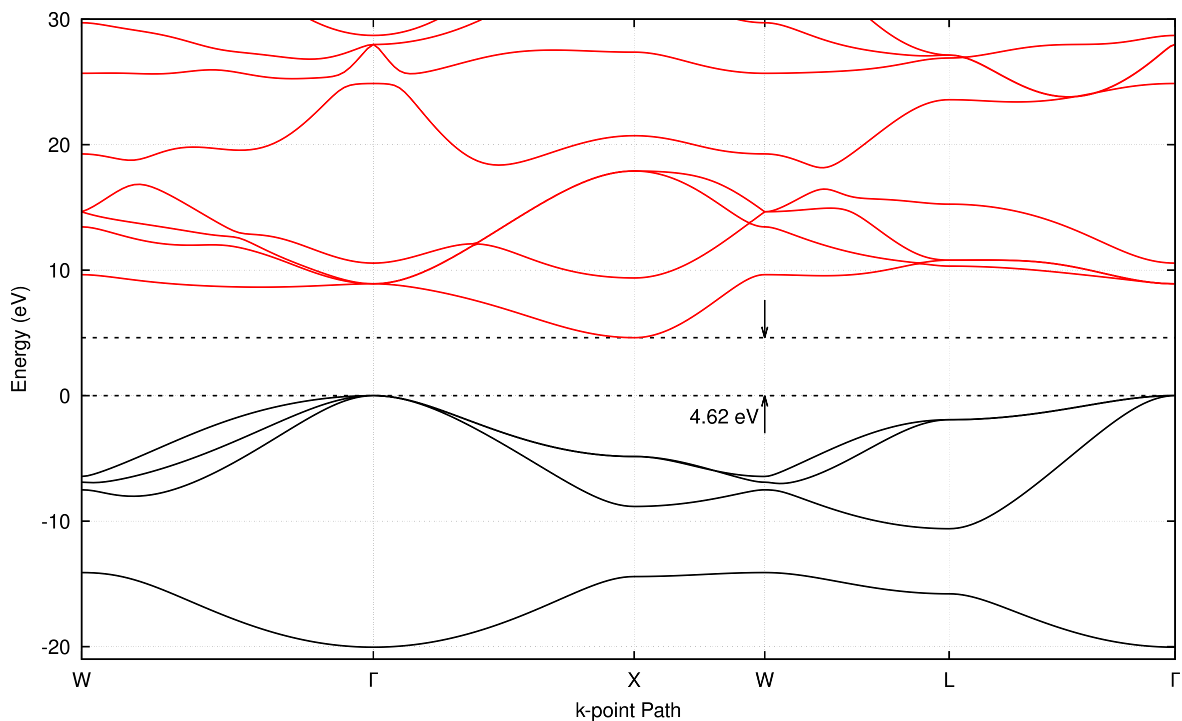

Figure 8.1: The band structure of cBN calculated via DFT with a prediction of 4.62eV for the bandgap. Black lines indicate the valence bands and red lines indicate the conduction band.

band structure at the valley minima. The longitudinal effective mass at the conduction band

minimum was found to be $m_l^* = 0.92m_e$ and the transverse effective mass was found to be $m_t^* = 0.30m_e$. Following equation 1.21, the effective mass used in the calculation of the analytic DOS is then found as the geometric mean of the longitudinal and transverse effective masses which gives $m^* = 0.44m_e$. The longitudinal and transverse effective masses from literature were given as $m_l^* = 1.20m_e$ and $m_t^* = 0.26m_e$ [36, 197], which gives a DOS effective mass of $m^* = 0.43m_e$ or $m_l^* = 1.15m_e$ and $m_t^* = 0.27m_e$ [73], which give a DOS effective mass of $m^* = 0.44m_e$. This means that despite the disagreement in the longitudinal and transverse effective masses, there is agreement in the geometric mean of the effective mass which means that the DOS should be in agreement with what has previously been used.

8.1.2 Comparison to AIMPRO DOS

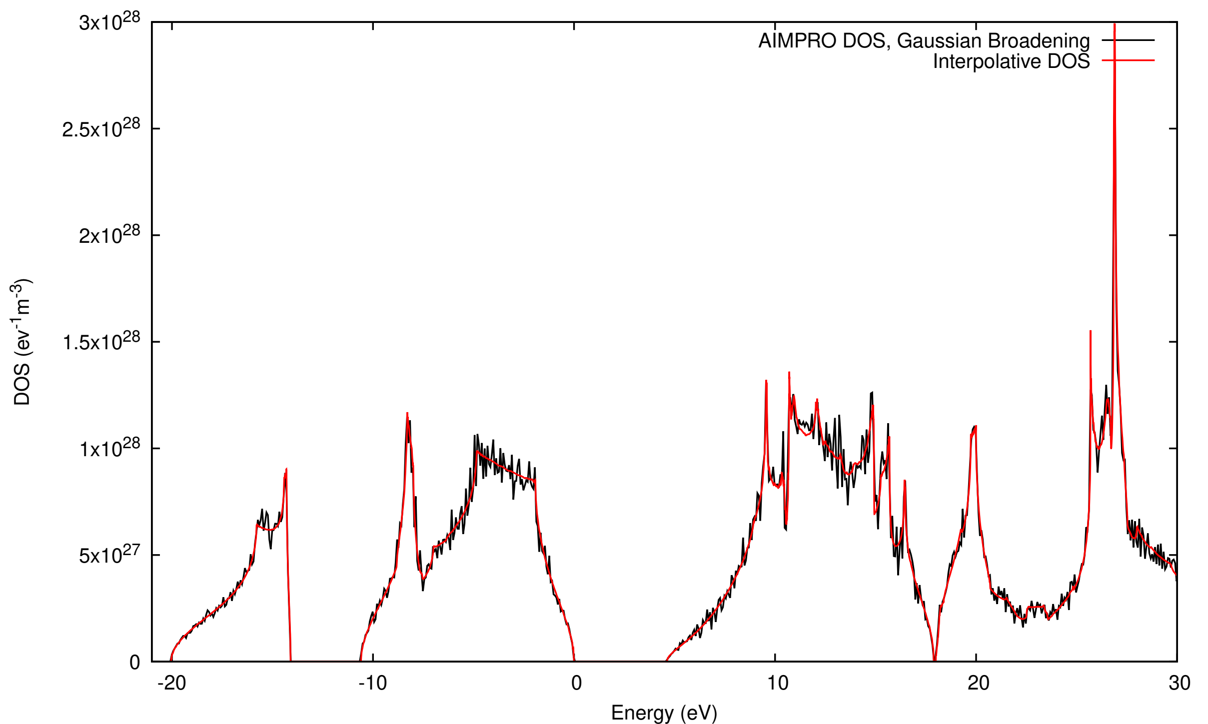

Figure 8.2: Comparison of the DOS calculated numerically via Gaussian broadening in AIMPRO (black) and tetrahedral interpolation (red).

Figure 8.2 shows a comparison of the DOS calculated using AIMPRO in black and using the interpolative DOS detailed in section 4.1. The interpolative DOS was calculated on a grid of 33754 vertices on the lowest 20 bands with an average of 55149 simplices per band. The tetrahedral edge length tolerance was set to be 5% of the length of the reciprocal lattice constant and the energy tolerance was set to be 0.05eV. The difference in energy when

sampling for the DOS was 0.002eV. In figure 7.2 there is good agreement between the two DOS which means that the interpolative DOS has been correctly applied to cBN. Once again the oscillations in the DOS calculated by AIMPRO could be dampened by more careful choice of the Gaussian broadening parameters.

8.1.3 Non-Parabolicity Constant Calculation

The modified gradient descent method of section 4.1.5 was applied to the tetrahedral grid generated for the band structure of cBN to assign tetrahedra to a valley. Figures 8.3 and 8.4 show a comparison of the DOS calculated numerically from the tetrahedral grid (black) and analytically from equations 1.13 and 1.18 (red) for the two lowest conduction band valleys. As stated previously, the first and third valleys were found to be at the X symmetry point and the second valley was found at the Γ symmetry point, with an energy separation of 4.29eV from the conduction band minimum to the Γ valley and 4.76eV from the conduction band minimum to the secondary X valley. Levinshtein *et al.* [36] report the energy difference from the conduction band minimum to the Γ to be somewhere between 2.1eV to 3.9eV therefore the DFT value could be somewhere between a slight overestimate and double the correct value. Levinshtein also reports the energy from the conduction band minimum to the L symmetry point to be $>$ 5.6eV above the conduction band minimum. The data for the energy difference in the band structure at high symmetry points given in Levinshtein *et al.* is taken from the work of Rodríguez-Hernández *et al.* [198] and Ferhat *et al.* [199]. These references calculate the band structure of cBN numerically using DFT and empirical tight-binding, respectively; and their band structure plots for cBN show agreement with figure 8.1, with a local minimum present at the X symmetry point with energy just higher than at Γ. Notably, they do not show minima at the L symmetry point and so the L-valley employed in references [75, 194–196] may be due to an error in the interpretation of these figures.

References [75, 194–196], the lower end of the band gap energy given by Levinshtein *et al.* [36] is used; in this work, several values will be employed in simulation at field strengths where intervalley scattering becomes relevant to see how varying the energy difference impacts electron transport. For the X and Γ valleys, the analytic DOS was found by calculating the curvature of the bands at the valley minimum to find the effective mass and then fitting

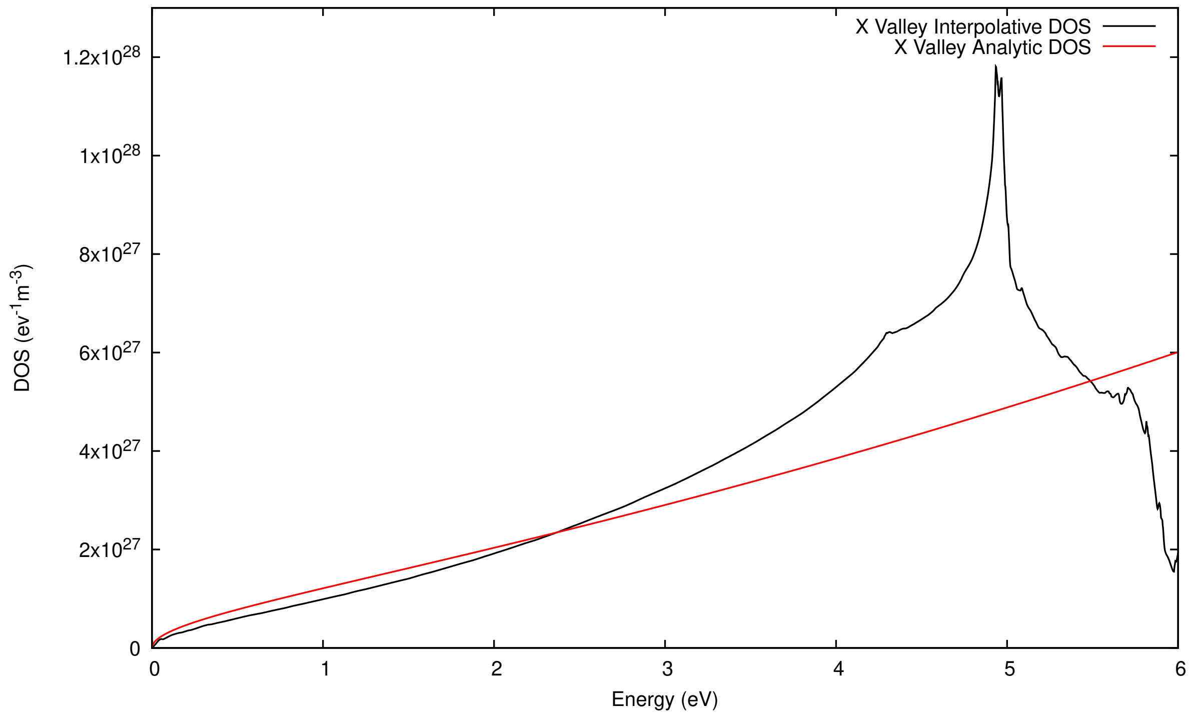

Figure 8.3: The numerically calculated DOS for the first conduction band valley of cBN (black) and the analytic DOS (red) with effective mass calculated from the curvature of the band structure and α calculated by fitting to the numerical DOS.

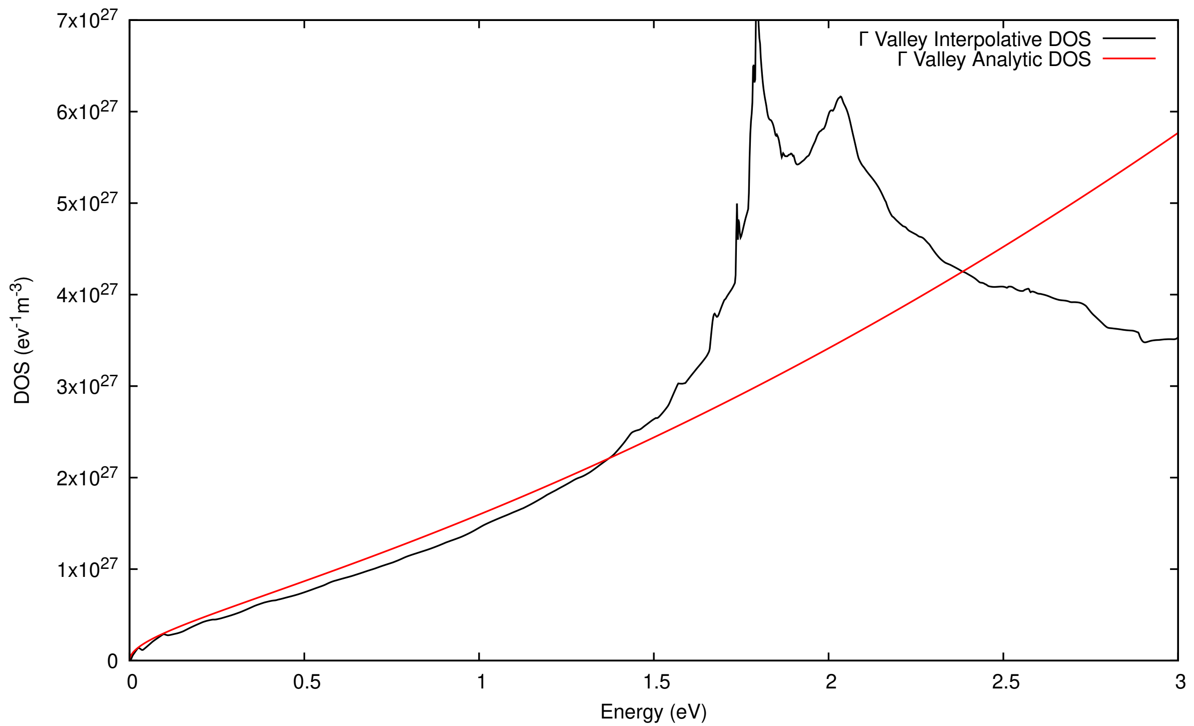

Figure 8.4: The numerically calculated DOS for the second conduction band valley of cBN (black) and the analytic DOS (red) with effective mass and α calculated by fitting to the numerical DOS.

equations 1.13 and 1.18 to find the non-parabolicity constant. The effective mass of DOS for the lowest valley is $m^* = 0.44m_e$, and from figure 8.3 the non-parabolicity constant was found to be 0.084eV^{-1}. From the curvature, the Γ valley was found to have an effective mass

of $m^* = 0.41m_e$ and, from fitting the analytic DOS in figure 8.4, a non-parabolicity constant of 0.29eV^{-1}. As stated in the previous section, the effective mass of DOS calculated for the conduction band minimum agrees with what is seen in the literature [36, 197, 73], however, in the MC simulations of references [75, 194–196] the second conduction band valleys has an effective masses equal to the electron free mass and all valleys are treated as parabolic. Although the first valley is only slightly non-parabolic, in the work of Siddiqua *et al.* [75], they show that even a slight non-parabolicity in only the first valley leads to a decrease in the saturation velocity. Therefore, using the DOS and non-parabolicity constants calculated here are expected to result in saturated drift velocities lower than what is seen in reference [75].

8.2 Scattering Parameters

8.2.1 Phonon Dispersion

Section 5.2.1 details how the pseudopotentials were chosen for the boron and nitrogen atoms in bulk cBN with Quantum Espresso. Figure 8.5 shows the phonon dispersion curves calculated for cBN with these chosen pseudopotentials along $\Gamma - X$, $X - W - X'$, $X' - K - \Gamma$ and $\Gamma - L$, where X' refers to a point outside the first BZ that would transform on to the X symmetry point. These dispersion curves are in agreement with what is seen in the literature [146]. For the POP scattering only the longitudinal optical modes produce polarisation effects that the electrons interact with [33], therefore the phonon energy for POP scattering can be taken here from the energy of the LO mode at the Γ point which is 0.161eV. In references [36, 75, 194–196], the POP energy is given as 130eV, however, Zhu *et al.* [146] and Sanders & Kioupakis [73] also found a value of roughly 160eV for the POP scattering using *ab initio* methods.

8.2.2 Acoustic Deformation Potential

Once again, the longitudinal and transverse acoustic deformation potentials were found using equation 4.16 with the polar angle between the phonon vector and the longitudinal axis of the k_z conduction band minimum valley found at twenty evenly spaced angles from 0 to π. For each polar angle, the azimuthal angle was varied and the average of the deformation

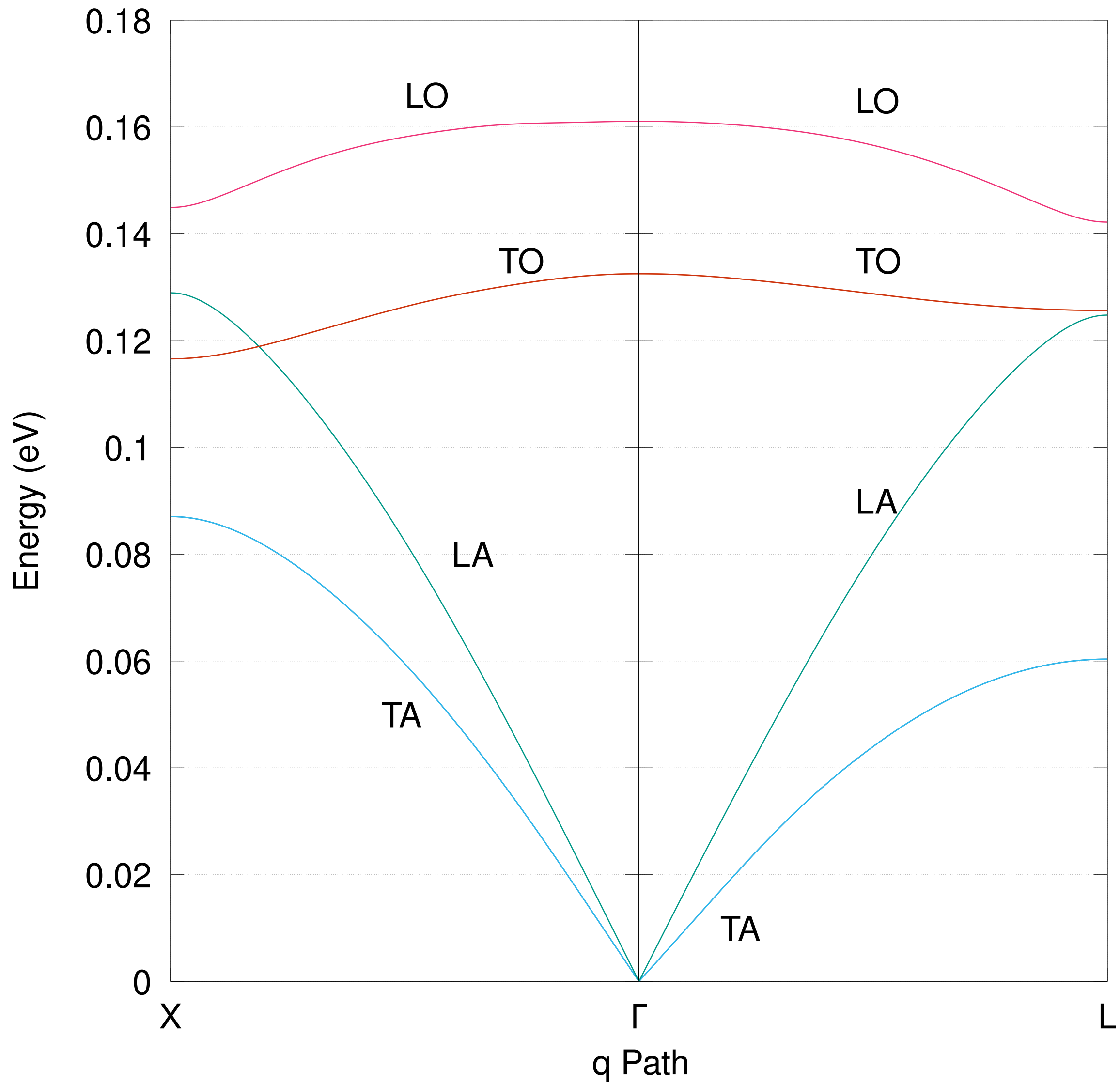

Figure 8.5: The phonon dispersion along lines of symmetry in cBN calculated via DFT.

potential found from eight evenly spaced points from 0 to 2π. Figure 8.6 shows the angular dependence of the acoustic deformation potentials for the longitudinal, red, and the sum of the two transverse, black, acoustic phonon modes. The points show the average deformation potential for a given polar angle and the bars show the range of values calculated while varying the azimuthal angle for a given polar angle. As cBN is a polar material, the long range effects were subtracted before the deformation potential was calculated. The lines in figure 8.6 show the fit of equations 4.18a and 4.18b to the calculated deformation potentials.

The lines in figure 8.6 show the fit of equations 4.18a and 4.18b to the calculated deformation potentials. The solid lines show the case where Ξ_u and Ξ_d were found separately by first fitting equation 4.18b to the average polar angle transverse acoustic deformation poten-

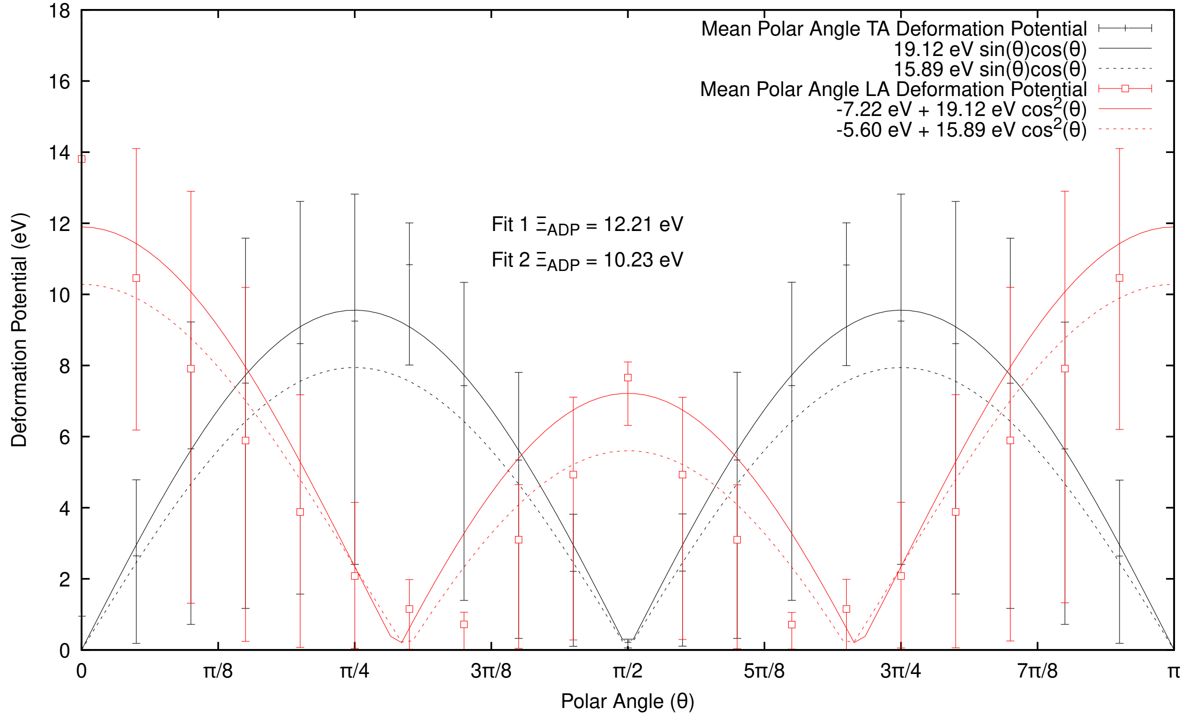

Figure 8.6: Polar dependence of the longitudinal (red) and transverse (black) acoustic deformation potential in the first conduction band valley of cBN calculated via Quantum Espresso (points) and equations 4.18a and 4.18b. The bars indicate the range of values found by varying the azimuthal angle for a given polar angle.

tial to find the value of Ξ_u and then fixing this while fitting equation 4.18a to the average polar angle longitudinal acoustic deformation potential to find the value of Ξ_d. The uniaxial and dilatation deformation potentials were found to be $\Xi_u = 19.12$eV and $\Xi_d = -7.22$eV. The dashed lines show the case where Ξ_u and Ξ_d were found together by fitting equation 4.18a to the average polar angle longitudinal acoustic deformation potential. The uniaxial and dilatation deformation potentials were found to be $\Xi_u = 15.89$eV and $\Xi_d = -5.60$eV. The black dashed line is then the plot of equation 4.18b for $\Xi_u = 14.89$eV.

Values for the longitudinal and transverse acoustic deformation potential can then be found using equations 4.19a and 4.19b, which are the average of the integrals of the square of equations 4.18a and 4.18b. The contributions of the longitudinal acoustic and transverse acoustic modes can then be combined into a single value using equation 4.20 with $v_l = 15.40 \times 10^3$ m/s and $v_t = 11.80 \times 10^3$ m/s [36]. The acoustic deformation potential found by fitting equation 4.18b to the mean polar angle transverse acoustic deformation potential to find Ξ_u and then fitting 4.18a to the mean polar angle longitudinal acoustic deformation potential to find Ξ_d, referred to as fit 1, was $\Xi_{ADP} = 12.21$eV. The acoustic deformation potential found by fitting equation 4.18a to the mean polar angle longitudinal acoustic deformation

potential to find both Ξ_d and Ξ_u, referred to as fit 2, was $\Xi_{ADP} = 10.23$eV. The deformation potential calculated here does compare well with what is seen in the work of Siddiqua *et al.* [75], however, they note that for the acoustic deformation potential, "reasonable estimates are employed" as the "particular material parameter has yet to be experimentally determined". It is unclear exactly how the value for the acoustic deformation potential was determined and so this similarity could be coincidental.

As with Si and diamond, the effective mass at the conduction band minimum was calculated using the curvature of the conduction band minimum produced by Quantum Espresso, similar to the method presented in section 8.1. These were found to be $m_l^* = 0.92m_0$ and $m_t = 0.30m_0$ which gives a DOS effective mass of $m_{DOS}^* = 0.44m_0$. As with diamond, there is excellent agreement with the values calculated using AIMPRO in section 8.1. The DOS effective mass compares well with the values of $m_{DOS}^* = 0.413m_0$ [146] and $m_{DOS}^* = 0.43m_0$ [75], however, the latter presents values for the longitudinal and transverse effective masses that have a greater anisotropy, $m_l^* = 1.2m_0$ and $m_t = 0.26m_0$, calculated via first principles from reference [197]. Most MC simulations use the DOS effective mass and assume the bands are isotropic and so in this case, this disagreement in the anisotropy wouldn't matter as there is good agreement in the DOS effective mass, however, if the MC simulation was intended to model valleytronics as in references [104, 182] for diamond, the anisotropy of the effective masses would be important as electrons in perpendicular valleys would experience the acceleration of an electric field differently.

Figure 8.6 shows a large variation in the acoustic deformation potential at different azimuthal angles. The figure also shows that, unlike the cases of Si and diamond, the angular dependence of the sum of the mean transverse acoustic deformation potential isn't as close a fit to equation 4.18b whereas the angular dependence of the mean longitudinal acoustic deformation potential does still follow the pattern of equation 4.18a. Therefore, the acoustic deformation potential from fit 2 are used in the MC simulation of cBN. The acoustic deformation potential calculated here compares well with the value of 10eV employed in references [75, 194–196].

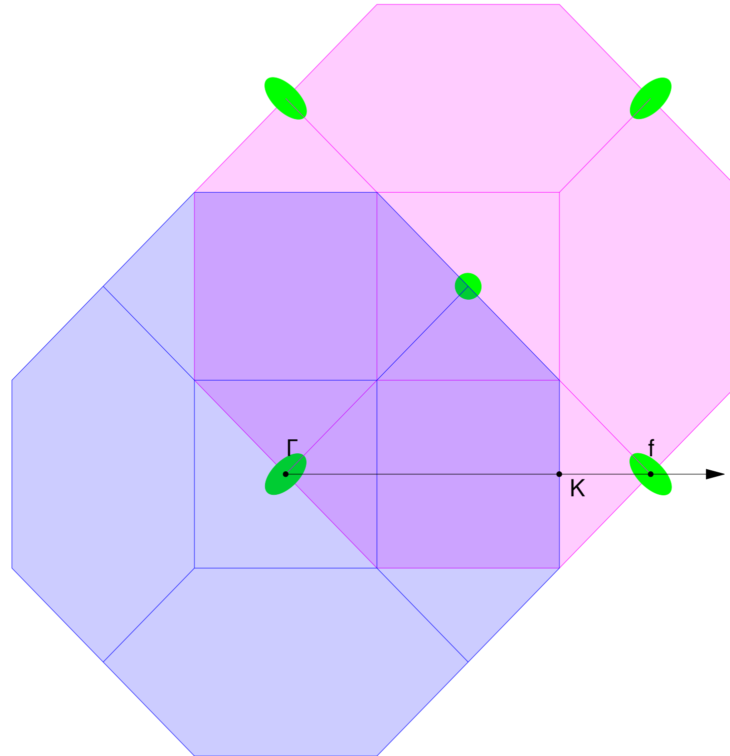

Figure 8.7: 2D projection of the electron (pink) and phonon (blue) BZ of cBN with conduction band minima indicated by the green ellipsoids. The arrow indicates the path of an electron scattering through a g-type Umklapp process.

8.2.3 Optical Deformation Potential

Like Si and diamond, there are six equivalent conduction band minimum valleys, however, unlike Si and diamond, these equivalent valleys are centred exactly on the X symmetry point. This increased symmetry has consequences for the equivalent valley scattering as described in the following sections. As with diamond, the inclusion of the secondary valley requires a deformation potential for the transition. In all cases, the optical deformation potential is found using equation 4.17 and taking the momentum vector, **k**, to be at the initial valley minimum; and the phonon vector, **q**, to be a line that goes from the initial valley minimum to the final valley minimum. Figures 8.7 and 8.8 show how the optical f- and g-type scattering deformation potentials were calculated for the first conduction band of diamond. In these figures, the pink region shows the 2D projection of the BZ for the electrons, with the first conduction band valley indicated by the green ellipsoids centred at the X symmetry point. To find the phonon wavevector that would transfer an electron from the initial conduction band minimum to an equivalent valley, the first BZ for the phonons is overlaid in blue with

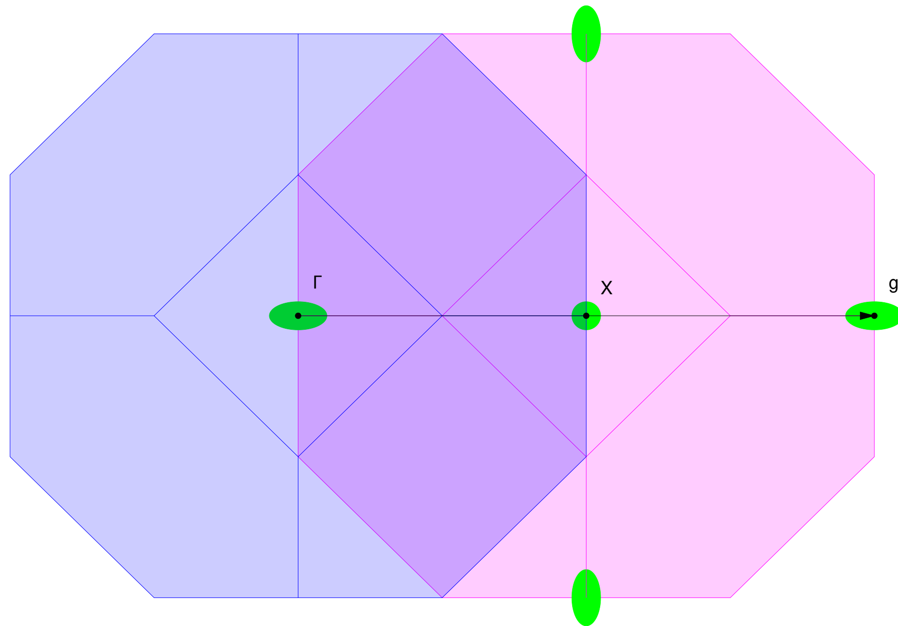

Figure 8.8: 2D projection of the electron (pink) and phonon (blue) BZ of cBN with conduction band minima indicated by the green ellipsoids. The arrow indicates the path of an electron scattering through a g-type Umklapp process.

the Γ point positioned at the initial conduction band minimum. The arrow then indicates a path through these combined BZ along which the electron phonon coupling matrix can be calculated, with the labels K and X indicating the high symmetry point on the surface of the phonon BZ that the path intersects. The deformation potential is then calculated at the point where the path intersects the new conduction band minimum labelled f and g for the f- and g-type scattering respectively. For f-type scattering, this moves the electron into an equivalent perpendicular valley within the first BZ, however, unlike Si and diamond, g-type scattering in cBN does not occurs via an Umklapp process and so the electron scatters to a parallel valley on the opposite side of the first BZ.

By calculating the electron-phonon coupling matrix for an electron with a wavevector at the conduction band minimum interacting with a phonon with a wavevector such that the electron is transferred to a perpendicular valley shows that only the LO phonon mode has significant coupling, indicating that this is the only mode that mediate f-type scattering. The deformation potential for the LO phonon mode was found to be 20.6eV/Å with a corresponding phonon energy of 0.145eV. This deformation potential is double what is used in references [75, 194–196] and the phonon energy is greater than the values of around 0.130eV given in references [36, 146].

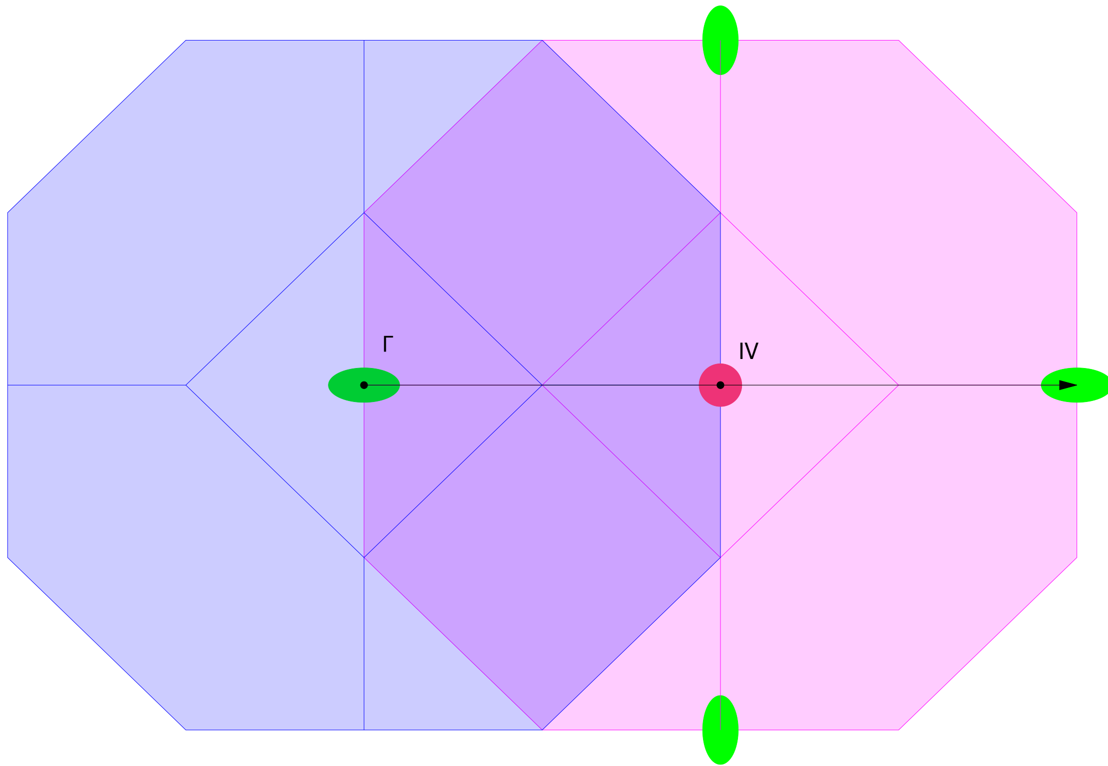

Figure 8.9

Similarly, the g-type scattering deformation potential was found by calculating the electron-phonon coupling matrix for an electron with a wavevector at the conduction band minimum interacting with a phonon with a wavevector such that the electron is transferred to a parallel valley. However, due to the symmetry of the system, the electron phonon coupling matrix terms for all phonon modes goes to 0 at the secondary valley, indicating that there is insignificant g-type scattering in cBN.

Figure 8.9 shows how the optical intervalley scattering deformation potentials were calculated for scattering between the first and second conduction band valleys. The pink region shows the 2D projection of the first BZ for the electron state. The second conduction band valley is indicated by the magenta circle at the Γ point in the centre of the BZ. The phonon vector, **q**, is then indicated by the blue region, which shows the 2D projection of the first BZ for the phonons with the Γ point centred on the conduction band minimum. The arrow then indicates the path taken along which the electron phonon coupling matrix was calculated. Where this line intersects the Γ-valley, IV, is then where the value for the deformation potential was taken. Similar to diamond, only the longitudinal optical phonon mode has a negligible contribution to the scattering process. Using equations 4.23 and 4.24, the effec-

tive deformation potential was found to be $D^*_{X\Gamma} = 16.9$eV/Å , with a corresponding effective phonon energy found to be $\hbar\omega^*_{X\Gamma} = 0.117$eV.

These deformation potentials and phonon energies are once again in disagreement with what is given in references [36, 75, 194–196] where the intervalley deformation potential is set to be 10eV/Å with an associated energy of 0.130eV.

8.3 MC Simulation

In the previous sections, the results for the numerical DOS and deformation potentials were presented for cBN, the following sections present how these are used in the simulation of electron transport in cBN.

8.3.1 Parameters

Table 8.1 details the parameters used in the MC simulation for cBN. The mass density, static dielectric constant, high frequency dielectric constant, piezoelectric constant, sound velocities and intervalley separations were taken from literature [36, 75, 194–196]. The calculation of the effective masses, non-parabolicity constants, deformation potentials and associated phonon energies are detailed in the previous sections of this chapter.

8.3.2 Scattering Rates

Figures 8.10 to 8.12 show the various scattering rates used in the MC simulation of cBN using the parameters presented in table 8.1. In all figures, solid lines indicate where analytic approximations have been used and dashed lines indicate where the numerical DOS has been employed in the scattering rate. Figures 8.10 and 8.11 show the low and high energy ranges for the lowest conduction band valley, and figure 8.12 shows the scattering rate for the Γ-valley. The acoustic phonon scattering is given by the magenta line, the f-type equivalent valley NPOP scattering is given by the dark-blue line, charged impurity scattering is given by the orange line, piezoelectric scattering is given by the cyan line and POP absorption and emission scattering are given by the olive and green lines, respectively.

The figures also show the intervalley scattering rate when the intervalley separations is

Parameter	Symbol	Value
Mass Density (kg/m^3)	ρ	3450
Static Dielectric Constant (ϵ_0)	ϵ_s	7.1
High frequency dielectric constant (ϵ_0)	ϵ_∞	4.46
Piezoelectric constant (Ccm^{-2})	e_{14}	3×10^{-5}
Longitudinal Sound Velocity (m/s)	v_l	15.4×10^3
Transverse Sound Velocity (m/s)	v_t	11.8×10^3
X-Valley Longitudinal Effective Mass (m_e)	m_{Xl}	0.92
X-Valley Transverse Effective Mass (m_e)	m_{Xt}	0.30
X-Valley Non-Parabolicity Constant (eV^{-1})	α_X	0.084
Γ-Valley Effective Mass (m_e)	m_Γ	0.41
Γ-Valley Non-Parabolicity Constant (eV^{-1})	α_Γ	0.29
Acoustic Deformation Potential (eV)	Ξ_{ADP}	10.6
Optical Deformation Potentials (eV/Å)	D_O	20.6
Optical Phonon Energies (eV)	$\hbar\omega_O$	0.145
X-Γ Intervalley Deformation Potential (eV/Å)	D^*_{iv}	16.9
X-Γ Intervalley Phonon Energy (eV)	$\hbar\omega^*_{iv}$	0.117
X-Γ Valley Separation (eV)	$E_{X\Gamma}$	2.1-3.9
Charged Impurity Concentration (m^{-3})	n_0	10^{23}

Table 8.1: Parameters for MC simulation of cBN.

2.5eV. This value of intervalley separation was chosen due to its similarity to the value used in [75] and because the intervalley separation was found to have little impact on the simulated electron transport. Appendix E shows the scattering rates and simulation results for a range of intervalley energy separation. The intervalley scattering rate between $X - \Gamma$ in figures 8.11 and 8.12 is shown by the light-blue line. Unlike diamond and Si, cBN is a polar material and so piezoelectric and POP scattering are present. Although piezoelectric scattering and

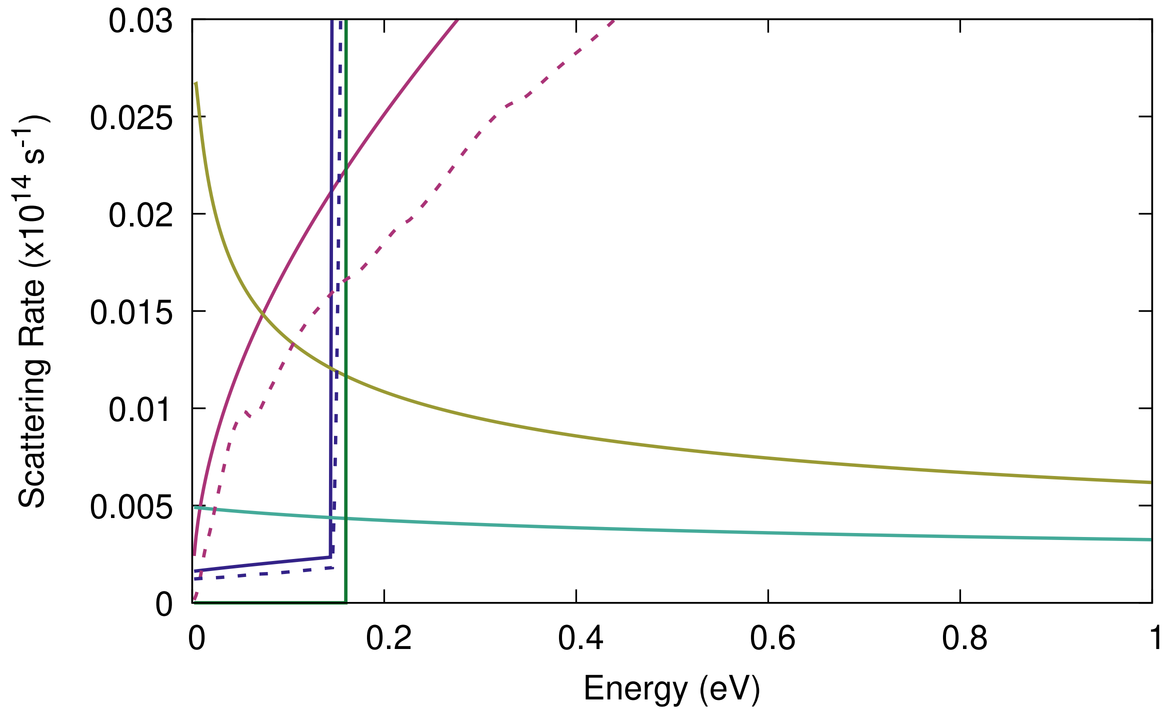

Figure 8.10: Comparison of the X-valley scattering rates calculated using analytic (solid) and numerical (dashed) DOS for cBN at 300K at electron energies below 1eV. With NPOP scattering (blue), ADP scattering (magenta), Piezoelectric scattering (cyan), and POP emission and absorption scattering (green and olive). The total scattering rate is given in black. Energy scale relative to the conduction band minimum.

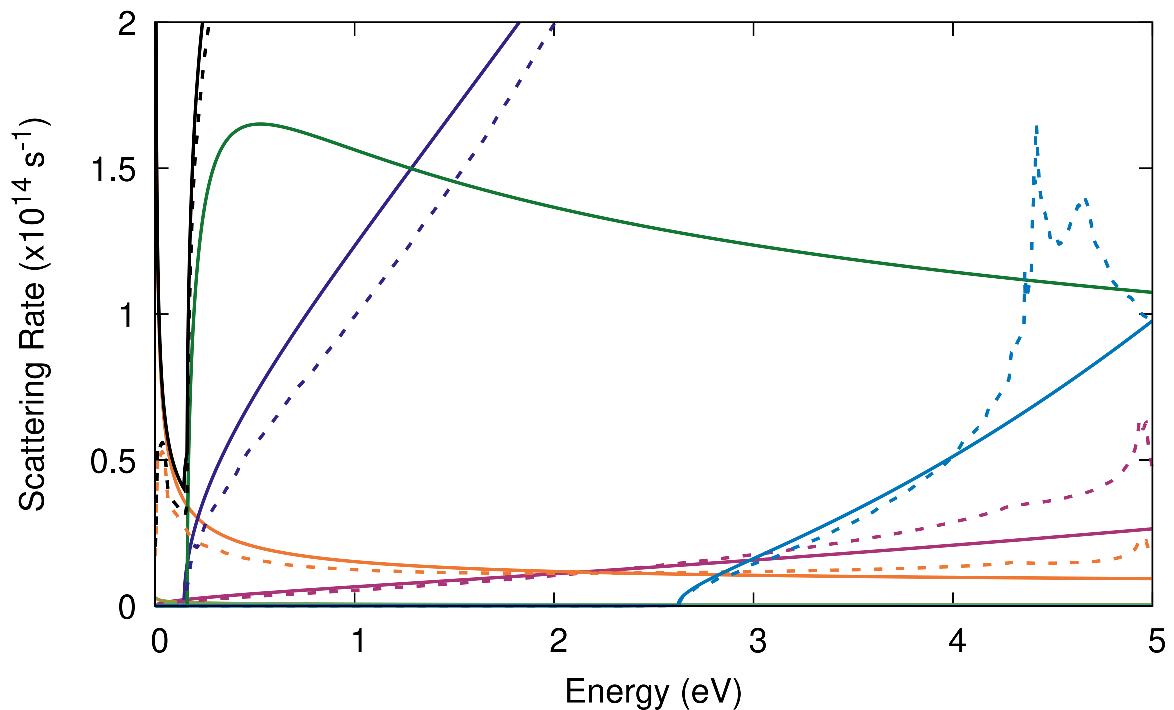

Figure 8.11: Comparison of the X-valley scattering rates calculated using analytic (solid) and numerical (dashed) DOS for cBN at 300K at electron energies below 5eV. With Charged Impurity scattering (orange), NPOP scattering (blue), ADP scattering (magenta), POP emission scattering (green), and $X - \Gamma$ intervalley scattering in light-blue. The total scattering rate is given in black. Energy scale relative to the conduction band minimum.

POP absorption have a negligible contribution to the overall scattering rate, as seen in figure 8.10; POP emission quickly becomes the dominant scattering rate once the electrons have the required energy to take part in this form of scattering. Figure 8.11 shows that POP emission scattering remains the dominant scattering technique up to roughly 1.25eV. As it is the dominant scattering mechanism and the analytic form of POP emission scattering is used in all simulations of cBN, the simulation of cBN using analytic DOS and numerical DOS will show similar trends. As with diamond and Si, there is good agreement between the scattering rates using the analytic and numerical DOS at lower energies. Also, similar to diamond and Si, the analytic DOS rises faster than the numerical DOS which means that the overall scattering rate will be lower, as such, the average velocity is expected to be higher in cBN simulations using the numerical DOS, as seen in diamond and Si. Beyond 1.25eV, the equivalent valley scattering begins to dominate, however as seen in the figures 6.8 and 7.13, showing the average velocity for the MC simulation of Si and diamond, this difference in the DOS has little effect on the average velocity at higher field strengths and so it is expected that the simulations using the numerical and analytic DOS will once again converge on the same saturation velocity.

These scattering rates can then be compared to what is seen in the literature for cBN as the work of Zhu *et al.* [146] presents the scattering rates of cBN calculated directly from DFPT in a method similar to the one presented here for the deformation potential. The NPOP and POP scattering rates presented here compare well with the corresponding scattering rates presented in reference [146], however the acoustic phonon scattering rate shown in reference [146] would suggest an acoustic deformation potential roughly 3 times as large as the one presented here and given in references [200, 194–196].

Similar to what is seen in diamond, figure 8.12 shows that in the Γ-valley the dominant scattering mechanism is the intervalley scattering that scatters the electron back to the conduction band minimum valley and as such the population of the secondary valleys is expected to stay comparatively low. Figure 8.12 shows large disagreement between the scattering rate calculated using analytic and numerical DOS for the intervalley scattering rate, this is because this is the probability to scatter back to the conduction band minimum from the secondary and so the energy range is shifted by the difference in the minima of the valleys. As such, the lower energy range of the DOS where the analytic and numerical methods are in better

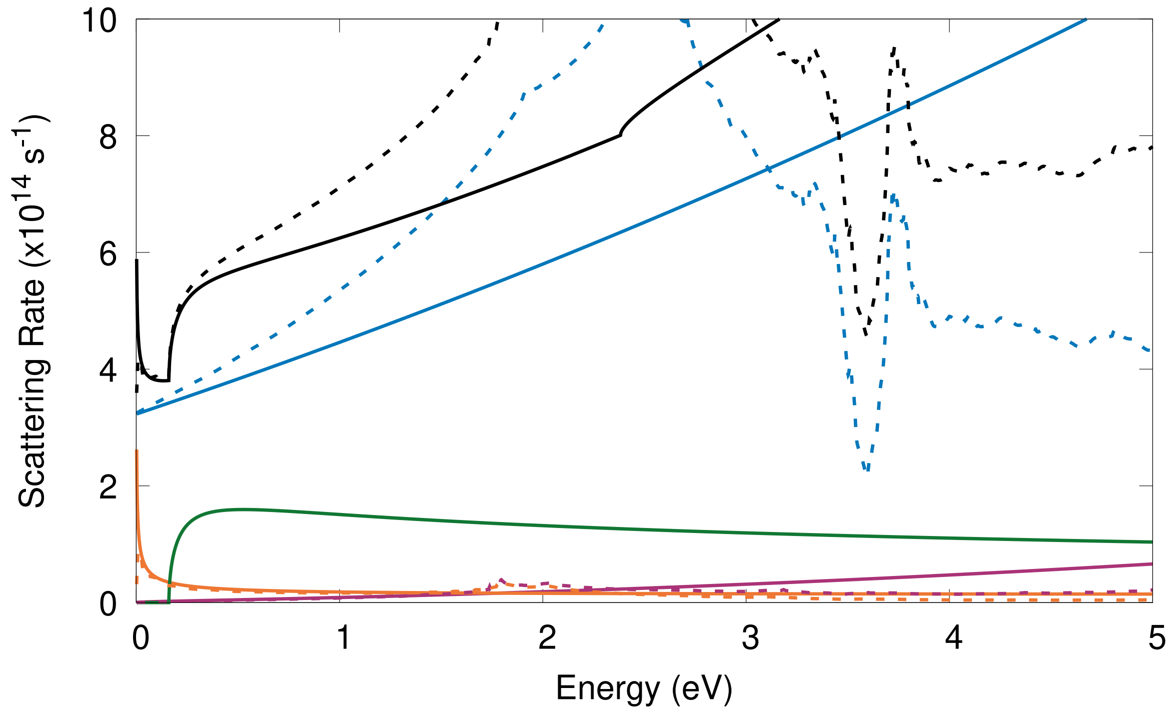

Figure 8.12: Comparison of the Γ-valley scattering rates calculated using analytic (solid) and numerical (dashed) DOS for cBN at 300K. With Charged Impurity scattering (orange), ADP scattering (magenta), POP emission scattering (green) and $\Gamma - X$ intervalley scattering in light-blue. The total scattering rate is given in black. Energy scale relative to the secondary valley minimum.

agreement is cut off and only the high energy range is shown.

8.3.3 Simulation Results

Figure 8.13 shows the steady-state velocity-field characteristics produced by MC simulation for cBN using parameters from Siddiqua *et al.* [75] with analytic DOS (olive-green line) and parameters presented in table 8.1 as calculated via methods presented in section 4.2 with analytic (light-blue line) and numerical (dark-blue line) DOS. The black points show data taken from Zhu *et al.* [146] where FBMC simulations were performed on cBN with scattering rates calculated directly from DFPT. All simulations were performed at 300K with the electric field parallel with the x-axis.

Similar to Si and diamond, at lower fields the simulation results using the numerical DOS have a higher average velocity than the corresponding simulations using analytic DOS. This is thought to be because of the difference in the total scattering rate due to the use of numerical DOS, this means that the electrons in simulations using the numerical DOS experience fewer scattering events and so can achieve higher average velocities. However, as the fields increase, the influence of POP and NPOP scattering increases and so all simulations converge on

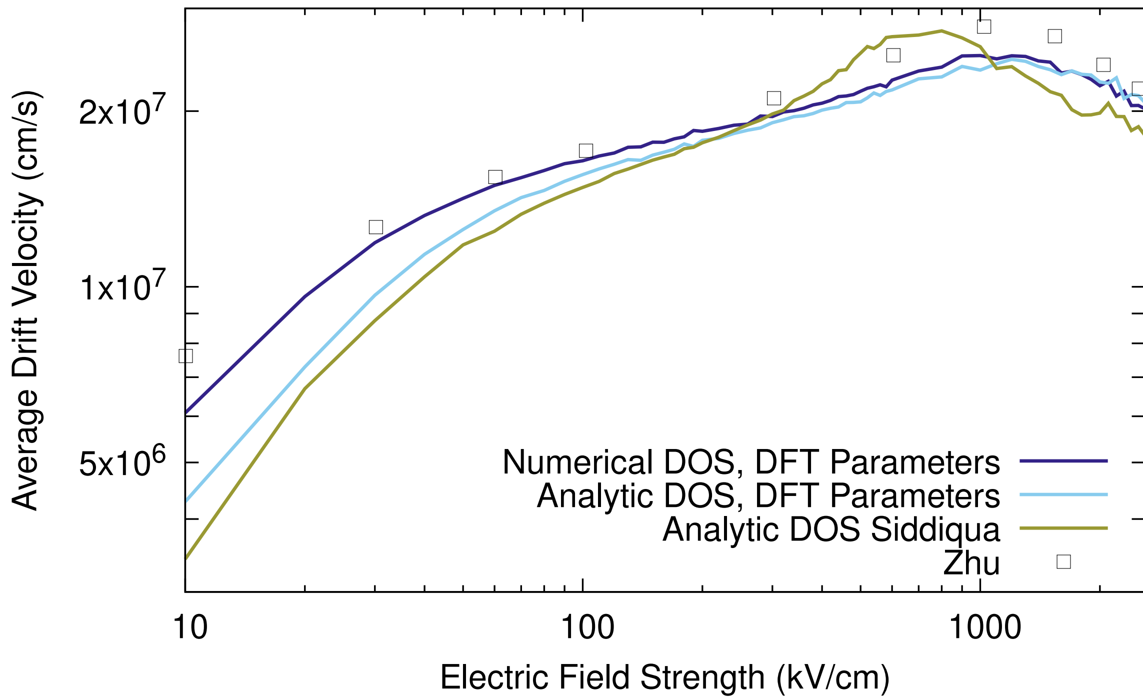

Figure 8.13: Velocity-field data for cBN. Solid olive-green line shows simulation results using analytic DOS and parameters from Siddiqua *et al.* [75]. The light-blue and dark-blue lines show the simulation results using parameters calculated here with analytic and numerical DOS, respectively. Open squares show data taken from FBMC simulation performed by Zhu *et al.* [146].

the same average velocity. The simulations employing the parameters from Siddiqua *et al.* [75] show an even lower average velocity in the low fields, however it rises much faster with increasing field before peaking at around 700kV/cm and decreasing again. Comparing this simulation data to the data presented in reference [75], the average velocity rises as shown here, however they do not observe the decrease in velocity at high fields observed here. Their simulations results show the average velocity continuing to rise before saturating at 4.3×10^7cm/s, exceeding the saturation velocity of all other III-V nitride semiconductors. The source of this difference could be due to the model of the bands employed as Siddiqua *et al.* employ parabolic bands and as stated, the inclusion of non-parabolicity reduces the peak of the average velocity and results in a decrease at higher fields. This difference could also be due to the inclusion of scattering methods that have not been employed here as in the work of Siddiqua *et al.* impact ionisation scattering is also employed. In impact ionisation scattering the high energy electrons in the conduction band interact with bound electrons in the valence band and promote them to the conduction band. However, the work of Zhu *et al.* [146] also includes impact ionisation scattering and the points show good agreement with the MC simulations using the parameters presented here and employing the numerical DOS in the

scattering mechanisms. Although it rises to a higher peak average velocity, the data from Zhu *et al.* also shows the same downward trend and converges onto simulation results calculated here. This suggests that the difference in simulations results using parameters presented here and from Siddiqua *et al.* is due to the difference in the shape of the bands.

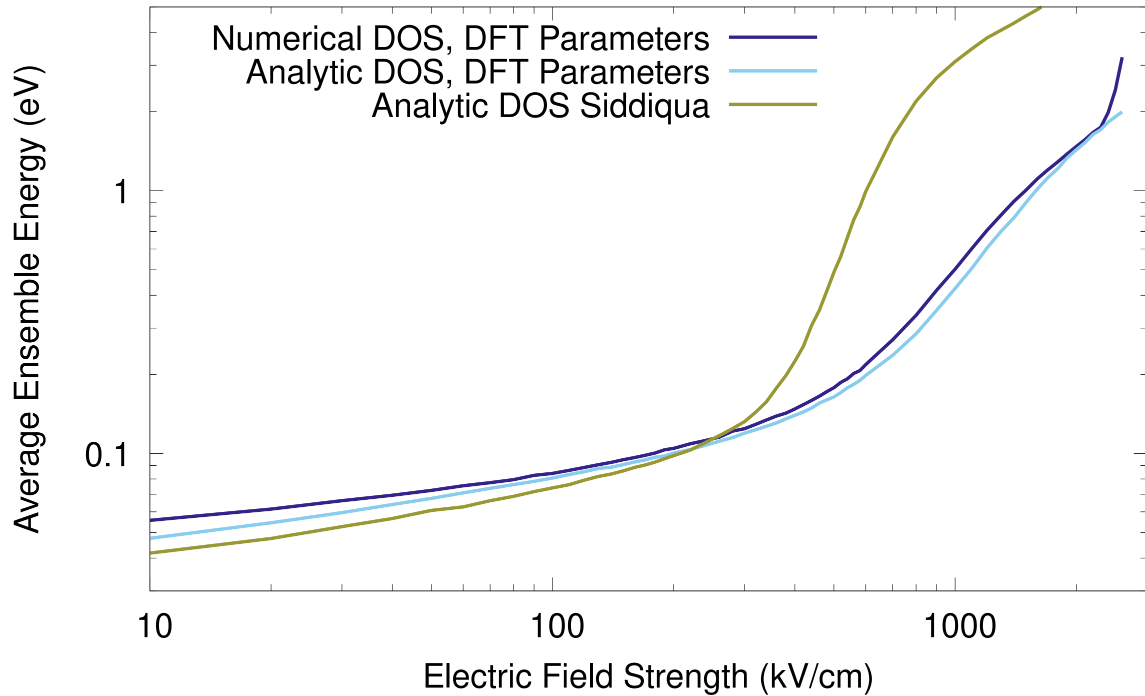

Figure 8.14: Energy-field characteristics for cBN. Solid olive-green line shows simulation results using analytic DOS and parameters from Siddiqua *et al.* [75]. The light-blue and dark-blue lines show the simulation results using parameters calculated here with analytic and numerical DOS, respectively.

This is further supported by figures 8.14 and 8.15. These figures show the energy-field and X-valley occupancy-field characteristics produced by MC simulation for cBN using parameters from Siddiqua *et al.* [75] with analytic DOS (olive green line) and parameters presented in table 8.1 as calculated via methods presented in section 4.2 with analytic (light blue line) and numerical (dark-blue line) DOS. The plots showing the energy-field and occupancy-field characteristic for the MC simulations using the parameters from Siddiqua *et al.* show an increase in the average energy and corresponding decrease in the X valley occupancy at a much lower field. This supports the idea that the difference in the velocity-field characteristic is due to the shape of the analytic bands employed as Siddiqua *et al.* assumes that the secondary and tertiary valleys have effective masses of $0.99m_e$. As this is roughly two and a half times larger than what was calculated via DFT, equation 1.18 shows that this would result in a DOS that is roughly 4 times as large, meaning that there are more states for the electrons

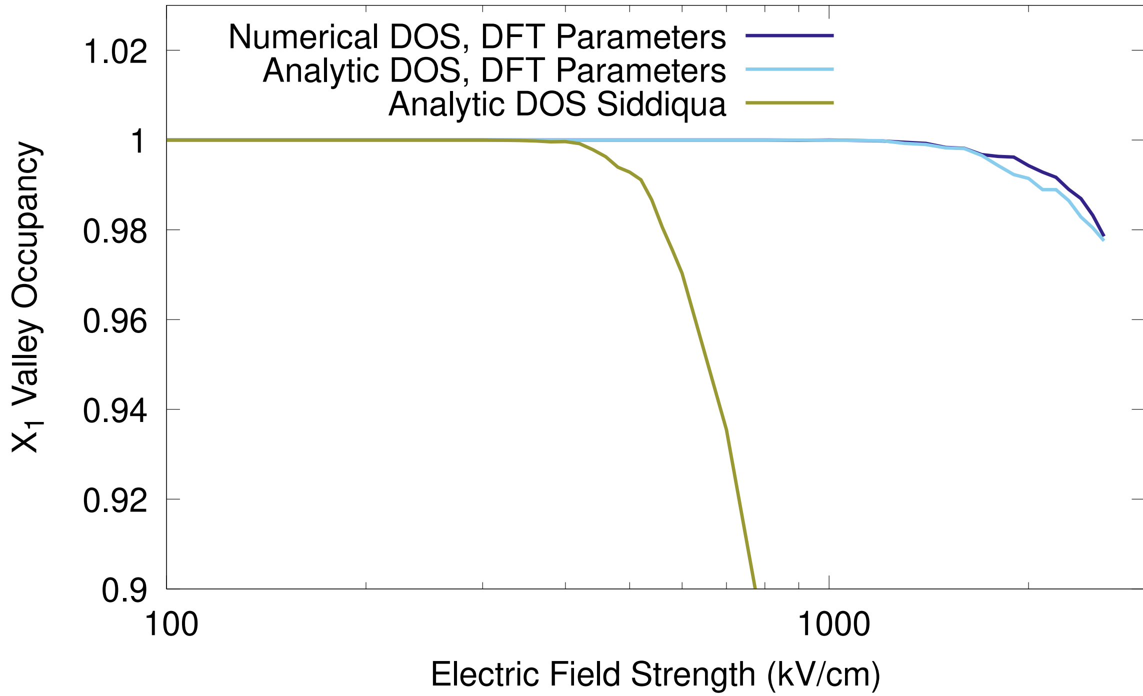

Figure 8.15: Occupancy-field characteristics for cBN. Solid olive-green line shows simulation results using analytic DOS and parameters from Siddiqua *et al.* [75]. The light-blue and dark-blue lines show the simulation results using parameters calculated here with analytic and numerical DOS, respectively.

to scatter to and so increasing the probability of scattering to the upper valley and reducing the probability of scattering back to the initial valley. Finally, it must be noted that similar to diamond, the MC simulations of cBN using the numerical DOS at the highest fields show a sudden increase. Once again this is thought to be due to the mismatch in the band structure approximations used in the drift and scattering steps of the simulation. As the analytic bands have no maximum, the electrons are free to accelerate to unphysical energies and won't be damped by the scattering as the numerical DOS reaches a maximum and decreases.

8.4 Summary

In this chapter, the methods detailed in chapter 4 have been applied to cBN. Section 8.1 presented the numerically calculated DOS for cBN found via tetrahedral interpolation from AIMPRO. This DOS was found to agree with the DOS calculated via Gaussian broadening in AIMPRO, found with a broadening width of $\sigma = 0.01$ eV.. The conduction band minimum as well as the secondary and tertiary valleys were also found using a modified steepest descent method. The positions of the conduction band minimum and the secondary valley were found

to agree with what was used previously in the literature, however the tertiary valley did not. It was found that the tertiary valley had a negligible effect on the simulation results due to the lack of scattering events to move electrons into the valley and the predominance of scattering events to move the electron back out again. Therefore, it was not included in the simulation so as to reduce the computational cost. From the band structure and DOS, the effective mass and non-parabolicity constant were then be calculated for use in the MC simulation.

In section 8.2, the values of the acoustic and optical deformation potentials were found and compared to what has been presented previously. The acoustic deformation potential compared well, however the optical deformation potential was found to be double what has been used previously. However, this optical deformation potential did produce a NPOP scattering rate that agreed with other work that calculated the scattering rates from first principles. Intervalley scattering rates were also found that were greater than what has been used previously.

The numerical DOS and scattering parameters were then brought together and used in a MC simulation of the electrons in cBN. A range of $X - \Gamma$ energy separations were used but due to the small DOS in the secondary valley, these were found to have very little impact on the simulation results, as shown in appendix E. There was excellent agreement between the velocity-field results found using the numerically calculated DOS and previous results using a FBMC simulator. This suggests that cBN exhibits a negative differential resistance, like other III-V semiconductors, however this is not due to the difference in the effective mass in higher bands, as all the bands are seen to have similar effective masses and the NDR is observed at fields where there is negligible intervalley scattering. Although the effective mass for the X-valley is non-isotropic, the drift step treats the bands as being isotropic with an effective mass found as the geometric mean of the longitudinal and transverse effective masses. The NDR could then be due to the interaction of the electrons with the POP scattering mechanism as the bump and peak in the average drift velocity correspond to energies where POP scattering initially turns on and where it reaches its peak, respectively.

Finally, as in diamond it was found that in the simulations using the numerical DOS there was a sudden increase in the average energy at very high fields. This is again thought to be due to the disagreement between the use of analytic bands in the drift step and numerical DOS in the scattering step. As there is no maximum energy in the analytic bands, there is nothing

other than scattering events stopping the electrons from being accelerated to higher energies. However, as the numerical DOS reaches a peak and then decreases, at higher energies there are reduced scattering rates which means that the electrons that reach really high energies may experience fewer scattering events.

These methods as applied to cBN give a deeper understanding of the charge transport, however as stated previously, there is a limit to what can be gleaned due to the mismatch in the approximations at high energies. This is discussed further in chapter 9.

Chapter 9

Conclusions and Further Work

Throughout this thesis, methods have been presented to better model the transport properties of new and emerging materials that lack experimental results or a consensus on material parameters. This is an essential step in the search for more efficient and hardy high power electronics required as the world moves to be ever more reliant on the power sector. UWBG materials prove to be indispensable due to their promise of smaller devices with fewer switching and conduction losses as well as their high breakdown voltage and resilience to harsh environments. The methods presented in this thesis focussed on improving the scattering step of a MC simulation by using the full band structure to calculate the DOS numerically and calculating scattering parameters from first principles. To demonstrate these methods, they were applied to Si, a material with a wealth of experimental results and material parameters; diamond, a material with similar properties to Si and a handful of experimental results with a range of material parameters; and cBN, a material with some similarities to diamond but with a complete lack of experimental results. In this chapter, the results of all three materials will be brought together and a conclusion drawn about the methods applied. Following this, suggestions for how this work could be extended will be given.

9.1 Density of States Calculation

As detailed in sections 6.2, 7.1 and 8.1, the band structure for Si, diamond and cBN were calculated via AIMPRO [13] and this was then used to generate a non-uniform tetrahedral grid from which the DOS could be interpolated, following the methods given in section 4.1.

From the band structure and the DOS, the effective mass and non-parbolicity constant were derived which were then used to produce an analytic DOS. In all three materials, there was good agreement between the effective masses calculated and what is seen in the literature and the non-parabolicity constants found in each case lead to good agreement between the numerical and analytic DOS. One thing that was noted in each case was that near the valley minima where the analytic and numerical DOS were expected to be in the best agreement, there were oscillations present in the numerical DOS that meant it deviated from the analytic DOS. This may have been due to the way the numerical DOS is calculated as it depends on the area of intersection of the equivalent energy surface as it passes through the tetrahedra. Near the valley minima, as the energy approaches 0, there are fewer tetrahedra and so fewer planes that approximate the equivalent energy surface. As there are fewer planes, this could mean that errors in the interpolative method have more of an impact. This error could be improved by tightening the tolerance of the grid refinement method close to points of interest, such as the conduction band minimum and the high symmetry points.

Another disagreement between the analytic and numerical DOS was the rate at which they grew near the minimum. In Si, the numerical and analytic DOS tracked each other fairly well but in diamond and cBN, the analytic DOS grew much faster at lower energies. This slightly lower DOS then resulted in a lower scattering rate in the scattering methods to which it was applied, which in turn resulted in reduced scattering and a higher average velocity at lower fields. This difference lead to better agreement between the MC simulations using numerical DOS and the experimental results in diamond, and the MC simulations using numerical DOS and the results from a FBMC simulation in cBN. This therefore shows that using the numerical DOS does introduce extra information about the materials even at lower energies, improving the predictive abilities of the MC simulation.

9.2 Deformation Potentials Calculations

As detailed in sections 6.3, 7.2 and 8.2, the deformation potentials were calculated via Quantum Espresso [148, 149] and the extension EPW [150] using the electron-phonon coupling matrix, following the methods of section 4.2.

The LA and TA deformation potentials were calculated for a range of angles from which

the angular average acoustic deformation potential could be found by fitting equations 4.18a and 4.18b. This method led to a prediction of the deformation potential in Si which was in excellent agreement with what has been seen previously, a deformation potential for diamond greater than what has been presented in the literature, and a deformation potential for cBN which supports the reasonable estimate employed by Siddiqua et al. [75]. The discrepancy in the deformation potential calculated for diamond, and the large range of values seen in the literature is thought to be due to their use as free parameters to fit the simulation output to experimental results. This is also impacted by the choice of the effective mass used in the acoustic phonon scattering rate and may also be impacted through the choice of the other parameters in equation **??**. As such, this range of values observed in diamond but not in Si could be because Si has been extensively studied as a semiconductor for decades, and so the other scattering parameters are better characterised giving less freedom to the deformation potential. Due to the agreement between the deformation potential calculated for Si and the values from literature, and the fact that deformation potential for diamond is just above the range of values reported; it is thought that the deformation potential calculated for cBN is a suitable value for use in MC simulation. Also, due to the fact that the DOS effective mass calculated here was in good agreement with what was used in references [75, 146], the acoustic phonon scattering rate will have a similar effect on modelling of electrons when used in a MC simulation. The source of the large spread of values in the angular dependent deformation potential in cBN may be due to the anisotropic band structure in cBN at the X symmetry point, where the conduction band minimum is located; however, it is not known what impact this azimuthal anisotropy has on the deformation potentials reported here for cBN.

The equivalent valley deformation potentials were found using equation 4.17 and finding the electron-phonon coupling matrix for an electron with wavevector at the band minima and a phonon with momentum that would scatter the electron to the valley minimum of an equivalent parallel or perpendicular valley. In the cases of Si and diamond, this produced equivalent valley scattering deformation potentials and corresponding phonon energies that were in good agreement with what had been seen previously (tables 6.2 and 7.2, respectively), including indicating which phonon modes mediated the scattering events. For cBN this method suggested that for the equivalent valley scattering only scattering to perpendicular equivalent

valleys was allowed and scattering to parallel valleys was forbidden due to symmetry. These methods were also employed to calculate the intervalley scattering using similar methods but considering the initial and final valleys to no longer be equivalent. Although deformation potentials and the corresponding phonon energies were calculated, the MC simulation results suggest that intervalley scattering is not a significant scattering mechanism in these materials and so it is hard to judge whether these deformation potentials are appropriate.

9.3 MC Simulations

Sections 6.4, 7.3 and 8.3 then presented the MC simulations using the parameters calculated from DFT. In all three cases, there was good agreement between scattering rates using numerical and analytic DOS, which was expected as there was good agreement between the numerical and analytic DOS. As stated previously, due to the difference in how the DOS grew in diamond and cBN, the scattering rates that relied on the numerical DOS subsequently grew slower than the corresponding scattering rate that used analytic DOS. However, this appears not to have been a problem with the model as the simulation results for diamond using the numerical DOS in the scattering had better agreement with the experimental results than the simulations using the analytic DOS. Similarly, in cBN the simulations that used the numerical DOS in the scattering rates had better agreement with the FBMC simulation of Zhu *et al.* [146] than the corresponding simulations using analytic DOS. This clearly indicates that including the numerical DOS and the scattering parameters calculated from first principles improves the accuracy of the MC simulation. However, in both diamond and cBN, at the highest fields there is a sudden increase in the average electron energy in the simulations using the numerical DOS. As stated, this is thought to be because of the different band structure schemes being used in the drift and scattering steps of the MC simulation. As the drift steps continue to use the analytic band structure in all simulations, during the drift step there is no limit on the upper energy that electrons can reach. However, the numerical DOS reaches a peak and then decreases, resulting in a decrease in the scattering rates. This means that once electrons get past a certain energy, they will experience ever fewer scattering events and so their energies will rapidly increase.

To conclude, first principles calculations have successfully been employed here to calculate

parameters for materials that have very few or no experimental results. These have then been used in MC simulation to accurately model Si, diamond and cBN as a first step in better understanding diamond and cBN as UWBG materials for applications in high power devices.

9.4 Sensitivity Analysis

The scattering rates presented in chapters 6, 7 and 8 all relied upon multiple parameters working together and so it is important to consider the sensitivity of these methods to the inputs and thus the sensitivity of the simulation results. As stated in chapter 6, all the parameters calculated numerically rely on the choice of pseudopotential and exchange-correlation functionals employed in the DFT calculation as these would affect the optimised lattice constant and band structure which in turn would impact the deformation potential and effective masses calculated. As further discussed in chapter 7, the non-polar phonon scattering rates depend on the square of the deformation potential and so this single parameter has large control over these scattering mechanisms, whereas the scattering rate depends on the effective mass to the power of 1.5. The effective masses were also in excellent agreement with what was seen in the literature for all three materials whereas the deformation potentials showed large ranges in the calculated and presented values. Therefore, the greatest improvement to the simulation is likely to be through the improvement of the calculation of the deformation potential through a better explanation of the source of the large ranges in the calculated value as seen in figures 6.4 and 8.6, and why this is absent in figure 7.6.

9.5 Further Work

As mentioned throughout the results, there are many areas in which this work can be expanded on.

Firstly, the tetrahedral interpolation methods could be improved to produce more accurate DOS. In the work of Jungemann *et al.* [21, 22, 96], the difference between the interpolated energy and the numerically calculated energy is found at 5 points along the edge being considered, and the edge is then split at the point that differs most from the band structure energy. Here, the difference in energy is only considered at the centre of an edge, however, as the

linearly interpolated energy is compared to an energy calculated using cubic splines and not the DFT band structure, a method could easily be implemented to find the point at which the two methods differ the most and split the edge there.

The interpolation of the DOS could also be improved by including more tetrahedra near the conduction band minimum and high symmetry points. This could be added by making the length and energy tolerance conditions scale with the proximity to these points so that the tolerances are smaller in areas of interest.

Another avenue is to extend the use of the tetrahedral grid to the MC drift step, giving a FBMC simulator. This would then mean that there wouldn't be disagreements in what states are available to the electrons at higher energies, giving more accurate simulation results. To better model materials at higher energies, impact ionisation scattering should also be implemented. This may also mean that the methods for calculating the electron free flight time, as detailed in section 2.2.2, would need to be updated. The free flight time currently depends on a single fixed value of the self scattering rate so that equation 2.7 can be calculated analytically. However, if there is a very large self scattering rate but also areas of low total scattering, for example between 0eV and 1eV in figure 7.11, then the vast majority of scattering events experienced by electrons in this energy range will be self-scattering. These have no impact on momentum of the electron, resulting in inflated average velocities. Also, as the time step is the inverse of the self-scattering rate, a large self-scattering rate leads to longer simulation times. The paper by Yorston [201] compares several different methods for the calculation of the free-flight time in MC simulations that could be implemented. However, some of these methods require analytic forms for the scattering rate and so may not be suitable for a FBMC simulator.

Finally, although the intervalley scattering rates were calculated for Si, diamond and cBN; the shapes of the upper valleys and the strength of the scattering meant that the vast majority of the electrons remained in the lowest valley. These methods could be explored further by looking at materials that have significant upper valley population during MC simulation to see if the deformation potentials calculated are correct. A further exploration of the angular and azimuthal dependence of the acoustic deformation potentials could also be done to better understand why there is spread in the values, in particular why these are present in Si and cBN

but not diamond.

Appendix A

Calculation of the Coefficients of Cubic Splines

The quantities necessary to define a cubic spline are the position vectors of the vertices on either end of the edge, $\underline{k}_0$ & $\underline{k}_1$; the band structure energies at these two points, E_0 & E_1; and the gradient of the energy at these points, $\frac{\partial E_0}{\partial \underline{k}}$ & $\frac{\partial E_1}{\partial \underline{k}}$.

The four vectors are transformed from three dimensions to just one dimension with variable r pointing along the edge. The vertices on either end of the edge are then denoted by r_0 & r_1, and the gradients $\frac{dE(r_0)}{dr} = m_0$ & $\frac{dE(r_1)}{dr} = m_1$. A third order polynomial is then defined between the two vertices,

$$P(r) = ar^3 + br^2 + cr + d, \tag{A.1}$$

with first derivative

$$P'(r) = 3ar^2 + 2br + c, \tag{A.2}$$

constrained by $P(r_0) = E_0$, $P(r_1) = E_1$, $P'(r_0) = m_0$ and $P'(r_1) = m_1$. Applying these constraints to equations A.1 and A.2 gives the matrix equation,

$$\begin{pmatrix} r_0^3 & r_0^2 & r_0 & 1 \\ r_1^3 & r_1^2 & r_1 & 1 \\ 3r_0^2 & 2r_0 & 1 & 0 \\ 3r_1^2 & 2r_1 & 1 & 0 \end{pmatrix} \begin{pmatrix} a \\ b \\ c \\ d \end{pmatrix} = \begin{pmatrix} E_0 \\ E_1 \\ m_0 \\ m_1 \end{pmatrix}, \tag{A.3}$$

and so the coefficients can be found by inverting the matrix on the left hand side and left

multiplying by the inversion,

$$\begin{pmatrix} r_0^3 & r_0^2 & r_0 & 1 \\ r_1^3 & r_1^2 & r_1 & 1 \\ 3r_0^2 & 2r_0 & 1 & 0 \\ 3r_1^2 & 2r_1 & 1 & 0 \end{pmatrix}^{-1} \begin{pmatrix} E_0 \\ E_1 \\ m_0 \\ m_1 \end{pmatrix} = \begin{pmatrix} a \\ b \\ c \\ d \end{pmatrix} \tag{A.4}$$

In practice, as the matrix is of the same form every time, Gaussian reduction can be applied to get equations for the four quantities.

$$a = \frac{m_0 + \frac{m_1 - 2(E_1 - E_0)}{r_1 - r_0}}{(r_0 - r_1)^2} \tag{A.5}$$

$$b = \frac{m_1 - m_0}{2(r_1 - r_0)} - \frac{3}{2}a(r_0 + r_1) \tag{A.6}$$

$$c = m_0 - 3r_0^2 a - 2r_0 b \tag{A.7}$$

$$d = E_0 - r_0^3 a - r_0^2 b - r_0 c \tag{A.8}$$

Appendix B

Formulation of Density Of States Equation

The contribution to the density of state from a single tetrahedron is given by

$$g_i^{tet}(E) = \frac{1}{(2\pi)^3} \frac{A_{n,i}(E)}{|\nabla_{\underline{k}} E_{n,i}(\underline{k})|}, \tag{B.1}$$

Where $A_{n,i}(E)$ is the area of intersection of the equivalent energy surface and the ith tetrahedron and $\nabla_{\underline{k}} E_{n,i}(\underline{k})$ is the interpolation gradient. As the interpolation gradient is constant inside given tetrahedron, the equivalent energy surface intersects the tetrahedron as a plane. Figure B.1 shows the three possible ways that this plane can intersect a tetrahedron and shows that the two possible shapes are a triangle, when $E_{n,t(n,i,0)} < E < E_{n,t(n,i,1)}$ and $E_{n,t(n,i,2)} < E < E_{n,t(n,i,3)}$; and a quadrilateral, when $E_{n,t(n,i,1)} < E < E_{n,t(n,i,2)}$. The quadrilateral ($c_{0,2}$, $c_{0,3}$, $c_{1,2}$, $c_{1,3}$) is found in case b by subtracting the triangle ($c_{1,3}$, $c_{1,2}$, $c_{0,1}$) from triangle ($c_{0,3}$, $c_{0,2}$, $c_{0,1}$)

The point of intersection of the equivalent energy surface with energy E and an edge between the vertices $\underline{k}_{n,t(n,i,j)}$ & $\underline{k}_{n,t(n,i,k)}$ is then be found as,

$$\begin{aligned} c_{n,i,j,k}(E) = \underline{k}_{n,t(n,i,j)} + & \frac{E - E_{n,t(n,i,j)}}{\nabla_{\underline{k}} E_n(\underline{k}) \cdot (\underline{k}_{n,t(n,i,k)} - \underline{k}_{n,t(n,i,j)})} \\ & \cdot (\underline{k}_{n,t(n,i,k)} - \underline{k}_{n,t(n,i,j)}) \end{aligned} \tag{B.2}$$

Subtracting one of these intersections from another gives the vector of one edge of the

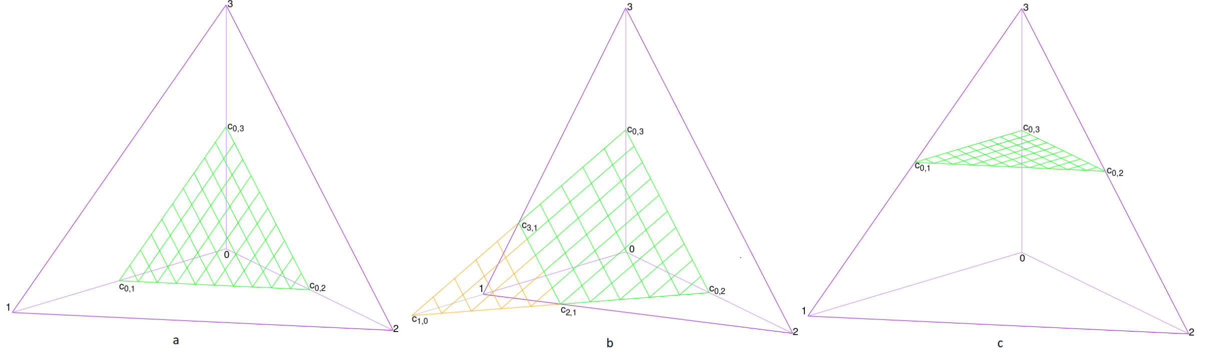

Figure B.1: Intersections of a Plane with a Tetrahedron. Case a: Energy less than that at vertex 1. Case b: Energy between that at vertex 1 and 2. Case c: Energy between that at vertex 2 and 3.

intersecting plane.

$$c_{n,i,j,k}(E) - c_{n,i,j,l}(E) = (E - E_{n,t(n,i,j)}) \left(\frac{\underline{k}_{n,t(n,i,k)} - \underline{k}_{n,t(n,i,j)}}{\nabla_{\underline{k}} E_n(\underline{k}) \cdot (\underline{k}_{n,t(n,i,k)} - \underline{k}_{n,t(n,i,j)})} - \frac{\underline{k}_{n,t(n,i,l)} - \underline{k}_{n,t(n,i,j)}}{\nabla_{\underline{k}} E_n(\underline{k}) \cdot (\underline{k}_{n,t(n,i,l)} - \underline{k}_{n,t(n,i,j)})} \right) \tag{B.3}$$

Using equation 4.2 and the shorthand notation from section 4.1.1, this can be re-written as

$$c_{n,i,j,k}(E) - c_{n,i,j,l}(E) = (E - E_{n,t(n,i,j)}) \left(\frac{\Delta \underline{k}_{k,j}}{\Delta E_{k,j}} - \frac{\Delta \underline{k}_{l,j}}{\Delta E_{l,j}} \right) \tag{B.4}$$

Considering just case a, the area of intersection in equation B.1 is found as,

$$A_{n,i}(E) = \frac{1}{2} \left| (c_{n,i,0,2}(E) - c_{n,i,0,1}(E)) \times (c_{n,i,0,3}(E) - c_{n,i,0,1}(E)) \right| \tag{B.5}$$

$$= \frac{1}{2} (E - E_{n,t(n,i,0)})^2 \left| \left(\frac{\Delta \underline{k}_{2,0}}{\Delta E_{2,0}} - \frac{\Delta \underline{k}_{1,0}}{\Delta E_{1,0}} \right) \times \left(\frac{\Delta \underline{k}_{3,0}}{\Delta E_{3,0}} - \frac{\Delta \underline{k}_{1,0}}{\Delta E_{1,0}} \right) \right| \tag{B.6}$$

$$A_{n,i}(E) = \frac{1}{2}(E - E_{n,t(n,i,0)})^2 \left| \begin{pmatrix} \left(\frac{\Delta \underline{k}_{2,0,y}}{\Delta E_{2,0}} - \frac{\Delta \underline{k}_{1,0,y}}{\Delta E_{1,0}}\right)\left(\frac{\Delta \underline{k}_{3,0,z}}{\Delta E_{3,0}} - \frac{\Delta \underline{k}_{1,0,z}}{\Delta E_{1,0}}\right) - \left(\frac{\Delta \underline{k}_{2,0,z}}{\Delta E_{2,0}} - \frac{\Delta \underline{k}_{1,0,z}}{\Delta E_{1,0}}\right)\left(\frac{\Delta \underline{k}_{3,0,y}}{\Delta E_{3,0}} - \frac{\Delta \underline{k}_{1,0,y}}{\Delta E_{1,0}}\right) \\ \left(\frac{\Delta \underline{k}_{2,0,z}}{\Delta E_{2,0}} - \frac{\Delta \underline{k}_{1,0,z}}{\Delta E_{1,0}}\right)\left(\frac{\Delta \underline{k}_{3,0,x}}{\Delta E_{3,0}} - \frac{\Delta \underline{k}_{1,0,x}}{\Delta E_{1,0}}\right) - \left(\frac{\Delta \underline{k}_{2,0,x}}{\Delta E_{2,0}} - \frac{\Delta \underline{k}_{1,0,x}}{\Delta E_{1,0}}\right)\left(\frac{\Delta \underline{k}_{3,0,z}}{\Delta E_{3,0}} - \frac{\Delta \underline{k}_{1,0,z}}{\Delta E_{1,0}}\right) \\ \left(\frac{\Delta \underline{k}_{2,0,x}}{\Delta E_{2,0}} - \frac{\Delta \underline{k}_{1,0,x}}{\Delta E_{1,0}}\right)\left(\frac{\Delta \underline{k}_{3,0,y}}{\Delta E_{3,0}} - \frac{\Delta \underline{k}_{1,0,y}}{\Delta E_{1,0}}\right) - \left(\frac{\Delta \underline{k}_{2,0,y}}{\Delta E_{2,0}} - \frac{\Delta \underline{k}_{1,0,y}}{\Delta E_{1,0}}\right)\left(\frac{\Delta \underline{k}_{3,0,x}}{\Delta E_{3,0}} - \frac{\Delta \underline{k}_{1,0,x}}{\Delta E_{1,0}}\right) \end{pmatrix} \right| \tag{B.7}$$

$$A_{n,i}(E) = \frac{1}{2}(E - E_{n,t(n,i,0)})^2 \left| \begin{pmatrix} \frac{\Delta \underline{k}_{2,0,y}\Delta \underline{k}_{3,0,z}}{\Delta E_{2,0}\Delta E_{3,0}} - \frac{\Delta \underline{k}_{2,0,y}\Delta \underline{k}_{1,0,z}}{\Delta E_{2,0}\Delta E_{1,0}} - \frac{\Delta \underline{k}_{3,0,z}\Delta \underline{k}_{1,0,y}}{\Delta E_{3,0}\Delta E_{1,0}} - \frac{\Delta \underline{k}_{2,0,z}\Delta \underline{k}_{3,0,y}}{\Delta E_{2,0}\Delta E_{3,0}} + \frac{\Delta \underline{k}_{2,0,z}\Delta \underline{k}_{1,0,y}}{\Delta E_{2,0}\Delta E_{1,0}} + \frac{\Delta \underline{k}_{3,0,y}\Delta \underline{k}_{1,0,z}}{\Delta E_{3,0}\Delta E_{1,0}} \\ \frac{\Delta \underline{k}_{2,0,z}\Delta \underline{k}_{3,0,x}}{\Delta E_{2,0}\Delta E_{3,0}} - \frac{\Delta \underline{k}_{2,0,z}\Delta \underline{k}_{1,0,x}}{\Delta E_{2,0}\Delta E_{1,0}} - \frac{\Delta \underline{k}_{3,0,x}\Delta \underline{k}_{1,0,z}}{\Delta E_{3,0}\Delta E_{1,0}} - \frac{\Delta \underline{k}_{2,0,x}\Delta \underline{k}_{3,0,z}}{\Delta E_{2,0}\Delta E_{3,0}} + \frac{\Delta \underline{k}_{2,0,x}\Delta \underline{k}_{1,0,z}}{\Delta E_{2,0}\Delta E_{1,0}} + \frac{\Delta \underline{k}_{3,0,z}\Delta \underline{k}_{1,0,x}}{\Delta E_{3,0}\Delta E_{1,0}} \\ \frac{\Delta \underline{k}_{2,0,x}\Delta \underline{k}_{3,0,y}}{\Delta E_{2,0}\Delta E_{3,0}} - \frac{\Delta \underline{k}_{2,0,x}\Delta \underline{k}_{1,0,y}}{\Delta E_{2,0}\Delta E_{1,0}} - \frac{\Delta \underline{k}_{3,0,y}\Delta \underline{k}_{1,0,x}}{\Delta E_{3,0}\Delta E_{1,0}} - \frac{\Delta \underline{k}_{2,0,y}\Delta \underline{k}_{3,0,x}}{\Delta E_{2,0}\Delta E_{3,0}} + \frac{\Delta \underline{k}_{2,0,y}\Delta \underline{k}_{1,0,x}}{\Delta E_{2,0}\Delta E_{1,0}} + \frac{\Delta \underline{k}_{3,0,x}\Delta \underline{k}_{1,0,y}}{\Delta E_{3,0}\Delta E_{1,0}} \end{pmatrix} \right| \tag{B.8}$$

$$A_{n,i}(E) = \frac{1}{2}\frac{(E - E_{n,t(n,i,0)})^2}{\Delta E_{1,0}\Delta E_{2,0}\Delta E_{3,0}} \cdot \left| \begin{pmatrix} (\Delta \underline{k}_{2,0,y}\Delta \underline{k}_{3,0,z} - \Delta \underline{k}_{2,0,z}\Delta \underline{k}_{3,0,y})\Delta E_{1,0} + (\Delta \underline{k}_{1,0,z}\Delta \underline{k}_{3,0,y} - \Delta \underline{k}_{1,0,y}\Delta \underline{k}_{3,0,z})\Delta E_{2,0} + (\Delta \underline{k}_{1,0,y}\Delta \underline{k}_{2,0,z} - \Delta \underline{k}_{1,0,z}\Delta \underline{k}_{2,0,y})\Delta E_{3,0} \\ (\Delta \underline{k}_{2,0,z}\Delta \underline{k}_{3,0,x} - \Delta \underline{k}_{2,0,x}\Delta \underline{k}_{3,0,z})\Delta E_{1,0} + (\Delta \underline{k}_{1,0,x}\Delta \underline{k}_{3,0,z} - \Delta \underline{k}_{1,0,z}\Delta \underline{k}_{3,0,x})\Delta E_{2,0} + (\Delta \underline{k}_{1,0,z}\Delta \underline{k}_{2,0,x} - \Delta \underline{k}_{1,0,x}\Delta \underline{k}_{2,0,z})\Delta E_{3,0} \\ (\Delta \underline{k}_{2,0,x}\Delta \underline{k}_{3,0,y} - \Delta \underline{k}_{2,0,y}\Delta \underline{k}_{3,0,x})\Delta E_{1,0} + (\Delta \underline{k}_{1,0,y}\Delta \underline{k}_{3,0,x} - \Delta \underline{k}_{1,0,x}\Delta \underline{k}_{3,0,y})\Delta E_{2,0} + (\Delta \underline{k}_{1,0,x}\Delta \underline{k}_{2,0,y} - \Delta \underline{k}_{1,0,y}\Delta \underline{k}_{2,0,x})\Delta E_{3,0} \end{pmatrix} \right| \tag{B.9}$$

This area is then divided by the norm of the interpolation gradient which is found using equation 4.5, re-written here.

$$|\nabla_{\underline{k}} E_{n,i}| = \left| \begin{pmatrix} \Delta \underline{k}_{1,0} \\ \Delta \underline{k}_{2,0} \\ \Delta \underline{k}_{3,0} \end{pmatrix}^{-1} \begin{pmatrix} \Delta E_{1,0} \\ \Delta E_{2,0} \\ \Delta E_{3,0} \end{pmatrix} \right| \tag{B.10}$$

Explicitly calculating this inverse gives,

$$|\nabla_{\underline{k}} E_{n,i}| = \left| \frac{1}{det \begin{pmatrix} \Delta \underline{k}_{1,0} \\ \Delta \underline{k}_{2,0} \\ \Delta \underline{k}_{3,0} \end{pmatrix}} \cdot \begin{pmatrix} (\Delta \underline{k}_{2,0,y} \Delta \underline{k}_{3,0,z} - \Delta \underline{k}_{2,0,z} \Delta \underline{k}_{3,0,y}) & (\Delta \underline{k}_{1,0,z} \Delta \underline{k}_{3,0,y} - \Delta \underline{k}_{1,0,y} \Delta \underline{k}_{3,0,z}) & (\Delta \underline{k}_{1,0,y} \Delta \underline{k}_{2,0,z} - \Delta \underline{k}_{1,0,z} \Delta \underline{k}_{2,0,y}) \\ (\Delta \underline{k}_{2,0,z} \Delta \underline{k}_{3,0,x} - \Delta \underline{k}_{2,0,x} \Delta \underline{k}_{3,0,z}) & (\Delta \underline{k}_{1,0,x} \Delta \underline{k}_{3,0,z} - \Delta \underline{k}_{1,0,z} \Delta \underline{k}_{3,0,x}) & (\Delta \underline{k}_{1,0,z} \Delta \underline{k}_{2,0,x} - \Delta \underline{k}_{1,0,x} \Delta \underline{k}_{2,0,z}) \\ (\Delta \underline{k}_{2,0,x} \Delta \underline{k}_{3,0,y} - \Delta \underline{k}_{2,0,y} \Delta \underline{k}_{3,0,x}) & (\Delta \underline{k}_{1,0,y} \Delta \underline{k}_{3,0,x} - \Delta \underline{k}_{1,0,x} \Delta \underline{k}_{3,0,y}) & (\Delta \underline{k}_{1,0,x} \Delta \underline{k}_{2,0,y} - \Delta \underline{k}_{1,0,y} \Delta \underline{k}_{2,0,x}) \end{pmatrix} \cdot \begin{pmatrix} \Delta E_{1,0} \\ \Delta E_{2,0} \\ \Delta E_{3,0} \end{pmatrix} \right| \tag{B.11}$$

By calculating the determinant and doing the matrix multiplication,

$$|\nabla_{\underline{k}} E_{n,i}| = \frac{1}{6V} \cdot \left| \begin{pmatrix} (\Delta \underline{k}_{2,0,y} \Delta \underline{k}_{3,0,z} - \Delta \underline{k}_{2,0,z} \Delta \underline{k}_{3,0,y}) \Delta E_{1,0} + (\Delta \underline{k}_{1,0,z} \Delta \underline{k}_{3,0,y} - \Delta \underline{k}_{1,0,y} \Delta \underline{k}_{3,0,z}) \Delta E_{2,0} + (\Delta \underline{k}_{1,0,y} \Delta \underline{k}_{2,0,z} - \Delta \underline{k}_{1,0,z} \Delta \underline{k}_{2,0,y}) \Delta E_{3,0} \\ (\Delta \underline{k}_{2,0,z} \Delta \underline{k}_{3,0,x} - \Delta \underline{k}_{2,0,x} \Delta \underline{k}_{3,0,z}) \Delta E_{1,0} + (\Delta \underline{k}_{1,0,x} \Delta \underline{k}_{3,0,z} - \Delta \underline{k}_{1,0,z} \Delta \underline{k}_{3,0,x}) \Delta E_{2,0} + (\Delta \underline{k}_{1,0,z} \Delta \underline{k}_{2,0,x} - \Delta \underline{k}_{1,0,x} \Delta \underline{k}_{2,0,z}) \Delta E_{3,0} \\ (\Delta \underline{k}_{2,0,x} \Delta \underline{k}_{3,0,y} - \Delta \underline{k}_{2,0,y} \Delta \underline{k}_{3,0,x}) \Delta E_{1,0} + (\Delta \underline{k}_{1,0,y} \Delta \underline{k}_{3,0,x} - \Delta \underline{k}_{1,0,x} \Delta \underline{k}_{3,0,y}) \Delta E_{2,0} + (\Delta \underline{k}_{1,0,x} \Delta \underline{k}_{2,0,y} - \Delta \underline{k}_{1,0,y} \Delta \underline{k}_{2,0,x}) \Delta E_{3,0} \end{pmatrix} \right| \tag{B.12}$$

Where V is the volume of the tetrahedron.

Substituting equations B.9 and B.12 into equation B.1 then gives the contribution of a tetrahedron to the DOS when the energy of the equivalent energy surface has an energy between that at vertices 0 and 1, $E_{n,t(n,i,0)} < E < E_{n,t(n,i,1)}$.

$$g_i^{tet}(E) = \frac{3V}{(2\pi)^3} \frac{(E - E_{n,t(n,i,0)})^2}{\Delta E_{1,0} \Delta E_{2,0} \Delta E_{3,0}} \tag{B.13}$$

as shown in equation 4.12. The other two cases follow with a similar argument for when $E_{n,t(n,i,1)} < E < E_{n,t(n,i,2)}$ and $E_{n,t(n,i,2)} < E < E_{n,t(n,i,3)}$.

Appendix C

Derivation of Density Functional Perturbation Theory

DFPT begins by applying a small perturbation, λ, to the KS Hamiltonian, equation 3.36, which can then be expanded following equation 3.35 to give,

$$\left(\hat{H} + \lambda \frac{\partial \hat{H}}{\partial \lambda}\bigg|_{\lambda=0} + \frac{\lambda^2}{2}\frac{\partial^2 \hat{H}}{\partial \lambda^2}\bigg|_{\lambda=0} + \dots\right)\left(\phi_i(\mathbf{r}) + \lambda \frac{\partial \phi_i(\mathbf{r})}{\partial \lambda}\bigg|_{\lambda=0} + \frac{\lambda^2}{2}\frac{\partial^2 \phi_i(\mathbf{r})}{\partial \lambda^2}\bigg|_{\lambda=0} + \dots\right)$$
$$= \left(\epsilon_i + \lambda \frac{\partial \epsilon_i}{\partial \lambda}\bigg|_{\lambda=0} + \frac{\lambda^2}{2}\frac{\partial^2 \epsilon_i}{\partial \lambda^2}\bigg|_{\lambda=0} + \dots\right)\left(\phi_i(\mathbf{r}) + \lambda \frac{\partial \phi_i(\mathbf{r})}{\partial \lambda}\bigg|_{\lambda=0} + \frac{\lambda^2}{2}\frac{\partial^2 \phi_i(\mathbf{r})}{\partial \lambda^2}\bigg|_{\lambda=0} + \dots\right) \tag{C.1}$$

By multiplying out the brackets and grouping like terms,

$$\hat{H}\phi_i(\mathbf{r}) + \lambda\left(\frac{\partial \hat{H}}{\partial \lambda}\phi_i(\mathbf{r}) + \hat{H}\frac{\partial \phi_i(\mathbf{r})}{\partial \lambda}\right) + \frac{\lambda^2}{2}\left(\frac{\partial^2 \hat{H}}{\partial \lambda^2}\phi_i(\mathbf{r}) + \frac{\partial \hat{H}}{\partial \lambda}\frac{\partial \phi_i(\mathbf{r})}{\partial \lambda} + \hat{H}\frac{\partial^2 \phi_i(\mathbf{r})}{\partial \lambda^2}\right) + \dots$$
$$= \epsilon_i\phi_i(\mathbf{r}) + \lambda\left(\frac{\partial \epsilon_i}{\partial \lambda}\phi_i(\mathbf{r}) + \epsilon_i\frac{\partial \phi_i(\mathbf{r})}{\partial \lambda}\right) + \frac{\lambda^2}{2}\left(\frac{\partial^2 \epsilon_i}{\partial \lambda^2}\phi_i(\mathbf{r}) + \frac{\partial \epsilon_i}{\partial \lambda}\frac{\partial \phi_i(\mathbf{r})}{\partial \lambda} + \epsilon_i\frac{\partial^2 \phi_i(\mathbf{r})}{\partial \lambda^2}\right) + \dots \tag{C.2}$$

Similarly, the orthogonal and normalised condition becomes,

$$\int \phi_i^*(\mathbf{r};\lambda)\phi_j(\mathbf{r};\lambda)d\mathbf{r} = \delta_{ij} = \overbrace{\int \phi_i^*(\mathbf{r})\phi_j(\mathbf{r})d\mathbf{r}}^{=\delta_{ij}} + \lambda\overbrace{\int \phi_i^*(\mathbf{r})\frac{\partial \phi_j(\mathbf{r})}{\partial \lambda} + \frac{\partial \phi_i^*(\mathbf{r})}{\partial \lambda}\phi_j(\mathbf{r})d\mathbf{r}}^{=0}$$
$$+ \frac{\lambda^2}{2}\underbrace{\int \phi_i^*(\mathbf{r})\frac{\partial^2 \phi_j(\mathbf{r})}{\partial \lambda^2} + \frac{\partial \phi_i^*(\mathbf{r})}{\partial \lambda}\frac{\partial \phi_j(\mathbf{r})}{\partial \lambda} + \frac{\partial^2 \phi_i^*(\mathbf{r})}{\partial \lambda^2}\phi_j(\mathbf{r})d\mathbf{r}}_{=0} + \dots \tag{C.3}$$

Then, using equation 3.22, the first term on the right-hand side of equation C.3 is equal to δ_{ij} and so all the higher order terms must be equal to zero.

Equating the first order terms of equation C.2 gives,

$$\frac{\partial \hat{H}}{\partial \lambda}\phi_i(\mathbf{r}) + \hat{H}\frac{\partial \phi_i(\mathbf{r})}{\partial \lambda} = \frac{\partial \epsilon_i}{\partial \lambda}\phi_i(\mathbf{r}) + \epsilon_i \frac{\partial \phi_i(\mathbf{r})}{\partial \lambda} \tag{C.4}$$

Premultiplying by $\phi_i^*(\mathbf{r})$ and integrating over all space then gives,

$$\int \phi_i^*(\mathbf{r})\frac{\partial \hat{H}}{\partial \lambda}\phi_i(\mathbf{r})d\mathbf{r} + \int \phi_i^*(\mathbf{r})\hat{H}\frac{\partial \phi_i(\mathbf{r})}{\partial \lambda}d\mathbf{r} = \frac{\partial \epsilon_i}{\partial \lambda}\int \phi_i^*(\mathbf{r})\phi_i(\mathbf{r})d\mathbf{r} + \epsilon_i \int \phi_i^*(\mathbf{r})\frac{\partial \phi_i(\mathbf{r})}{\partial \lambda}d\mathbf{r} \tag{C.5}$$

As $\hat{H}$ is a Hermitian operator,

$$\int \phi_i^*(\mathbf{r})\hat{H}\frac{\partial \phi_i(\mathbf{r})}{\partial \lambda}d\mathbf{r} = \epsilon_i \int \phi_i^*(\mathbf{r})\frac{\partial \phi_i(\mathbf{r})}{\partial \lambda}d\mathbf{r} \tag{C.6}$$

Therefore, the second term on both sides of equation C.5 cancel and from equation 3.22, the integral in the first term on the right-hand side becomes one. The first order change in the eigenenergy with respect to λ is given by,

$$\frac{\partial \epsilon_i}{\partial \lambda} = \int \phi_i^*(\mathbf{r})\frac{\partial \hat{H}}{\partial \lambda}\phi_i(\mathbf{r})d\mathbf{r} \tag{C.7}$$

which is the Hellmann-Feynman theorem [130–133]. To calculate the first order change in the eigenenergy with respect to some variable, λ, only the change in the Hamiltonian with respect to λ is needed. What then is the first order change to the hamiltonian with respect to λ? This can be found by expanding the terms of the hamiltonian as in equation 3.35

$$\begin{aligned}\hat{H} + \lambda\frac{\partial \hat{H}}{\partial \lambda} + \frac{\lambda^2}{2}\frac{\partial^2 \hat{H}}{\partial \lambda^2} + \ldots = \hat{T} + \hat{V}_{ext} + \hat{V}_H + \hat{V}_{XC} + \lambda\left(\frac{\partial \hat{V}_{ext}}{\partial \lambda} + \frac{\partial \hat{V}_H}{\partial \lambda} + \frac{\partial \hat{V}_{XC}}{\partial \lambda}\right) \\ + \frac{\lambda^2}{2}\left(\frac{\partial^2 \hat{V}_{ext}}{\partial \lambda^2} + \frac{\partial^2 \hat{V}_H}{\partial \lambda^2} + \frac{\partial^2 \hat{V}_{XC}}{\partial \lambda^2}\right)\end{aligned} \tag{C.8}$$

Once again, equating like terms,

$$\frac{\partial \hat{H}}{\partial \lambda} = \frac{\partial \hat{V}_{ext}}{\partial \lambda} + \frac{\partial \hat{V}_H}{\partial \lambda} + \frac{\partial \hat{V}_{XC}}{\partial \lambda} = \frac{\partial \hat{V}_{ext}}{\partial \lambda} + \frac{\partial}{\partial \lambda}\left(\frac{\delta E_H[\rho](\mathbf{r})}{\delta \rho(\mathbf{r})} + \frac{\delta E_{XC}[\rho](\mathbf{r})}{\delta \rho(\mathbf{r})}\right) \tag{C.9}$$

which, becomes

$$\frac{\partial \hat{H}}{\partial \lambda} = \frac{\partial \hat{V}_{ext}}{\partial \lambda} + \int \frac{\partial \rho(\mathbf{r})}{\partial \lambda} \left(\frac{\delta^2 E_H[\rho](\mathbf{r})}{\delta \rho(\mathbf{r}) \delta \rho(\mathbf{r}')} + \frac{\delta^2 E_{XC}[\rho](\mathbf{r})}{\delta \rho(\mathbf{r}) \delta \rho(\mathbf{r})} \right) d\mathbf{r}' \tag{C.10}$$

Similarly, $\frac{\partial \rho(\mathbf{r})}{\partial \lambda}$, is found as,

$$\frac{\partial \rho(\mathbf{r})}{\partial \lambda} = \sum_{i}^{n} \left(\phi_i^*(\mathbf{r}) \frac{\partial \phi_i(\mathbf{r})}{\partial \lambda} + \frac{\partial \phi_i^*(\mathbf{r})}{\partial \lambda} \phi_i(\mathbf{r}) \right) \tag{C.11}$$

and to find $\frac{\partial \phi_i(\mathbf{r})}{\partial \lambda}$ requires the Sternheimer equation [134, 135],

$$\left(\hat{H} - \epsilon_i \right) \frac{\partial \phi_i(\mathbf{r})}{\partial \lambda} = - \left(\frac{\partial \hat{H}}{\partial \lambda} - \frac{\partial \epsilon_i}{\partial \lambda} \right) \phi_i(\mathbf{r}) \tag{C.12}$$

Appendix D

DFT Input Parameters

D.1 Si

	Number of Basis Functions	Exponents
14-Si-4 LDA dddd HGH	40	0.1061938, 0.2657508, 0.6650433, 1.6642759
14-Si-4 LDA dddpp HGH	42	0.1402388, 0.3941019, 1.1075133, 3.1123565, 8.7464077
14-Si-4 LDA dddppp HGH	48	0.1400229, 0.3925795, 1.1006677, 3.0859211, 8.6519380, 24.2572734
14-Si-4 LDA ddpp HGH	28	0.16145, 0.46343, 1.31473, 3.75324
14-Si-4 LDA fddd HGH	50	0.1469945, 0.3347113, 0.7621487, 1.7354378
14-Si-4 GGA dddd HGH	40	0.1061938, 0.2657508, 0.6650433, 1.6642759
14-Si-4 GGA ddpp HGH	28	0.16145, 0.46343, 1.31473, 3.75324

Table D.1: Description of the AIMPRO inputs as well as the size of the basis set and the expoents used in AIMPRO for Si.

D.2 Diamond

	Number of Basis Functions	Exponents
6-C-4 LDA dddd HGH	40	0.24466000, 0.67115000, 1.84112000, 5.05059000
6-C-4 LDA ddpp HGH	28	0.27548000, 0.83021000, 2.39934000, 5.82253000
6-C-4 LDA pdp HGH	18	0.27409000, 1.04983000, 4.02102000
6-C-4 LDA pdpp HGH	22	0.24496000, 0.68680000, 1.92554000, 5.39856000
6-C-4 LDA pppp HGH	16	0.18865730, 0.55921810, 1.65763480, 4.91356240
6-C-4 GGA dddd HGH	40	0.239530, 0.666469, 1.854387, 5.159660
6-C-4 GGA ddpp HGH	28	0.29951910, 0.79366430, 2.10304794, 5.57264655
6-C-4 GGA pdpp HGH	22	0.2454673, 0.6925258, 1.9537916, 5.5121437
6-C-4 GGA ddpp Krack	28	0.27548000, 0.83021000, 2.39934000, 5.82253000
6-C-4 GGA pdpp Krack	22	0.24496000, 0.68680000, 1.92554000, 5.39856000

Table D.2: Description of the AIMPRO inputs as well as the size of the basis set and the exponents used in AIMPRO for diamond.

D.3 Boron

	Number of Basis Functions	Exponents
5-N-3 GGA ddpp HGH	28	0.227590, 0.575184, 1.453650, 3.673781
5-N-3 GGA dppp HGH	22	0.245170, 0.603412, 1.485119, 3.655174
5-N-3 GGA dddd HGH	40	0.1847729, 0.4054578, 0.9195348, 3.0361337
5-N-3 GGA dddp HGH	34	0.3357163,p 0.7392055, 2.1618277, 4.6377991
5-N-3 GGA pddd HGH	34	0.0864178, 0.3220370, 0.8469513, 2.9016646

Table D.3: Description of the AIMPRO inputs as well as the size of the basis set and the exponents used in AIMPRO for boron in cBN.

D.4 Nitrogen

	Number of Basis Functions	Exponents
7-N-5 GGA dddd HGH	40	0.297582, 0.859612, 2.483124, 7.172893
7-N-5 GGA dppp HGH	34	0.4293560, 1.1348151, 2.9993883, 7.9275735
hline 7-N-5 GGA ddpp HGH	28	0.3334929, 0.9479083, 2.6943007, 7.6581843
hline		

Table D.4: Description of the AIMPRO inputs as well as the size of the basis set and the exponents used in AIMPRO for nitrogen in cBN.

Appendix E

Results for Variable Intervalley Separation in cBN

The simulations for cBN were conducted for a range of $X_1 - \Gamma$ intervalley separations, with figures E.1, E.2 and E.3 showing the plots velocity-field, energy-field and occupancy-field over this range of intervalley separations, respectively. As can be seen, the intervalley separation has very little impact on the average velocity or energy over the range of fields simulated here. Figure E.3 shows that at the very highest fields, there is some occupancy of the higher valleys with higher proportions of electrons scattering to the upper valleys where the separation is lower; however this is only beyond 1000kV/cm and is less than 4% of the electrons. In comparison, due to the larger DOS of the higher valleys in the work of Siddiqua *et al.* [75], there is a significant population of electrons in the upper valleys at much lower fields.

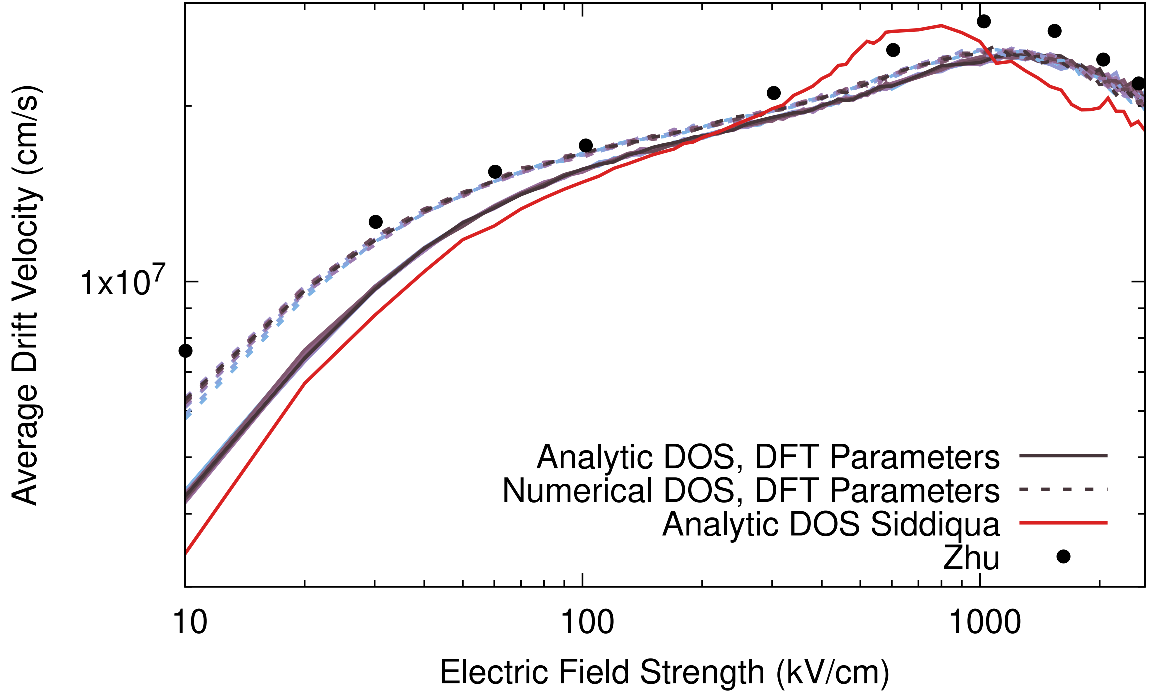

Figure E.1: Velocity-field data for cBN. Solid red line shows simulation results using analytic DOS and parameters from Siddiqua *et al.* [75]. Blue lines show the simulation results using parameters calculated here with analytic (solid) and numerical (dashed) DOS for a range of $X_1 - \Gamma$ valley separation, darker lines indicate a wider energy separation. Black points show data taken from FBMC simulation performed by Zhu *et al.* [146].

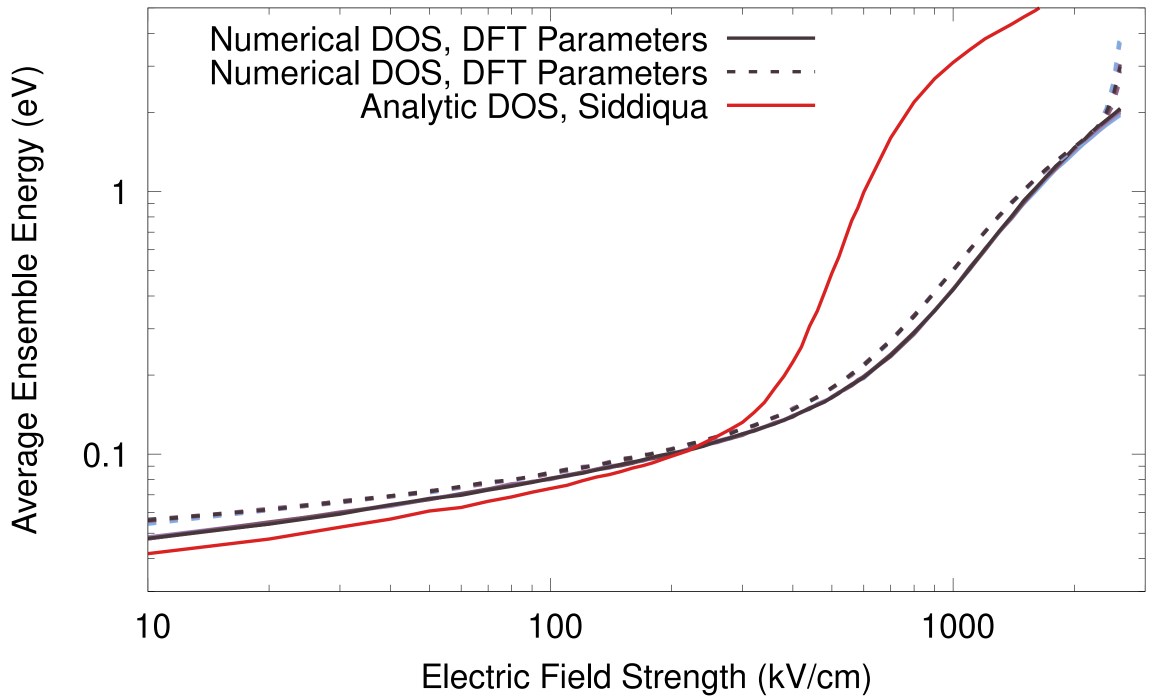

Figure E.2: Energy-field characteristics for cBN. Solid red line shows simulation results using analytic DOS and parameters from Siddiqua *et al.* [75]. Blue lines show the simulation results using parameters calculated here with analytic (solid) and numerical (dashed) DOS for a range of $X_1 - \Gamma$ valley separation, darker lines indicate a wider energy separation.

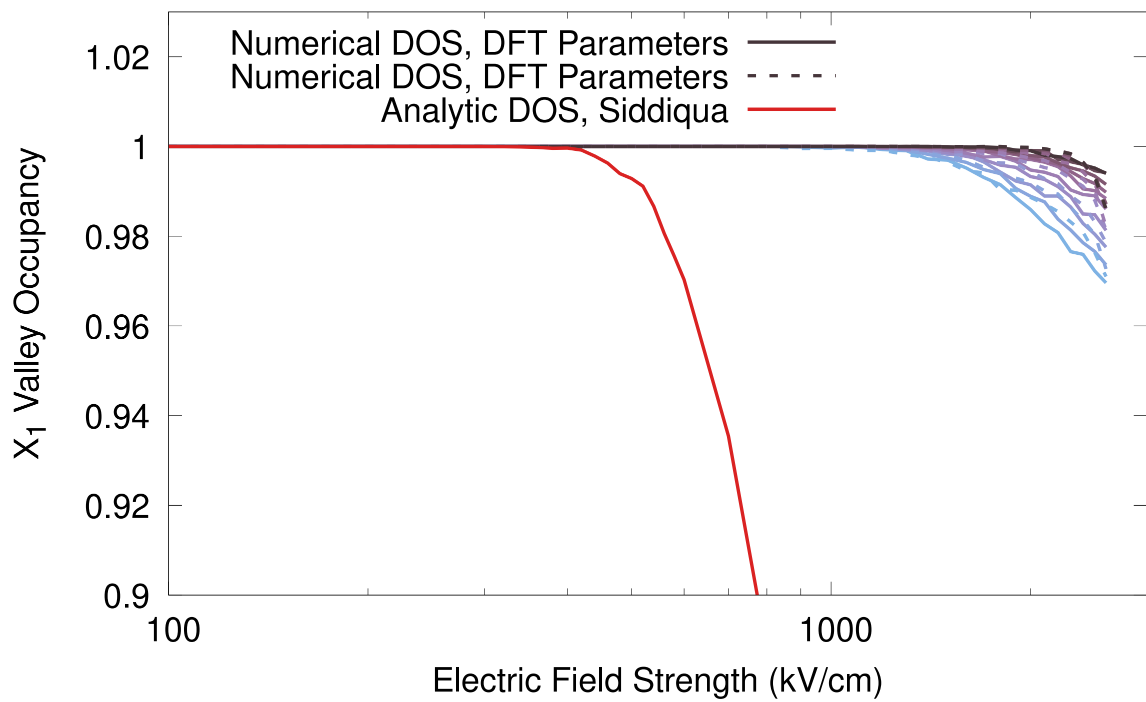

Figure E.3: Occupancy-field characteristics for cBN. Solid red line shows simulation results using analytic DOS and parameters from Siddiqua *et al.* [75]. Blue lines show the simulation results using parameters calculated here with analytic (solid) and numerical (dashed) DOS for a range of $X_1 - \Gamma$ valley separation, darker lines indicate a wider energy separation.

Bibliography

[1] G. E. Moore, "Cramming more components onto integrated circuits, reprinted from electronics, volume 38, number 8, april 19, 1965, pp.114 ff.," *IEEE Solid-State Circuits Society Newsletter*, vol. 11, pp. 33–35, 2006.

[2] S. J. Pearton, A. Aitkaliyeva, M. Xian, F. Ren, A. Khachatrian, A. Ildefonso, Z. Islam, M. A. J. Rasel, A. Haque, A. Y. Polyakov, and J. Kim, "Review—radiation damage in wide and ultra-wide bandgap semiconductors," *ECS Journal of Solid State Science and Technology*, vol. 10, p. 055008, 5 2021.

[3] A. Kumar, M. Moradpour, M. Losito, W. T. Franke, S. Ramasamy, R. Baccoli, and G. Gatto, "Wide band gap devices and their application in power electronics," 12 2022.

[4] K. Takahashi, A. Yoshikawa, and A. Sandhu, *Wide bandgap semiconductors fundamental properties and modern photonic and electronic devices*. Berlin: Springer, 2007.

[5] J. Y. Tsao, S. Chowdhury, M. A. Hollis, D. Jena, N. M. Johnson, K. A. Jones, R. J. Kaplar, S. Rajan, C. G. V. de Walle, E. Bellotti, C. L. Chua, R. Collazo, M. E. Coltrin, J. A. Cooper, K. R. Evans, S. Graham, T. A. Grotjohn, E. R. Heller, M. Higashiwaki, M. S. Islam, P. W. Juodawlkis, M. A. Khan, A. D. Koehler, J. H. Leach, U. K. Mishra, R. J. Nemanich, R. C. Pilawa-Podgurski, J. B. Shealy, Z. Sitar, M. J. Tadjer, A. F. Witulski, M. Wraback, and J. A. Simmons, "Ultrawide-bandgap semiconductors: Research opportunities and challenges," 1 2018.

[6] M. Shur, "(invited) ultrawide bandgap transistors for high temperature and radiation hard applications," *ECS Transactions*, vol. 109, pp. 21–30, 9 2022.

[7] M. H. Wong, O. Bierwagen, R. J. Kaplar, and H. Umezawa, "Ultrawide-bandgap semi-

conductors: An overview," *Journal of Materials Research*, vol. 36, pp. 4601–4615, 12 2021.

[8] M. Xu, D. Wang, K. Fu, D. H. Mudiyanselage, H. Fu, and Y. Hao, "A review of ultrawide bandgap materials: Properties, synthesis and devices," 2022.

[9] M. Lundstrom, *Fundamentals of Carrier Transport*. Cambridge University Press, second ed., 2000.

[10] C. Kittel, *Introduction to Solid State Physics*. John Wiley & Sons, 8 ed., 2005.

[11] R. D. L. Kronig, W. G. Penney, and R. H. Fowler, "Quantum mechanics of electrons in crystal lattices," *Proceedings of the Royal Society of London. Series A, Containing Papers of a Mathematical and Physical Character*, vol. 130, no. 814, pp. 499–513, 1931.

[12] W. Setyawan and S. Curtarolo, "High-throughput electronic band structure calculations: Challenges and tools," *Computational Materials Science*, vol. 49, no. 2, pp. 299–312, 2010.

[13] R. Jones and P. Briddon, "Chapter 6 the ab initio cluster method and the dynamics of defects in semiconductors," in *Identification of Defects in Semiconductors* (M. Stavola, ed.), vol. 51 of *Semiconductors and Semimetals*, pp. 287–349, Elsevier, 1998.

[14] E. Kane, "Chapter 3 the k •p method," in *Semiconductors and Semimetals* (R. Willardson and A. C. Beer, eds.), vol. 1 of *Semiconductors and Semimetals*, pp. 75–100, Elsevier, 1966.

[15] K. Tomizawa, *Numerical simulation of submicron semiconductor devices*. 1993.

[16] U. Kovac, *3D Drift Diffusion and 3D Monte Carlo simulation of On-Current variability due to Random Dopants*. PhD thesis, University of Glasgow, 2010.

[17] H. Shichijo and K. Hess, "Band-structure-dependent transport and impact ionization in gaas," *Phys. Rev. B*, vol. 23, pp. 4197–4207, 4 1981.

[18] R. K. Smith and J. Bude, "Highly efficient full band monte carlo simulations," *Proc. International Workshop on Computational Electronics*, pp. 224–230, 8 1993.

[19] D. R. Naylor, *Development of Monte-Carlo Simulations for III-V Semiconductors employing an analytic band-structure*. PhD thesis, University of Hull, 2012.

[20] M. V. Fischetti and S. E. Laux, "Monte carlo simulation of electron transport in si: The first 20 years," in *ESSDERC '96: Proceedings of the 26th European Solid State Device Research Conference*, pp. 813–820, 1996.

[21] C. Jungemann, S. Yamaguchi, and H. Goto, "Efficient full band monte carlo hot carrier simulation for silicon devices," in *ESSDERC '96: Proceedings of the 26th European Solid State Device Research Conference*, pp. 821–824, 1996.

[22] C. Jungemann, S. Keith, M. Bartels, and B. Meinerzhagen, "Efficient full-band monte carlo simulation of silicon devices," *IEICE Transactions on Electronics*, vol. 82, pp. 870–879, 1999.

[23] J. Bude and R. K. Smith, "Phase-space simplex monte carlo for semiconductor transport," *Semiconductor Science and Technology*, vol. 9, pp. 840–843, 5 1994.

[24] M. V. Fischetti and S. E. Laux, "Monte carlo analysis of electron transport in small semiconductor devices including band-structure and space-charge effects," *Phys. Rev. B*, vol. 38, pp. 9721–9745, 11 1988.

[25] K. Hess, *Monte Carlo Device Simulation: Full Band and Beyond*. Kluwer Academic Publishers, 1991.

[26] J. Y. Tang and K. Hess, "Impact ionization of electrons in silicon (steady state)," *Journal of Applied Physics*, vol. 54, pp. 5139–5144, 1983.

[27] T. Kunikiyo, M. Takenaka, Y. Kamakura, M. Yamaji, H. Mizuno, M. Morifuji, K. Taniguchi, and C. Hamaguchi, "A monte carlo simulation of anisotropic electron transport in silicon including full band structure and anisotropic impact-ionization model," *Journal of Applied Physics*, vol. 75, pp. 297–312, 1994.

[28] H.-E. Nilsson, M. Hjelm, C. Fröjdh, C. Persson, U. Sannemo, and C. S. Petersson, "Full band monte carlo simulation of electron transport in 6h-sic," *Journal of Applied Physics*, vol. 86, pp. 965–973, 1999.

[29] G. J. Iafrate, R. J. Malik, J. Y. Tang, and K. Hess, "Transient transport and transferred electron behavior in gallium arsenide under the condition of high-energy electron injection," *Solid State Communications*, vol. 45, pp. 255 – 258, 1983.

[30] J. Y. . Tang and K. Hess, "Investigation of transient electronic transport in gaas following high energy injection," *IEEE Transactions on Electron Devices*, vol. 29, pp. 1906–1911, 1982.

[31] K. Brennan, K. Hess, J. Y. Tang, and G. J. Iafrate, "Transient electronic transport in inp under the condition of high-energy electron injection," *IEEE Transactions on Electron Devices*, vol. 30, pp. 1750–1754, 1983.

[32] J. Fang, M. V. Fischetti, R. D. Schrimpf, R. A. Reed, E. Bellotti, and S. T. Pantelides, "Transport properties of al_xga_1-xn/gan transistors based on first-principles calculations and boltzmann-equation monte carlo simulations," *Phys. Rev. Applied*, vol. 11, p. 44045, 4 2019.

[33] B. K. Ridley, *Quantum Processes In Semiconductors*. Oxford University Press, 5th ed., 2013.

[34] S. Nakamura and M. R. Krames, "History of gallium-nitride-based light-emitting diodes for illumination," *Proceedings of the IEEE*, vol. 101, no. 10, pp. 2211–2220, 2013.

[35] B. K. Bose, "Global energy scenario and impact of power electronics in 21st century," *IEEE Transactions on Industrial Electronics*, vol. 60, no. 7, pp. 2638–2651, 2013.

[36] M. Levinshtein, S. Rumyantsev, and M. Shur, *Properties of Advanced Semiconductor Materials: GaN, AIN, InN, BN, SiC, SiGe*. A Wiley-Interscience publication, Wiley, 2001.

[37] H. P. Maruska and J. J. Tietjen, "The preparation and properties of vapor-deposited single-crystal-line gan," *Applied Physics Letters*, vol. 15, pp. 327–329, 11 1969.

[38] M. K. Prasad, O. A. Al-Ani, J. P. Goss, and J. D. Mar, "Charge transfer due to defects in hexagonal boron nitride/graphene heterostructures: An ab initio study," *Phys. Rev. Mater.*, vol. 7, p. 094003, Sep 2023.

[39] M. Ohring, "Materials science of thin films (second edition)," 2002.

[40] L. S. Pan and D. R. Kania, *Diamond: Electronic Properties and Applications*. Springer New York, NY, 1 ed., 1994.

[41] L. Vel, G. Demazeau, and J. Etourneau, "Cubic boron nitride: synthesis, physicochemical properties and applications," *Materials Science and Engineering: B*, vol. 10, no. 2, pp. 149–164, 1991.

[42] J. Narayan, A. Bhaumik, and W. Xu, "Direct conversion of h-bn into c-bn and formation of epitaxial c-bn/diamond heterostructures," *Journal of Applied Physics*, vol. 119, 5 2016.

[43] W. J. Zhang, Y. M. Chong, I. Bello, and S. T. Lee, "Nucleation, growth and characterization of cubic boron nitride (cbn) films," *Journal of Physics D: Applied Physics*, vol. 40, p. 6159, oct 2007.

[44] H. Sumiya, S. Uesaka, and S. Satoh, "Mechanical properties of high purity polycrystalline cbn synthesized by direct conversion sintering method," *Journal of Materials Science*, vol. 35, pp. 1181–1186, Mar 2000.

[45] T. Taniguchi and K. Watanabe, "Synthesis of high-purity boron nitride single crystals under high pressure by using ba-bn solvent," *Journal of Crystal Growth*, vol. 303, no. 2, pp. 525–529, 2007.

[46] R. H. Wentorf, "Cubic form of boron nitride," *The Journal of Chemical Physics*, vol. 26, pp. 956–956, 04 1957.

[47] R. H. Wentorf, "Synthesis of the cubic form of boron nitride," *The Journal of Chemical Physics*, vol. 34, pp. 809–812, 1961.

[48] R. H. Wentorf, "Preparation of semiconducting cubic boron nitride," *The Journal of Chemical Physics*, vol. 36, pp. 1990–1991, 1961.

[49] M. Schreck, S. Gsell, R. Brescia, and M. Fischer, "Ion bombardment induced buried lateral growth: The key mechanism for the synthesis of single crystal diamond wafers," *Scientific Reports*, vol. 7, 3 2017.

[50] S. W. Kim, R. Takaya, S. Hirano, and M. Kasu, "Two-inch high-quality (001) diamond heteroepitaxial growth on sapphire (1120) misoriented substrate by step-flow mode," *Applied Physics Express*, vol. 14, 11 2021.

[51] E. Yamasue, M. Susa, H. Fukuyama, and K. Nagata, "Thermal conductivities of silicon and germanium in solid and liquid states measured by non-stationary hot wire method with silica coated probe," *Journal of Crystal Growth*, vol. 234, no. 1, pp. 121–131, 2002.

[52] C. J. Glassbrenner and G. A. Slack, "Thermal conductivity of silicon and germanium from 3°k to the melting point," *Phys. Rev.*, vol. 134, pp. A1058–A1069, May 1964.

[53] S. J. Pearton, F. Ren, E. Patrick, M. E. Law, and A. Y. Polyakov, "Review—ionizing radiation damage effects on gan devices," *ECS Journal of Solid State Science and Technology*, vol. 5, pp. Q35–Q60, 2016.

[54] C. Abbate, G. Busatto, F. Iannuzzo, S. Mattiazzo, A. Sanseverino, L. Silvestrin, D. Tedesco, and F. Velardi, "Experimental study of single event effects induced by heavy ion irradiation in enhancement mode gan power hemt," *Microelectronics Reliability*, vol. 55, pp. 1496–1500, 8 2015.

[55] M. Zerarka, P. Austin, A. Bensoussan, F. Morancho, and A. Durier, "Tcad simulation of the single event effects in normally-off gan transistors after heavy ion radiation," *IEEE Transactions on Nuclear Science*, vol. 64, pp. 2242–2249, 8 2017.

[56] E. Mizuta, S. Kuboyama, Y. Nakada, A. Takeyama, T. Ohshima, Y. Iwata, and K. Suzuki, "Single-event damage observed in gan-on-si hemts for power control applications," *IEEE Transactions on Nuclear Science*, vol. 65, pp. 1956–1963, 8 2018.

[57] A. F. Witulski, D. R. Ball, K. F. Galloway, A. Javanainen, J. M. Lauenstein, A. L. Sternberg, and R. D. Schrimpf, "Single-event burnout mechanisms in sic power mosfets," *IEEE Transactions on Nuclear Science*, vol. 65, pp. 1951–1955, 8 2018.

[58] A. F. Witulski, R. Arslanbekov, A. Raman, R. D. Schrimpf, A. L. Sternberg, K. F. Galloway, A. Javanainen, D. Grider, D. J. Lichtenwalner, and B. Hull, "Single-event burnout of sic junction barrier schottky diode high-voltage power devices," *IEEE Transactions on Nuclear Science*, vol. 65, pp. 256–261, 1 2018.

[59] J. Kim, S. Nigam, F. Ren, D. Schoenfeld, G. Y. Chung, and S. J. Pearton, "High dose gamma-ray irradiation of sic schottky rectifiers," *Electrochemical and Solid-State Letters*, vol. 6, 8 2003.

[60] R. A. Johnson, A. F. Witulski, D. R. Ball, K. F. Galloway, A. L. Sternberg, E. Zhang, L. D. Ryder, R. A. Reed, R. D. Schrimpf, J. A. Kozub, J. M. Lauenstein, and A. Javanainen, "Enhanced charge collection in sic power mosfets demonstrated by pulse-laser two-photon absorption see experiments," *IEEE Transactions on Nuclear Science*, vol. 66, pp. 1694–1701, 7 2019.

[61] R. A. Johnson, A. Javanainen, A. Raman, P. S. Chakraborty, R. R. Arslanbekov, A. F. Witulski, D. R. Ball, K. F. Galloway, A. L. Sternberg, R. A. Reed, R. D. Schrimpf, M. L. Alles, and J. M. Lauenstein, "Unifying concepts for ion-induced leakage current degradation in silicon carbide schottky power diodes," *IEEE Transactions on Nuclear Science*, vol. 67, pp. 135–139, 1 2020.

[62] R. A. Johnson, A. F. Witulski, B. D. Sierawski, D. R. Ball, K. F. Galloway, A. L. Sternberg, R. A. Reed, R. D. Schrimpf, M. L. Alles, J. M. Lauenstein, and J. M. Hutson, "Influence of radiation environment variability on cumulative heavy-ion-induced leakage current in sic power devices," *IEEE Transactions on Nuclear Science*, vol. 70, pp. 322–327, 4 2023.

[63] A. Javanainen, K. F. Galloway, V. Ferlet-Cavrois, J. M. Lauenstein, F. Pintacuda, R. D. Schrimpf, R. A. Reed, and A. Virtanen, "Charge transport mechanisms in heavy-ion driven leakage current in silicon carbide schottky power diodes," *IEEE Transactions on Device and Materials Reliability*, vol. 16, pp. 208–212, 6 2016.

[64] A. Javanainen, K. F. Galloway, C. Nicklaw, A. L. Bosser, V. Ferlet-Cavrois, J. M. Lauenstein, F. Pintacuda, R. A. Reed, R. D. Schrimpf, R. A. Weller, and A. Virtanen, "Heavy ion induced degradation in sic schottky diodes: Bias and energy deposition dependence," *IEEE Transactions on Nuclear Science*, vol. 64, pp. 415–420, 1 2017.

[65] K. F. Galloway, A. F. Witulski, R. D. Schrimpf, A. L. Sternberg, D. R. Ball, A. Ja-

vanainen, R. A. Reed, B. D. Sierawski, and J. M. Lauenstein, "Failure estimates for sic power mosfets in space electronics," *Aerospace*, vol. 5, 9 2018.

[66] J. M. Lauenstein, M. C. Casey, R. L. Ladbury, H. S. Kim, A. M. Phan, and A. D. Topper, "Space radiation effects on sic power device reliability," vol. 2021-March, Institute of Electrical and Electronics Engineers Inc., 3 2021.

[67] T. Satoh, K. Osawa, and N. Atsushi, *GaN HEMT for Space Applications*. 2018.

[68] Y. M. Hongchao Yang and Y. Dai, "Progress of structural and electronic properties of diamond: a mini review," *Functional Diamond*, vol. 1, no. 1, pp. 150–159, 2021.

[69] W. Saslow, T. K. Bergstresser, and M. L. Cohen, "Band structure and optical properties of diamond.," *Phys. Rev. Lett.*, vol. 21, pp. 715–715, Sep 1968.

[70] C. J. Wort and R. S. Balmer, "Diamond as an electronic material," *Materials Today*, vol. 11, no. 1, pp. 22–28, 2008.

[71] P.-N. Volpe, P. Muret, J. Pernot, F. Omnès, T. Teraji, F. Jomard, D. Planson, P. Brosselard, N. Dheilly, B. Vergne, and S. Scharnholtz, "High breakdown voltage schottky diodes synthesized on p-type cvd diamond layer," *physica status solidi (a)*, vol. 207, no. 9, pp. 2088–2092, 2010.

[72] B. Baliga, "Power semiconductor device figure of merit for high-frequency applications," 1989.

[73] N. Sanders and E. Kioupakis, "Phonon- and defect-limited electron and hole mobility of diamond and cubic boron nitride: A critical comparison," *Applied Physics Letters*, vol. 119, 8 2021.

[74] J. Isberg, J. Hammersberg, E. Johansson, T. Wikstrom, D. J. Twitchen, A. J. Whitehead, S. E. Coe, and G. A. Scarsbrook, "High carrier mobility in single-crystal plasma-deposited diamond," *Science*, vol. 297, pp. 1670–1672, 9 2002.

[75] P. Siddiqua, M. S. Shur, and S. K. O'Leary, "Electron transport within bulk cubic boron nitride: A monte carlo simulation analysis," *Journal of Applied Physics*, vol. 128, 11 2020.

[76] J. P. Goss, P. R. Briddon, M. J. Rayson, S. J. Sque, and R. Jones, "Vacancy-impurity complexes and limitations for implantation doping of diamond," *Physical Review B - Condensed Matter and Materials Physics*, vol. 72, 7 2005.

[77] J. P. Goss, P. R. Briddon, R. Sachdeva, R. Jones, and S. J. Sque, "Quantum mechanical modeling of the structure and doping properties of defects in diamond," vol. 772, pp. 91–94, 6 2005.

[78] J. P. Goss, P. R. Briddon, S. J. Sque, and R. Jones, "Boron-hydrogen complexes in diamond," *Physical Review B - Condensed Matter and Materials Physics*, vol. 69, 4 2004.

[79] S. J. Sque, R. Jones, J. P. Goss, and P. R. Briddon, "Shallow donors in diamond: Chalcogens, pnictogens, and their hydrogen complexes," *Physical Review Letters*, vol. 92, p. 4, 2004.

[80] O. Mishima, J. Tanaka, S. Yamaoka, and O. Fukunaga, "High-temperature cubic boron nitride p-n junction diode made at high pressure," *Science*, vol. 238, pp. 181–183, Oct. 1987.

[81] O. Mishima, K. Era, J. Tanaka, and S. Yamaoka, "Ultraviolet light-emitting diode of a cubic boron nitride pn junction made at high pressure," *Applied Physics Letters*, vol. 53, pp. 962–964, 1988.

[82] T. Joshi, P. Kumar, B. Poudyal, S. P. Russell, P. Manchanda, and P. Dev, "Doping limitations of cubic boron nitride: Effects of unintentional defects on shallow doping," *Phys. Rev. B*, vol. 105, p. 054101, Feb 2022.

[83] X. Li, S. Feng, X. Liu, L. Hou, Y. Gao, Q. Wang, N. Liu, H. Zhang, Z. Chen, J. Zheng, and G. Jia, "Investigation on cubic boron nitride crystals doped with si by high temperature thermal diffusion," *Applied Surface Science*, vol. 308, pp. 31–37, 7 2014.

[84] E. M. Shishonok, A. R. Philipp, N. A. Shishonok, and N. G. Anichenko, "Luminescence in cubic boron nitride doped by rare-earth impurity," *Physica Status Solidi (B) Basic Research*, vol. 242, pp. 1700–1704, 7 2005.

[85] E. M. Shishonok, V. G. Luhin, and J. W. Steeds, "Xrd doping control of light-emitting cbn with a large size mismatch between the dopant and intrinsic atoms," *World Journal of Engineering and Technology*, vol. 04, pp. 174–185, 2016.

[86] J. Ying, X. W. Zhang, Z. G. Yin, H. R. Tan, S. G. Zhang, and Y. M. Fan, "Electrical transport properties of the si-doped cubic boron nitride thin films prepared by in situ cosputtering," *Journal of Applied Physics*, vol. 109, 1 2011.

[87] B. He, W. J. Zhang, Y. S. Zou, Y. M. Chong, Q. Ye, A. L. Ji, Y. Yang, I. Bello, S. T. Lee, and G. H. Chen, "Electrical properties of be-implanted polycrystalline cubic boron nitride films," *Applied Physics Letters*, vol. 92, 2008.

[88] T. Taniguchi, T. Teraji, S. Koizumi, K. Watanabe, and S. Yamaoka, "Appearance of n-type semiconducting properties of cbn single crystals grown at high pressure," *Japanese Journal of Applied Physics, Part 2: Letters*, vol. 41, 2 2002.

[89] A. Haque and J. Narayan, "Tunable n-type conductivity and transport properties of cubic boron nitride via carbon doping," *ACS Applied Electronic Materials*, vol. 3, pp. 1359–1367, 3 2021.

[90] K. Kojima, K. Nose, M. Kambara, and T. Yoshida, "Effects of magnesium doping on growth and electric conductivity of nanocrystalline cubic boron nitride thin films," *Journal of Physics D: Applied Physics*, vol. 42, 2009.

[91] K. Hirama, Y. Taniyasu, H. Yamamoto, and K. Kumakura, "Control of n-type electrical conductivity for cubic boron nitride (c-bn) epitaxial layers by si doping," *Applied Physics Letters*, vol. 116, 4 2020.

[92] D. Dolgos, *Full-Band Monte Carlo Simulation of Single Photon Avalanche Diodes*. PhD thesis, Eidgenössische Technische Hochschule (ETH) Zürich, 2011.

[93] D. Dolgos, H. Meier, A. Schenk, and B. Witzigmann, "Full-band monte carlo simulation of high-energy carrier transport in single photon avalanche diodes with multiplication layers made of inp, inalas, and gaas," *Journal of Applied Physics*, vol. 111, p. 104508, 2012.

[94] D. Dolgos, H. Meier, A. Schenk, and B. Witzigmann, "Full-band monte carlo simulation of single photon avalanche diodes," in *2013 IEEE Photonics Conference*, pp. 360–361, 2013.

[95] E. X. Wang, M. D. Giles, S. Yu, F. A. Leon, A. Hiroki, and S. Odanaka, "Recursive m-tree method for 3-d adaptive tetrahedral mesh refinement and its application to brillouin zone discretization," pp. 67–68, 1996.

[96] C. Jungemann and B. Meinerzhagen, *Hierarchical Device Simulation The Monte-Carlo Perspective*. Springer-Verlag Wien, first ed., 2003.

[97] G. Karlowatz, E. Ungersboeck, W. Wessner, and H. Kosina, "Full-band monte carlo analysis of electron transport in arbitrarily strained silicon," in *2006 International Conference on Simulation of Semiconductor Processes and Devices*, pp. 63–66, 2006.

[98] G. Karlowatz, W. Wessner, and H. Kosina, "Effect of band structure discretization on the performance of full-band monte carlo simulation," *Mathematics and Computers in Simulation*, vol. 79, pp. 972 – 979, 2008. 5th Vienna International Conference on Mathematical Modelling/Workshop on Scientific Computing in Electronic Engineering of the 2006 International Conference on Computational Science/Structural Dynamical Systems: Computational Aspects.

[99] E. Leitner and S. Selberherr, "Three-dimensional grid adaptation using a mixed-element decomposition method," pp. 464–467, Springer Vienna, 1995.

[100] B. Fischer and K. R. Hofmann, "Discretization of the brillouin zone by an octree/delaunay method with application to full-band monte carlo transport simulation," pp. 181–184, Springer Vienna, 1998.

[101] D. R. Naylor, A. Dyson, and B. K. Ridley, "Steady-state and transient electron transport in bulk gan employing an analytic bandstructure," *Solid State Communications*, vol. 152, pp. 549 – 551, 2012.

[102] J. Bardeen and W. Shockley, "Deformation potentials and mobilities in non-polar crystals," *Phys. Rev.*, vol. 80, pp. 72–80, 10 1950.

[103] C. Herring and E. Vogt, "Transport and deformation-potential theory for many-valley semiconductors with anisotropic scattering," *Phys. Rev.*, vol. 101, pp. 944–961, 2 1956.

[104] J. Hammersberg, S. Majdi, K. K. Kovi, N. Suntornwipat, M. Gabrysch, D. J. Twitchen, and J. Isberg, "Stability of polarized states for diamond valleytronics," *Applied Physics Letters*, vol. 104, 6 2014.

[105] R. M. Martin, L. Reining, and D. M. Ceperley, *Interacting Electrons: Theory and Computational Approaches*. Cambridge University Press, 5 2016.

[106] M. Born and V. Fock, "Beweis des adiabatensatzes," *Zeitschrift für Physik*, vol. 51, pp. 165–180, Mar 1928.

[107] V. Fock, "Chapter 4 proof of the adiabatic theorem," in *V.A. Fock - Selected Works Quantum Mechanics and Quantum Field Theory* (L. Faddeev, L. Khalfin, and I. Komarov, eds.), pp. 69–86, CRC Press, 2004.

[108] M. Born and R. Oppenheimer, "Zur quantentheorie der molekeln," *Annalen der Physik*, vol. 389, pp. 457–484, 1927.

[109] R. M. Martin, *Electronic Structure: Basic Theory and Practical Methods*. Cambridge University Press, 4 2004.

[110] H. A. Jahn, E. Teller, and F. G. Donnan, "Stability of polyatomic molecules in degenerate electronic states - i—orbital degeneracy," *Proceedings of the Royal Society of London. Series A - Mathematical and Physical Sciences*, vol. 161, no. 905, pp. 220–235, 1937.

[111] *CRAY-1 COMPUTER SYSTEMS HARDWARE REFERENCE MANUAL*, 1982.

[112] *The CRAY-2 Computer System*, 1985.

[113] T. Sato, "The earth simulator: Roles and impacts," *Nuclear Physics B - Proceedings Supplements*, vol. 129-130, pp. 102–108, 2004. Lattice 2003.

[114] B. R. D., M. Berrill, E. Markus, J. G. R., J. Wayne, N. Stephen, R. D. M., T. Arnold, and B. M. O. E, "Ready for the frontier: Preparing applications for the world's first exascale system," in *High Performance Computing* (Jeff, B. Marc, K. C. B. Abhinav, and Hammond, eds.), pp. 182–201, Springer Nature Switzerland, 2023.

[115] T. Smith, "An exabyte of disk storage at CERN — home.cern." https://www.home.cern/news/news/computing/exabyte-disk-storage-cern, 2023. [Accessed 20-08-2024].

[116] D. R. Hartree, "The wave mechanics of an atom with a non-coulomb central field part i theory and methods," *Mathematical Proceedings of the Cambridge Philosophical Society*, vol. 24, pp. 89–110, 1928.

[117] V. Fock, "'Selfconsistent field' mit austausch für natrium," *Zeitschrift für Physik*, vol. 62, pp. 795–805, 1930.

[118] V. Fock, "Näherungsmethode zur lösung des quantenmechanischen mehrkörperproblems," *Zeitschrift für Physik*, vol. 61, pp. 126–148, 1 1930.

[119] D. R. Hartree and W. Hartree, "Self-consistent field, with exchange, for beryllium," *Proceedings of the Royal Society of London. Series A - Mathematical and Physical Sciences*, vol. 150, pp. 9–33, 1935.

[120] P. Hohenberg and W. Kohn, "Inhomogeneous electron gas," *Phys. Rev.*, vol. 136, p. B864–B871, 11 1964.

[121] W. Kohn and L. J. Sham, "Self-consistent equations including exchange and correlation effects," *Phys. Rev.*, vol. 140, p. A1133–A1138, 11 1965.

[122] M. Levy, "Universal variational functionals of electron densities, first-order density matrices, and natural spin-orbitals and solution of the v-representability problem," *Proceedings of the National Academy of Sciences of the United States of America*, vol. 76, no. 12, pp. 6062–6065, 1979.

[123] D. C. Langreth and J. P. Perdew, "Theory of nonuniform electronic systems. i. analysis of the gradient approximation and a generalization that works," *Phys. Rev. B*, vol. 21, pp. 5469–5493, Jun 1980.

[124] D. C. Langreth and M. J. Mehl, "Easily implementable nonlocal exchange-correlation energy functional," *Phys. Rev. Lett.*, vol. 47, pp. 446–450, Aug 1981.

[125] D. C. Langreth and M. J. Mehl, "Beyond the local-density approximation in calculations of ground-state electronic properties," *Phys. Rev. B*, vol. 28, pp. 1809–1834, Aug 1983.

[126] J. P. Perdew, K. Burke, and M. Ernzerhof, "Generalized gradient approximation made simple," *Phys. Rev. Lett.*, vol. 77, pp. 3865–3868, Oct 1996.

[127] J. Heller, *Catch-22*. Corgi, 1979.

[128] P. Haynes and M. Payne, "Localised spherical-wave basis set for o(n) total-energy pseudopotential calculations," *Computer Physics Communications*, vol. 102, no. 1, pp. 17–27, 1997.

[129] S. Baroni, S. de Gironcoli, A. Dal Corso, and P. Giannozzi, "Phonons and related crystal properties from density-functional perturbation theory," *Rev. Mod. Phys.*, vol. 73, pp. 515–562, Jul 2001.

[130] P. Güttinger, "Das verhalten von atomen im magnetischen drehfeld," *Zeitschrift für Physik*, vol. 73, pp. 169–184, 3 1932.

[131] R. P. Feynman, "Forces in molecules," *Phys. Rev.*, vol. 56, pp. 340–343, 8 1939.

[132] W. Pauli, "Principles of wave mechanics," *Handbuch der Physik*, vol. 24, p. 162, 1933.

[133] H. Hellmann, *Einführung in die Quantenchemie*. Deuticke, Leipzig and Wien, 1937.

[134] R. M. Sternheimer, "Electronic polarizabilities of ions from the hartree-fock wave functions," *Phys. Rev.*, vol. 96, pp. 951–968, 11 1954.

[135] G. D. Mahan, "Modified sternheimer equation for polarizability," *Phys. Rev. A*, vol. 22, pp. 1780–1785, 11 1980.

[136] R. F. Pierret, *Advanced Semiconductor Fundamentals*. Pearson Education, 2003.

[137] B. Klingner, *Tetrahedral Mesh Improvement*. PhD thesis, epartment of Electrical Engineering and Computer Sciences University of California at Berkeley, 2008.

[138] G. Gilat and L. J. Raubenheimer, "Accurate numerical method for calculating frequency-distribution functions in solids," *Phys. Rev.*, vol. 144, pp. 390–395, 4 1966.

[139] L. J. Raubenheimer and G. Gilat, "Accurate numerical method of calculating frequency distribution functions in solids. ii. extension to hcp crystals," *Phys. Rev.*, vol. 157, pp. 586–599, 5 1967.

[140] Z. Kam and G. Gilat, "Accurate numerical method for calculating frequency distribution functions in solids. iii. extension to tetragonal crystals," *Phys. Rev.*, vol. 175, pp. 1156–1163, 5 1968.

[141] E. Finkman, Z. Kam, E. Cohen, and G. Gilat, "Accurate numerical method for calculating spectra in solids—iv. extension to trigonal crystals," *Journal of Physics and Chemistry of Solids*, vol. 32, pp. 2423–2427, 1971.

[142] G. Gilat, "General analytic method of zone integration for joint densities of states in metals," *Phys. Rev. B*, vol. 26, pp. 2243–2246, 8 1982.

[143] J. E. Müller and J. W. Wilkins, "Band-structure approach to the x-ray spectra of metals," *Phys. Rev. B*, vol. 29, pp. 4331–4348, 4 1984.

[144] Z. Li, P. Graziosi, and N. Neophytou, "Deformation potential extraction and computationally efficient mobility calculations in silicon from first principles," *Physical Review B*, vol. 104, 11 2021.

[145] Q. L. Yang, W. Li, Z. Wang, F. L. Ning, and J. W. Luo, "Uncovering the important role of transverse acoustic phonons in the carrier-phonon scattering in silicon," *Physical Review B*, vol. 109, 3 2024.

[146] M. Zhu, M. Matsubara, and E. Bellotti, "Carrier transport in cubic boron nitride: First-principles and semiempirical models," *Physical Review Applied*, vol. 20, 9 2023.

[147] M. V. Fischetti, "Monte carlo simulation of transport in technologically significant semiconductors of the diamond and zinc-blende structures. i. homogeneous transport," *IEEE Transactions on Electron Devices*, vol. 38, pp. 634–649, 1991.

[148] P. Giannozzi, S. Baroni, N. Bonini, M. Calandra, R. Car, C. Cavazzoni, D. Ceresoli, G. L. Chiarotti, M. Cococcioni, I. Dabo, A. D. Corso, S. D. Gironcoli, S. Fabris, G. Fratesi, R. Gebauer, U. Gerstmann, C. Gougoussis, A. Kokalj, M. Lazzeri, L. Martin-Samos,

N. Marzari, F. Mauri, R. Mazzarello, S. Paolini, A. Pasquarello, L. Paulatto, C. Sbraccia, S. Scandolo, G. Sclauzero, A. P. Seitsonen, A. Smogunov, P. Umari, and R. M. Wentzcovitch, "Quantum espresso: A modular and open-source software project for quantum simulations of materials," *Journal of Physics Condensed Matter*, vol. 21, 2009.

[149] P. Giannozzi, O. Andreussi, T. Brumme, O. Bunau, M. B. Nardelli, M. Calandra, R. Car, C. Cavazzoni, D. Ceresoli, M. Cococcioni, N. Colonna, I. Carnimeo, A. D. Corso, S. D. Gironcoli, P. Delugas, R. A. Distasio, A. Ferretti, A. Floris, G. Fratesi, G. Fugallo, R. Gebauer, U. Gerstmann, F. Giustino, T. Gorni, J. Jia, M. Kawamura, H. Y. Ko, A. Kokalj, E. Kücükbenli, M. Lazzeri, M. Marsili, N. Marzari, F. Mauri, N. L. Nguyen, H. V. Nguyen, A. Otero-De-La-Roza, L. Paulatto, S. Poncé, D. Rocca, R. Sabatini, B. Santra, M. Schlipf, A. P. Seitsonen, A. Smogunov, I. Timrov, T. Thonhauser, P. Umari, N. Vast, X. Wu, and S. Baroni, "Advanced capabilities for materials modelling with quantum espresso," *Journal of Physics Condensed Matter*, vol. 29, 10 2017.

[150] H. Lee, S. Poncé, K. Bushick, S. Hajinazar, J. Lafuente-Bartolome, J. Leveillee, C. Lian, J. M. Lihm, F. Macheda, H. Mori, H. Paudyal, W. H. Sio, S. Tiwari, M. Zacharias, X. Zhang, N. Bonini, E. Kioupakis, E. R. Margine, and F. Giustino, "Electron–phonon physics from first principles using the epw code," *npj Computational Materials*, vol. 9, 12 2023.

[151] C. Hartwigsen, S. Goedecker, and J. Hutter, "Relativistic separable dual-space gaussian pseudopotentials from h to rn," *Phys. Rev. B*, vol. 58, pp. 3641–3662, Aug 1998.

[152] M. Krack, "Pseudopotentials for h to kr optimized for gradient-corrected exchange-correlation functionals," *Theoretical Chemistry Accounts*, vol. 114, pp. 145–152, Sep 2005.

[153] S. Goedecker, M. Teter, and J. Hutter, "Separable dual-space gaussian pseudopotentials," *Phys. Rev. B*, vol. 54, pp. 1703–1710, Jul 1996.

[154] D. R. Hamann, "Optimized norm-conserving vanderbilt pseudopotentials," *Phys. Rev. B*, vol. 88, p. 085117, Aug 2013.

[155] D. Vanderbilt, "Soft self-consistent pseudopotentials in a generalized eigenvalue formalism," *Phys. Rev. B*, vol. 41, pp. 7892–7895, Apr 1990.

[156] J. Xie, S. P. Chen, J. S. Tse, S. d. Gironcoli, and S. Baroni, "High-pressure thermal expansion, bulk modulus, and phonon structure of diamond," *Phys. Rev. B*, vol. 60, pp. 9444–9449, Oct 1999.

[157] F. Aguado and V. G. Baonza, "Prediction of bulk modulus at high temperatures from longitudinal phonon frequencies: Application to diamond, $c-$BN, and 3$c-$SiC," *Phys. Rev. B*, vol. 73, p. 024111, Jan 2006.

[158] T. Hom, W. Kiszenik, and B. Post, "Accurate lattice constants from multiple reflection measurements. II. Lattice constants of germanium silicon, and diamond," *Journal of Applied Crystallography*, vol. 8, pp. 457–458, Aug 1975.

[159] M. A. Hopcroft, W. D. Nix, and T. W. Kenny, "What is the young's modulus of silicon?," *Journal of Microelectromechanical Systems*, vol. 19, pp. 229–238, 4 2010.

[160] H. J. McSkimin and J. Andreatch, P., "Elastic moduli of diamond as a function of pressure and temperature," *Journal of Applied Physics*, vol. 43, pp. 2944–2948, 07 1972.

[161] P. Scherpelz, M. Govoni, I. Hamada, and G. Galli, "Implementation and validation of fully relativistic gw calculations: Spin–orbit coupling in molecules, nanocrystals, and solids," *Journal of Chemical Theory and Computation*, vol. 12, pp. 3523–3544, Aug 2016.

[162] P. Lam, R. Wentzcovitch, and M. Cohen, "High density phases of bn," in *Synthesis and Properties of Boron Nitride*, vol. 54 of *Materials Science Forum*, pp. 165–192, Trans Tech Publications Ltd, 1 1990.

[163] J. P. Perdew, R. G. Parr, M. Levy, and J. L. Balduz, "Density-functional theory for fractional particle number: Derivative discontinuities of the energy," *Phys. Rev. Lett.*, vol. 49, pp. 1691–1694, Dec 1982.

[164] J. P. Perdew and M. Levy, "Physical content of the exact kohn-sham orbital energies: Band gaps and derivative discontinuities," *Phys. Rev. Lett.*, vol. 51, pp. 1884–1887, Nov 1983.

[165] L. J. Sham and M. Schlüter, "Density-functional theory of the band gap," *Phys. Rev. B*, vol. 32, pp. 3883–3889, Sep 1985.

[166] J. P. Perdew, M. Ernzerhof, and K. Burke, "Rationale for mixing exact exchange with density functional approximations," *The Journal of Chemical Physics*, vol. 105, pp. 9982–9985, 12 1996.

[167] A. D. Becke, "Density-functional thermochemistry. iii. the role of exact exchange," *The Journal of Chemical Physics*, vol. 98, pp. 5648–5652, 04 1993.

[168] C. Lee, W. Yang, and R. G. Parr, "Development of the colle-salvetti correlation-energy formula into a functional of the electron density," *Phys. Rev. B*, vol. 37, pp. 785–789, Jan 1988.

[169] S. Chen, L. Liu, and T. Wang, "Investigation of the mechanical properties of thin films by nanoindentation, considering the effects of thickness and different coating–substrate combinations," *Surface and Coatings Technology*, vol. 191, no. 1, pp. 25–32, 2005.

[170] J. Czochralski, "Ein neues verfahren zur messung der kristallisationsgeschwindigkeit der metalle," *Zeitschrift für Physikalische Chemie*, vol. 92U, no. 1, pp. 219–221, 1918.

[171] C. Canali and G. Ottaviani, "Saturation values of the electron drift velocity in silicon between 300°k and 4.2°k," *Physics Letters A*, vol. 32, no. 3, pp. 147–148, 1970.

[172] C. Jacoboni, C. Canali, G. Ottaviani, and A. A. Quaranta, "A review of some charge transport properties of silicon," *Solid-State Electronics*, vol. 20, pp. 77–89, 1977.

[173] H. Barber, "Effective mass and intrinsic concentration in silicon," *Solid-State Electronics*, vol. 10, no. 11, pp. 1039–1051, 1967.

[174] A. J. Morris, R. J. Nicholls, C. J. Pickard, and J. R. Yates, "Optados: A tool for obtaining density of states, core-level and optical spectra from electronic structure codes," *Computer Physics Communications*, vol. 185, pp. 1477–1485, 2014.

[175] C. Canali, C. Jacoboni, F. Nava, G. Ottaviani, and A. Alberigi-Quaranta, "Electron drift velocity in silicon," *Phys. Rev. B*, vol. 12, pp. 2265–2284, 9 1975.

[176] S. Poncé, E. R. Margine, and F. Giustino, "Towards predictive many-body calculations of phonon-limited carrier mobilities in semiconductors," *Phys. Rev. B*, vol. 97, p. 121201, Mar 2018.

[177] F. Nava, C. Canali, C. Jacoboni, L. Reggiani, and S. Kozlov, "Electron effective masses and lattice scattering in natural diamond," *Solid State Communications*, vol. 33, no. 4, pp. 475–477, 1980.

[178] K. Tsukioka, "Scattering mechanisms of carriers in natural diamond," *Japanese Journal of Applied Physics*, vol. 40, p. 3108, may 2001.

[179] K. Tsukioka, "Energy distributions and scattering mechanisms of carriers in diamond," *Diamond and Related Materials*, vol. 18, pp. 792–795, 5 2009.

[180] J. Pernot, C. Tavares, E. Gheeraert, E. Bustarret, M. Katagiri, and S. Koizumi, "Hall electron mobility in diamond," *Applied Physics Letters*, vol. 89, p. 122111, 2006.

[181] S. Majdi, M. Gabrysch, K. K. Kovi, N. Suntornwipat, I. Friel, and J. Isberg, "Low temperature conduction-band transport in diamond," *Applied Physics Letters*, vol. 109, 10 2016.

[182] V. Djurberg, S. Majdi, N. Suntornwipat, and J. Isberg, "Determination of the acoustic phonon deformation potentials in diamond," *Physical Review B*, vol. 106, p. 045205, 7 2022.

[183] C. Jacoboni and L. Reggiani, "The monte carlo method for the solution of charge transport in semiconductors with applications to covalent materials," *Rev. Mod. Phys.*, vol. 55, pp. 645–705, Jul 1983.

[184] J. Isberg, M. Gabrysch, S. Majdi, and D. J. Twitchen, "Negative electron mobility in diamond," *Applied Physics Letters*, vol. 100, 4 2012.

[185] W. C. Walker and J. Osantowski, "Ultraviolet optical properties of diamond," *Phys. Rev.*, vol. 134, pp. A153–A157, Apr 1964.

[186] W. Saslow, T. K. Bergstresser, and M. L. Cohen, "Band structure and optical properties of diamond," *Phys. Rev. Lett.*, vol. 16, pp. 354–356, Feb 1966.

[187] L. J. Warren, R. G. Wenzel, and J. L. Yarnell, "Dispersion curves for phonons in diamond," in *Inelastic Scattering of Neutrons Vol I Proceedings of the Symposium on Inelastic Scattering of Neutrons*, (International Atomic Energy Agency (IAEA)), pp. 361–371, IAEA, 1965.

[188] J. L. Warren, J. L. Yarnell, G. Dolling, and R. A. Cowley, "Lattice dynamics of diamond," *Phys. Rev.*, vol. 158, pp. 805–808, Jun 1967.

[189] S.-F. Wang, Y.-F. Hsu, J.-C. Pu, J. C. Sung, and L. Hwa, "Determination of acoustic wave velocities and elastic properties for diamond and other hard materials," *Materials Chemistry and Physics*, vol. 85, no. 2, pp. 432–437, 2004.

[190] E. Gheeraert, N. Casanova, S. Koizumi, T. Teraji, and H. Kanda, "Low temperature excitation spectrum of phosphorus in diamond," *Diamond and Related Materials*, vol. 10, no. 3, pp. 444–448, 2001. 11th European Conference on Diamond, Diamond-like Materials, Carbon Nanotubes, Nitrides and Silicon Carbide.

[191] H. Löfås, A. Grigoriev, J. Isberg, and R. Ahuja, "Effective masses and electronic structure of diamond including electron correlation effects in first principles calculations using the gw-approximation," *AIP Advances*, vol. 1, p. 032139, 08 2011.

[192] N. Naka, K. Fukai, Y. Handa, and I. Akimoto, "Direct measurement via cyclotron resonance of the carrier effective masses in pristine diamond," *Phys. Rev. B*, vol. 88, p. 035205, Jul 2013.

[193] H. Jansen, *Chemical Vapour Deposition Diamond Charge Carrier Movement at Low Temperatures and Use in Time-Critical Applications*. PhD thesis, Bonn University, Faculty of Mathematics and Natural Sciences, Department of Physics, 2013.

[194] J. Chilleri, P. Siddiqua, M. S. Shur, and S. K. O'Leary, "Cubic boron nitride as a material for future electron device applications: A comparative analysis," *Applied Physics Letters*, vol. 120, 3 2022.

[195] J. Chilleri, Y. Wang, and S. K. O'Leary, "Threading dislocation lines and their impact on bulk cubic boron nitride's low-field electron transport response," *Solid State Communications*, vol. 356, 11 2022.

[196] J. Chilleri, Y. Wang, M. S. Shur, and S. K. O'Leary, "A low-field electron mobility analysis of cubic boron nitride," *Solid State Communications*, vol. 352, 9 2022.

[197] Y.-N. Xu and W. Y. Ching, "Calculation of ground-state and optical properties of boron nitrides in the hexagonal, cubic, and wurtzite structures," *Phys. Rev. B*, vol. 44, pp. 7787–7798, Oct 1991.

[198] P. Rodríguez-Hernández, M. González-Diaz, and A. Muñoz, "Electronic and structural properties of cubic bn and bp," *Phys. Rev. B*, vol. 51, pp. 14705–14708, May 1995.

[199] M. Ferhat, A. Zaoui, M. Certier, and H. Aourag, "Electronic structure of bn, bp and bas," *Physica B: Condensed Matter*, vol. 252, no. 3, pp. 229–236, 1998.

[200] P. Siddiqua and S. K. O'Leary, "Electron transport within the wurtzite and zinc-blende phases of gallium nitride and indium nitride," *Journal of Materials Science: Materials in Electronics*, vol. 29, pp. 3511–3567, 3 2018.

[201] R. M. Yorston, "Free-flight time generation in the monte carlo simulation of carrier transport in semiconductors," *Journal of Computational Physics*, vol. 64, no. 1, pp. 177–194, 1986.